Steam reforming of methane ans ethanol over Co Mg Al , Ru/Co Mg Al and Cu/Co Mg Al catalysts

Doris Homsi

STEAM REFORMING OF METHANE AND ETHANOL OVER $Co_xMg_{6-x}Al_2$, $Ru/Co_xMg_{6-x}Al_2$ AND $Cu/Co_xMg_{6-x}Al_2$ CATALYSTS

By

Doris Homsi El Murr

A thesis submitted to the Department of Chemistry in partial fulfillment of the requirements for the doctor's degree in Chemistry

Faculty of Sciences – University of Balamand

And

Unité de Chimie Environnementale et Interaction sur le Vivant – Université du Littoral Côte d'Opale

December 2012

University of Balamand

Faculty of Sciences

This is to certify that I have examined this copy of a PhD thesis by

Doris Homsi El Murr

and have found that it is complete and satisfactory in all respects,
and that any and all revisions required by the final
examining jury have been made.

JURY MEMBERS:

Approved: ----------
Antoine Aboukaïs, Ph.D.
President of the Jury

Approved: ----------
Béchara Taouk, Ph.D.
External Reporter

Approved: ----------
Madona Labaki, Ph.D.
External Reporter

Approved: ----------
Cédric Gennequin, Ph.D.
External Examiner

Approved: ----------
Toufic Wéhbe, Ph.D.
External Examiner

Approved: ----------

Bilal Nsouli, Ph.D.

External Examiner

Approved: ----------

Edmond Abi-Aad, Ph.D.

Co-Supervisor

Approved: ----------

Samer Aouad, Ph.D.

Co-Supervisor

Date of thesis defense: December 14, 2012

To my beloved family, "Mom", "Dad", "Elian", "Maya" and "Melanie"

To my precious husband "Wissam"

ACKNOWLEDGMENT

This thesis could not have been written without many people's help and encouragement.

*I would first like to thank the **AUF** and **CNRS-L** for their financial support and for giving me the opportunity to work on my thesis in France and Lebanon.*

*My gratitude goes to **Pr. Pirouz SHIRALI**, director of the U.C.E.I.V. at the University of Littoral Côte d'Opale and **Dr. Jihad ATTIEH**, Dean of the Faculty of Sciences at the University of Balamand for their efforts and help.*

*I greatly appreciate **Pr. Edmond ABI-AAD** my supervisor at the University of Littoral Côte d'Opale for giving me confidence to work with him and his continuous inspiring supervision and productive suggestions and discussions during my stay in France.*

*I would also like to express my gratitude to **Dr. Samer AOUAD** for his supervision at the University of Balamand, step-by-step guidance, encouragement and great help throughout the entire work.*

*I would like to express my full gratitude to **Pr. Antoine ABOUKAIS**, President of my jury, for his help and stimulating discussion about research issues and EPR spectra. I was fortunate enough to know and work with him.*

*My gratitude goes to **Dr. Cédric GENNEQUIN**, for his time, valuable councils, and for his great sympathy.*

*Special thanks to **Dr. Hanna EL NAKAT** for his extensive advice and support during my study at UOB. I cannot forget his love, encouragement and readiness either.*

*I would like to thank sincerely the team working at the U.O.B. **(Mrs. Amal EL MURR**, **Miss Mira YOUNIS**, **Miss Dima MOUSSA**, **Mr. Bilal KHOURY**) and U.C.E.I.V. (**Pr. Dominique COURCOT**, **Pr. Stéphane SIFFERT**, **Dr. Lucette TIDAHY**, **Dr. Helena***

ZHILINSKAYA, ***Dr. Frederic LEDOUX*** *and* ***Dr. Renaud COUSIN****) for their availability, kindness and for providing excellent experimental equipment and facility to fulfill the accurate and reliable experimental tests.*

My gratitude goes also towards my colleagues in the catalysis laboratory for providing a pleasant atmosphere during my stay in France: ***Mira SKAF***, ***Mira NAWFAL***, ***Sara HANI***, ***Mireille BORGIE***, ***Tarek BARAKAT***, ***Adib KFOURY***, ***Dima HAMMOUD***, ***Raya MRAD*** *and* ***Eric GENTY****.*

Special thanks to ***Pr. Madona LABAKI*** *for giving me concrete and non-concrete support and for accepting to judge my work.*

I also thank ***Pr. Bechara TAOUK****, director of the L.S.P.C. for accepting to judge my work.*

Outside supports have been received from the "Physical Chemistry Laboratory" at the ***Lebanese University*** *(Fanar). I would like to thank them for providing me the SEM and EDX results.*

My biggest thanks go to ***my family*** *and* ***husband Wissam*** *for their love, moral support, advice and encouragement throughout not only my Ph.D. studies, but throughout my entire life. Nothing in a simple paragraph can express the love and gratitude I have for them: "You knew that I could do this even before I did".*

ABSTRACT

This work focuses on methane and ethanol conversion to hydrogen in the presence of a catalyst in order to increase the selectivity of the desired product (H_2) and reduce carbon monoxide emission and coke formation. Two kinds of active phase were used (copper and ruthenium) and impregnated on calcined hydrotalcites $Co_xMg_{6-x}Al_2$ in order to be evaluated in the methane and ethanol steam reforming reactions. For both reactions, the influence of several factors was evaluated in order to adjust the reaction parameters. It has been shown that catalysts performances for the reforming reactions depend on the content of cobalt and magnesium. High cobalt content enhanced the catalytic activity. $1Ru/Co_6Al_2$ catalyst presented the highest activity and stability in the methane steam reforming reaction among the other industrial and prepared catalysts even under a low GHSV and with no hydrogen pretreatment. Reduced ruthenium and cobalt were detected after the reaction by XRD. EPR technique was able to detect negligible amount of two kinds of carbonaceous species formed during the reaction: coke and carbon. On the other hand, $5Cu/Co_6Al_2$ catalyst revealed the highest hydrogen productivity in the ethanol steam reforming reaction. However, it suffers from coke formation that deactivated the catalysts after few hours. $5Cu/Co_2Mg_4Al_2$ catalyst showed a much lower quantity of carbonaceous species with no deactivating during 50 hours due to the basic character of the magnesium oxide phase present in the support.

TABLE OF CONTENTS

LIST OF TABLES

LIST OF FIGURES

GENERAL INTRODUCTION

The diversification of energy sources is a characteristic of the evolution of the energy system since the industrial revolution. Fuels have provided and still provide an essential contribution to the economy development. Besides, the most commercial energy in the world is produced currently by the burning of fossil fuels. However, they are now seen as a source that contributes to greenhouse effect through their emission to polluting compounds. In this context, hydrogen seems to be a promising energy vector that provides clean energy for transportation, residential and industrial sectors by lowering the emission of many pollutants (aromatics, particulates, alkenes…) compared to emissions from combustion of pure gasoline or diesel fuel [1]. It can be used either as a fuel for direct combustion in an internal combustion engines or in fuel cells [2]. It can be produced through different methods (electrolysis, thermolysis, photolysis…) however it is primarily produced in small scale "reformers" or large scale through steam reforming reactions (hydrocarbons or alcohols). Currently, the steam reforming of hydrocarbons includes almost 60% of the world feedstock for hydrogen production; in the United States, about 96% of hydrogen is currently produced through steam reforming [3].

Steam reforming of hydrocarbons, especially of methane, which is a principal constituent of biogas (47-65% CH_4), is the most widely used and generally the most economically competitive method for hydrogen production [4, 5]. Methane usually yields 4 moles of hydrogen for every mole of feed stock; therefore it is advantageous when hydrogen production needs to be maximized [6]. It should be noted that biogas methane energy is a green and renewable technology that uses various forms of biomass (animal dung, crop waste) and converts it into a useful energy source in the form of a gas, via anaerobic microbial digestion. Biogas is now the fifth of global energy consumption and it is considered the fossil fuel of the century. However, it can contain impurities such as

halogens and sulfur that can damage the fuel cell system if no clean-up treatment is performed [7].

Ethanol steam reforming reaction is another alternative for hydrogen production. Ethanol is non-toxic and available as it can be produced renewably by fermentation of biomass [8]. Since the 1970s, Brazil has started developing ethanol as a major fuel source. More recently, the USA has become a major ethanol producer, with production doubling from 8 billion $L.yr^{-1}$ in 2002 to 15 billion $L.yr^{-1}$ in 2005 and increasing further by 25% to 20 billion $L.yr^{-1}$ in 2006 [3]. However, on a large industrial scale, ethanol steam reforming is not feasible and competitive as methane steam reforming because it produces the lowest energy gain (50 $MJ.kg^{-1}$ and 26.9 $MJ.kg^{-1}$ for methane and ethanol respectively) [9].

This thesis focuses on the above mentioned reactions by optimizing several parameters. In order to obtain sufficiently high reaction rates, the steam reforming reaction has to be catalyzed. A catalyst must have sufficient selectivity to the desired products and reduce the production of CO and coke. In this study, two kinds of catalysts have been developed: systems based on noble metal (ruthenium) and systems based on transition metal (copper). These active phases are impregnated on hydrotalcites. Ruthenium-based catalysts are very selective in the methane steam reforming reactions [10-12] whereas copper-based catalysts show important catalytic activity in the ethanol steam reforming [13, 14]. Due to their low cost, thermal stability and high basicity, hydrotalcites can be used in the steam reforming reaction [15, 16].

After a bibliographic review covering hydrogen energy, methane/ethanol steam reforming reactions, ruthenium and copper-based solids supported on hydrotalcites, chapter 2 focuses on the synthesis of these catalysts and their characterization by several physico-chemical techniques. The third and the fourth chapter of this thesis deal with the evaluation of the catalytic performance in the methane and ethanol steam reforming reactions by

varying several parameters. A series of physico-chemical techniques is performed after test to check the presence of coke and highlight the final state of the catalyst after the reaction. These chapters lead to a conclusion on the performance of the studied catalysts.

CHAPTER 1

BIBLIOGRAPHIC REVIEW

1.1 Introduction

Since a few decades, increasing attention is being paid to global climate and public health problems. Particularly, the automotive sector had to work hard on pollution control being one of the major contributors to the atmospheric pollution. Therefore, both catalytic converters on gasoline-fueled engines and filters for particulates on diesel-fueled engines were implemented [17].

However, in order to overpass the regulations on CO_2 emissions according to the Kyoto's Protocol (in Europe, 8% reduction compared to the 1990s emissions by 2008-2012), the development of both new engines and alternative fuels is required [17].

In fact, the decrease of fossil fuel reserves and the continuous energy demands and crisis make it necessary to develop and adopt renewable and clean energy alternatives independent of fossil fuels. Among them, the use of fuel cells has been recognized as one of the most promising technologies that produce clean energy [18]. It converts the chemical energy stored in a fuel, such as "hydrogen", into an electrical energy output by electrochemical reactions that is able to provide clean and highly efficient electric power for both mobile and stationary applications. If a fuel, such as methane or ethanol, is used, a fuel processor, "reformer", is needed to transform it into hydrogen rich gas so that the fuel cell can perform the electrochemical conversion [19].

Fuel cells can generate power to large scale stationary systems, vehicles engines, as well as to small scale portable power supply devices such as micro-electronic equipment and auxiliary power units (APU) in vehicles [20].

1.2 Hydrogen Energy

Hydrogen is produced commercially on a large scale mainly by reforming of hydrocarbons (steam reforming of natural gas, alcohols and coal gasification) and water (electrolysis, photolysis and thermolysis of water). Its current worldwide production is around 5.10^{11} Nm^3 per year [21]. Hydrogen is an attractive alternative energy vector through its combination with oxygen in fuel cells to produce heat or by conventional flame combustion. Therefore, it is considered as a potential source of energy that can be produced from any available primary energy source which can support sustainable economic growth as well as reduce atmospheric pollution and greenhouse gas emissions [22].

Unfortunately, it is not freely available in nature and it must be produced by some means. And until all technical problems related to storage and transportation of hydrogen are resolved, its generation is expected to be accomplished on site by reformation of various gaseous or liquid feedstock [23]. That's why, its production from steam reforming of natural gas and alcohols is receiving increased attention as a potential source of renewable energy [24].

1.3 Hydrogen Production from Methane

1.3.1 Biogas

Biogas is a mixture of methane and carbon dioxide and is produced by anaerobic digestion of organic matter. The organic matter can consist of sewage, manure, crops… The proportion of CO_2 and CH_4 is dependent on the nature of the substrate. A substrate rich in H and C produces high methane proportions (up to 90%). Moderately rich substrate, such as cellulose, produces biogas containing 55% of CH_4 and 45% of CO_2. Therefore, biogas is a methane rich gas but it can contain impurities difficult to be treated such as

halogens (chlorine and fluorine) coming from toxic wastes and plastics [7]. It must be noted that the produced methane is the same as that of natural gas and has the same commercial value and opposed to natural gas, the use of biogas has an almost zero net CO_2 contribution [25].

1.3.2 Methane Steam Reforming (MSR)

Methane is one of several fuel candidates for on-board reforming, which have been discussed by the automotive industry. Sabatier and Senderens discovered the formation of synthesis gas in the presence of methane and steam [26]. This successful result obtained by steam reforming was first summarized in 1924 by Neumann and Jacob [27], and steam reforming has since then become an important technology for synthesis gas and hydrogen production [28, 29]. In the recent decade, there have been given several reviews on this topic [28-30].

MSR chemical reaction equation (Equation 1.1) can be written as follows:

$$CH_4 + H_2O \leftrightarrow 3\ H_2 + CO \qquad \Delta H° = 206\ kJ.mol^{-1} \qquad \text{(Equation 1.1)}$$

Several reactions can be considered in the methane steam reforming process. A detailed thermodynamic study of the main reactions is displayed in the chapter 3 (section 3.1.2).

1.3.3 Catalysts Used in the Methane Steam Reforming

In order to obtain acceptable rates in many reactions, a catalyst is required to accelerate the process. In the steam reforming of methane, a catalyst can reduce the reaction temperature range and thus avoid the occurrence of side reactions. Moreover, the catalyst should be stable under the rather extreme conditions under which high CH_4

conversions can be reached (i.e., high temperatures and high probabilities of unwanted side reactions involving carbon deposition).

Development has long been conducted around nickel-based component in the steam reforming of hydrocarbons [31-34] and particularly in the steam reforming of methane [35, 36]. Nickel-based catalysts showed an important methane conversion and a high H_2/CO ratio [37] and it has been widely employed as the conventional industrial steam reforming catalyst [38, 39]. However, it suffers from coke formation. Therefore, the development of active steam reforming catalysts with high durability against coking is thus desirable.

Noble metals (Ru, Rh, Pd, Pt…) have gained increasing interest in the methane steam reforming reactions due to their high hydrogen production rates, important activity and stability, and strong resistance to coke formation compared to nickel catalysts [8, 40, 41]. One of the first studies of ranking within steam reforming activity was done by Kikuchi et al. [42], where they measured the relative order in activity at atmospheric conditions and 350-600°C and observed the following order: Rh~Ru > Ni > lr > Pd ~ Pt >> Co, Fe.

Later studies were reported by Rostrup Nielsen and Hansen. They conducted a series of experiments with Ru, Rh, Pd, Pt and Ni on MgO support, measuring steam reforming activity at 550°C and under atmospheric pressure [40]. Relative activities were reported to be: Ru~Rh > Ir > Pt~Pd.

Qin and Lapszewicz [43] performed similar experiments to those of Rostrup-Nielsen [31] with noble metals on a MgO support in the temperature range of 600-800°C and under atmospheric pressure and found an almost identical activity relationship for the noble metal catalysts in methane steam reforming reaction as the two previous mentioned studies: Ru > Rh > Ir > Pt > Pd.

Jakobsen performed several studies on noble metals supported on ZrO_2, Al_2O_3 and $MgAl_2O_4$. He also found the following ranking: Rh~Ru > Ni~Pt~Ir~Pd [9].

To conclude, the above mentioned studies seem to point to a general trend for the order of reactivity among the noble metals: Ru and Rh based catalysts are the most active, Ni and Ir have intermediate activities and Pd and Pt are less active.

Ruthenium has been widely used in the methane steam reforming reaction [7-9, 40-44]. Ru catalysts are also very active in steam reforming reactions under water deficient conditions and very low amount of carbon is formed on catalysts during the reaction without any change to the mechanical properties of the catalyst [7, 45]. They increased the conversion percentage and strongly improved the selectivity for syngas production. It was also reported that Ru-based catalysts, especially Ru supported on magnesia and alumina present high activity and high hydrogen selectivity as well as stable performance [46]. The pronounced reactivity of ruthenium oxide catalysts seem to result from the reducibility of the oxide itself [47]. For example, Ru doped in Ni/Al_2O_3 and Ni/Mg(Al)O exhibited self-activation resulted from the hydrogen spillover via Ru metal and Ru-Ni alloy [8, 48]. In addition, the incorporation of Ru in the lattice of the support favored their reduction behavior, and increased their stability during the reaction leading to a negligible formation of carbonaceous deposits [49].

Ru-based catalysts have been also proved to be among the best catalytic systems for partial oxidation of methane reaction with excellent coke resistance at elevated temperature [50, 51].

Several studies were done in the laboratory on the effect of the addition of ruthenium on CeO_2-Al_2O_3, CeO_2-ZrO_2 supports. They concluded that the presence of ruthenium enhanced the activity of the dry and steam reforming of methane [52, 53].

However, even though noble metal catalysts present higher activity than other metal catalysts, their manufacturing cost remains relatively high. Therefore, efforts are done to develop transition metal oxides catalysts with high activity.

Copper is a transition metal that is extensively used as an active phase to catalyze different types of reactions [54, 55]; however, it is not well-known in the methane steam reforming reaction. It was shown that CuO exhibits a high activity in the catalytic reactions by the release of active oxygen species from Cu (II) species [56] and the increase of the reducibility of the support [57]. In addition, it is reported that the presence of copper as an active metal can suppress carbon formation step and can improve the water gas shift reaction (WGS) in methane steam reforming [58-60]. In fact, Cu played a role in promoting the gasification of deposited carbon, and its addition to Ni led to the enhancement of the WGS activity in the overall process and decreased the coke deposit [58-60]. In addition, a system based on doping $LaCoO_3$ with copper showed that the presence of this metal increased the reducibility of the support in the reaction of alcohols and hydrocarbons synthesis from syngas [57].

Copper is also used in the dry reforming [61] and partial oxidation of methane leading to a high conversion of this latter [62].

1.3.4 Proposed Reaction Mechanism for Methane Steam Reforming Reaction

Several authors [63, 64] pointed out that the methane steam reforming reaction takes place at the metal-support interface, through the reaction between the water adsorbed on the support and the methane adsorbed on the metal. A molecular mechanism of the steam reforming reaction in the presence of $Rh/CeZrO_2$ catalysts is elucidated in table 1.1 (*l* is an active site on the active phase, *S* is an active site on the support) [65].

Table 1.1 Steam reforming molecular reaction mechanism [65]

Elementary steps of the proposed reaction mechanism	
$CH_4 + 2l \leftrightarrow CH_3\text{-}l + H\text{-}l$	(1)
$CH_3 + l \leftrightarrow CH_2\text{-}l + H\text{-}l$	(2)
$CH_2 + l \leftrightarrow CH\text{-}l + H\text{-}l$	(3)
$CH\text{-}l + O\text{-}S \leftrightarrow CHO\text{-}l + S$	(4)
$CHO\text{-}l + S \leftrightarrow CO\text{-}l + H\text{-}S$	(5)
$CO\text{-}l + O\text{-}S \leftrightarrow CO_2\text{-}l + S$	(6)
$CHO\text{-}l + O\text{-}S \leftrightarrow CO_2\text{-}l + H\text{-}S$	(7)
$CO\text{-}l \leftrightarrow CO + l$	(8)
$CO_2\text{-}l \leftrightarrow CO_2 + l$	(9)
$2H\text{-}l \leftrightarrow H_2\text{-}l + l$	(10)
$H_2\text{-}l \leftrightarrow H_2 + l$	(11)
$2H\text{-}S \leftrightarrow H_2\text{-}S + S$	(12)
$H_2\text{-}S \leftrightarrow H_2 + S$	(13)
$H_2O + S \leftrightarrow O\text{-}S + H_2$	(14)

The elementary reaction steps can be explained as follows [65]:

- Steam is dissociatively adsorbed on the support sites (*S*), yielding adsorbed oxygen atoms (lattice oxygen O-*S*) and gaseous hydrogen.
- Methane is dissociatively adsorbed on the active sites (*l*), yielding adsorbed carbon containing species CH_3, CH_2, CH and adsorbed hydrogen atoms.
- The adsorbed CH species on the active sites (*l*) react with the lattice oxygen from the support at the interface (O-*S*) yielding an adsorbed CHO species at the (*l*) sites and a vacant lattice oxygen sites (*S*) at the support
- CHO species interact with the adjacent vacant sites (*S*), yielding adsorbed CO and H atoms, or react in parallel with adjacent lattice oxygen from the support sites (O-*S*) at the interface, yielding adsorbed CO_2 and H atoms.

- Adsorbed CO atoms on (*l*) sites may react with the lattice oxygen at the interface (O-*S*) to produce adsorbed CO_2 atoms at (*l*) sites and a vacant oxygen site (*S*) at the interface or they desorb into the gas phase.
- Formed hydrogen and CO_2 are directly released into the gas phase or are in equilibrium with their adsorbed atoms.
- Surface reactions of adsorbed CHO species and CO molecules with adjacent vacant sites (*S*) or lattice oxygen (O-*S*) resulting in adsorbed CO and CO_2 are considered to be the rate determining steps.
- H_2 resulted either from steam dissociation on the support surface or CH_4 decomposition on the active site can also be dissociatively adsorbed on both surfaces. H_2 adsorbed on the active site surface (step 11) suppresses the sequential loss of H from CH_4 fragments on the active site by accelerating the backward reactions of CH_4 dissociation on the active site surface (steps 1-3). H_2 adsorbed on the support (step 13) reduces the oxidation state of ceria leading to (i) lower rate of H_2O dissociation on the support surface (step 14) and (ii) less lattice oxygen to be incorporated with the adsorbed CHO precursor in the surface reactions (steps 5, 7).

1.4 Hydrogen Production from Ethanol

1.4.1 Ethanol

Natural gas is a fossil fuel. Its use as a secondary energy production is non-sustainable. As a result, there is a growing interest in the search for effective alternatives to produce renewable hydrogen cleanly and safely. Among the various renewable feedstock alternatives, ethanol is very attractive because of its relatively high hydrogen content, good availability, low production costs, non-toxicity, and storage and handling ease and safety.

But one of the most important reasons for choosing ethanol is that it can be produced renewably in large quantities from several biomass sources (energy plants, waste materials from agro-industries or forestry residue materials) and therefore it does not increase the greenhouse effect [66-68].

1.4.2 Ethanol Steam Reforming (ESR)

The production of hydrogen from the ethanol steam reforming could favor the use of hydrogen as an alternative fuel. In this context, the ethanol may represent a potential source for hydrogen production. Its chemical reaction equation can be written according to steam supply as follows:

Ethanol steam reforming reaction with sufficient steam supply:

$CH_3CH_2OH + 3\ H_2O \leftrightarrow 6\ H_2 + 2\ CO_2$ $\Delta H° = 173\ kJ.mol^{-1}$ (Equation 1.2)

Ethanol steam reforming reaction with insufficient steam supply:

$CH_3CH_2OH + H_2O \leftrightarrow 2\ CO + 4\ H_2$ $\Delta H° = 256\ kJ.mol^{-1}$ (Equation 1.3)

Other reactions can take place during the ESR reactions like ethanol decomposition (to CH_3COCH_3, CH_4, CO_2, CO, H_2), dehydration (to ethylene), dehydrogenation (to acetaldehyde)... They are all detailed in chapter 4 (section 4.1.2).

The scheme in figure 1.1 describes the main reactions occurring during the conversion of ethanol to hydrogen. Both the dehydrogenation to the acetaldehyde and dehydration to ethylene occur depending on the nature of the support. Acidic supports - like alumina- induce ethanol dehydration to produce ethylene, which is a precursor of coke formation [69, 70]. However, a high surface basicity will favor dehydrogenation rather than dehydration [70]. Acetaldehyde formed has a very low coking activity and it can be subjected to steam reforming. Therefore, the addition of alkali metals like magnesium has

been suggested to neutralize acid sites and reduce carbon formation by suppressing cracking and polymerization reactions, improving catalyst stability [71, 72].

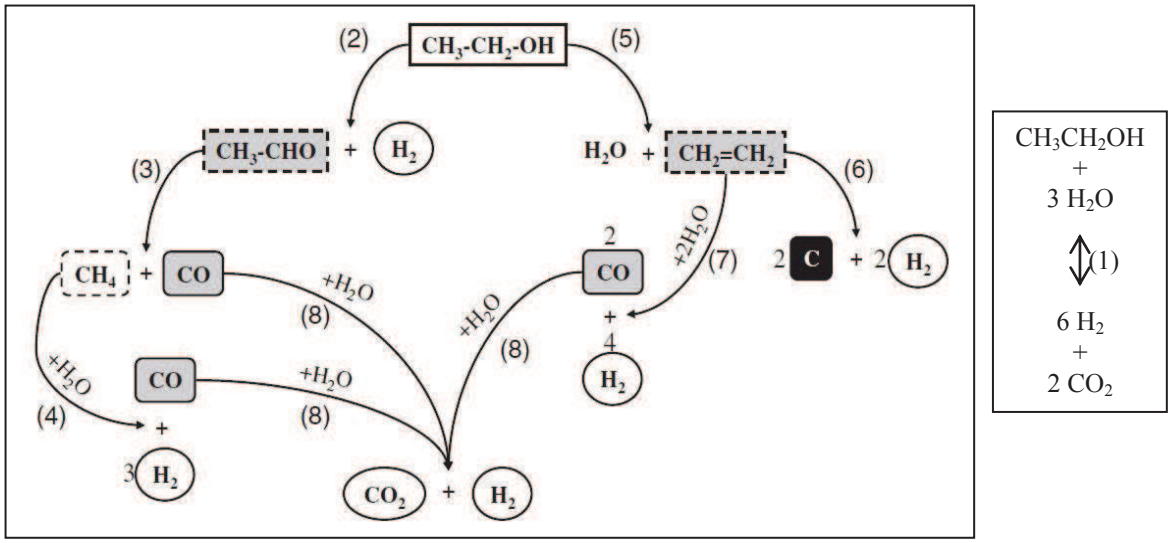

Figure 1.1 Reaction network of ethanol steam reforming [69]

1.4.3 Catalysts Used in the Ethanol Steam Reforming Reaction

Steam reforming has been extensively investigated in the recent years. Several reviews about the development of catalysts applied to ESR have been published [11, 55]. It can be seen that among the two main categories of active phases, Rh and Ni exhibited respectively the best performance in terms of bio-ethanol conversion and hydrogen yield. In fact, the catalysts play a critical role both for driving ethanol conversion towards thermodynamic limits (i.e., complete conversion) but also for achieving a maximum hydrogen production with the highest possible yields.

As mentioned before, noble metal catalysts are well-known for their high catalytic activity in any type of reactions involving hydrocarbon activation, especially when the formation of coke by cracking has to be avoided. For ethanol steam reforming, Rh, Ru, Pd and Pt have been extensively investigated, in combination with conventional non reducible supports like alumina or redox materials able to store/release oxygen like ceria-based

systems. Aupretre et al. [14], has investigated the influence of the noble metal (Rh, Pt) and the role of the support (Al_2O_3, Al_2O_3-CeO_2, CeO_2, $Ce_{0.63}Zr_{0.37}O_2$) for the ethanol steam reforming. It was found that the activity of the catalyst in the reaction increased with increasing OH group mobility at the catalyst surface and that the selectivity of the catalyst towards CO_2 decreased with increasing efficiency of the catalyst in the reverse WGS (RWGS) reaction [14]. In addition, Liguras et al. [73], compared the catalytic performance of Rh, Ru, Pt and Pd catalysts in the temperature range of 600-850°C with a metal loading of 0-5wt%. Ru showed a catalytic activity comparable to Rh at high loading (5wt%). The 5%Ru/Al_2O_3 could completely convert ethanol into syngas with hydrogen selectivity above 95% [73]. Ru over Al_2O_3 and MgO has also been studied in ethanol steam reforming reaction [14, 73-75]. These catalysts were able to completely convert ethanol.

Catalysts using non-noble metals like Cu have been also widely investigated for ethanol steam reforming, essentially for their lower cost as compared to noble metals containing ones. Cu is a good dehydrogenation catalyst [76] and is selected for its activity in the WGSR [14, 70]. Marino et al. [77], have studied the effect of Cu loading on catalytic behavior of $Cu/Ni/K/Al_2O_3$ catalyst. They have found an acceptable performance to hydrogen at low temperature (300°C). From the comparison with monometallic systems, ethanol dehydrogenation and C-C bond rupture were easily favored over Cu and Ni, respectively [77]. It was proposed that Cu is the active agent in the steam reforming. Velu et al. [78], have used Cu-Ni-Mg-Al mixed metal oxide catalysts in oxidative steam reforming of ethanol. They found that the dehydrogenation of ethanol to acetaldehyde is favored by Cu-rich catalysts while the introduction of Ni leads to C-C bond rupture producing CO, CO_2 and CH_4. Freni et al. [79], studied steam reforming of ethanol over Cu/SiO_2 and found that at temperatures in the range 573-723 K, ethanol conversion was

100% and acetaldehyde and H_2 were the major reaction products. Traces of methane and CO were also detected.

$CuO/ZnO/Al_2O_3$, $Cu/Zn/Cr/Al_2O_3$ and $NiO/CuO/SiO_2$ catalysts activity was also measured in ESR at 600-750 K. They exhibit good activity with no traces of oxygenated products (acetic acid, acetaldehyde, ethyl acetate…) and coke [10].

$Cu_{1-x}Ni_xZnAl$ mixed metal oxide has also been used in autothermal reforming of bio-ethanol [78]. But compared to autothermal reforming, steam reforming of bio-ethanol has received more attention due to its relatively higher conversion efficiency [11].

1.4.4 Proposed Reaction Mechanism for Ethanol Steam Reforming Reaction

A mechanistic approach was proposed for ethanol steam reforming reaction by Palma et al. [5]. The following elementary steps in figure 1.2 may describe the process during the reaction, where (ads) is an adsorption site:

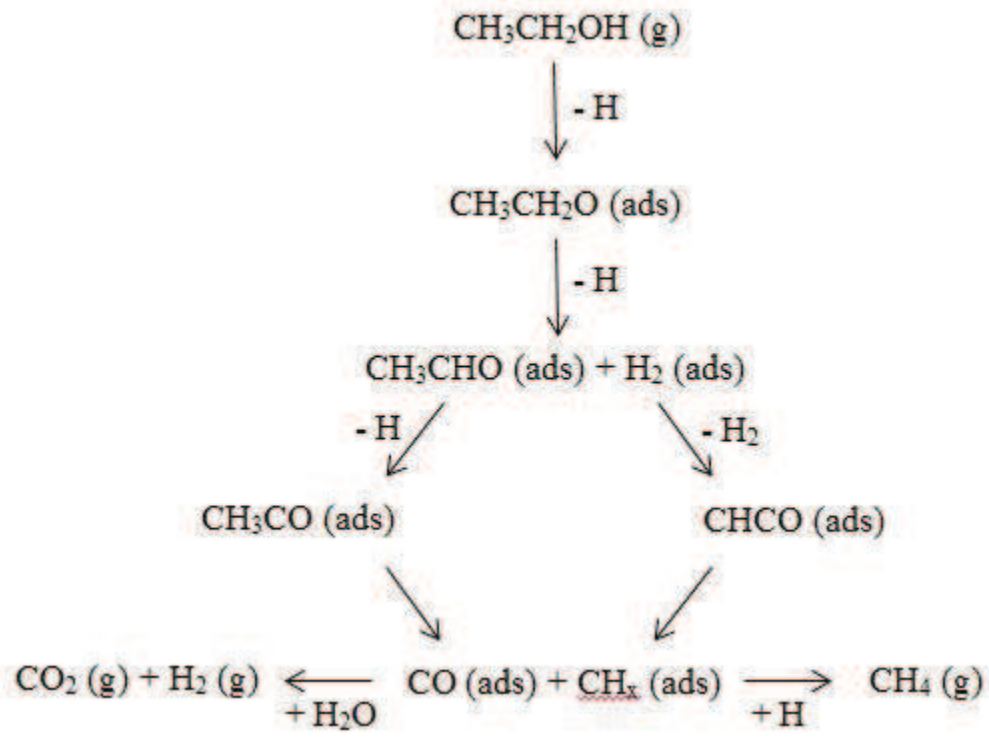

Figure 1.2 Scheme of ESR reaction mechanism [5]

The surface reaction mechanism reported in figure 1.2 involves the following steps:

- Ethanol dissociative adsorption on catalyst surface to form ethoxide then acetaldehyde intermediate
- Acetaldeyde dehydrogenation to form metastable intermediate such as a ketenyl or an acetyl
- C-C bond rupture (decarbonylation) of these intermediates to form CO and CH_x groups
- WGS reaction of CO adsorbed on active sites to produce H_2 and CO_2
- Hydrogenation of CH_x to produced CH_4

1.5 Hydrotalcites or Anionic Clays

1.5.1 Structural Properties

Hydrotalcite-like compounds are layered double hydroxides (LDH) having the following general formula: $[M^{II}_{1-x}M^{III}_{x}(OH)_2]^{x+}(A^{n-})_{x/n}.mH_2O$ (where M is a divalent or trivalent cation, A^{n-} is the interlayer anion that exists in the octahedral positions and *x* varies between 0.2 and 0.33) [80].They have a structure closely related to that of the mineral hydrotalcite $Mg_6Al_2(OH)_{16}CO_3.4H_2O$ [80]. Their structure can be derived from a brucite structure $Mg(OH)_2$ (Figure 1.3) where Mg^{2+} ions (octahedrally surrounded by six OH^- ions) share edges to form infinite sheets.

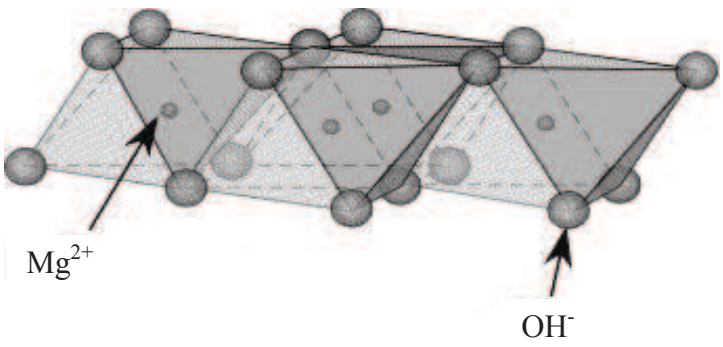

Figure 1.3 Brucite $Mg(OH)_2$ structure [81]

When these brucite-like sheets are stacked on top of each other via hydrogen bonds, a three-dimensional structure can be formed, which is iso-structural to the natural compound $Mg(OH)_2$ [82]. Once divalent cations are substituted by a trivalent metal, a net positive charge is generated in the hydroxyl sheet. This positive charge is compensated by anions that lay in the interlayer space (A^{n-} = CO_3^{2-}, NO_3^-, SO_4^{2-}, $[Fe(CN)_6]^{3-}$…) between two brucite-like sheets (Figure 1.4). And the most stable anion with the highest affinity to occupy in the interlayer space is the carbonate. The number, size, orientation and strength of the bonds between the anions and the hydroxyl groups of the brucite-like layers determine the thickness of the interlayer [82].

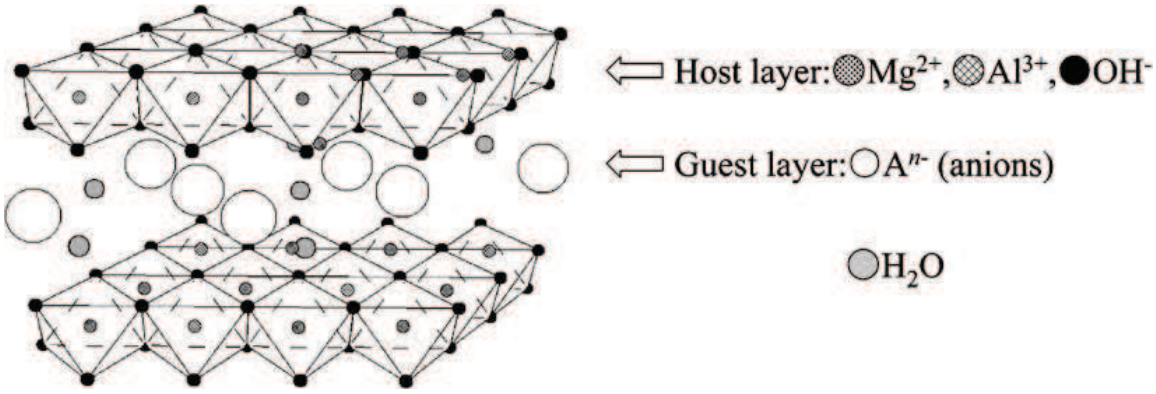

Figure 1.4 Schematic representation of hydrotalcite structure [83]

However, the only limitation to the nature of the anion (A^{n-}) is that it should not form complexes with the present cations in the hydroxide sheet. In fact, anions play an important role in the thermal decomposition of hydrotalcites. For example, carbonates or nitrates can be eliminated under the form of CO_2 and NO_x [84]. Whereas, anions that are forming complexes with the metal, can stay in the calcined sample even after calcination [85]. In addition, when preparing hydrotalcites containing anions different from carbonate, it is very difficult to avoid contamination from the CO_2 present in the aqueous solution [86].

Water molecules are located in the interlayer in those sites which are not occupied by the anions. Usually, the amount of water can be determined by thermo-gravimetric measurements of weight loss [87].

1.5.2 Hydrotalcites Properties

Hydrotalcites have important characteristics that make them interesting for various applications. The most interesting properties of the oxides (i.e. $MgAl_2O_4$, Co_3O_4, Co_2AlO_4 or $CoAl_2O_4$) obtained after the calcination of hydrotalcites are the following:

1) High surface area obtained after calcination. In fact, after calcination, carbonates anions leave the structure under the form of CO_2, leading to the formation of a porous structure (mesopores of about 8 nm) [88].
2) Hydrotalcites have a high anionic exchange capacity related to their lamellar structure that allows the exchange of its original anions with those present in an aqueous solution [86].
3) Basic properties useful for catalysis. In fact the presence of basic or acidic sites on solids plays an important role in catalytic reactions. The acid-base properties of catalysts surface depend on the ionic or covalent character of metal-oxygen bonds. Mg-Al hydrotalcites and their calcination products are very relevant as basic catalysts [80].
4) "Memory effect", which allows the reconstruction of the initial layered structure when contacting the oxide product with water solutions containing metallic ions. Moreover, the reconstruction step of decomposed hydrotalcite and the exchange of counter anions have an impact on the basicity of the sample [88].
5) Formation of homogeneous mixtures of oxides with very small crystal size and high specific surface area, stable to thermal treatments, which by reduction form small and thermally stable crystallites with absence of chemical segregation [80].

6) Hydrotalcites are stable against sintering, provide high metal dispersion and they are inexpensive [86].

1.5.3 Preparation Method

Several methods are used for hydrotalcite synthesis but on the basis of structural considerations, co-precipitation is one of the most reliable and reproducible techniques for the preparation of the layered double hydroxides. This technique allows homogeneous precursors to be used as starting materials, where two or more metallic cations are dissolved together and slowly added to the basic solution to obtain homogeneous crystal growth and good organization of the prepared phases [86].

In order to co-precipitate two or more cations it is necessary to carry out the precipitations under super saturation conditions. Usually, these latter are reached by physical (evaporation) or chemical (variation of pH etc.) methods. In particular, it is necessary to precipitate at a pH higher than or equal to the one at which the more soluble hydroxide precipitates. It is shown that at pH 8-10 practically all the metal hydroxides form hydrotalcite precipitate [86].

In certain cases, precipitation must be held in a free CO_2 atmosphere to prevent the formation of phases containing carbonates ions [89]. Certain hydrotalcite synthesis cannot be done using the co-precipitation method because of the possible complexation between anions and metals presents in the solution. Therefore, anionic exchange method can be adopted.

1.5.4 Hydrotalcites Co/Mg/Al in Methane and Ethanol Steam Reforming

In the present study, hydrotalcites (Co/Mg/Al) are used as supports on which Ru and Cu metals are impregnated. In fact, dispersing the active metal on a high surface area

support material can improve the stability and activity of the surface of a catalyst. Thus, the support determines the dispersion of the catalytically active metal particles and the resistance to sintering at high temperature under steam. In general, strong interaction between metal and support makes a catalyst more resistant to sintering and coking, thus resulting in a longer time of catalyst stability [90]. Furthermore, pore structure, morphology and phase transitions of the support determine the final particle size of the metal. It must have good porosity, which results in a long contact-time between reactants and catalysts. It can also affect the reactivity and may even participate in the catalytic reaction itself [70]. The nature of the support also plays a key role in determining the selectivity to the formation of H_2 [91]. In other words, the support is a fundamental part of the catalyst and cannot be considered separately.

Hydrotalcite-like compounds are successfully applied in the steam reforming reactions of methane and ethanol [12, 13].

Cobalt was found to have high catalytic activity for the reforming of methane [92-94]. Catalysts containing cobalt showed the highest activity and selectivity to hydrogen for ESR [13, 91, 95]. In fact, supported cobalt has shown similar activity to noble metals for the C-C bond cleavage, even around 400°C, producing hydrogen from ESR [91]. Moreover, the increase of ethanol conversion and the reduction of the amount of liquid products and CO are observed for the catalysts with higher cobalt contents [91].

Moreover, MgO basic supports resist to metal coking. This effect results from the enhancement in the oxidation rate of CH_x fragments adsorbed on the active metal [96]. Frusteri et al. [97], evaluated the catalytic performance of MgO supported Pd, Rh, Ni and Co for hydrogen production by ethanol steam reforming. Rh/MgO showed the best performance in terms of ethanol conversion and stability. Coke formation rate on Rh/MgO was very low as MgO was basic [97]. Cavallaro et al. [98] investigated the support

influence on the catalytic stability of several supported catalysts. They observed that Co/Al_2O_3 catalysts were deactivated after 2-3 h in the ESR (650°C) due to cobalt oxidation and coke formation, and MgO represented a more suitable support for Co catalysts because of its lower acidity compared to Al_2O_3 [98].

Finally, the acidity in the support (Al_2O_3) is known to facilitate the decomposition of methane. In addition, alumina-supported catalysts were found very active at low temperatures (400°C) for the dehydration of ethanol to ethylene which was converted into H_2, CO and CO_2 as major products and CH_4 as a minor one at higher temperatures (above 600°C). However, acidic supports induced ethanol dehydration producing ethylene, which was a source of coke formation [99]. It can also promote cracking and polymerization, producing carbon [11].

1.6 Catalyst Deactivation

One of the major problems related to the operation of heterogeneous catalysis is the catalyst loss of activity with time-on-stream, i.e. ``deactivation''. There can be many reasons for catalyst deactivation. Deactivation can occur by a number of different mechanisms, both chemical and physical in nature. These are commonly divided into four classes, namely sintering, poisoning, coking, and oxidation. It should be mentioned here that a distinction between poisoning and thermal deactivation can be made: if, on continued use, the activity decreases more rapidly than surface area, then poisoning may be suspected, whereas, if a decrease in surface area is concomitant with a decrease in activity, then thermal deactivation is indicated. The latter is for instance the case with “sintering” [100].

1.6.1 Sintering:

Sintering usually refers to the loss of active surface via structural modification of the catalyst due to crystallite growth of either the support material or the active phase [101]. This is generally a thermally activated process and is physical in nature. Sintering occurs both in supported metal catalysts and unsupported catalysts. Elevated temperature and the atmosphere in contact with the catalyst are the most important factors that enhance sintering [100].

1.6.2 Poisoning:

Poisoning is the loss of activity due to the chemisorption on the active sites of impurities present in the feed stream [101]. Many of the catalyst poisons act by blocking active surface sites or altering the adsorptivity of other species, thus reducing catalytic activity. Sulfur is the most severe poison for steam reforming catalysts [100]. It is present under reforming reactions in the form of H_2S, which is chemisorbed on transition-metal surfaces:

$$H_2S + M \leftrightarrow M\text{-}S + H_2 \qquad \text{(Equation 1.4)}$$

Sulfur may be removed by oxidation and controlled re-reduction of the catalyst (the reverse of Equation 1.4).

1.6.3 Coking:

For catalytic reactions involving hydrocarbons (or even carbon oxides), side reactions occur on the catalyst surface leading to the formation of carbonaceous residues (usually referred to as coke or carbon) which tend to physically cover the active surface. Coke deposits may deactivate the catalyst either by covering of the active sites, and by pore

blocking. Sometimes, a distinction is made between coke and carbon: usually carbon is considered the product of CO disproportionation (Boudouard reaction), whereas coke is referred to the material originated by decomposition (cracking) or condensation of hydrocarbons [100].

1.6.4 Oxidation:

Oxidation of the metal particles may occur at a high steam to carbon ratio and a low catalyst activity. It leads sometimes to catalytic deactivation. Under "regular" steam reforming conditions though, sufficient hydrogen will be present to keep most of the active metal surface reduced. Usually, noble metals are not sensitive to oxidation [101].

1.7 Conclusion

Through this literature overview, catalytic steam reforming reaction for hydrogen production meets the requirements of many applications. Steam reforming of methane and ethanol require good catalytic systems that provide high activity in steam reforming and high hydrogen productivity, and an optimal activity in response to water gas shift reactions which would limit CO concentration.

In the present study, Co/Mg/Al hydrotalcites have been investigated as supports on which copper or ruthenium active metals are impregnated and tested in methane and ethanol steam reforming reactions. Co and Mg-rich mixed oxides have been studied with keeping the Al content unchanged in order to try to optimize their activity. In literature, Ru, Cu and hydrotalcites showed interesting results in limiting coke and carbon monoxide formation and yielding high amount of hydrogen.

In chapter 2, a series of physico-chemical techniques will be used to characterize the prepared catalysts: scanning electron microscopy/energy dispersive X-ray (MEB-EDX), differential scanning calorimetry/ thermo gravimetric analysis (DSC/TG), X-ray diffraction (XRD), Brunauer Emmet Teller specific surface area analysis (BET), temperature programmed reduction/oxidation (TPR/TPO), Fourier Transform Infrared (FTIR), porosimetry and electron paramagnetic resonance (EPR).

Chapter 3 is a complete catalytic evaluation of $Co_xMg_{6-x}Al_2$, $Ru/Co_xMg_{6-x}Al_2$ and $Cu/Co_xMg_{6-x}Al_2$ catalysts in methane steam reforming reaction. Different parameters as catalyst content, nature of the active phase, pretreatment, calcination temperature, steam/carbon ratios, gas hourly space velocity are studied.

Finally, in chapter 4, ethanol reforming reaction was studied over the prepared catalysts by varying several parameters in order to optimize the reaction conditions.

CHAPTER 2

CATALYSTS SYNTHESIS AND CHARACTERIZATION

2.1 Supports and Catalysts Preparation

2.1.1 Synthesis of $Co_xMg_{6-x}Al_2$ HT

Different hydrotalcites (Co-Mg-Al layered double hydroxides) were synthesized with a ratio $\frac{n_{cations(II)}\,(Mg^{2+}+Co^{2+})}{n_{cations(III)}\,(Al^{3+})}=3$ where n is the number of moles of the metal oxides. They were prepared by co-precipitating ions in an aqueous solution with appropriate quantities of $Co(NO_3)_2.6H_2O$ (SIGMA-ADRICH, 98%), $Mg(NO_3)_2.6H_2O$ (FLUKA, 98%) and $Al(NO_3)_3.9H_2O$ (FLUKA, 98%) which were added drop wise under vigorous stirring into a 1M sodium carbonate Na_2CO_3 (HIMEDIA, 99.5%) aqueous solution. The pH of the solution was maintained constant (pH~10) by adding some drops of a 2M sodium hydroxide solution NaOH (HIMEDIA, 99%). In fact, in order to combine many metals into one homogeneous phase, the co-precipitation at constant pH is adopted. During this synthesis, the structure of the formed hydrotalcites is directly related to the fixed pH value [86, 102-104]. The resulting slurry was heated at 60°C and kept under stirring during 2 hours for maturation and then placed in the drying oven for 24 h. The obtained precipitate is filtered, washed several times with hot deionized water (60°C) until its pH reaches 6-7 (to eliminate excess OH^-, Na^+ and NO_3^- ions) and dried for 48 h in a drying oven at 60°C, then grinded to obtain fine powders.

The obtained solids are named $Co_xMg_{6-x}Al_2HT$ (with x= 0, 2, 4, 6). The terminology HT will be used for the dried solids, and the calcined solids are named by their formula without HT. The calcination treatment at 500°C was performed under an air flow of 33 $mL.min^{-1}$ ($1°C.min^{-1}$) in order to stabilize these mixed oxides before metal impregnation. The latter temperature was chosen as the thermo-gravimetric analysis (section 2.3) revealed that at this temperature stable oxides are obtained with no further weight loss.

2.1.2 Synthesis of Cu Based Catalysts

An adequate amount of copper (II) nitrate $Cu(NO_3)_2.3H_2O$ (PROLABO, 99%) was dissolved in 100 mL of deionized water in order to obtain 5 wt.% of Cu in the final solid. This solution is then added to 1 g of the support and mixed during two hours. The excess of water is slowly eliminated in a rotary evaporator (75°C, 60 revolutions.min^{-1}, under vacuum). The obtained residue is kept in an oven at 100°C during 24 h. The dried solids are then thermally stabilized by calcination at 500°C (1°C.min^{-1}) under an air flow (33 mL.min^{-1}) for four hours. The obtained calcined catalysts are named $5Cu/Co_xMg_{6-x}Al_2$ (with x = 0, 2, 4, 6). Different copper contents were impregnated on Co_6Al_2 support (0.5, 3, 15 and 25wt.% Cu). Non-calcined catalysts are designated with an HT as suffix.

2.1.3 Synthesis of Ru Based Catalysts

Different methods are used in order to impregnate Ru metal. Each method differs with respect to the nature of the precursors, the state of the impregnated support and the conditions of preparation [47]. In this work, dry impregnation method of ruthenium (III) nitrosyl nitrate solution $Ru(NO)(NO_3)_3$ (ACROS organics) with 1.5wt.% Ru on different calcined supports was adopted. In fact, impregnation leads to the best possible dispersion of the active phase contributing to a better ability to interact in catalytic reactions. An adequate volume of $Ru(NO)(NO_3)_3$ solution has been impregnated in order to obtain solids with 1wt.% ruthenium. The mixture is then stirred and left during one hour under air and dried in a drying oven for 24 hours. Catalysts are then thermally stabilized by calcination at 500°C (1°C.min^{-1}) under an air flow (33 mL.min^{-1}) for 4 h. The obtained catalysts are named $1Ru/Co_xMg_{6-x}Al_2$ (with x= 0, 2, 4, 6). Different ruthenium contents were prepared and impregnated on Co_6Al_2 support (0.5, 3 and 5 wt.% Ru). Non-calcined catalysts are designated with an HT as suffix.

Figure 2.1 is a schematic representation that summarizes the different steps during catalysts synthesis and stabilization.

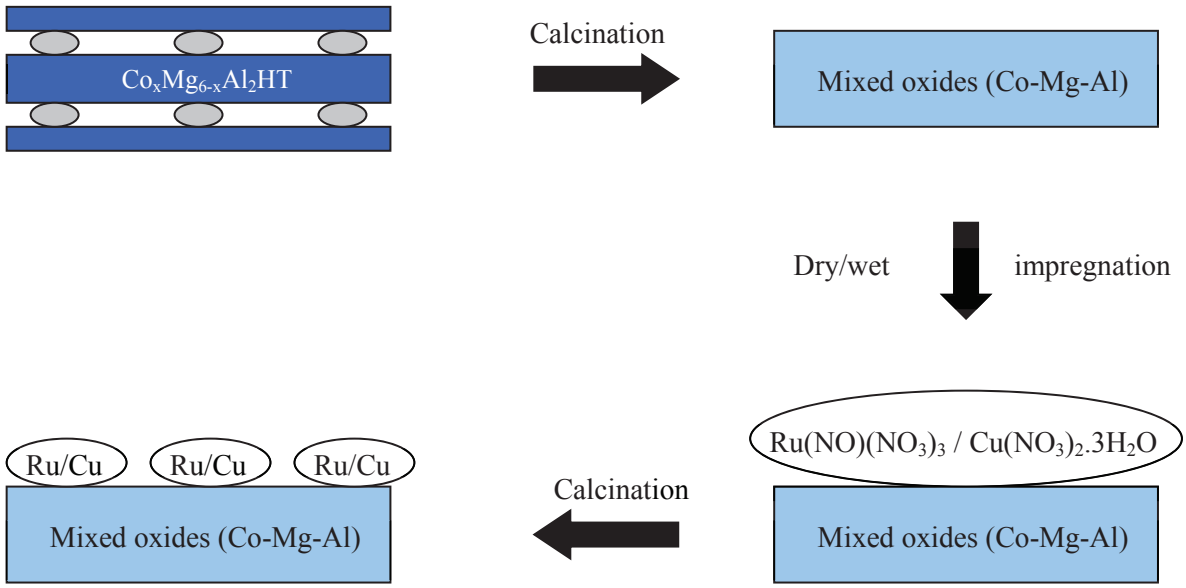

Figure 2.1 Schematic representation of a catalyst preparation

2.2 Scanning Electron Microscopy Coupled to an Energy Dispersive X-Ray Spectrometer

2.2.1 Scanning Electron Microscopy (SEM) and Energy Dispersive X-Ray Spectroscopy (EDX) Techniques

Heterogeneous catalysts are often complex in composition, texture, and structure of the phases. Their study by scanning electron microscopy (SEM) can visualize them with a resolving power adjustable between 10^{-4} m and 10^{-8} m. The energy dispersive X-Ray spectroscopy (EDX) coupled to SEM allows the determination of the chemical composition of the examined surface, its homogeneity, distribution, dispersion, and the mean size of the metal species. The measurements were carried out on a "SERON AIS 2100C" microscope operating at 20 kV under a vacuum of 10^{-6} torr. Samples were

prepared by suspending the catalyst on carbon films and they were pulverized by a beam of graphitic carbon in order to enhance the conductivity.

2.2.2 SEM of 1Ru/$Co_xMg_{6-x}Al_2$ Solids

Figure 2.2 represents SEM image of 1Ru/$Co_xMg_{6-x}Al_2$ solids calcined at 500°C.

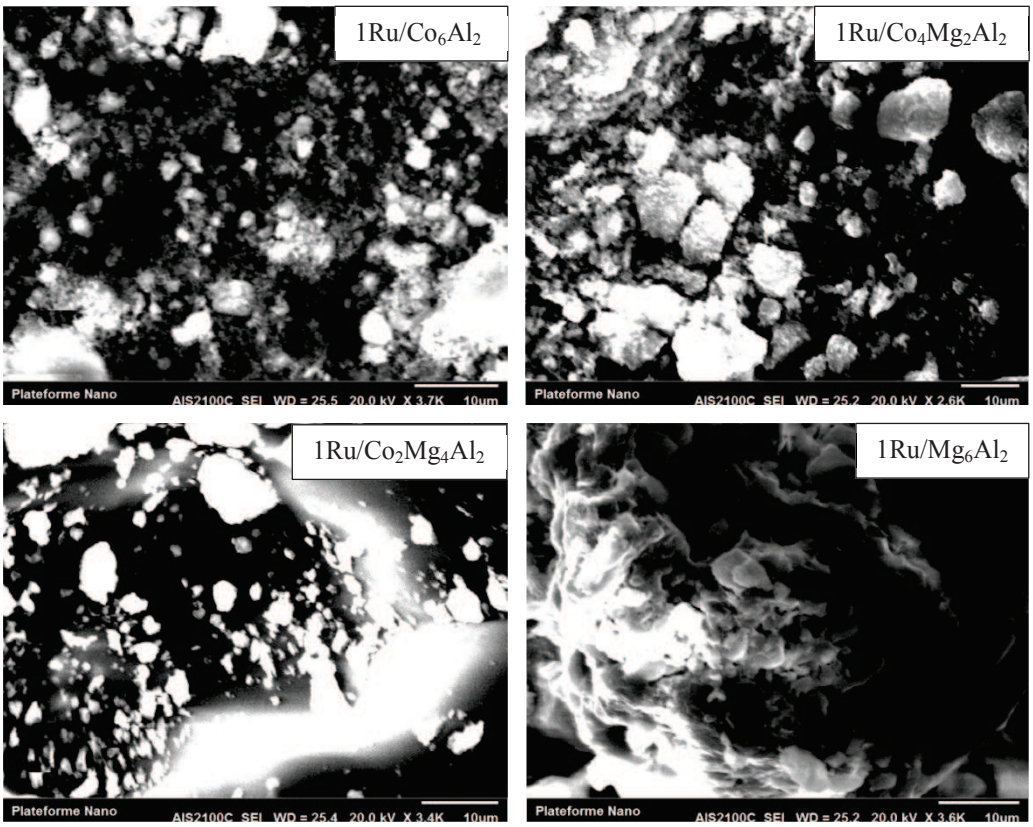

Figure 2.2 SEM micrographs of 1Ru/$Co_xMg_{6-x}Al_2$ solids

A remarkable difference is observed between the cobalt-containing catalysts and 1Ru/Mg_6Al_2. Cobalt particles have an irregular shape with an inhomogeneity in the particle size distribution. Whereas for 1Ru/Mg_6Al_2, particles are in the form of disordered platelets.

2.2.3 EDX of 1Ru/$Co_xMg_{6-x}Al_2$ Solids

EDX analysis of the calcined ruthenium-based catalysts is represented in table 2.1. Atomic ratio and weight percentage are almost respected. The small difference may be due to the area at which the SEM image was taken or some loss during the synthesis steps (washing, drying, calcination…).

Table 2.1 EDX analyses of the ruthenium-based catalysts

Calcined catalysts	Theoretical atomic ratio Co/Al (Co+Mg)/Al	Experimental atomic ratio Co/Al (Co+Mg)/Al	Weight percentage of Ru (%)
1Ru/Mg_6Al_2 (500°C)	3	2.59	1.27
1Ru/$Co_2Mg_4Al_2$ (500°C)	3	2.83	1.30
1Ru/$Co_4Mg_2Al_2$ (500°C)	3	2.24	1.15
1Ru/Co_6Al_2 (500°C)	3	2.71	1.10
3Ru/Co_6Al_2 (500°C)	3	3.30	2.70
5Ru/Co_6Al_2 (500°C)	3	2.68	4
1Ru/Co_6Al_2 (800°C)	3	2.27	0.94

2.3 Thermal Behaviors of the Non-Calcined Solids

2.3.1 Differential Scanning Calorimetry and Thermogravimetry Analysis (DSC/TG)

When a solid is subjected to a temperature increase, it is susceptible to undergo structural and state changes. These changes are accompanied by a release (exothermic reaction) or absorption (endothermic reaction) of heat, and generally by a loss or a gain of mass.

Thermo gravimetric analysis (TG) measures the loss or gain of mass as a function of temperature and time. TG curves allow following any phase change resulting from decomposition, dehydration or oxidation/reduction processes.

Differential scanning calorimetry (DSC) analyses measures the difference in temperature due to a change of the enthalpy of the sample heated as a function of temperature and time. It gives information on the endothermic and exothermic phenomena that take place during the heating of the sample.

DSC/TG analysis were done simultaneously on a NETZSCH STA 409 apparatus equipped with a microbalance (TG), a differential scanning calorimetry (DSC) and a gas inlet system Two alumina crucibles are symmetrically put on a support inside a furnace. The first crucible is empty, it is the reference crucible. Solids are introduced in the other crucible and then heated from room temperature up to 900°C at a rate of 5°C.min^{-1} under an air flow equal to 75 mL.min^{-1}. A thermocouple system controls and measures the temperature of the sample. The measured difference between the sample and the reference allows thermal differential (temperature difference) and gravimetric analysis (loss or gain of mass of the sample).

2.3.2 Thermal Analysis of $Co_xMg_{6-x}Al_2HT$

Figure 2.3a represents the DSC curves obtained during the calcination of hydrotalcites $Co_xMg_{6-x}Al_2HT$ hydrotalcites from room temperature up to 900°C. Three endothermic peaks (marked I, II and III) are observed. In literature, the destruction of the hydrotalcite structure can be summarized into four steps [86,105-107]:

(1) Elimination of physisorbed water (on the external surface of crystallites)

(2) Elimination of the interlayer water [86]

(3) Dehydroxylation of the brucite layer [105]

(4) Loss of the interlayer anions as carbonates [106, 107]

Therefore, the first endothermic peak I (below 150°C) corresponds to step (1), but the layered double hydroxide (LDH) structure remains intact [105] leading to the formation of a hydrotalcite-dehydrated (ex. $Mg_6Al_2(OH)_{16}CO_3$) [108]. Peaks II and III are attributed to the collapse of the hydrotalcite structure and the formation of metal oxides spinel-type [109-112]. Step (2) (between 200-215°C) is associated with peak II. However, it is not possible to differentiate between steps (3) and (4) which are taking place at close temperatures (between 230-390°C). These steps coincide with peak III which is assigned to the destruction of the hydrotalcite structure and the formation of spinel phase due to the complete dehydroxylation of the brucite-like sheet and the loss of carbonate anions. This will lead to the collapse of the layered structure and the formation of oxide phases [106, 110, 111, 113].

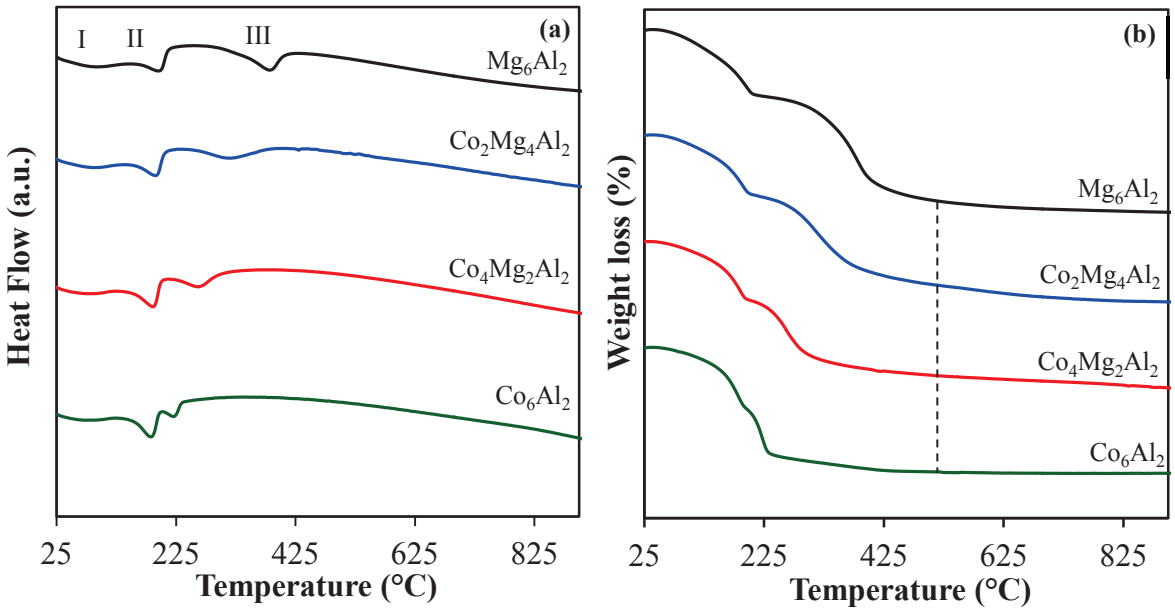

Figure 2.3 a) DSC b) TG curves obtained during the calcination of $Co_xMg_{6-x}Al_2HT$

In addition, the substitution of Mg^{2+} with Co^{2+} leads to different temperatures on the DSC signals, especially for peak III that occurs at a lower temperature with higher cobalt content. In fact, the thermal stability of hydrotalcites depends on the nature of the cations present in the brucite type layer. It decreases with the increase of cobalt content in the sample. In fact, this peak is between 350-400°C for Mg_6Al_2, 250-300°C for $Co_2Mg_4Al_2HT$, and 200-250°C for $Co_4Mg_2Al_2HT$ and Co_6Al_2HT. This is explained by the different affinity of the cations (Mg^{2+} or Co^{2+}) towards the CO_3^{2-} interlayer anions [112, 114] and their removal becomes easier. Thus, the stability of hydrotalcites decreases when Mg^{2+} is replaced by Co^{2+} [115].

Figure 2.3b represents the TG curves obtained during the calcination of the hydrotalcites $Co_xMg_{6-x}Al_2HT$ from room temperature up to 900°C. Fresh hydrotalcites are highly hydrated materials. Thermogravimetric analysis reveals three successive weight losses during the temperature rise [116, 117]. Each endothermic peak in the DSC curve corresponds to a weight loss. Thus, the first loss corresponds to the departure of adsorbed water on the surface of the solids. The second loss corresponds to the departure of interlayer water. And the final loss is attributed to the hydrotalcite destruction, the formation of spinel phase due to the loss of hydroxyl groups from the brucite-like structure and the loss of carbonate anions between the sheets [106, 110, 111]. It is worth to mention that at 500°C, hydrotalcites are totally decomposed into stable oxides with no further weight loss. Hence, the choice of this temperature for the treatment of synthesized solids.

Theoretical weight losses were calculated and compared with the experimental values in Table 2.2. Peaks II and III were taken into consideration in the theoretical weight loss without peak I which is due to the loss of physisorbed water. The differences observed between the experimental and theoretical values are due to the partial dehydration of HT in

the oven at 60°C (step 1) and the stoichiometry of the prepared hydrotalcites (EDX results in table 2.1) showing a difference between the prepared and theoretical HT.

Table 2.2 Theoretical and experimental weight losses of the different hydrotalcites

Hydrotalcites	Theoretical weight loss (%) (peaks II & III)	Experimental weight loss (%)
Mg_6Al_2HT	43	36
$Co_2Mg_4Al_2HT$	37	34
$Co_4Mg_2Al_2HT$	34	29
Co_6Al_2HT	28	26

2.3.3 Thermal Analysis of 1Ru/$Co_xMg_{6-x}Al_2$HT and 5Cu/$Co_xMg_{6-x}Al_2$HT

Figure 2.4 illustrates the DSC/TG curves obtained during the heating of the non-calcined 1Ru/$Co_xMg_{6-x}Al_2$HT and 5Cu/$Co_xMg_{6-x}Al_2$HT solids from room temperature up to 900°C. A partial reconstruction or "memory effect" of the hydrotalcite structure during the impregnation step is detected especially for solids with high Mg amount (especially for 5Cu/Mg_6Al_2 and 1Ru/Co_6Al_2). In fact, endothermic peaks below 410°C and the important weight losses are due to the destruction of the hydrotalcite structure and the formation of spinel phase [112, 118-120]. The presence of water during the impregnation step and the presence of CO_2 dissolved in the aqueous medium are sufficient to partially reconstruct the lamellar structure. And the basic properties of the MgO oxide obtained after calcination permit to adsorb, as carbonates, the CO_2 present in the medium providing the anionic species required for the formation of the interlayer space [80]. It must be noted also that nitrates coming from the precursor, can also serve as species for the formation of the interlayer space. The reconstruction allows the incorporation of ruthenium and copper in

the Mg^{2+} and Al^{3+} sites inside the hydrotalcites layers and water fits again in their interlayer. This will lead to a good dispersion of the active phase.

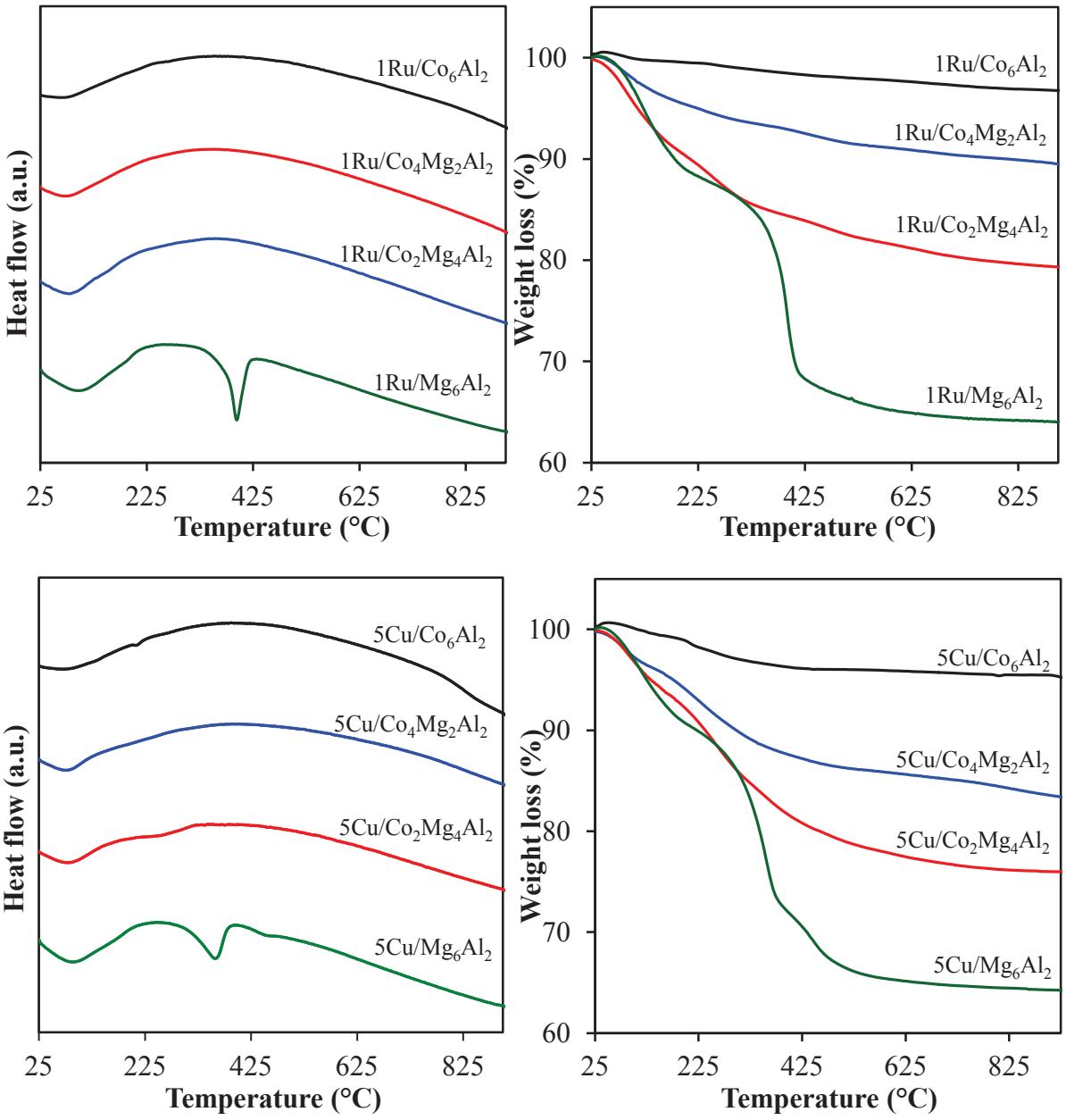

Figure 2.4 DSC and TG curves obtained during the oxidation of the non-calcined $1Ru/Co_xMg_{6-x}Al_2HT$ and $5Cu/Co_xMg_{6-x}Al_2HT$ solids

No clear reconstruction effect is seen for the other catalysts because of the slow rate of the reconstruction. A second peak around 430°C seen for $5Cu/Mg_6Al_2$ is due to the decomposition of the copper nitrate precursor. In literature, the temperature of the decomposition of copper nitrate was found to be lower than the one obtained in this case [121]. But the high interaction between copper and the support will lead to a higher thermal decomposition temperature. However, the peak of the thermal decomposition of the ruthenium precursor is not observed due to the low content of this active phase (1wt.%) compared to 5wt.% of Cu.

Marchi and Apesteguia [118], proposed a reconstruction mechanism of hydrotalcites in the presence of water and carbonates as follows:

$$H_2O_{(HT)} \rightarrow H_2O_{(g)}$$

$$2OH^-_{(HT)} \rightarrow H_2O_{(g)} + O^{2-}$$

$$CO_3^{2-}{}_{(HT)} \rightarrow CO_{2(g)} + O^{2-}$$

Hydrotalcite calcination

$$CO_3^{2-}{}_{(aq)} + 2\,H_2O_{(l)} + O^{2-} \rightarrow CO_3^{2-}{}_{(HT)} + 2OH^-_{(HT)} + H_2O_{(HT)}$$

Hydrotalcite reconstruction

During this reconstruction, copper and ruthenium ions are incorporated in the Mg^{2+}, Co^{2+} and Al^{3+} sites inside the hydrotalcites layers leading to a better dispersion of the active phase [122, 123]. This reconstruction or “memory effect” is more important for supports with high Mg content [111].

Table 2.3 displays the theoretical weight loss due to the departure of copper or ruthenium precursors and the experimental weight losses of the different non-calcined $1Ru/Co_xMg_{6-x}Al_2HT$ and $5Cu/Co_xMg_{6-x}Al_2HT$.

Table 2.3 Theoretical and experimental weight losses of the different non-calcined 1Ru/$Co_xMg_{6-x}Al_2$HT and 5Cu/$Co_xMg_{6-x}Al_2$HT

Catalyst	Theoretical weight loss (%)	Experimental weight loss (%)
1Ru/Mg_6Al_2HT	1.8	36.1
1Ru/$Co_2Mg_4Al_2$HT		20.7
1Ru/$Co_4Mg_2Al_2$HT		10.4
1Ru/Co_6Al_2HT		3.3
5Cu/Mg_6Al_2HT	11.3	35.7
5Cu/$Co_2Mg_4Al_2$HT		24.1
5Cu/$Co_4Mg_2Al_2$HT		16.5
5Cu/Co_6Al_2HT		4.6

By comparing the theoretical and experimental weight loss, it can be seen that for the magnesium containing catalysts, an important difference is observed (for example, 36.1% and 35.7% compared to 1.8 % and 11.3% for 1Ru/Mg_6Al_2HT and 5Cu/Mg_6Al_2HT respectively). This confirms that the obtained experimental results are mainly due to the destruction of the hydrotalcite structure that was reconstructed during impregnation. Whereas it is not the case for 5Cu/Co_6Al_2 and 1Ru/Co_6Al_2 catalysts.

2.4 Study of the Structure of the Different Solids Using X-Ray Diffraction Technique

2.4.1 X ray Diffraction Technique (XRD)

A solid can exist under different crystallographic phases where each phase has a distinct catalytic property. X-Ray Diffraction (XRD) analysis allows identifying the crystallographic structure of the studied compounds. The XRD technique is based on

sending an X-ray beam on a sample placed on a pyrex support. When X-ray reaches the sample, it will diffract by an angle "θ", and then it is detected by a scintillation counter. This phenomenon is governed by Bragg's law: $2d_{hkl} \times \sin\theta = n\lambda$

Where d_{hkl} : Interreticular distance (Å)

2θ : angle between incident and diffracted beam (º)

n : serial diffraction order of Bragg (integer)

λ : wavelength of the beam Kα (1.5405Å for Cu)

Experiments were performed at ambient temperature on a BRUKER D8 Advance Diffractometer using CuKα radiation (1.5405 Å), which components are subtracted from the rough spectrum. The scattering intensities were measured over an angular range of 20°< 2θ< 80° for all the samples with a step-size of (2θ) = 0.02°. The diffraction patterns have been indexed by comparison with the "Joint Committee on Powder Diffraction Standards" (JCPDS) files.

2.4.2 XRD of $Co_xMg_{6-x}Al_2$HT and $Co_xMg_{6-x}Al_2$ Solids

XRD patterns for dried $Co_xMg_{6-x}Al_2$HT solids are shown in figure 2.5. They indicate the presence of the hydrotalcite phase (Rhombohedral 3R Symmetry - JCPDS N°22-0700) in all the dried solids. In addition, a weak diffraction peak at 2θ= 33.45°, ascribed to cobalt hydroxide phase $Co(OH)_2$ (JCPDS N°46-0605), was seen only for samples containing high Co content (Co_6Al_2 and $Co_4Mg_2Al_2$). Furthermore, it should be pointed that the intensity of the lines decreased with increasing Co content, indicating less crystallinity of the hydrotalcite phase with Co loadings [124]. A correlation can be established between the XRD and DSC results. DSC shows that high Co content lead to a thermally unstable hydrotalcites, and XRD reveals a low crystallinity of the hydrotalcite

samples with high cobalt content. The least thermally stable hydrotalcites are less crystallized while thermally stable hydrotalcites exhibit better crystallization.

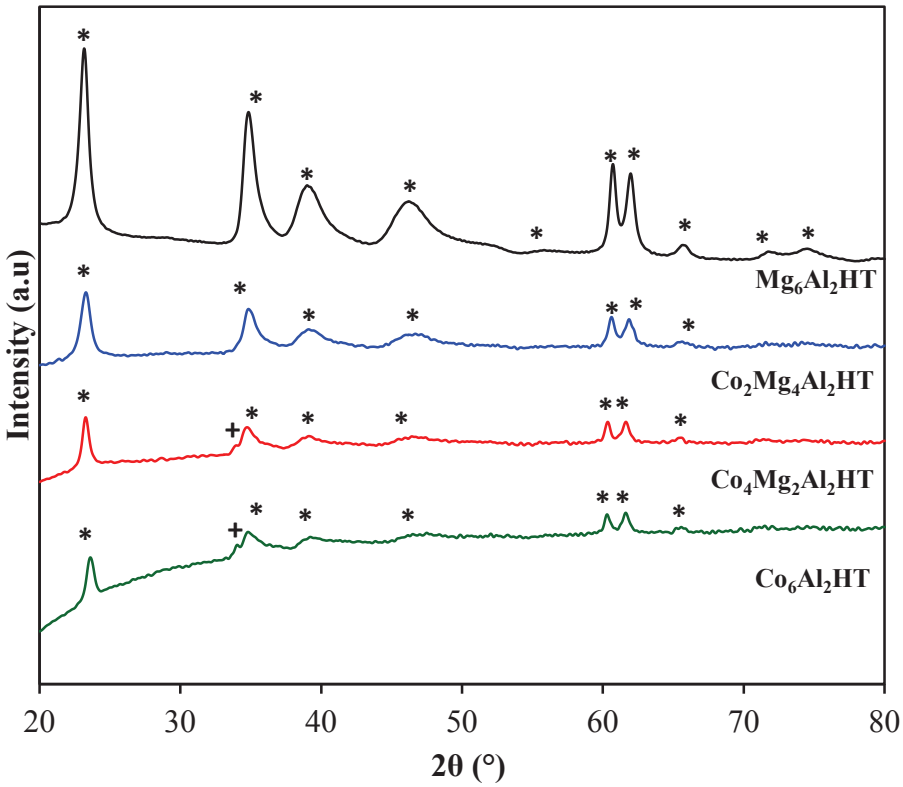

Figure 2.5 XRD patterns of $Co_xMg_{6-x}Al_2HT$ solids. "*" Hydrotalcite phase (JCPDS N°22-0700) and "+" Cobalt hydroxide (JCPDS N°46-0605)

The lattice parameters of the prepared dried hydrotalcites are listed in table 2.4. Y-J. Lin et al. [111], have obtained similar *a* and *c* parameters values. Moreover, the lattice parameter "*a*" decreases linearly with decreasing Co content from 3.0805 Å (Co_6Al_2) to 3.0596 Å (Mg_6Al_2). These observations were attributed to the shrinkage of the lattice due to the replacement of Co^{2+} (rCo^{2+}= 0.74 Å) with a smaller Mg^{2+} cation (rMg^{2+}= 0.65 Å). On the contrary, "*c*" decreases with the increase of Co content. This can be explained by the increase in the electrostatic attraction between negative and positive charges. In fact,

"*c*" decreases when $Al^{3+}/Al^{3+}+M^{2+}$ ratio increases due to a formation of another phase of Co [124].

Table 2.4 Values of the unit cell parameters for $Co_xMg_{6-x}Al_2HT$ solids

Sample	a (Å)	c (Å)	$d_{(110)}$ (Å)
Co_6Al_2HT	3.0805	22.875	1.5402
$Co_4Mg_2Al_2HT$	3.0744	23.170	1.5372
$Co_2Mg_4Al_2HT$	3.0636	23.133	1.5312
Mg_6Al_2HT	3.0596	23.327	1.5298

Figure 2.6 represents the XRD patterns of $Co_xMg_{6-x}Al_2$ calcined at 500°C. It is clearly observed that hydrotalcite peaks are absent.

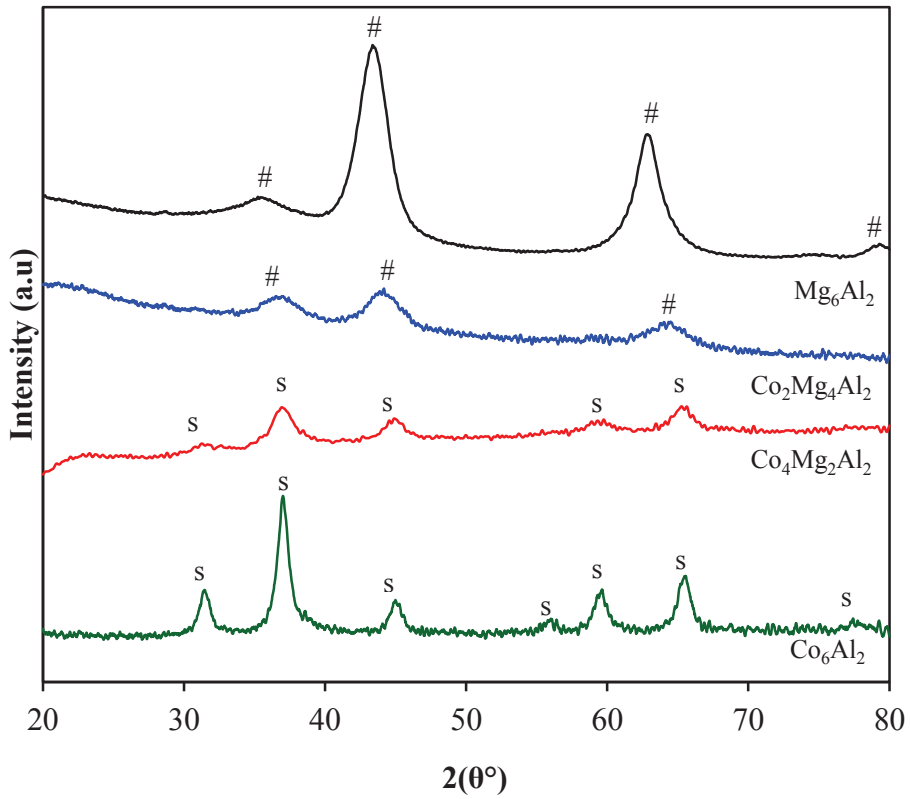

Figure 2.6 XRD patterns for calcined $Co_xMg_{6-x}Al_2$ supports. "S" spinel Co_3O_4 (JCPDS N°42-1467) $CoAl_2O_4$ (JCPDS N°44-0160) Co_2AlO_4 (JCPDS N°38-0814) and "#" MgO periclase (JCPDS N°45-0946)

This is in agreement with the thermal analysis of $Co_xMg_{6-x}Al_2HT$ where total destruction of the hydrotalcite structure was observed at this temperature. Diffraction peaks ascribed to the formation of magnesium oxides solid solutions of MgO periclase type (JCPDS N°45-0946) were observed for the high magnesium containing solids. Mg_6Al_2 shows intense peaks that decrease with $Co_2Mg_4Al_2$ sample. $MgAl_2O_4$ phase (JCPDS N°73-1959) cannot be excluded; it might be masked by the more intense diffraction lines of MgO. For $Co_4Mg_2Al_2$ and Co_6Al_2 solids, the observed peaks are attributed to a spinel type structure.

Nevertheless, it is not possible to precisely identify the nature of these oxides. In fact, diffraction peaks attributed to Co_3O_4 (JCPDS N°42-1467), $CoAl_2O_4$ (JCPDS N°44-0160) and Co_2AlO_4 (JCPDS N°38-0814) have very close 2θ values and very close intensities. The formation of Co_3O_4 is due to the facile oxidation of Co^{2+} ions and the thermodynamic stability of Co_3O_4 compared to CoO in air [125-127]. It is noticed that the intensities of the $Co_4Mg_2Al_2$ peaks are lower than those obtained for Co_6Al_2. On the other hand, the presence of magnesium oxide in $Co_2Mg_4Al_2$ and $Co_4Mg_2Al_2$ solids cannot be neglected, even if the XRD patterns did not show them clearly. This is due to their low contents and dispersion inside the solid matrix. Aluminum oxides are not observed because at this calcination temperature, they are in the amorphous state. It is also known that Al^{3+} cations occupy octahedral sites in the hydrotalcite before calcination [122, 128]. After calcination at high temperature, the structure is rearranged and Al^{3+} cations migrate from the octahedral position to tetrahedral by a substitution of Mg^{2+} cations in the oxide. A positive charge is generated by this substitution and it is compensated by the formation of cationic vacancies or oxygen insertion into the interstices of the structure [124].

2.4.3 XRD of 1Ru/$Co_xMg_{6-x}Al_2$ and 5Cu/$Co_xMg_{6-x}Al_2$ Solids

Figure 2.7 displays XRD patterns of 1Ru/$Co_xMg_{6-x}Al_2$, 3Ru/Co_6Al_2, 5Ru/Co_6Al_2 solids calcined at 500°C. All impregnated 1Ru/$Co_xMg_{6-x}Al_2$ catalysts showed diffraction lines similar to those obtained for the corresponding calcined supports (see figure 2.6).

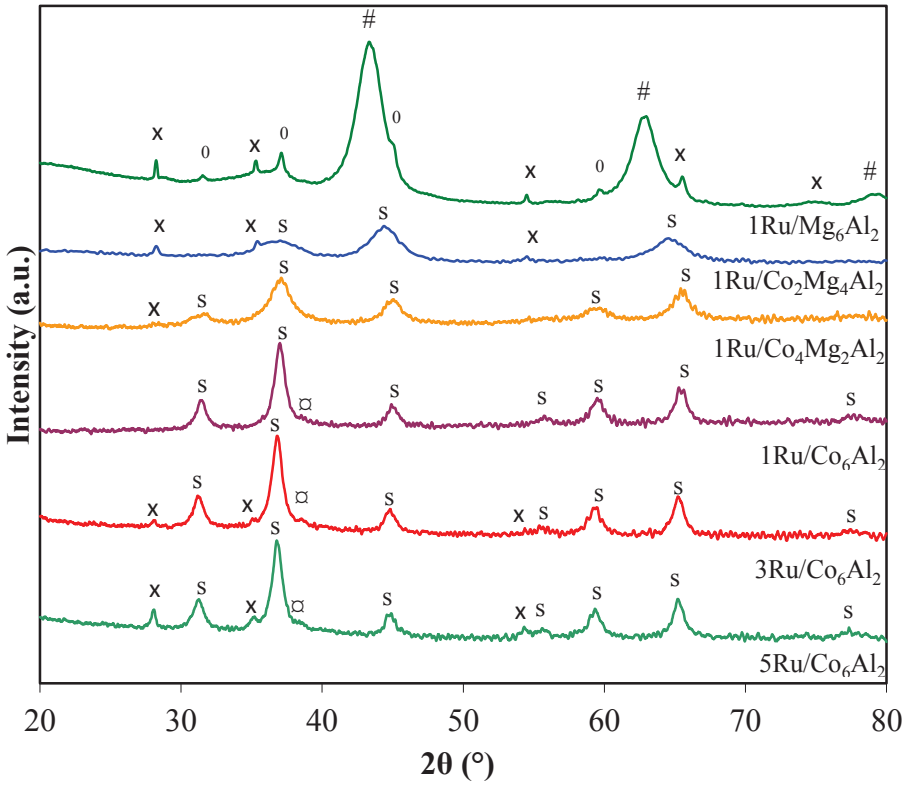

Figure 2.7 XRD patterns for all the calcined ruthenium-based catalysts. "S" spinel Co_3O_4 (JCPDS N°42-1467) $CoAl_2O_4$ (JCPDS N°44-0160) Co_2AlO_4 (JCPDS N°38-0814), "#" MgO periclase (JCPDS N°45-0946), "0" $MgAl_2O_4$ spinel (JCPDS N°73-1959), "×" tetragonal RuO_2 (JCPDS N°40-1290), "¤" Co_2RuO_4 (JCPDS N°73-1048)

In addition to MgO phase, $MgAl_2O_4$ spinel phase is also detected for 1Ru/Mg_6Al_2. In fact, the calcination of hydrotalcites (Mg-Al HT) at 500°C leads to the formation of MgO, Mg-Al[+]O and Al_2O_3 oxides where [+] is a cationic vacancy [124]. However, solids with high Mg content showed additional and more intense diffraction peaks attributed to RuO_2 tetragonal phase (JCPDS N°40-1290). Therefore, Ru interaction with Mg rich

supports is different from that with Co rich supports. The interaction of ruthenium with supports rich in Co will lead to a good dispersion of RuO_2 species so they are not detected by XRD; while it seems that RuO_2 species agglomerate on Mg rich supports forming detectable species in XRD. Additionally, more intense RuO_2 lines are observed for higher ruthenium content, while they are absent for $1Ru/Co_6Al_2$ solid. This indicates that for Ru contents higher than 1 wt.%, agglomerated RuO_2 species are formed. The diffraction line at 37.8° attributed to the presence of Co_2RuO_4 phase is observed for all the ruthenium based catalysts supported on Co_6Al_2, indicating that an interaction between the two metals occurred following the impregnation.

Figure 2.8 represents the XRD lines of $5Cu/Co_xMg_{6-x}Al_2$, $3Cu/Co_6Al_2$, $15Cu/Co_6Al_2$ and $25Cu/Co_6Al_2$ calcined at 500°C. All the diffraction patterns, except that obtained for $5Cu/Mg_6Al_2$, show diffraction lines corresponding to the three cobalt oxide spinel phase which are very difficult to differentiate by XRD: Co_3O_4 (JCPDS N°42-1467), $CoAl_2O_4$ (JCPDS N°44-0160), Co_2AlO_4 (JCPDS N°38-0814). MgO periclase and $MgAl_2O_4$ phases (JCPDS N°45-0946 and JCPDS N°73-1959) are present on the $5Cu/Mg_6Al_2$ pattern. However, MgO lines are broader and less intense than those obtained before impregnation (figure 2.6).

Diffraction lines of the CuO tenorite phase (JCPDS N°45-0937) are only obtained for solids with the Co_6Al_2 support. It seems that copper oxide species are well dispersed on the other solids. Moreover, the intensity of these lines increases with the copper content and additional CuO lines are observed indicating that copper oxide species are present as agglomerates for $15Cu/Co_6Al_2$ and $25Cu/Co_6Al_2$.

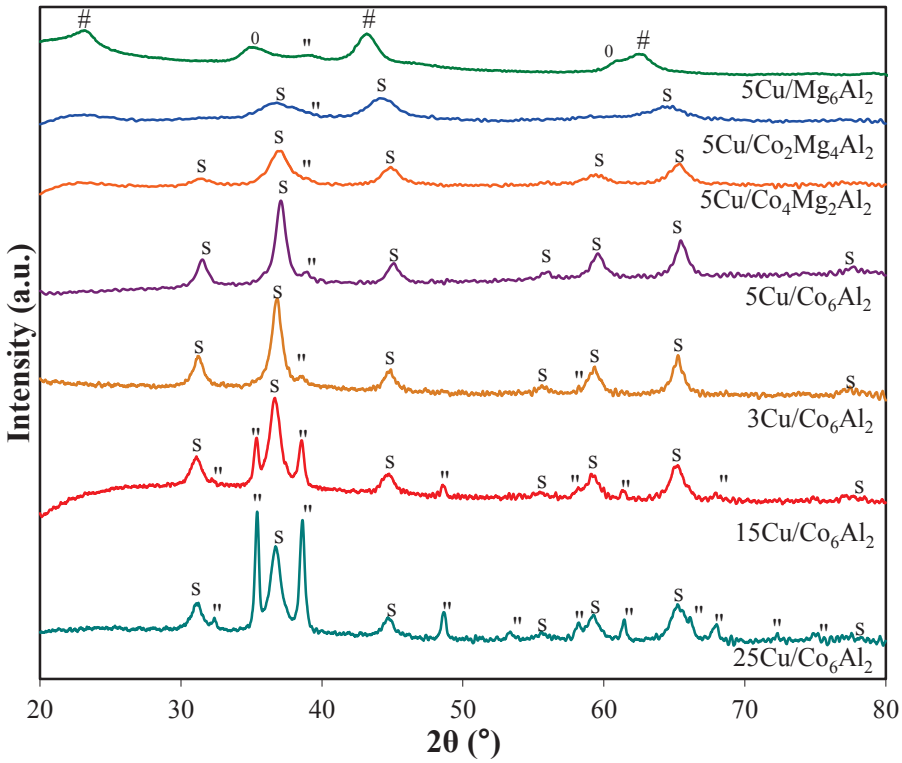

Figure 2.8 XRD patterns for all the calcined copper-based catalysts. "#" MgO periclase (JCPDS N°45-0946), "0" $MgAl_2O_4$ spinel (JCPDS N°73-1959), "S" spinel Co_3O_4 (JCPDS N°42-1467) $CoAl_2O_4$ (JCPDS N°44-0160) Co_2AlO_4 (JCPDS N°38-0814), "ˮ" CuO tenorite (JCPDS N°45-0937)

Peaks attributed to Cu-Co mixed oxide phase at 31.2°, 36.7°, 44.7°, 65.1° and 79.1° (JCPDS N°37-0878) cannot be excluded as these latter may be present but masked by the more intense diffraction lines of the mixed cobalt oxide. These peaks indicate the presence of an interaction between copper and cobalt metals that become more important at higher Co content.

Figure 2.9 illustrates XRD patterns of Co_6Al_2, $1Ru/Co_6Al_2$ and $5Cu/Co_6Al_2$ calcined at 800°C. The reason for the calcination of these solids at 800°C is to compare their catalytic performance in the methane steam reforming reaction to the ones calcined at 500°C as the reaction takes place at temperatures as high as 800°C (section 3.3.4). After the calcination at 800°C, spinel lines are more intense due to the higher crystallintiy of the

different obtained phases at higher calcination temperature, and they are shifted to significantly lower diffraction angles (from 36.9° to 36.7°) characteristics of the $CoAl_2O_4$ phase due to the substitution of Co^{2+} with a smaller cation Al^{3+} (rCo^{2+}= 0.74 Å> rAl^{3+}= 0.50 Å) [129].

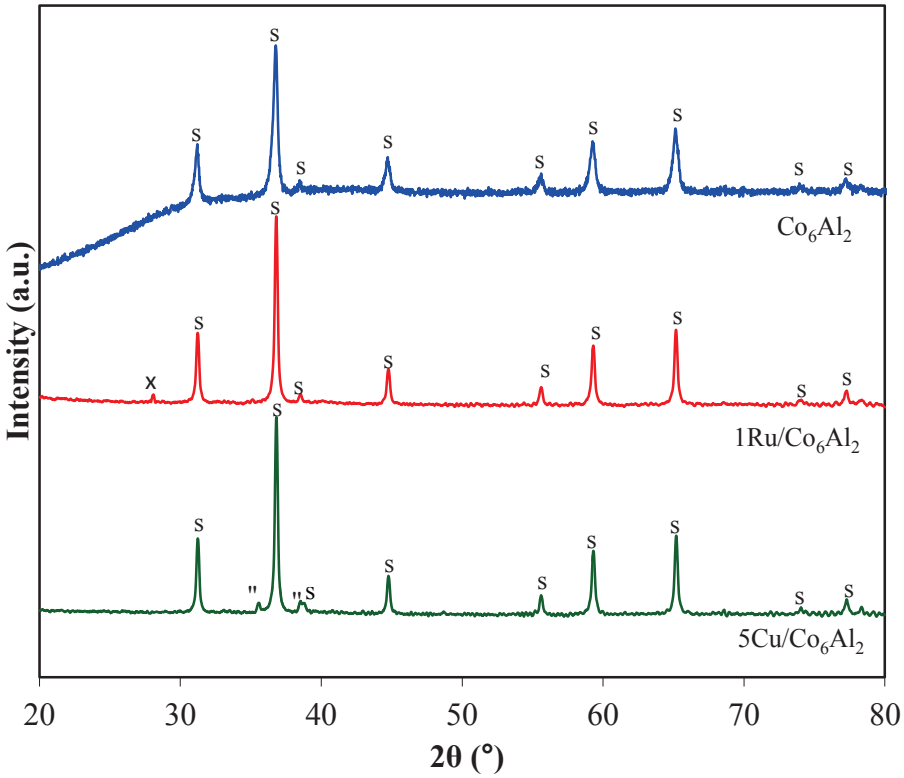

Figure 2.9 XRD patterns for Co_6Al_2, 1Ru/Co_6Al_2 and 5Cu/Co_6Al_2 catalysts calcined at 800°C. "S" spinel Co_3O_4 (JCPDS N°42-1467) $CoAl_2O_4$ (JCPDS N°44-0160) Co_2AlO_4 (JCPDS N°38-0814), "ˮ" CuO tenorite (JCPDS N°45-0937) and "×" tetragonal RuO_2 (JCPDS N°40-1290)

Crystallite size was calculated from the line broadening of the most intense reflection of cobalt oxide (2θ= 36.8°), copper oxide (2θ= 35.4°) and ruthenium oxide (2θ= 28°) peaks. Results are included in table 2.5. XRD analysis shows that the increase of cobalt content has a significant influence on the crystallite size and nanoparticles of cobalt oxide are seen only for the catalysts calcined at 500°C. In addition, with a higher

calcination temperature (800°C), the increase of the particle size is normally observed due to the higher crystallinity seen in figure 2.9.

Table 2.5 Spinel, CuO and RuO_2 particle size (nm) in the calcined supports and catalysts

Sample	Spinel particle size (nm)	Active phase particle size (nm) (CuO/RuO_2)
Mg_6Al_2 (500°C)	-	-
$Co_2Mg_4Al_2$ (500°C)	3.2	-
$Co_4Mg_2Al_2$ (500°C)	5.1	-
Co_6Al_2(500°C)	10.5	-
Co_6Al_2 (800°C)	29.2	-
5Cu/Mg_6Al_2 (500°C)	-	-
5Cu/$Co_2Mg_4Al_2$ (500°C)	3.1	-
5Cu/$Co_4Mg_2Al_2$ (500°C)	5.7	-
5Cu/Co_6Al_2 (500°C)	10.9	-
3Cu/Co_6Al_2 (500°C)	10.4	-
15Cu/Co_6Al_2 (500°C)	5.9	66.7
25Cu/Co_6Al_2 (500°C)	3.8	35.3
5Cu/Co_6Al_2 (800°C)	52.4	83.3
1Ru/Mg_6Al_2 (500°C)	-	79.3
1Ru/$Co_2Mg_4Al_2$ (500°C)	3.1	62.1
1Ru/$Co_4Mg_2Al_2$ (500°C)	5.3	27.9
1Ru/Co_6Al_2 (500°C)	10.3	-
3Ru/Co_6Al_2 (500°C)	10.9	4.3
5Ru/Co_6Al_2 (500°C)	4.3	33.9
1Ru/Co_6Al_2 (800°C)	49.4	49.4

Furthermore, the decrease of the active phase particle size with the increase of copper or ruthenium content can be explained by the incorporation of Cu^{2+} or Ru^{4+} ions into the cobalt oxide lattice to form mixed Cu-Co or Ru-Co oxides leading to the inhibition of the crystal growth of the metal oxides. Finally, the increase in the particle size observed for $1Ru/Co_xMg_{6-x}Al_2$ catalysts is probably caused by the formation of ruthenium oxide agglomerates as seen in figure 2.7.

2.5 Measurement of the Specific Surface Areas of the Solids Using the "Brunauer Emmet Teller" Technique

2.5.1 Brunauer Emmet Teller Technique (BET)

Solids present on their surface some defects and some pores of variable sizes, which increase the contact area of the solid with the outside (reactant). The value of the specific surface area is directly related to the number of pores on the surface of the solid. The higher the number, the larger the specific surface area value will be. An important surface area increases the probability of adsorption of molecules on the solid. When the solid is crystallized, the surface area decreases due to the presence of crystallized agglomerates. Therefore, to provide a high dispersion of the active phase, supports must possess a reasonably high specific surface area. The specific surface areas (S_{sp}) were measured based on the "Brunauer Emmet Teller" method (BET) using a surface area analyzer "Qsurf M1" apparatus. Samples are pretreated at 60°C for non calcined supports and 130°C for the other solids under a nitrogen flow for 15 minutes. The adsorption of a "30 vol.% N_2 (adsorbed gas) + 70 vol.% He (carrier gas)" mixture is then carried out at -196°C. After the completion of adsorption, the sample is removed from liquid nitrogen and left at room temperature. This quick heating of the sample desorbs the gaseous nitrogen

which is quantized using a thermal conductivity detector. However, it is necessary to note that the specific surface area gives no information on the quality of the catalytic site (the nature and the density of the active centers).

2.5.2 S_{sp} of the $Co_xMg_{6-x}Al_2HT$ and $Co_xMg_{6-x}Al_2$ Solids

Figure 2.10 displays the evolution of the specific surface areas (S_{sp}) of $Co_xMg_{6-x}Al_2$ and $Co_xMg_{6-x}Al_2HT$ solids.

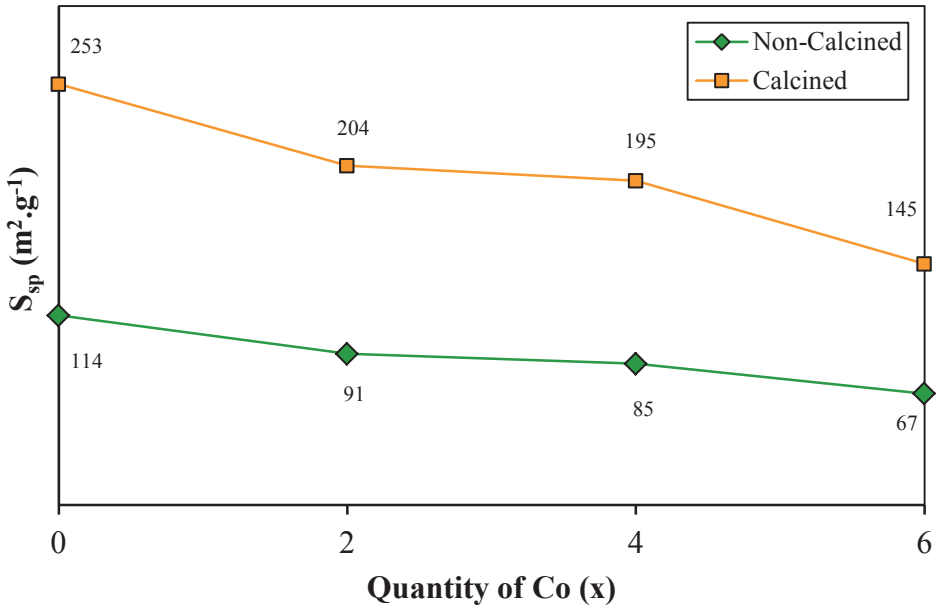

Figure 2.10 Specific surface areas ($m^2.g^{-1}$) of $Co_xMg_{6-x}Al_2HT$ and $Co_xMg_{6-x}Al_2$ solids

Dried Mg_6Al_2HT, showed the highest specific surface areas (S_{sp}= 114 $m^2.g^{-1}$). This value decreases when the Mg is gradually replaced with Co. Thus, the lowest specific surface area is obtained for Co_6Al_2HT (S_{sp}= 67 $m^2.g^{-1}$). After calcination, an increase in the specific surface areas was observed with a similar relative decrease when Mg is substituted with Co. In accordance with the XRD results, dried solids are mostly crystallized hydrotalcites. After calcination at 500°C, the hydrotalcite structure is destroyed following the departure of water molecules and CO_2 (from the interlayer), and the crystalline phase is

lost. Therefore, their specific surface area will increase [88, 130]. In fact, Stanimirova et al. [131], suggested a thermal evolution of Mg-Al hydrotalcite (Mg/Al=3) leading to a "metahydrotalcite P periclase amorphous" phase between 400°C and 900°C and a solid solution of $MgO+MgAl_2O_4$. "Metahydrotalcite P periclase", which is an amorphous phase, can be partly responsible for the high specific surface area of the oxides [131]. In addition, the thermal analysis revealed a difference in the stability of the solids according to their Mg content. This can be explained by the fact that the amorphous phase that follows the destruction of the hydrotalcite phase occurs for the Mg rich samples at higher temperature than solids containing cobalt which is in agreement with the obtained high specific surface area of the solids containing magnesium [124]. The difference between the values of specific surface areas for the different solids at a same calcination temperature is due to the difference in the crystallized phase. Thus, higher crystallization leads to lower surface areas [112].

2.5.3 S_{sp} of the Ruthenium and Copper-Based Catalysts

Figure 2.11 represents the values of the specific surface areas of all the impregnated solids before and after calcination. It is noticed that when $Ru(NO)(NO_3)_3$ solution is impregnated on calcined Co_6Al_2, the specific surface area of $1RuCo_6Al_2$ catalyst is almost the same compared to Co_6Al_2 taking in consideration the error margin in the BET technique (±10%). Since, the ruthenium content didn't affect the Ssp, it is concluded that for this catalyst, the interaction with cobalt support is good enough to disperse ruthenium oxide species on its surface without clusters formation that may clog pore entrances. This is in correlation with the XRD result for $1Ru/Co_6Al_2$ as no characteristic peaks for agglomerated RuO_2 species were observed. Concerning $5Cu/Co_xMg_{6-x}Al_2$ and $1Ru/Mg_6Al_2$ catalysts, it is observed that a drastic decrease in Ssp is obtained between the catalysts and

their relative supports. This can be explained by the fact that copper and ruthenium oxides were formed as agglomerates following impregnation and calcination as was seen in XRD results (figure 2.7 and 2.8). These agglomerates probably block the pores on the support surface leading to a decrease in the specific surface area [127, 132].

In addition, the specific surface areas of $1Ru/Mg_6Al_2$, $1Ru/Co_2Mg_4Al_2$, $5Cu/Mg_6Al_2$ and $5Cu/Co_2Mg_4Al_2$ catalysts increase following their calcination. This is due to the destruction of the reconstructed hydrotalcite phase (memory effect) that reappeared after impregnation with excess solution. Thus, the destruction of the hydrotalcite phase to oxide form (periclase) leads to an increase in the specific surface areas. The remaining solids exhibited similar specific surface areas compared to uncalcined precursors.

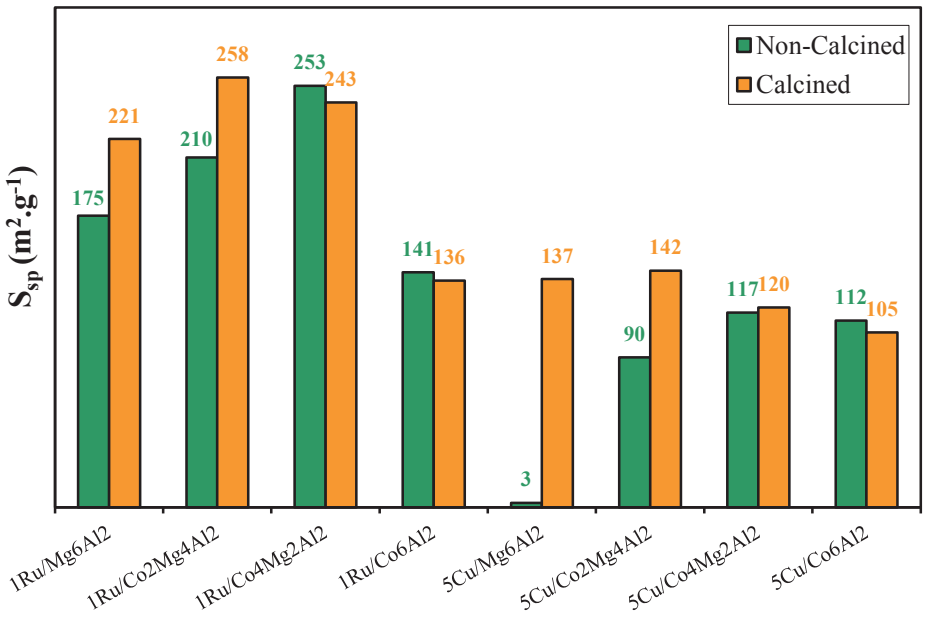

Figure 2.11 Specific surface areas ($m^2.g^{-1}$) of $1Ru/Co_xMg_{6-x}Al_2$ and $5Cu/Co_xMg_{6-x}Al_2$ solids before and after calcination at 500°C

Figure 2.12 illustrates the specific surface areas for $1Ru/Co_6Al_2$ and $5Cu/Co_6Al_2$ calcined at 800°C and yRu/Co_6Al_2, zCu/Co_6Al_2 calcined at 500°C (where y= 0.5, 1, 3, 5 and z= 0.5, 3, 5, 15, 25).

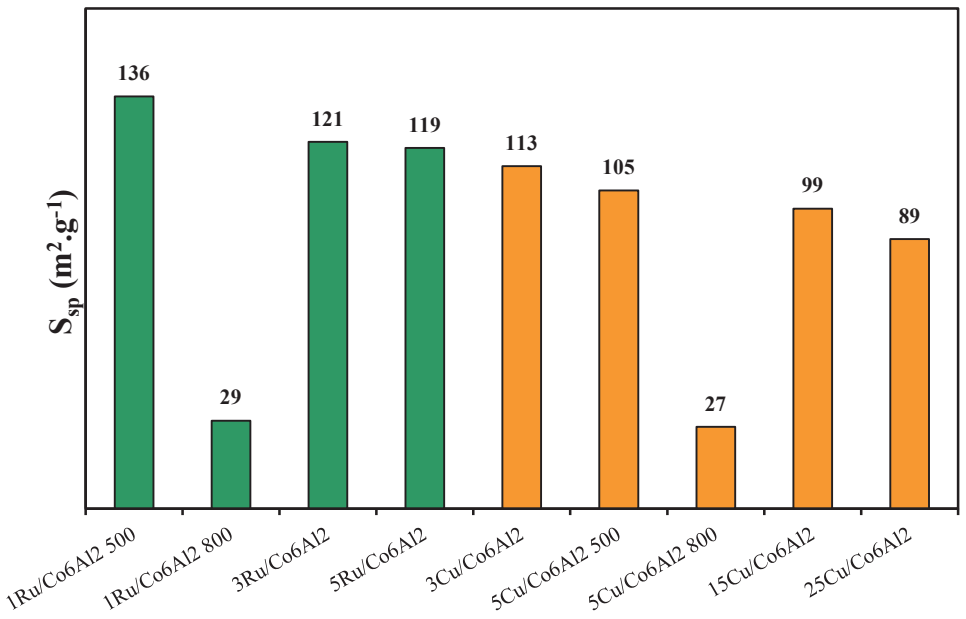

Figure 2.12 Specific surface areas ($m^2.g^{-1}$) of *y*Ru/Co_6Al_2 and *z*Cu/Co_6Al_2 solids calcined at 500°C and 1Ru/Co_6Al_2 and 5Cu/Co_6Al_2 calcined at 800°C

A decrease in the surface area is observed with higher active phase contents. This is attributed to the presence of RuO_2 and CuO agglomerates (detected in XRD) due to a weak interaction between the support and the active phase. These agglomerates can plug the pores at the surface and decrease the specific surface area. It is noteworthy that the specific surface area significantly decreases with the increase of the calcination temperature where samples calcined at 500°C present higher surface areas compared to those calcined at 800°C. This decrease in the specific surface area for the catalysts calcined at 800°C is due to the enhanced crystallization of the solids as was shown by XRD technique (figure 2.9).

2.6 Redox Behavior of the Different Catalysts

2.6.1 Temperature Programmed Reduction Technique (TPR)

Temperature programmed reduction (TPR) is a widely used technique for the characterization of metal oxides dispersed on a support in order to study their redox

behavior; every reduction reaction will induce an oxidation reaction. TPR method yields quantitative information on the reducibility of the oxides surface, as well as the heterogeneity of the reducible catalytic sites present on the surface.

TPR experiments were carried out on a ZETON ALTAMIRA AMI-200 apparatus. Around 25 mg of each solid were introduced in a U-shaped quartz reactor.

The analysis is done in 3 consecutive steps:

- The first step consists of the calibration of the hydrogen consumption. 5 calibration pulses are done with an argon flow of 30 $mL.min^{-1}$ as well as 5% H_2/Ar mixture.
- The second step consists of pretreating the sample at 150°C with an inert gas (argon) for 1 h in order to eliminate water and adsorbed surface impurities.
- The third step consists of a temperature programmed reduction (or oxidation). The analysis was done from ambient temperature up to 900°C with a heating rate of $5°C.min^{-1}$ under a hydrogen (or oxygen) flow diluted in argon (or helium) (30 $mL.min^{-1}$/ 5 vol.% in Ar or 30 $mL.min^{-1}$ in 10 vol.% in He) under atmospheric temperature. The amount of H_2 (or O_2) consumed was monitored with a thermal conductivity detector (TCD) used to measure changes in the thermal conductivity of the gas stream. The TCD signal is then converted to concentration of active gas using a level calibration. Integrating the area under the concentration as a function of temperature (or time) yields the total consumed gas quantity.

2.6.2 TPR of the $Co_xMg_{6-x}Al_2$ Solids

Figure 2.13 shows the TPR profiles of the $Co_xMg_{6-x}Al_2$ supports calcined at 500°C and Co_6Al_2 calcined at 800°C. It is observed that Mg_6Al_2 did not reduce in the considered temperature range. This can be explained by the fact that the magnesium and/or the aluminum oxides are not easily reduced in this temperature range [127]. On the other hand,

supports containing cobalt present two reduction peaks. The first between 300°C and 360°C (peak I) and the second at temperatures higher than 600°C (peak II). It is noticed that the maximum temperature of peak II is lower when more cobalt is present in the solid. This decrease reflects the fact that the increase in the amount of active species (in this case: cobalt) accelerates the reduction, therefore making it faster at lower temperature. This is mostly due to kinetic considerations where an increase in reactive sites content affects the rate of the reaction making it faster at lower temperature [133].

XRD patterns of these supports (figure 2.6) show the presence of cobalt oxide Co_3O_4 in addition to Co_2AlO_4 and/or $CoAl_2O_4$ that give almost similar XRD lines. The reduction steps of these oxides are shown in equations 2.1 to 2.4.

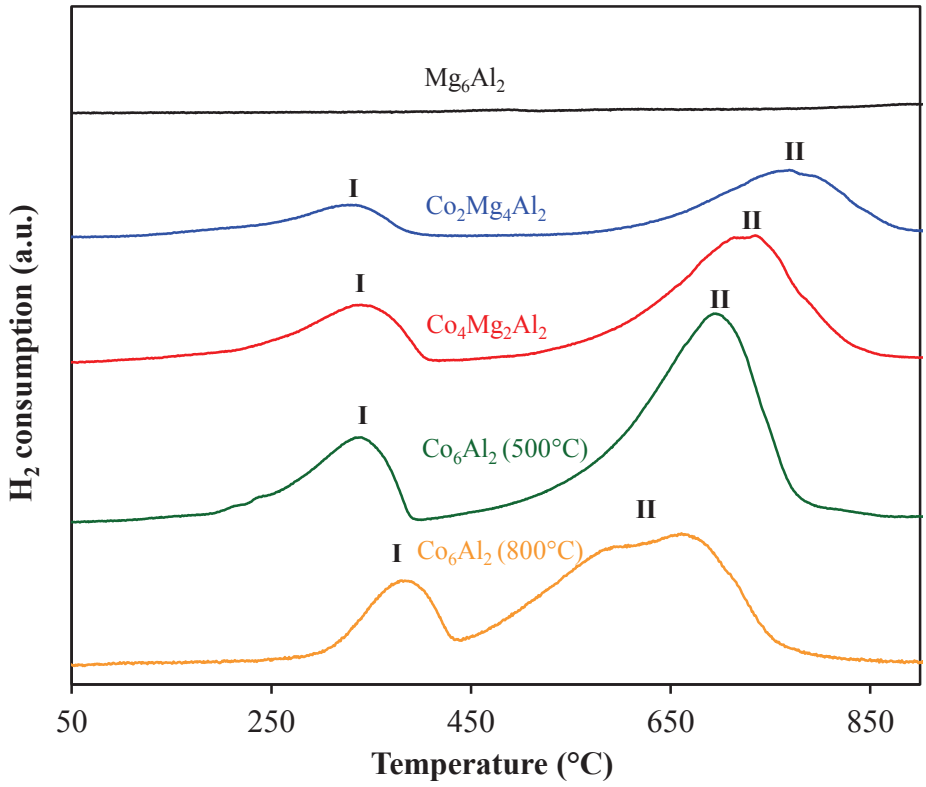

Figure 2.13 H_2-TPR profiles obtained for the $Co_xMg_{6-x}Al_2$ supports calcined at 500°C and Co_6Al_2 solid calcined at 800°C

Cobalt oxide Co_3O_4 will reduce in two steps as follows:

$$Co_3O_4 + H_2 \rightarrow 3\ CoO + H_2O \quad \text{(Equation 2.1)}$$

$$3\ CoO + 3\ H_2 \rightarrow 3\ Co + 3\ H_2O \quad \text{(Equation 2.2)}$$

Co_2AlO_4 or $CoAl_2O_4$ will reduce as follows:

$$2\ Co_2AlO_4 + H_2 \rightarrow CoAl_2O_4 + 3\ CoO + H_2O \quad \text{(Equation 2.3)}$$

$$CoAl_2O_4 + H_2 \rightarrow Co + Al_2O_3 + H_2O \quad \text{(Equation 2.4)}$$

Thus peak I can be attributed to Co_3O_4 reduction into CoO and then to metallic cobalt Co^0 (Equations 2.1 and 2.2) [115]. However, it is not possible to distinguish between them. Moreover, peak II corresponds then to the reduction of cobalt aluminate species Co^{2+}-Al^{3+} or Co^{3+}-Al^{3+} (Equations 2.3 and 2.4) [127, 134-136].

The integration of the reduction peaks in figure 2.13 shows that the consumed H_2 quantity increases with the cobalt content (table 2.6). This confirms that TPR peaks observed are essentially related to the reduction of cobalt species. The decrease in the hydrogen consumption of Co_6Al_2 calcined at 800°C may be due to the formation of more $CoAl_2O_4$ and Co_2AlO_4 spinel (as detected by XRD) which are more difficult to reduce than Co_3O_4. In addition, the experimental hydrogen consumption is lower than the theoretical one required for the reduction of the cobalt oxides to Co indicating that cobalt ions has not been reduced completely.

Table 2.6 Experimental and theoretical hydrogen consumptions of $Co_xMg_{6-x}Al_2$ solids calcined at 500°C and Co_6Al_2 calcined at 800°C

Sample	H_2 consumption [µmol $H_2.g^{-1}$ catalyst]		Theoretical H_2 consumption [µmol $H_2.g^{-1}$ catalyst] (Cobalt oxide→Co)
	I	II	
Mg_6Al_2	-	-	-
$Co_2Mg_4Al_2$	1328	3202	6294
$Co_4Mg_2Al_2$	2038	5615	10590
Co_6Al_2 (500°C)	2570	9132	13709
Co_6Al_2 (800°C)	1845	8727	13709

2.6.3 TPR of the $Ru/Co_xMg_{6-x}Al_2$ Solids

Figure 2.14 represents the TPR profiles obtained for yRu/$Co_xMg_{6-x}Al_2$ catalysts. According to previous results, it is considered that the RuO_2 phase is the most abundant ruthenium species present in the calcined solids [47].

RuO_2 will be reduced into Ru^0 according to:

$$RuO_2 + 2\ H_2 \rightarrow Ru^0 + 2\ H_2O \qquad \text{(Equation 2.5)}$$

This reduction of Ru^{4+} into Ru^0 is done in a stepwise manner [137, 138] as follows:

$$2\ RuO_2 + H_2 \rightarrow Ru_2O_3 + H_2O \qquad (Ru^{4+} \rightarrow Ru^{3+}) \qquad \text{(Equation 2.6)}$$

$$RuO_2 + H_2 \rightarrow RuO + H_2O \qquad (Ru^{4+} \rightarrow Ru^{2+}) \qquad \text{(Equation 2.7)}$$

$$2\ RuO_2 + 3\ H_2 \rightarrow Ru_2O + 3\ H_2O \qquad (Ru^{4+} \rightarrow Ru^{+}) \qquad \text{(Equation 2.8)}$$

$$RuO_2 + 2\ H_2 \rightarrow Ru + 2H_2O \qquad (Ru^{4+} \rightarrow Ru^{0}) \qquad \text{(Equation 2.9)}$$

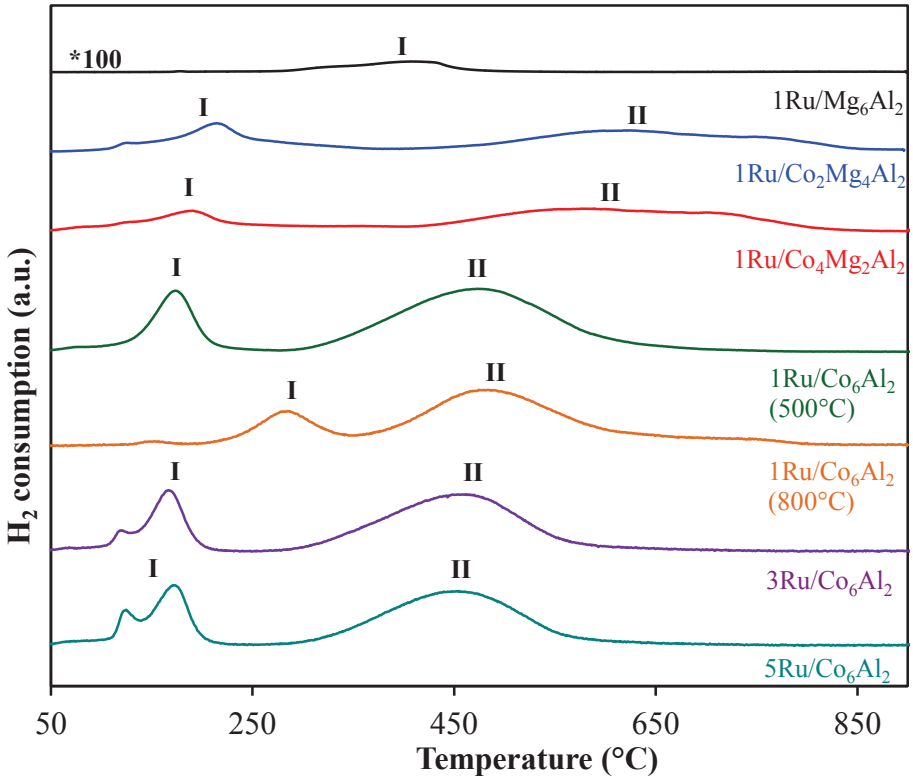

Figure 2.14 H_2-TPR profiles obtained for the *y*Ru/$Co_xMg_{6-x}Al_2$ solids calcined at 500°C and 1Ru/Co_6Al_2 solid calcined at 800°C

It can be noticed the remarkable decrease in the temperature of the reduction peaks after metal impregnation. The incorporation of noble metals enhances the reducibility of the cobalt ions via hydrogen spillover [139, 140]. All cobalt containing solids -except 1Ru/Co_6Al_2 calcined at 800°C- present in their TPR profile a reduction peak in the 150-230°C temperature range (peak I). 1Ru/Mg_6Al_2 presents one reduction peak in the temperature range of 280-420°C. This latter is attributed to the reduction of RuO_2 according to the above reactions because of the non-reducibility of the Mg/Al oxides species in the studied temperature range [133].

Peak I around 170°C for yRu/Co_6Al_2 solids can be attributed to the reduction of bulk RuO_2 species [141]. As all the 1Ru/$Co_xMg_{6-x}Al_2$ catalysts contain the same ruthenium weight percentage (1wt.%) and knowing that the sample mass used in each experiment is

the same approximately, the increase in the H_2 consumption corresponding to peak I is attributed to the reduction of ruthenium oxide and some of the cobalt oxides present in the different solids. Moreover, peak II occurs at lower temperatures compared to profiles obtained for the non-impregnated supports. The decrease in the reduction temperature suggests the formation of readily reducible species arising from the interaction between Co and Ru.

In addition, experimental hydrogen consumptions in table 2.7 are much higher than the theoretical ones attributed to the reduction of RuO_2 into Ru except for $1Ru/Mg_6Al_2$ catalyst.

Table 2.7 Experimental and theoretical H_2 consumptions of calcined Ru-based catalysts

Sample	H_2 consumption [µmol $H_2.g^{-1}$ catalyst]		
	Experimental		Theroretical
	I	II	$RuO_2 \rightarrow Ru$
$1Ru/Mg_6Al_2$ (500°C)	64	-	198
$1Ru/Co_2Mg_4Al_2$ (500°C)	908	4018	
$1Ru/Co_4Mg_2Al_2$ (500°C)	1753	4125	
$1Ru/Co_6Al_2$ (500°C)	1936	8344	
$3Ru/Co_6Al_2$ (500°C)	2556	7853	594
$5Ru/Co_6Al_2$ (500°C)	2961	8003	989
$1Ru/Co_6Al_2$ (800°C)	1633	7197	198

This indicates that cobalt is reduced simultaneously with ruthenium [142] and confirms the interaction between the two metals as shown in XRD results (presence of Co_2RuO_4 phase in section 2.4.3). In the case of $1Ru/Mg_6Al_2$, experimental hydrogen consumption is lower than the theoretical one required for the reduction of RuO_2 to Ru

indicating that Ru^{4+} has not been completely reduced. The reason might be due to strong interaction with the support leading to the formation of solid solutions not easily to be reduced [142].

With the increase of the ruthenium content from 1wt.% to 3wt.% and 5wt.% on Co_6Al_2 support, the area of peak I increases confirming its attribution to ruthenium species reduction. Furthermore, shoulders appear on peak I suggesting clearly the presence of agglomerated ruthenium species as seen in the XRD results (section 2.4.3). However, lower peaks around 110°C for $3Ru/Co_6Al_2$ and $5Ru/Co_6Al_2$ and around 70°C for $1Ru/Co_6Al_2$ are attributed to the reduction of free RuO_2 species [143].

$1Ru/Co_6Al_2$ calcined at 800°C shows a decrease in the hydrogen consumption compared to the same catalysts calcined at 500°C, and peak I is shifted to higher temperatures attributed to the reduction of Co_3O_4 as if it is not well-interacted with ruthenium compared to the catalyst calcined at 500°C. A shoulder around 740°C is observed for peak II attributed to $CoAl_2O_4$. In fact, Wang and Ruckenstein [129], reported that the reducibility of cobalt oxide species decreases as follows: Co_3O_4> Co_2AlO_4> $CoAl_2O_4$. Therefore, the two different cobalt aluminate oxides can be differentiated in this case. They also stated that Co_3O_4 is the major phase obtained in the cobalt-aluminate catalysts calcined at 500°C, whereas at higher calcination temperature, Co_3O_4 is more converted to Co_2AlO_4 and $CoAl_2O_4$. A small peak is found at 150°C due to the reduction of ruthenium species. It is concluded that at high calcination temperatures, Co_3O_4 are reduced at higher temperatures and part of it is converted to Co_2AlO_4 and $CoAl_2O_4$ which are less reducible species explaining the decrease in the hydrogen consumption.

2.6.4 TPR of the Cu/$Co_xMg_{6-x}Al_2$ Solids

Figure 2.15 shows the TPR profiles of *z*Cu/$Co_{6-x}Mg_xAl_2$ catalysts.

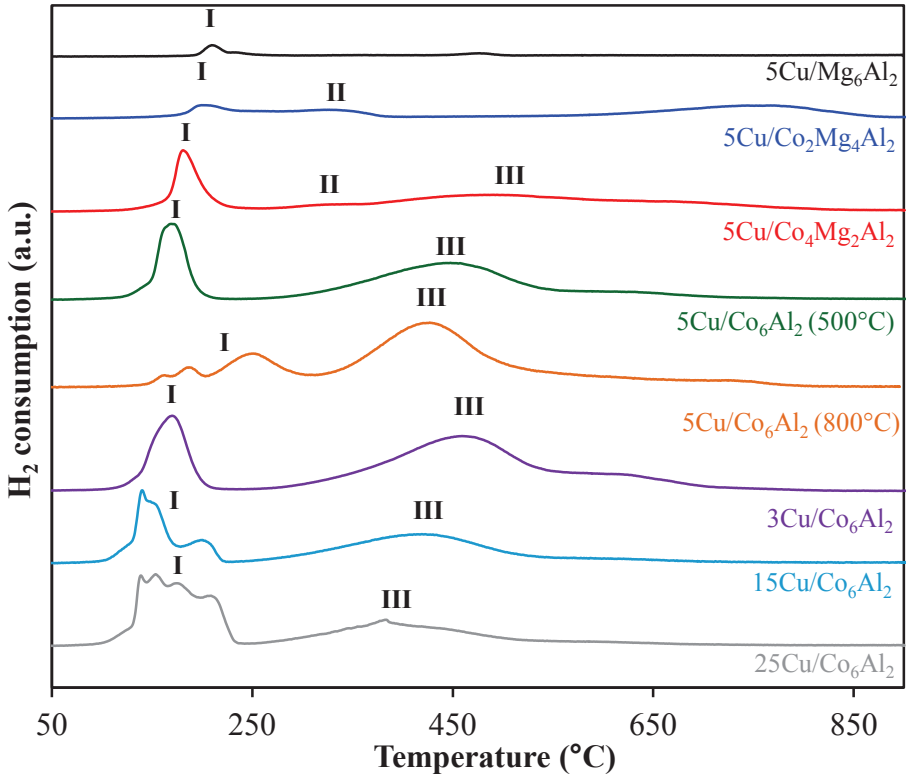

Figure 2.15 H_2-TPR profiles obtained for z$Cu/Co_xMg_{6-x}Al_2$ solids calcined at 500°C and the 5Cu/Co_6Al_2 solid calcined at 800°C

All the profiles present reduction peaks in the 150-230°C temperature range (Peak I). This latter is attributed to the presence of copper (II) oxide that is reduced to Cu^+ (Cu_2O) then into Cu^0 (hard to be distinguished) as follows:

$2\ CuO + H_2 \rightarrow Cu_2O + H_2O\ (Cu^{2+} \rightarrow Cu^+)$ (Equation 2.10)

$Cu_2O + H_2 \rightarrow 2\ Cu + H_2O\ (Cu^+ \rightarrow Cu^0)$ (Equation 2.11)

Moreover, many different Cu^{2+} species may exist: isolated Cu^{2+} ions, Cu^{2+} clusters, small well dispersed CuO particles, CuO agglomerates, or even bulk CuO [144]. Thus, the presence of small peaks and shoulderings (peak I) for 5-15-25Cu/Co_6Al_2 catalysts may be

the result of the reduction of these different species at different temperatures. The peak at lower temperatures (around 140°C) correspond to isolated Cu^{2+} and Cu^{2+} clusters that are well dispersed and are in an interaction with the surface of the support [144]. Whereas peaks between 195°C and 200°C are attributed to the reduction of different Cu^{2+} species where a big amount of agglomerated CuO and bulk species on the surface of the support are present [144, 145]. This is in agreement with the XRD results (figure 2.8). For $5Cu/Mg_6Al_2$, peak I shows a hydrogen consumption that corresponds only to the reduction of copper species into metallic Cu^0 because magnesium and aluminum oxides do not reduce in this temperature range [88].

Furthermore, it is clear in table 2.8 that the experimental hydrogen consumptions at low temperatures are greater than the theoretical values attributed to the reduction of CuO into Cu with the exception of $5Cu/Mg_6Al_2$.

Table 2.8 Experimental and theoretical H_2 consumptions of calcined Cu-based catalysts

Sample	H_2 consumption [µmol $H_2.g^{-1}$ catalyst]			
	Experimental			Theroretical
	I	II	III	CuO → Cu
$5Cu/Mg_6Al_2$ (500°C)	334	-	-	787
$5Cu/Co_2Mg_4Al_2$ (500°C)	1279	983	2950	
$5Cu/Co_4Mg_2Al_2$ (500°C)	2265	793	5200	
$5Cu/Co_6Al_2$ (500°C)	3120	-	7868	
$3Cu/Co_6Al_2$ (500°C)	3626	-	11787	472
$15Cu/Co_6Al_2$ (500°C)	4301	-	6717	2360
$25Cu/Co_6Al_2$ (500°C)	5350	-	5167	3934
$5Cu/Co_6Al_2$ (800°C)	3190	-	5577	787

This indicates that cobalt is reduced simultaneously with copper as a result of the interaction between copper and cobalt oxide. For $15Cu/Co_6Al_2$ and $25Cu/Co_6Al_2$ catalysts, the increase of the H_2 consumption corresponding to peak I is observed due to the presence of higher copper content. In the case of $5Cu/Mg_6Al_2$, hydrogen consumption is far lower than that required for the quantitative reduction of CuO to Cu indicating that Cu^{2+} has not been reduced completely. The reason might be that some Cu^{2+} ions enter the MgO lattice and form Cu-Mg-O solid solution which cannot be easily reduced in the required temperature range [146].

For $5Cu/Co_4Mg_2Al_2$ and $5Cu/Co_2Mg_4Al_2$ catalysts, peak II in the temperature range 280-370°C is observed. It can be attributed to the reduction of new mixed copper-cobalt oxide species that are formed in the presence of magnesium. Peak III is attributed to the reduction of cobalt aluminate species Co^{3+}-Al^{3+} or Co^{2+}-Al^{3+} species [127, 147]. The temperature at which this peak occurs is lower when the cobalt content is higher as was observed with the non-impregnated supports. In fact, when CuO is reduced, Cu^0 helps in splitting H_2 molecules "spill-over" and makes the reduction of cobalt oxide species occur at lower temperatures.

Finally, as in the case of ruthenium catalyst calcined at 800°C, the reduction peak of cobalt oxide (peak I) is shifted to higher temperatures indicating the weakness of the interaction between Co and Cu as in the case of ruthenium. Copper presents two reduction peaks showing that it is found in different forms.

2.7 Fourier Transform Infrared Study

2.7.1 FTIR Spectroscopy Technique

Fourier Transform Infrared spectroscopy allows the analysis of chemical functions present in a solid by detecting the vibration characteristics of the chemical bonds. This technique is based on the infrared radiation by the material being analyzed (between 400 and 4000 cm^{-1} which corresponds to the domain of vibrational and rotational energy state of the molecules depending on the geometry of the molecule and its symmetry).

FTIR analyses were performed at room temperature on a BRUKER EQINOX 55 FTIR spectrometer equipped with a DTGS (Deuterated Triglycine Sulfate) detector. Spectra are recorded in the range 400-4000 cm^{-1} with an accumulation of 64 scans and a resolution of 4 cm^{-1} using the KBr pellet technique. All spectra are presented after the subtraction of the absorption signal of KBr.

2.7.2 FTIR Spectroscopy of the $Co_xMg_{6-x}Al_2HT$ and the $Co_xMg_{6-x}Al_2$ Solids

Figure 2.16 shows the infrared spectra of the $Co_xMg_{6-x}Al_2HT$ and the $Co_xMg_{6-x}Al_2$ solids calcined at 500°C. Almost similar FTIR spectra for all the solids are detected at higher wavenumber whereas at low wavenumbers, differences are observed.

Three types of vibration bands in infrared spectroscopy characterize the hydrotalcite structure-type [111, 148-150]:

- Vibration bands of the hydroxyl group
- Vibration bands of the octahedral brucite sheet
- Vibration bands of the species present in the interlayer

Thus, the broad band at about 3450-3500 cm^{-1} for calcined and uncalcined solids is attributed to the elongation of the O-H bond in a hydroxyl group, water molecules in the

interlayer and physisorbed water. In other words, it is attributed to the vibration of OH groups attached to Co, Mg and Al in the layers. A transmittance minimum around 1690 cm^{-1} and 1680 cm^{-1} is assigned to the HOH angular deformation of the interlayer water molecules [151]. The shoulder at 3040 cm^{-1} is due to the hydrogen bonding of interlayer water with carbonates anions (CO_3^{2-}) in the interlayer. The peaks at 1407 cm^{-1} and 935 cm^{-1} can be also attributed to the vibrations of bidendate CO_3^{2-} [152-154]. Peaks observed in the lower wavenumber region (< 800 cm^{-1}) are due to Co-O, Mg-O and Al-O vibrations at 610 cm^{-1}, 580 cm^{-1}, 460 cm^{-1} respectively [110]. The vibration peak at 790 cm^{-1} is due to Al-OH bond [110, 150, 155-158]. All these results highlight the presence of species in a hydrotalcite -like structure in the solid.

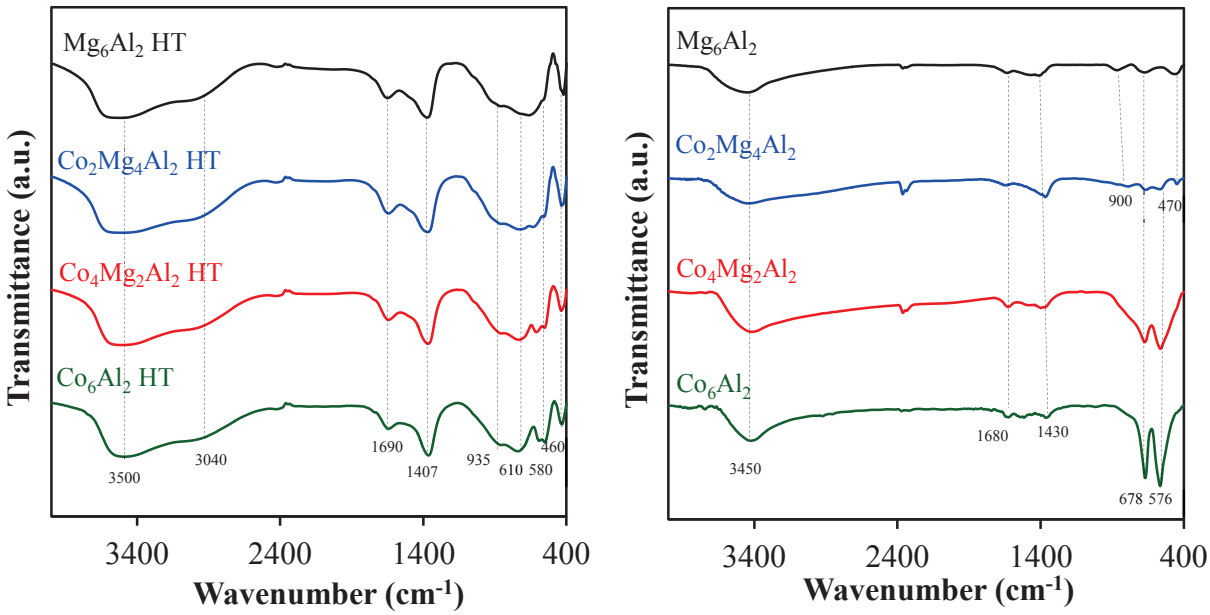

Figure 2.16 FTIR spectra of (a) $Co_xMg_{6-x}Al_2HT$ and (b) $Co_xMg_{6-x}Al_2$ calcined at 500°C

After calcination, the hydrotaclite structure is destroyed and carbonate ions are quasi absent. Nevertheless, vibration bands around 1430 cm^{-1} are attributed to free carbonate ions (wavenumber is higher than that observed for carbonates in the

interalyer) [159]. Vibration bands at 900 cm^{-1} are attributed to the vibrations of bidendate CO_3^{2-}. This result can be explained by the basic characters of these solids tending to easily absorb CO_2 in the form of cabronates. However, a large difference in the spectra at lower wavenumbers is observed compared to the uncalcined solids: two absorption bands at about 678 cm^{-1} and 576 cm^{-1} for $Co_4Mg_2Al_2$ and Co_6Al_2 calcined at 500°C are present and attributed to a mixture of different spinel. These values are similar to those reported for Co_3O_4 in literature (672 cm^{-1}, 590 cm^{-1}) [160]. These bands are broader for $Co_4Mg_2Al_2$ which is the result of a mixture of different spinels. These results are in accordance with XRD analysis that revealed the presence of more than one type of spinel.

2.7.3 FTIR Spectroscopy of the 1Ru/$Co_xMg_{6-x}Al_2$HT and the 1Ru/$Co_xMg_{6-x}Al_2$ Solids

Figure 2.17 presents FTIR spectra for uncalcined 1Ru/$Co_xMg_{6-x}Al_2$HT and calcined 1Ru/$Co_xMg_{6-x}Al_2$ solids.

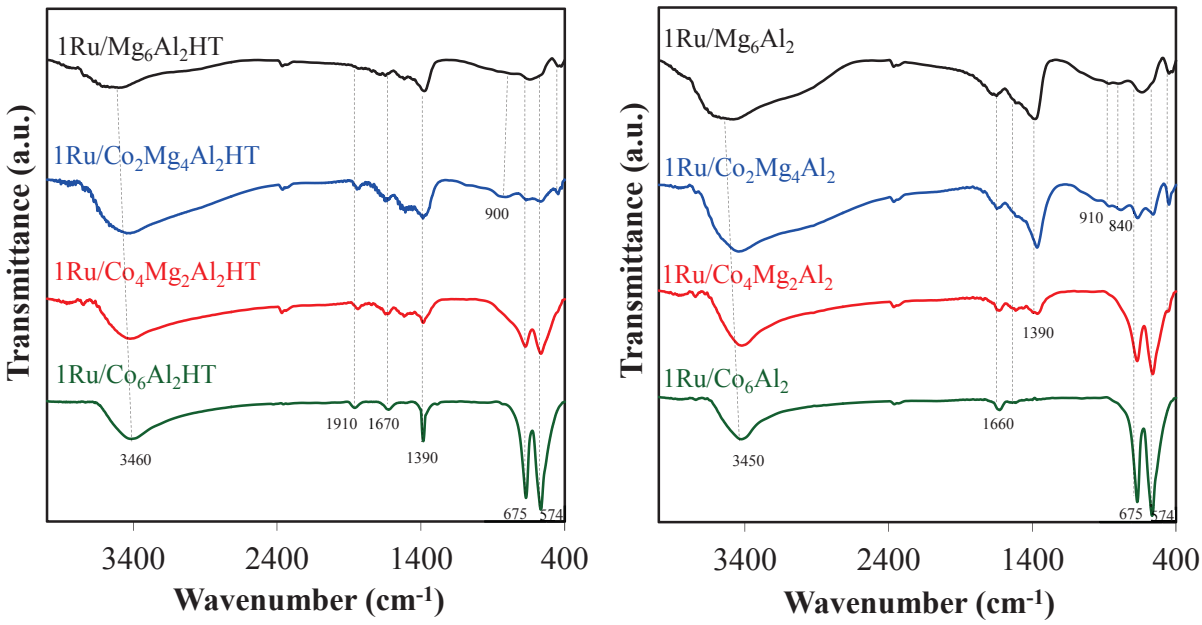

Figure 2.17 FTIR spectra of (a) 1Ru/$Co_xMg_{6-x}Al_2$HT and (b) 1Ru/$Co_xMg_{6-x}Al_2$ calcined at 500°C

The characteristic bands of spinel structures are observed for calcined and non-calcined catalysts between 574-675 cm^{-1} especially for the catalysts supported on $Co_4Mg_2Al_2$ and Co_6Al_2. The peaks around 3450 cm^{-1} and 1660 cm^{-1} are always present due to the elongation and deformation of water molecule. The peaks at 1390 cm^{-1} are present for $1Ru/Co_xMg_{6-x}Al_2$ HT and Mg containing calcined solids as these latter are highly basic and can adsorb CO_2 in the form of carbonates as mentionned before. Vibrations of Ru-OH can be masqued with water vibrations between 3200-3250 cm^{-1} [161]. This shouldering is mostly seen for catalysts with higher magnesium content, because as seen in XRD, Ru aggomerates are more detected in the catalsysts with high magnesium content. For the non-calcined catalysts, at 1910 cm^{-1}, the elongation of the nitrosyl group from $Ru(NO)(NO_3)_3$ precursor is detected [162]. For calcined $1Ru/Mg_6Al_2$ and $1Ru/Co_2Mg_4Al_2$ solids, the peak around 840 cm^{-1} is attributed to Ru-O species penta-coordinated [163-165]. Vibration bands around 900 cm^{-1} are attributed to the vibrations of bidendate CO_3^{2-}.

Other IR spectra are not illustrated due to similarities with the above results. But it must be noted that O-Cu-O vibration band is found at a wavenumber of 450 cm^{-1} for the copper based catalysts especially for higher copper content [166].

2.8 Porosity Study

The calcination of hydrotalcites containing carbonates and nitrates in the interlayer contributes to the of porous oxide solids. The presence of pores at the surface increases the contact surface and the probability of adsorption of the gaseous mixture on the catalyst.

Pore size, pore volume and pore size distribution measurement of the catalysts were determined from the nitrogen adsorption isotherms obtained by Sorptomatic 1990 series

apparatus after evacuation under vacuum and treatment at a high temperature (to remove impurities from the sites of adsorption).

N_2 adsorption desorption isotherms and pores distribution of calcined $Co_xMg_{6-x}Al_2$ catalysts are presented on figure 2.18.

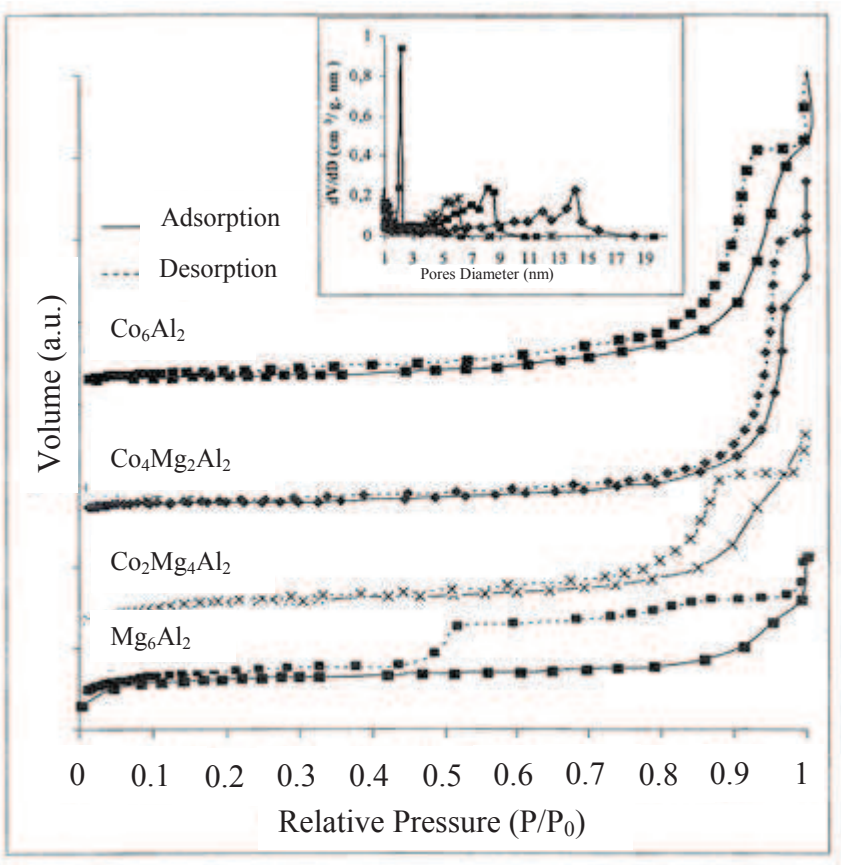

Figure 2.18 N_2-adsorption desorption isotherms and pores distribution for the calcined $Co_xMg_{6-x}Al_2$ solids

A visible difference is observed regarding the hysteresis loops. In fact, the morphology of the adsorbent can affect the shape and position of hysteresis loop. In accordance to IUPAC classifications, all N_2-adsorption-desorption isotherms show a type IV (see appendix C) pattern typical of mesoporous materials (with pores size of 8 nm, 14 nm, 2-6 nm and 2 nm for Co_6Al_2, $Co_4Mg_2Al_2$, $Co_2Mg_4Al_2$ and Mg_6Al_2 respectively. This

pore size distribution can lead to a strong interaction between the adsorbate and adsorbent [124, 167]. Type IV is characteristic of gradual increase in adsorption at low p/p0 range due to monolayer-multilayer adsorption followed by a great uprising in adsorption at a medium p/p0 range, together with an evident adsorption hysteresis loops.

The substitution of Mg with Co leads to the modification of the hysteresis loop. Mg_6Al_2 presents an H4 type hysteresis loop associated with narrow-slit like pores [168]. For the other supports containing cobalt, an H1 type hysteresis loop is seen with parallel adsorption-desorption branches, and an enlargement of the pore size. H1 hysteresis is associated with porous materials exhibiting a narrow distribution of relatively uniform cylindrical pores [169].

2.9 Electron Paramagnetic Resonance Study

2.9.1 EPR Technique

EPR technique is widely used in the study of species with one or more unpaired electron. The nature of the obtained information can vary from the detection of paramagnetic entity to a detailed description of the symmetry, the oxidation state of the neighboring atoms, the number of ligands, the nature of the bonds, and the coordination sphere of a paramagnetic species in a matrix or deposited on a support.

EPR spectra of species with S= 1/2 and I≠ 0 are obtained from the equation of spin Hamiltonian:

$$\mathcal{H} = \beta.H_z.g_{//}.S_z+\beta.H_x.g_{\perp}.S_x+\beta.H_y.g_{\perp}.S_y+A_{//}.I_z.S_z+A_{\perp}.I_y.S_y+ A_{\perp}.I_x.S_x \qquad \text{(Equation 2.12)}$$

With “H”: magnetic field, “S”: electron spin, “I”: nuclear spin, “A”: hyperfine coupling constant and “D”: dipole interaction constant. The first term corresponds to Zeeman Effect, the second to the hyperfine structure and the third to the fine structure.

“g” factor and the hyperfine coupling constant “A” are both EPR parameters characteristic of a paramagnetic species present in a given environment. The factor “g” is determined at a frequency and for a given magnetic field by the following relation:

$h\nu = g.\beta.H$ (Equation 2.13)

Where “h” is the Planck’s constant, “ν”: frequency, “β”: the Bohr magneton and “H”: magnetic field.

To record an EPR signal, the magnetic field is varied at a given frequency. When resonance occurs, the absorbed energy is then recorded and the first derivative of the absorption curve is obtained as resultant energy of the applied magnetic field. The EPR spectrum is the derivative of the absorption signal as a function of the magnetic field.

EPR technique stands out from the other spectroscopic techniques by its high sensitivity (1011 spins.cm^3 that corresponds to 0.1 ppb). This allows the study of solids containing low concentrations of paramagnetic entities. This advantage can become a disadvantage since in the presence of an excessive amount of paramagnetic species, broadening and even disappearance of the EPR signal affect the study.

The apparatus used is a spectrometer BRUKER EMX brand. All spectra were recorded at a frequency of 9.5 GHz (X-band). The magnetic field is modulated at 100 kHz with a power of 12mW to avoid the saturation of the signal. Frequency and the magnetic field are measured simultaneously. Spectra were recorded at room temperature and at -196°C. They were processed through the program of BRUKER WINEPR.

All the ruthenium and copper-based catalysts were characterized by EPR. A vacuum treatment was performed before doing the EPR analysis. In fact, the purpose of the

vacuum is to remove oxygen molecules adsorbed on the catalyst surface (physisorbed) and that could interfere with the interpretation of the spectrum. However, vacuum treatment may cause a partial reduction of the catalyst; therefore, EPR analysis was performed after a vacuum and heat treatment at a given temperature to study the reducibility of the catalyst. Three temperatures were used (125°C, 250°C and 350°C) with a temperature rise of 1°C.min^{-1}. Once the temperature is reached, the treatment is maintained at the given temperature for one hour.

2.9.2 EPR Spectra of 1Ru/Mg_6Al_2 Solid

EPR spectra of 1Ru/Mg_6Al_2 calcined at 500°C recorded at the temperature of liquid nitrogen and treated under vacuum at different temperatures (125°C, 250°C and 350°C) are represented in figure 2.19.

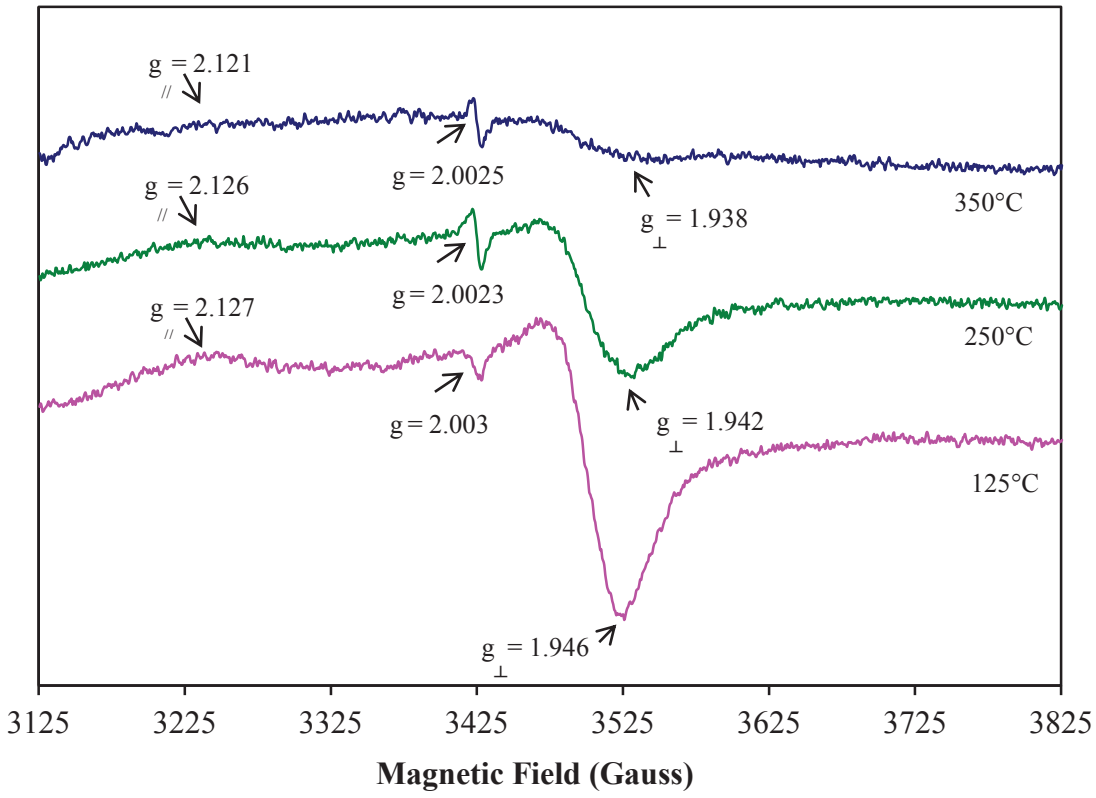

Figure 2.19 EPR spectra of 1Ru/Mg_6Al_2 calcined catalyst recorded at the temperature of liquid nitrogen after treatment under vacuum at 125°C, 250°C and 350°C

The EPR spectra of $1Ru/Mg_6Al_2$ represent an axial anisotropy signal characterized by the following parameters: $g_{//}$= 2.127, 2.126, 2.121 and $g_{\perp}$= 1.946, 1.942, 1.938 for the catalyst treated at 125°C, 250°C and 350°C respectively. The observed signal can be attributed to Ru^{+} (d^7) [170-172]. The intensity of these spectra decreases with increasing the treatment temperature due to the reduction of Ru^{+} to Ru^{0}. Another signal around g= 2.0023 is due to a trapped electron during the reduction of ruthenium species.

2.9.3 EPR Spectra of $5Cu/Mg_6Al_2$ Solid

EPR spectra of $5Cu/Mg_6Al_2$ calcined at 500°C and treated under vacuum at different temperatures (125°C, 250°C and 350°C) are represented in figure 2.20. The EPR spectrum of copper solid represents an axial anisotropy and hyperfine structure with $g_{//} > g_{\perp} > g_e$= 2.0023. The spectrum is due to the interaction of free electrons of Cu^{2+} ($3d^9$) with the magnetic nuclear moment of copper (I=3/2) that gives rise to a 4-fold hyperfine splitting of all the anisotropic components. We can distinguish two signals related to different Cu^{2+} species: S1 and S2. The first signal (S1) having the following component: $A_{//}$= 150 Gauss, $g_{//}$= 2.3451, g_{iso}= 2.1582, A_{iso}= 68 Gauss. While the second (S2) has other components: $A'_{//}$= 170 Gauss, $g'_{//}$= 2.2804, g'_{iso}= 2.1366, A'_{iso}= 75 Gauss. One series of hyperfine perpendicular lines is seen whatever the treatment temperature with $A_{\perp}$=~27-30 Gauss and $g_{\perp}$= 2.06475. Perpendicular components of the copper species with $A'_{//}$= 170 Gauss are either not resolved or very close to those of the second copper species (those with $A_{//}$= 150 Gauss). First, this high $A_{//}$ and $A'_{//}$ values ($A_{//}$ > 140 Gauss) for both signals may be due to the fact that Cu^{2+} is surrounded by more than six ligands in the support lattice [173, 174].

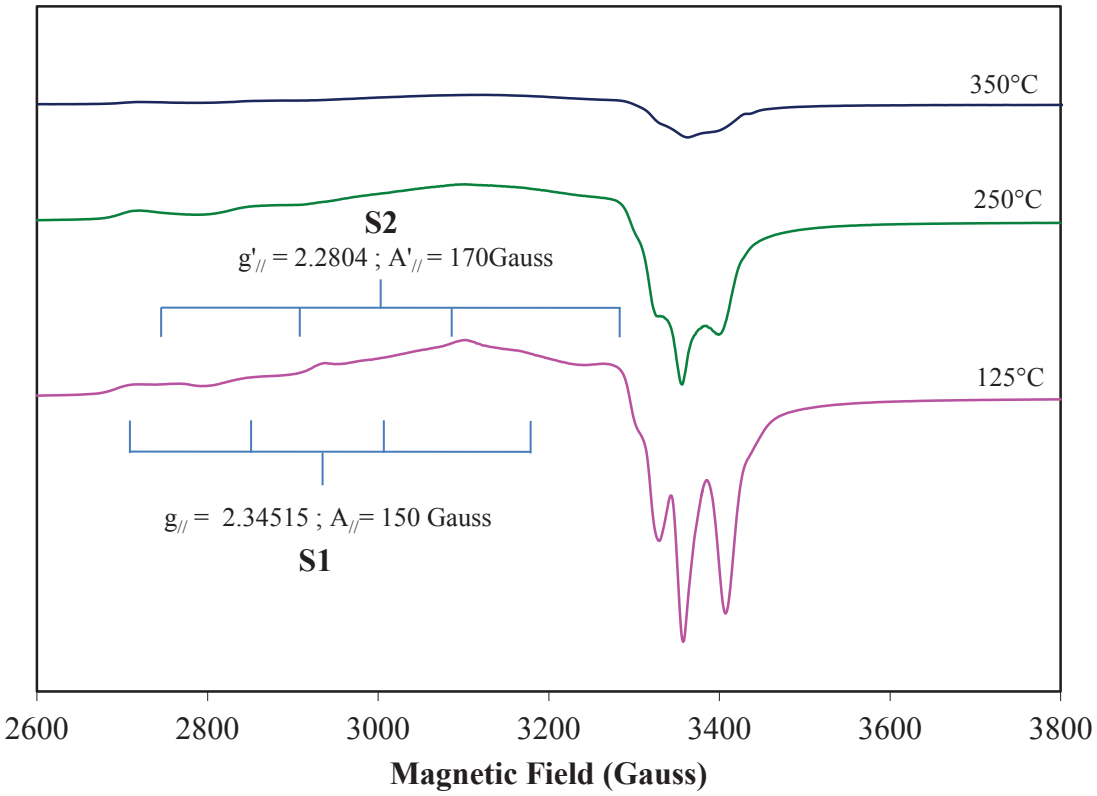

Figure 2.20 EPR spectra of 5Cu/Mg_6Al_2 calcined catalyst recorded at the temperature of liquid nitrogen after treatment under vacuum at different temperatures (125°C, 250°C and 350°C)

However, $A_{//}$ is lower than $A'_{//}$, therefore, we can deduce than the number of ligands surrounded Cu^{2+} in the S1 signal is lower than that of S2. S1 components may be attributed to Cu^{2+} ions (I=3/2) located in octahedral sites in the bulk of the support [174-177]. EPR parameters of S2 show that isolated Cu^{2+} ions are located in the surface in either square planar sites, or in the center of tetrahedron with high distortion [178].

With the increase of the treatment temperature, a significant diminution of the total intensity is observed and S2 signal disappeared. It seems that one of the Cu^{2+} sites (S2) is more easily reduced than the other (S1) as they are on the surface of the support.

In addition, DI/N values calculated for each EPR spectra are the following: $4.266*10^3$; $2.3*10^3$ and $1.034*10^3$ for 5Cu/Mg_6Al_2 treated under vacuum at 125°C, 250°C

and 350°C. This decrease in the values with the increase of the treatment temperature is due to the reduction of copper species and particularly to S2.

TPR profile of $5Cu/Mg_6Al_2$ calcined at 500°C is represented in a different scale in figure 2.21. Peak intensity is multiplied in order to be clearly visualized. It was demonstrated that this latter is attributed to the reduction of copper oxide. Two different peaks can be differentiated: I and II. This can confirm the EPR results that showed two different copper species reduced. We can attribute the first peak (I) to the S2 reduction of isolated copper species and the second to the reduction of S1 isolated copper species located in bulk that are not easily reduced as S2.

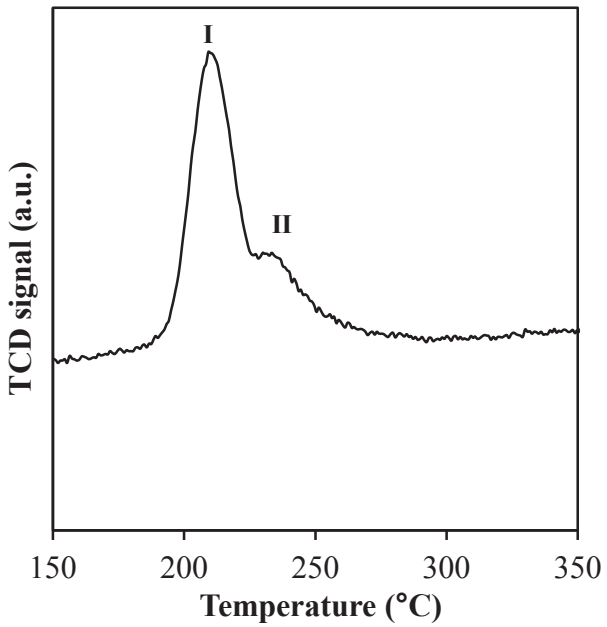

Figure 2.21 Hydrogen consumption of $5Cu/Mg_6Al_2$ calcined at 500°C

It must be noted that EPR results of the catalysts containing cobalt are not represented as they did not show any significant signal.

2.10 Conclusion

A series of $Co_xMg_{6-x}Al_2$ hydrotalcite was prepared via co-precipitation at constant pH. After the calcination of these hydrotalcites, ruthenium and copper precursors were impregnated and then calcined at 500°C/800°C. It was demonstrated that a partial reconstruction or "memory effect" of the hydrotalcite structure during the impregnation step of the active phase is detected especially for solids with high Mg amount due to the basic properties of the support.

XRD pattern showed the formation of the hydrotalcite phase in all prepared $Co_xMg_{6-x}Al_2$ solids before calcination and showed the decrease in the cristallinity with the increase in cobalt content as well. After calcination, XRD study revealed the destruction of the hydrotalcite phase and the presence of MgO phase periclase in $(Cu/Ru)Mg_6Al_2$, and the presence of Co_3O_4, $CoAl_2O_4$ and Co_2AlO_4 spinel phase for all cobalt containing catalysts. In addition, a copper oxide phase is observed for all $5Cu/Co_xMg_{6-x}Al_2$ whereas diffraction peaks attributed to RuO_2 phase are seen for solids with high Mg content indicating that the interaction of ruthenium with supports rich in Co will lead to a good dispersion of RuO_2 species at the surface of the support. It was noticed that with higher ruthenium and copper content, more intense CuO and RuO_2 lines are observed due to the formation of agglomerates.

Analyses of the specific surface area showed an increase in the S_{sp} after calcination due to the destruction of the hydrotalcite phase. Furthermore, a decrease in the surface area was observed with higher active phase contents attributed to the presence of RuO_2 and CuO agglomerates plugging the pores.

TPR profiles of Mg_6Al_2 showed no reduction peaks in the studied temperature range, while the solids with cobalt content showed two reduction peaks revealing the

presence of two cobalt oxide species; Co_3O_4 that reduce at 300-400°C and $CoAl_2O_4$ or Co_2AlO_4 that reduce at higher temperatures. The quantity of these reducible species increases with the amount of cobalt. The presence of copper and ruthenium oxides decreases the reduction temperature of $Co_xMg_{6-x}Al_2$ solids due to the incorporation of metals enhancing the reducibility of the cobalt ions.

The higher calcination temperature leads to a higher crystallinity and an increase in the particle size that will lead to a decrease of the specific surface area of the calcined solids at 800°C. In addition, the reduction peak of cobalt oxide is shifted to higher temperatures indicating the weakness of the interaction between Co and active phase at higher calcination temperature.

Infrared spectra showed the vibration bands of the hydrotalcite structure for the uncalcined solids. After calcination, vibration bands attributed to a mixture of different spinels are detected which in accordance with XRD analysis that revealed the presence of more than one type of spinel. Ru-OH vibration bands are detected for catalysts with higher magnesium content, because as seen in XRD, Ru agglomerates are more detected in the catalysts with high magnesium content. And finally for the copper based catalysts, O-Cu-O vibration band is observed especially with high copper content.

N_2-adsorption-desorption isotherms experiments show a pattern typical of mesoporous materials for $Co_xMg_{6-x}Al_2$. This pore size distribution can lead to a strong interaction between the adsorbate and adsorbent.

At the end, EPR analysis revealed the formation of Ru^+ in the case of $1Ru/Mg_6Al_2$. $5Cu/Mg_6Al_2$ catalyst showed two types of isolated copper(II) species: the first one is located in octahedral sites that is not easily reduced and the other in tetrahedral sites that is primarily reduced.

CHAPTER 3

CATALYTIC STEAM REFORMING OF METHANE OVER $Co_xMg_{6-x}Al_2$, $Ru/Co_xMg_{6-x}Al_2$ AND $Cu/Co_xMg_{6-x}Al_2$ SOLIDS

3.1 Steam Reforming of Methane

3.1.1 Introduction

Catalytic methane steam reforming process is one of the most widespread, attractive route and economically feasible method for hydrogen production which is a clean energy carrier used for transportation and stationary power generation [179, 180]. However, it requires high temperatures and may promote carbon formation (as seen in section 1.6) on the catalysts unless high steam-to-carbon ratios (S/C) are used. In addition, coke formation can be overcome in the presence of noble (ruthenium), transion metals (copper) and hydrotalcites [59, 181-187].

In the first section of this chapter, a thermodynamic study of the above reaction with its side reactions is displayed. Then, the experimental procedure with the operating catalytic test conditions are described.

In the second section, methane steam reforming reaction is studied in the presence of ruthenium and copper-based catalysts in order to evaluate their catalytic performance in this reaction. Furthermore, the influence of many parameters is studied in order to optimize the catalytic reaction: the content of the active phase and its content, the pretreatment, the steam-to-carbon ratio, the calcination temperature and the gas hourly space velocity (GHSV). Aging tests are also carried to study the stability of the most performant catalytic system over time and under practical conditions.

In a third section, a comparison between the best catalyst and an industrial one is displayed for the sake of showing that the prepared catalysts can be potentially use on an industrial scale.

At the end, an EPR study is performed as this technique helps in the interpretation of the catalysts before and after catalytic test.

3.1.2 Thermodynamics of the Reaction

In a system where there are many reactions equilibria, there may be several routes to the desired products and by-products. This system is governed by the thermodynamics of the reaction equilibria. The steam reforming of methane constitute an example of such systems [188]. Steam reforming of methane is a highly endothermic reaction (Equation 3.1). Thermodynamic calculation indicates that this reaction at 1 atm and below 600ºC is not spontaneous (i.e., $\Delta G > 0$). In addition, methane molecule has a high C-H bond dissociation energy of 435 kJ/mol, it is very stable and requires high temperatures to achieve a high conversion during the methane steam reforming reaction [189].

$CH_4 + H_2O \leftrightarrow CO + 3\ H_2$ $\Delta H° = +206$ kJ/mol (Equation 3.1)

Methane steam reforming reaction is followed by the water-gas-shift reaction which converts CO into CO_2 with additional hydrogen production according to equation 3.2:

$CO + H_2O \leftrightarrow CO_2 + H_2$ $\Delta H° = -41$ kJ/mol (Equation 3.2)

Combining these two reactions gives equation 3.3:

$CH_4 + 2\ H_2O \leftrightarrow CO_2 + 4\ H_2$ $\Delta H° = +165$ kJ/mol (Equation 3.3)

However, at high temperatures where the reforming is spontaneous, other secondary reactions may occur, which will have significant impact on the reaction: the Boudouard reaction (or CO disproportionation) (Equation 3.4), methane decomposition (Equation 3.5) and CO reduction (or reverse carbon gasification reaction) (Equation 3.6) causing carbon formation which can deactivate and block the

active sites of a catalyst. It is important to know that Boudouard reaction is about 3 to 10 times faster than the methane decomposition reaction [190].

$2\ CO \leftrightarrow C + CO_2$ $\Delta H° = -171$ kJ/mol (Equation 3.4)

$CH_4 \leftrightarrow C + 2\ H_2$ $\Delta H° = +75$ kJ/mol (Equation 3.5)

$CO + H_2 \leftrightarrow C + H_2O$ $\Delta H° = -132$ kJ/mol (Equation 3.6)

Other reactions may occur like the reverse water-gas-shift (Equation 3.7) and the carbon gasification (Equation 3.8) reactions:

$CO_2 + H_2 \leftrightarrow CO + H_2O$ $\Delta H° = +41$ kJ.mol^{-1} (Equation 3.7)

$C + H_2O \leftrightarrow CO + H_2$ $\Delta H° = +132$ kJ.mol^{-1} (Equation 3.8)

Figure 3.1 shows the variation of the equilibrium constants of the above reactions as function of temperature.

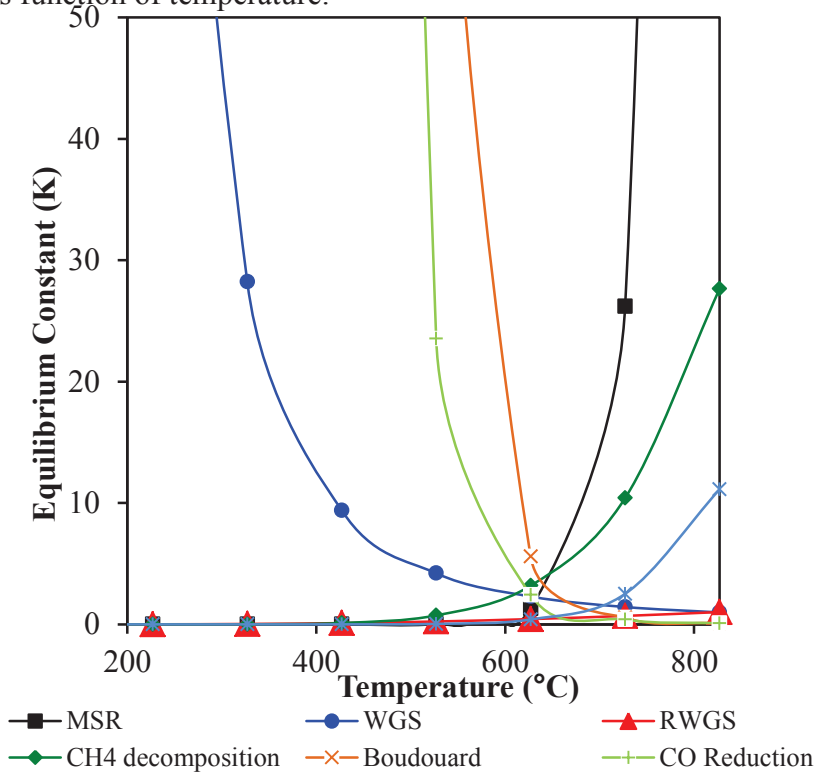

Figure 3.1 Equilibrium constants for the reactions (1) to (7) as a function of temperature

The equilibrium constant for the methane steam reforming reaction (Equation 3.1) increases dramatically with increasing the reaction temperature. Thus, high conversion is favored at high temperatures. The equilibrium constants of the moderate endothermic reactions: methane decomposition, reverse water-gas shift and carbon gasification reactions (Equations 3.5, 3.7 and 3.8) also increase with temperature. Boudouard and CO reduction (Equations 3.4 and 3.6) are exothermic and thermodynamically unfavorable at high temperatures [191, 192]. Thermodynamic calculations are shown in appendix D.

Theoretical converion of methane (%) for S/C= 1 and 3 under atmospheric pressure is represented in figure 3.2 as a function of temperature from 400°C to 1000°C. 100% of methane is converted above 700°C at a S/C= 3. Whereas at the same temperature 80% of methane is converted in the case of S/C= 1. Theoretical methane conversion is represented in details in appendix E.

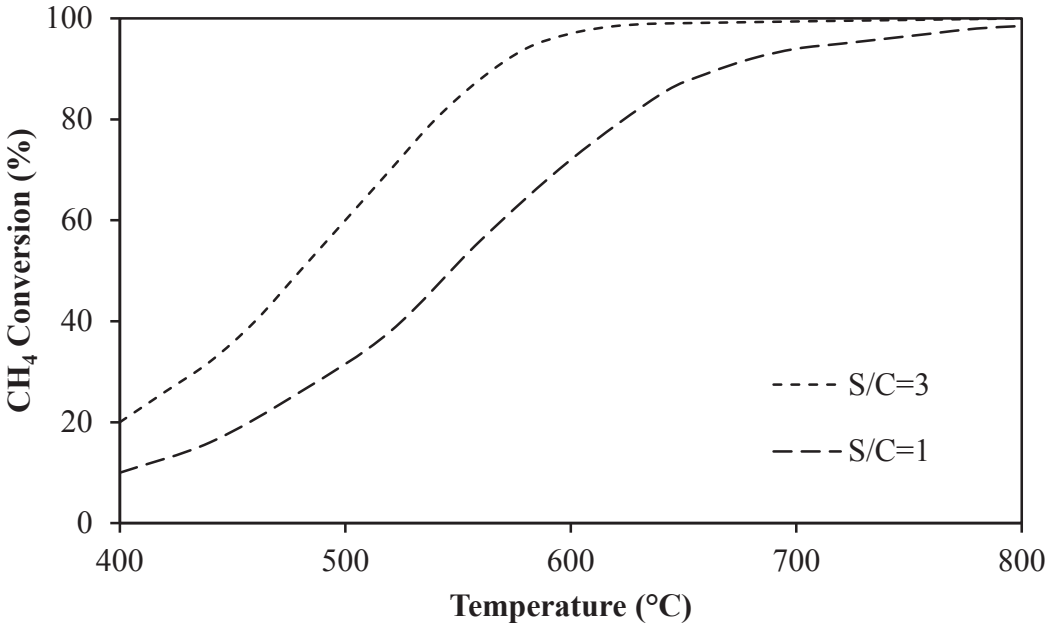

Figure 3.2 Theoretical methane conversion (%) at S/C= 1 or 3 at 1 atm as a function of temperature

3.1.3 Experimental Procedure and Operating Conditions

Catalysts reactivities are evaluated in the methane steam reforming reaction which was carried out under atmospheric pressure in a fixed catalytic bed reactor. The diagram of the experimental setup is illustrated in figure 3.3.

The experimental apparatus consists of three main parts:

- Steam generator and gaseous reactant regulators (CH_4 and Ar). The reactant gas flow (50 $mL.min^{-1}$) consists of a precise steam to methane mixture and argon was used for balancing. CH_4, Ar and H_2O vapor are premixed in a pre-heater before introducing it into the reactor at a proper H_2O/CH_4 molar ratio
- A catalytic U-shaped quartz fixed bed reactor (with 6.6 mm internal diameter) introduced in a programmable electrically heated furnace. The temperature of the catalytic bed was measured by a thermocouple placed at the level of the catalyst. At the outlet of the reactor, a cold trap was used to condense water from the product gas stream.

An analytical system is used at the end to separate, detect and quantify dry outlet gaseous products (H_2, CO, CO_2 and non-reacted CH_4). It consists of a micro-GC (Varian CP-4900) equipped with two analysis modules: the first one is a molecular sieve that separates CH_4, H_2 and CO with argon as a carrier gas, and the second module is Poraplot Q type (P.P.Q.) column separating CO_2 with helium as a carrier gas. The detection of these products was done using thermal conductivity detectors (TCD).

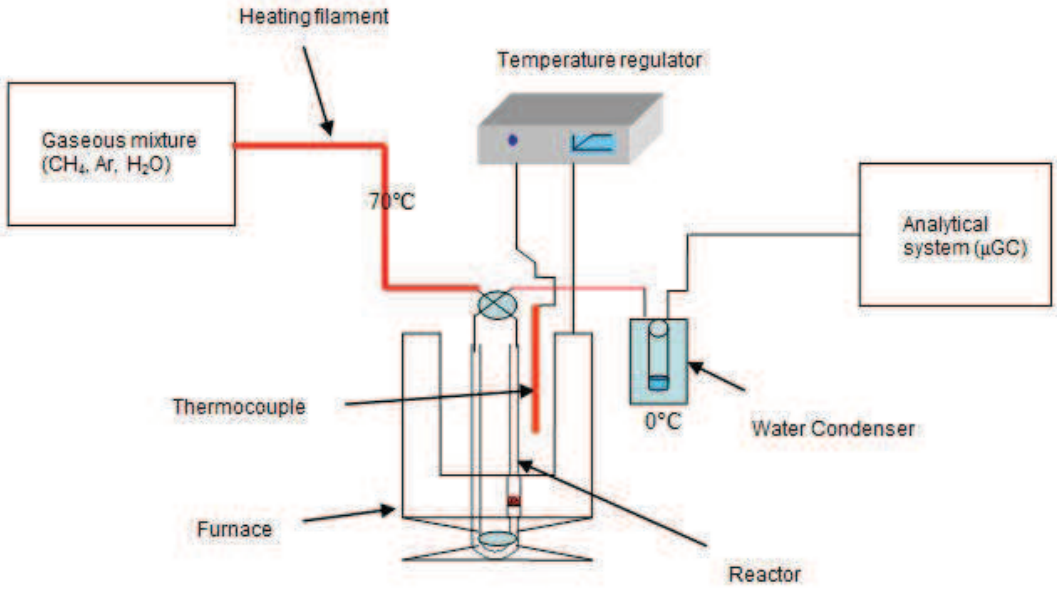

Figure 3.3 Schematic of the experimental apparatus

The methane steam reforming reaction was studied under different conditions:

- Steam/carbon ratios: S/C= 1, 2, 3 and 4
- Catalytic bed mass was varied between 25-200 mg under a constant gas flow
- Temperature ranging from 400°C up to 800°C

3.1.4 Calculation for Conversion, Selectivity and Gas Hourly Space Velocity

3.1.4.1 Methane conversion

The values obtained from the chromatograms and the calibration curves performed on each gas (CH_4, H_2, CO and CO_2) can quantify the amount of the reactants and products present during the reaction. The general formulas used to calculate conversions and selectivities are given below.

Methane conversion (X_{CH_4}) is the fraction of CH_4 molecules converted to gaseous products (H_2, CO and CO_2).

$$X_{CH_4} = \frac{n_i CH_4 - n_f CH_4}{n_i CH_4} \times 100$$

Where *i* and *f* subscripts are used to indicate the inlet and outlet number of moles respectively.

3.1.4.2 CO, CO_2 and H_2 selectivities

The selectivity of a product is the fraction of the methane converted into this product. For example, in the case of carbon monoxide selectivity, it can be calculated as follows:

$$S_{CO} = \frac{n_f CO}{n_i CH_4 - n_f CH_4} \times 100$$

Similarly, carbon dioxide and hydrogen selectivities are expressed using the following equations:

$$S_{CO_2} = \frac{n_f CO_2}{n_i CH_4 - n_f CH_4} \times 100 \quad \text{and} \quad S_{H_2} = \frac{n_f H_2}{2(n_i CH_4 - n_f CH_4)} \times 100$$

3.1.4.3 Gas hourly space velocity

The catalytic activity can be influenced by the gas hourly space velocity (GHSV) [193, 194]. Therefore, different GHSV values are used in this study in order to compare their influence on the catalytic performance.

GHSV (in $mL.g^{-1}.h^{-1}$) is the reactant gas flow over the mass of the catalyst. It is calculated as follows:

$$GHSV = \frac{\text{Total flow rate}}{\text{Catalyst mass}}$$

3.2 The Non-Catalyzed Reaction

A blank methane steam reforming test using carborundum (SiC) loaded in the reactor is done as a reference to study the conversion of methane without the presence

of an active metal or catalyst. Two hundred milligrams of SiC are introduced in the catalytic reactor. H_2O/CH_4 ratio equal to 3 and a total volume of 50 $mL.min^{-1}$ (Ar, CH_4 and H_2O) corresponding to a GHSV equal to 15000 $mL.g^{-1}.h^{-1}$ were used.

Methane conversion (%) and the molar concentration of the gaseous mixture (H_2, CO and CO_2) for the uncatalyzed reaction using carborundum (SiC) are represented in figure 3.4. The molar concentration of the gaseous mixture is obtained by multiplying the value of the area of each gas by their calibration coefficient factor. The performance of the uncatalyzed reaction reveals a very slow reaction that yields small product quantities (H_2, CO and CO_2) in the studied temperature range. For instance, the methane conversion barely reached 5% even at 800°C indicating that methane steam reforming or methane decomposition reactions were not likely to occur at a considerable rate under these conditions.

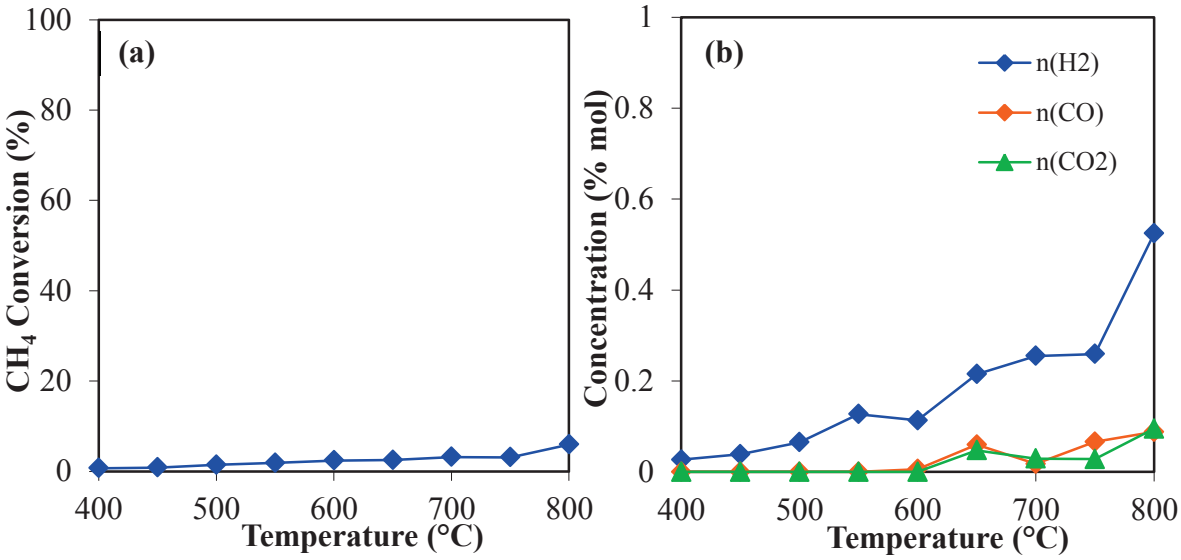

Figure 3.4 a) Methane conversion (%) and b) molar concentration of the gaseous mixture (H_2, CO and CO_2) for the uncatalyzed reaction using carborundum (SiC)

3.3 The Catalyzed Reaction

3.3.1 Catalytic Performance in the Absence of an Active Phase

3.3.1.1 Catalytic performance of $Co_xMg_{6-x}Al_2$ supports

Figure 3.5 illustrates methane conversion in the temperature range 400-800°C and the molar concentration of the gaseous mixture (H_2, CO and CO_2) at 800°C in the presence of the four different calcined $Co_xMg_{6-x}Al_2$ supports. The reaction conditions are the following: H_2O/CH_4 ratio equal to 3, a total volume of 50 $mL.min^{-1}$ (Ar, CH_4 and H_2O) and a GHSV= 15000 $mL.g^{-1}.h^{-1}$. No pretreatment under hydrogen was performed before the catalytic reaction.

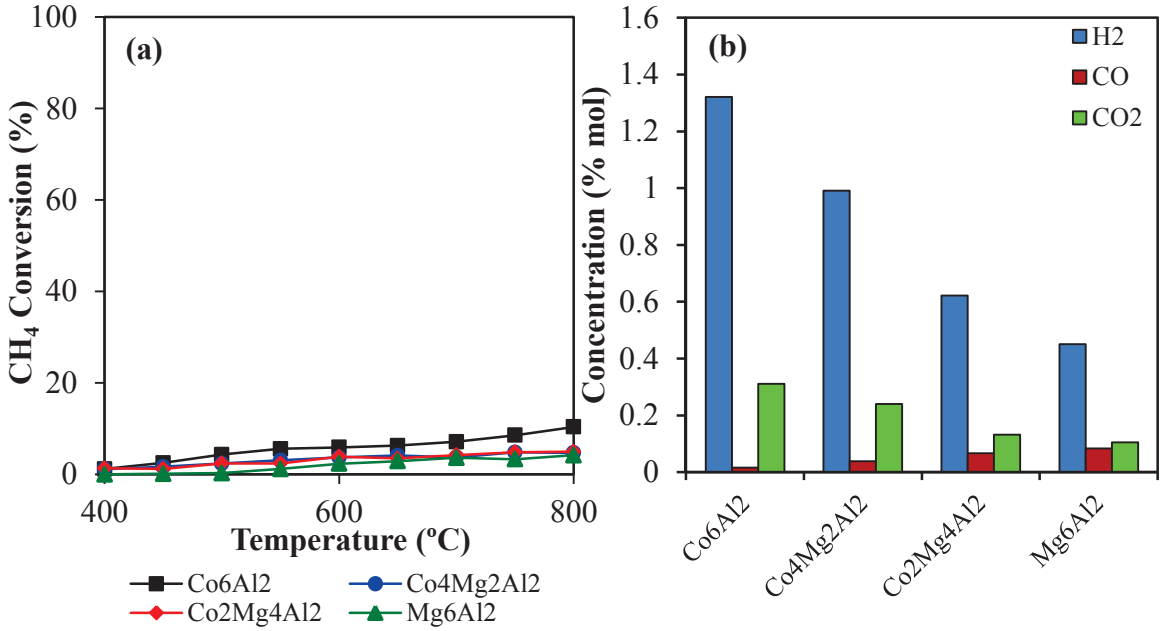

Figure 3.5 a) Methane conversion (%) and b) molar concentration at 800°C of the gaseous mixture (H_2, CO and CO_2) for calcined $Co_xMg_{6-x}Al_2$ supports

At 800°C, methane conversion also did not exceed 10% for the four calcined solids. In parallel, small quantities of the gaseous products are detected. However, a slight increase in the H_2 and CO_2 molar compositions are observed with the increase of the cobalt content. Oppositely, an increase in the CO amount is seen with the

increase of the magnesium content. In literature, it has been demonstrated that the low conversion of methane in the presence of cobalt species could be related to their partial oxidation in the presence of water molecules [94]. Furthermore, active species in the support are not activated due to the absence of hydrogen pretreatment leading to this low reactivity.

3.3.1.2 Influence of the pretreatment on the catalytic performance of Co_6Al_2

In order to observe the effect of a pretreatment on the catalytic activity of the support, Co_6Al_2 was reduced under a hydrogen flow at 430°C which is the temperature at which all cobalt oxides are reduced as mentioned in a previous section (section 2.6.2). Then, this solid was purged with an argon flow to ensure that the reaction started in a hydrogen-free feed. The reactant gas flow consists of H_2O/CH_4= 3 with a total volume equal to 50 mL.min^{-1} and a GHSV= 15000 mL.g^{-1}.h^{-1}.

Figure 3.6 represents methane conversion and gaseous molar composition (H_2, CO and CO_2) for the calcined support as a function of the reaction temperature.

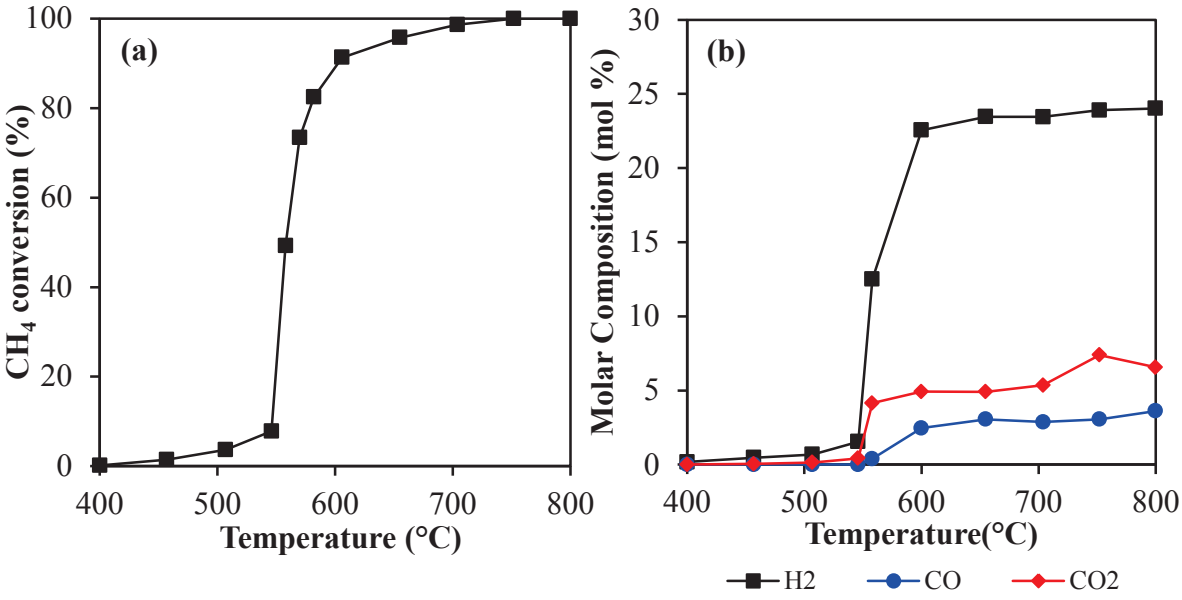

Figure 3.6 a) Methane conversion (%) and b) molar concentration of the gaseous product mixture (H_2, CO and CO_2) for reduced Co_6Al_2

A remarkable increase in the catalytic activity of this solid compared to its performance without any pretreatment is observed. CH_4 conversion is significantly improved with the increase of the reaction temperature. It starts from lower temperatures and reaches 98% at 700°C. This can be explained by the activation of cobalt species after the reduction treatment which forms metallic active centers that are stable and does not easily oxidize in the presence of steam. In addition, the obtained CH_4 conversion is very close to the theoretical one above 600°C, whereas it is below at lower temperatures (see figure 3.2). Furthermore, a small increase in the gaseous product composition was noticed over the studied temperature range.

3.3.2 Influence of the Active Phase Impregnation on the Catalytic Reactivity

Catalytic performance of $1Ru/Co_xMg_{6-x}Al_2$ and $5Cu/Co_xMg_{6-x}Al_2$ calcined at 500°C under the same conditions mentioned above (section 3.3.1.1) are displayed in figure 3.7.

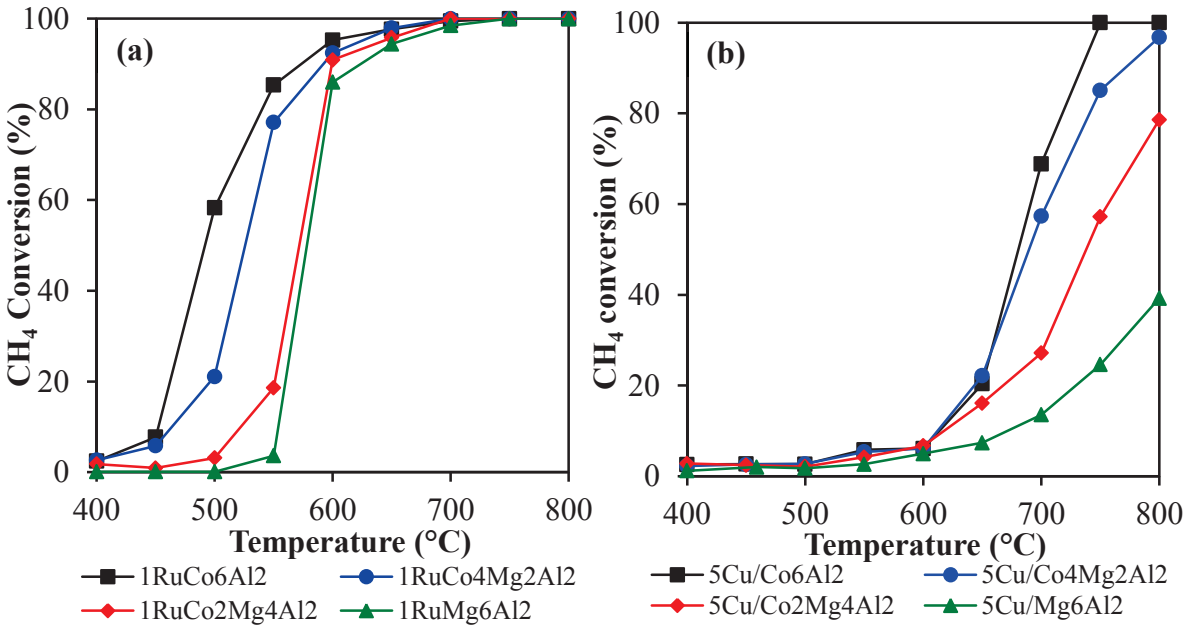

Figure 3.7 Methane conversion (%) over a) $1Ru/Co_{6-x}Mg_xAl_2$ b) $5Cu/Co_{6-x}Mg_xAl_2$ catalysts

In the presence of the impregnated solids, steam reforming of methane proceeds at a perceptible extent even at the lowest temperature studied without any pretreatment. In addition, ruthenium based catalysts show better catalytic performances than the copper based catalysts. 85% of methane is converted over $1Ru/Co_6Al_2$ at 550°C, whereas at the same temperature for $5Cu/Co_6Al_2$, methane conversion reached only 64%. Moreover, in the case of the lowest active system, it is observed that methane conversion reached 95% at 650°C for $1Ru/Mg_6Al_2$, while it is almost 40% for $5Cu/Mg_6Al_2$. It must be noted that for $5Cu/Co_6Al_2$ catalyst, the obtained CH_4 conversion is very close to the theoretical one (figure 3.2) starting from 500°C indicating that the reaction is very close to the thermodynamic equilibrium.

Firstly, high activities are mainly attributed to the in-situ reduction and formation of metallic active species [195]. Moreover, the addition of active phases avoided the re-oxidation of the catalysts and cobalt sites remained in the reduced state during the methane steam reforming reaction [196]. It was also shown that the reducibility of the $1Ru/ Co_xMg_{6-x}Al_2$ and $5Cu/Co_xMg_{6-x}Al_2$ catalytic systems (sections 2.6.3 and 2.6.4) depends on an interaction between the active phase and Co facilitating the reduction of cobalt oxide at lower temperatures leading to this higher methane conversion even with no pretreatment. For example, Cu^{2+} is reduced to Cu^0 at lower temperatures than Co^{4+} or Co^{3+}, and the generated metallic copper crystallites favor the reduction of cobalt cations.

In addition, it is reported in the literature [197] the presence of both Cu^0 and Cu^+ species in Cu/ZnO catalysts in the water-gas shift reaction. They stated that Cu^+ was the actual active species in the reaction conditions, and it may influence the catalytic activity via a reduction-oxidation mechanism between Cu^0 and Cu^+, in which the Cu^+ sites oxidize chemisorbed CO to CO_2 to form Cu^0, whereas the reduced Cu^0

sites were re-oxidized by H_2O to form Cu^+ and H_2. Furthermore, it seems that catalysts with higher Mg content are less reactive and the reactivity of the catalysts increased with cobalt content in a logical way for both active phases which could be reasonably attributed to differences in the surface properties of the support. Carvalho et al. reported that the addition of magnesium increases metal dispersion, prevent coke deposition but does not increase methane conversion [198]. However this is not the case in this study because Ru is more dispersed on Co_6Al_2 support (as seen in section 2.4.3). It is well-known that a better dispersion of the active metal on the high surface area support improves the stability and activity of the catalyst [199, 200].

Hydrogen molar composition (%) for $1Ru/Co_xMg_{6-x}Al_2$ and $5Cu/Co_xMg_{6-x}Al_2$ catalysts is shown as a function of the reaction temperature in figure 3.8.

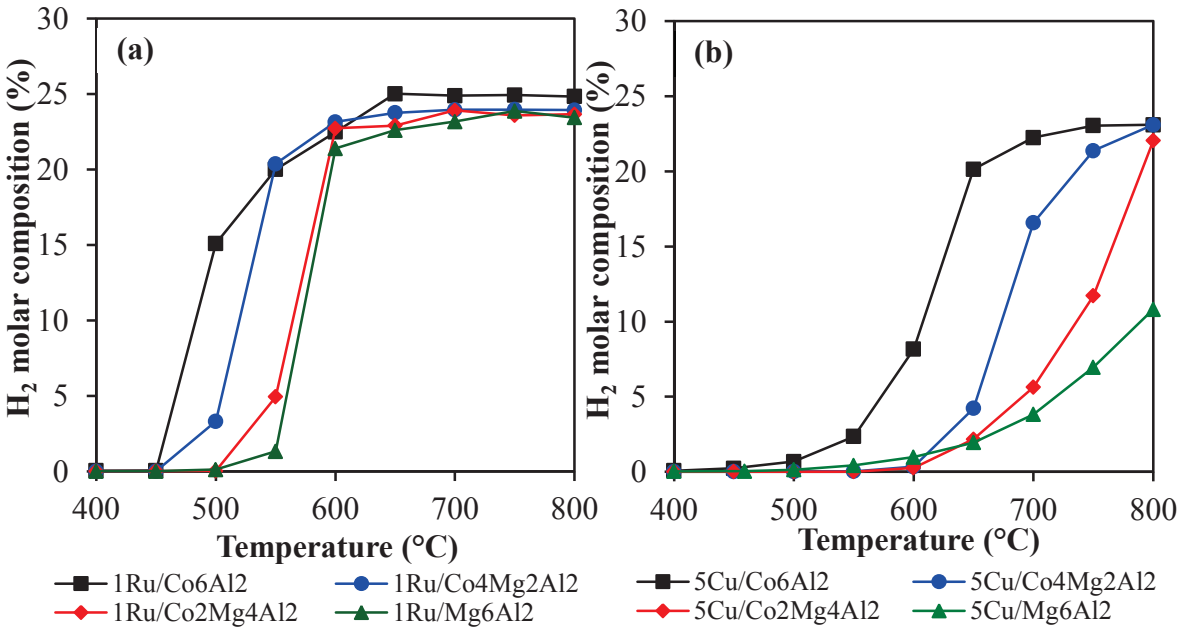

Figure 3.8 Hydrogen molar composition (%) for a) $1Ru/Co_xMg_{6-x}Al_2$ and b) $5Cu/Co_xMg_{6-x}Al_2$ catalysts

As the temperature is raised from 400°C to 800°C the concentration of H_2 increases as expected from the thermodynamic calculations. However, ruthenium

based catalysts showed higher hydrogen production from the lowest temperatures compared to the copper based catalysts.

CO and CO_2 selectivities (%) are presented in figure 3.9 for $1Ru/Co_xMg_{6-x}Al_2$ and $5Cu/Co_xMg_{6-x}Al_2$ at 800°C.

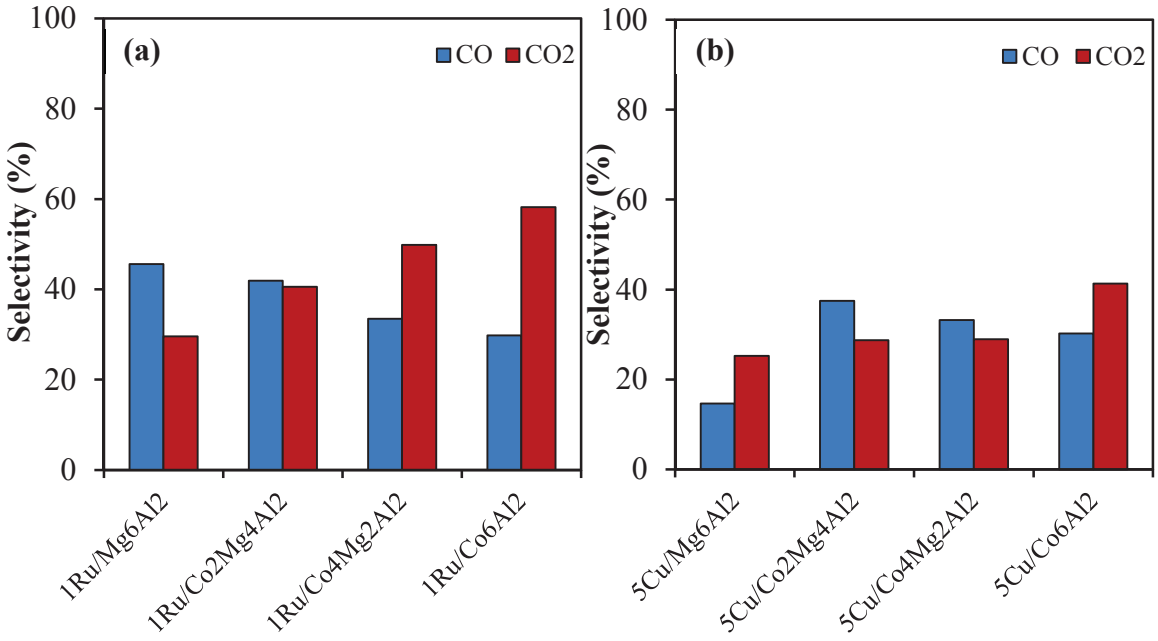

Figure 3.9 CO and CO_2 selectivity (%) over a) $1Ru/Co_xMg_{6-x}Al_2$ and b) $5Cu/Co_xMg_{6-x}Al_2$ catalysts at 800°C

$1Ru/Mg_6Al_2$ catalyst showed the highest CO amount with the lowest CO_2 production among $1Ru/Co_xMg_{6-x}Al_2$ catalysts. This indicates the maximum contribution of the reverse water-gas-shift reaction during the experiment to consume CO_2 and produce CO. On the contrary, $1Ru/Co_6Al_2$ showed the best CO_2 production and lowest CO amount even at higher temperatures. Furthermore, the increase in the hydrogen and carbon dioxide production with $1Ru/Co_6Al_2$ catalyst compared to the other ruthenium based catalysts at high temperatures even though displaying the same level of methane conversion (~100% ≥ 700°C) is due to the enhancement of the

water-gas-shift reaction in the presence of cobalt. An intermediate behavior is seen for $1Ru/Co_4Mg_2Al_2$ and $1Ru/Co_2Mg_4Al_2$ catalysts.

For $5Cu/Co_xMg_{6-x}Al_2$ catalysts, $5Cu/Co_6Al_2$ catalyst displays the highest CO_2 selectivity. $5Cu/Mg_6Al_2$ catalyst represents the lowest CO selectivity which can be obviously interpreted by its lowest CH_4 conversion. It must be noted that in the literature, Cu species enhance the water-gas-shift reaction to produce hydrogen and carbon dioxide [201, 202].

It is concluded from the above results that the presence of easily reducible and highly dispersed metal oxide species (ruthenium or copper oxide) promotes the reduction of cobalt species contributing to an enhanced activity. Supports have an important role by interacting with water molecules and dissociating them which is the case of Co_6Al_2. This can facilitate the oxidation of carbon monoxide to carbon dioxide [45, 203].

In the remaining part of this study, only $1Ru/Co_6Al_2$ and $5Cu/Co_6Al_2$ catalysts will be only considered by the variation of the catalytic test parameters in order to optimize the operating conditions.

3.3.3 Influence of the Pretreatment on the Catalytic Activity of $1Ru/Co_6Al_2$ and $5Cu/Co_6Al_2$ Catalysts

In the methane steam reforming reaction, metallic active site species are considered as the active phase [197, 204]. Therefore, the catalysts are reduced before test under a hydrogen flow of 15 $mL.min^{-1}$ at 230°C during 1 h in order to activate $1Ru/Co_6Al_2$ and $5Cu/Co_6Al_2$ catalysts respectively. The catalyst was then purged with an argon flow to ensure that the reaction started in a hydrogen-free feed. A steam-to-methane ratio is equal to 3 used.

Figure 3.10 represents the evolution of the methane conversion with the temperature for pretreated and non-pretreated $1Ru/Co_6Al_2$ and $5Cu/Co_6Al_2$ catalysts.

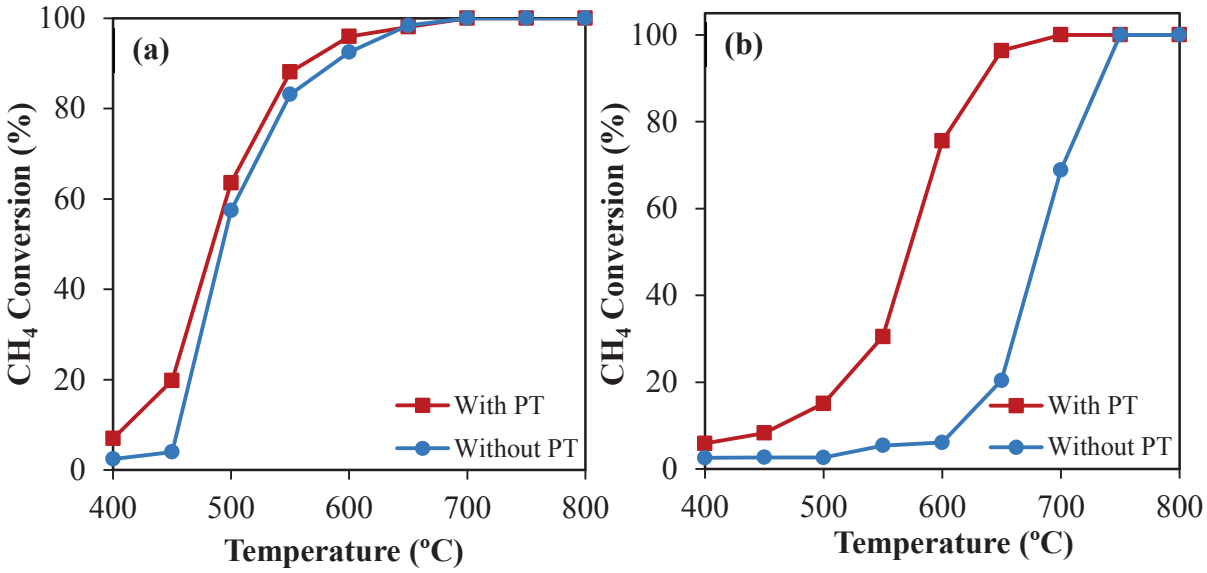

Figure 3.10 Methane conversion (%) for pretreated and non-pretreated a) $1Ru/Co_6Al_2$ and b) $5Cu/Co_6Al_2$ solids

Starting with $1Ru/Co_6Al_2$ catalyst, it can be seen that the pretreated solid shows higher methane conversion at low temperatures (400°C and 450°C) compared to the non-reduced catalyst. The difference between the two curves (figure 3.10 a) is within experimental error. The difference at low temperature can be explained by the presence of metallic ruthenium active sites following the reduction treatment. These active sites can induce the methane steam reforming reaction at lower temperatures. Moreover, for the non-pretreated catalyst, the reduced metallic ruthenium active sites are only produced when the hydrogen content in the product gas stream is considerable. According to figure 3.8, hydrogen is produced starting from 500°C, leading to the activation of the catalyst thus matching the conversion between the pretreated and non-pretreated catalysts.

On the other hand, $5Cu/Co_6Al_2$ presents different behavior. An obvious enhancement in the catalytic activity is observed all over the temperature range after the reduction treatment. This can indicate that hydrogen produced during the reaction may be not capable to activate the active sites as in the case of ruthenium. Therefore, copper and cobalt species could be confronted to water molecules that may delay their activation.

Figure 3.11 represents the H_2, CO and CO_2 molar compositions obtained at 800°C for the reduced and non-reduced $5Cu/Co_6Al_2$.

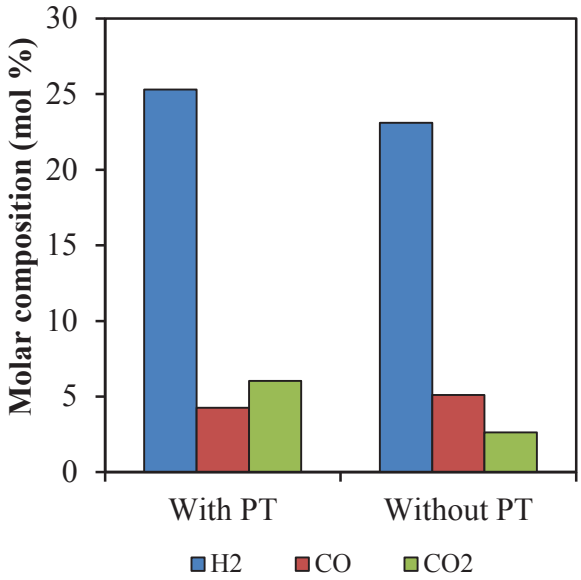

Figure 3.11 H_2, CO and CO_2 molar composition over $5Cu/Co_6Al_2$ catalyst at 800°C

It can be seen that hydrogen and CO_2 produced are greater in the case of the reduced catalyst, whereas the non-reduced one presents higher CO quantity. It is concluded from the above results that pretreatment of $1Ru/Co_6Al_2$ catalyst under hydrogen is not a determining factor in its catalytic performance, but it is not the case for $5Cu/Co_6Al_2$. An active catalyst must be in a reduced state which may be achieved by an in-situ hydrogen reduction produced during the reaction. Therefore, a

pretreatment for the copper-based catalyst must be achieved before the beginning of the reaction to activate their active sites.

3.3.4 Influence of the Calcination Temperature on 1Ru/Co_6Al_2 and 5Cu/Co_6Al_2 Catalytic Activity

In order to study the influence of the calcination temperature on the catalytic performance of 1Ru/Co_6Al_2 and 5Cu/Co_6Al_2, two calcination temperatures were chosen: 500°C and 800°C.

As mentioned in section 2.1, the calcination is carried out under an air flow of 2 $L.h^{-1}$ with a rate of 1°C.min^{-1} during four hours at the desired temperature. Catalytic tests were performed in the temperature range between 400°C and 800°C under a H_2O/CH_4 ratio equal to 3 and a GHSV= 15000 $mL.g^{-1}.h^{-1}$.

Figure 3.12 represents the obtained CH_4 conversion for both catalysts calcined at 500°C and 800°C.

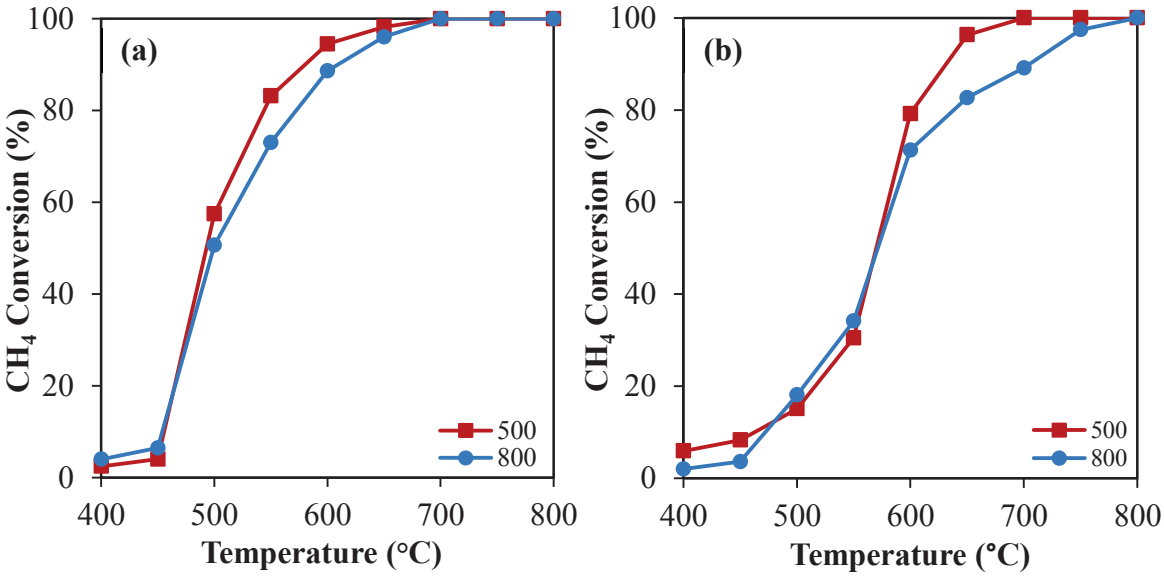

Figure 3.12 Methane conversion (%) over a) 1Ru/Co_6Al_2 and b) 5Cu/Co_6Al_2 calcined at 500°C and 800°C

$1Ru/Co_6Al_2$ catalysts calcined at 500°C and 800°C show similar catalytic performances at the beginning of the reaction (400-450°C) and at higher temperature (≥ 700°C). In fact, at higher temperatures, thermal effects dominate over the catalytic system leading to similar results over catalysts calcined at different temperatures. However, between 500°C and 650°C, $1Ru/Co_6Al_2$ catalyst calcined at 500°C is more active than the one calcined at 800°C. For example, at 550°C, CH_4 conversion was 73% and 83% for catalyst calcined at 500°C and 800°C respectively. In the case of $5Cu/Co_6Al_2$, similar catalytic activities are obtained at low temperatures (< 600°C), but the activity for the solid calcined at 800°C is also lowered with increasing the calcination temperature at higher temperatures (≥ 600°C).

H_2/CO molar ratio for both catalysts calcined at 500°C and 800°C are displayed in figure 3.13. First, a decrease in the H_2/CO ratio is observed with increasing the temperature due to the fact that the water-gas shift reaction is thermodynamically not favored at high temperatures [205]. It is noticed that the obtained H_2/CO ratios are higher than the stoichiometric one (equal to 3). This fact confirms that hydrogen and carbon monoxide are not only produced by steam reforming reaction. Excess of hydrogen is related to the presence of side reactions like water-gas shift and methane decomposition. Second, it is observed that higher ratios are obtained for catalysts calcined at 500°C. This can be explained by the formation of agglomerates and the increase in the crystallinity with the increase of the calcination temperature (see section 2.4.3). As seen in sections 2.6.3 and 2.6.4, the reduction of Co_3O_4 at higher temperatures for $1Ru/Co_6Al_2$ and $5Cu/Co_6Al_2$ calcined at 800°C can explain also this decrease in their catalytic activity compared to the one calcined at 500°C as the less reducible species formed and found during the reaction can decrease the catalytic performance [129].

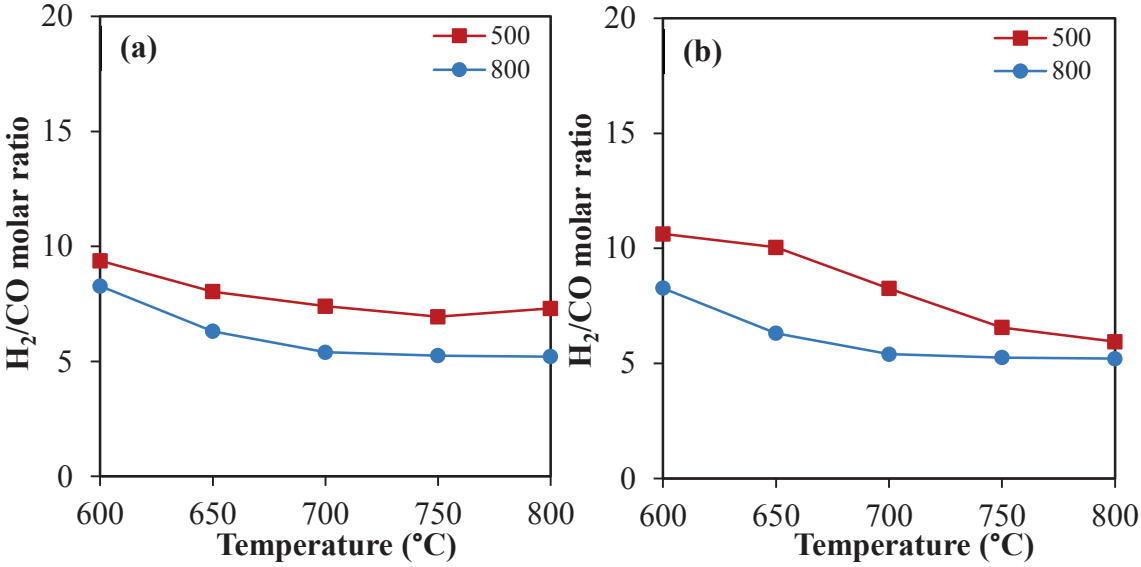

Figure 3.13 H_2/CO molar ratio over a) 1Ru/Co_6Al_2 and b) 5Cu/Co_6Al_2 catalysts calcined at 500°C and 800°C as a function of the temperature

So we can conclude that it is not necessary for now to increase the calcination temperature up to the reaction temperature. Moreover, it will be proven later in this chapter that the activity is not altered when doing several consecutive tests.

3.3.5 Influence of the Active Phase Content

Methane steam reforming reaction was carried out in the temperature range between 400°C and 800°C under the same conditions mentioned before. Figure 3.14 shows the methane conversion as a function of the reaction temperature over yRu/Co_6Al_2 with different Ru loading: 0.5; 1; 3 and 5 wt.% and over zCu/Co_6Al_2 with different Cu loading: 0.5; 3; 5; 15 and 25 wt.%. 0.5Ru/Co_6Al_2 and 0.5Cu/Co_6Al_2 show the lowest catalytic performance among yRu/Co_6Al_2 and zCu/Co_6Al_2 catalysts. Methane conversion increases with the metal loading for the ruthenium-based catalysts indicating that ruthenium is the site of activation of the methane molecule. Similar conversions are obtained for ruthenium loading≥ 1wt.% starting from 550°C.

For copper based catalysts, the conversion increases with the copper loading up to 550°C. At higher temperatures, 3 and 5Cu/Co_6Al_2 show better conversion. At 650°C, around 20% difference in the methane conversion is observed between 15-25Cu/Co_6Al_2 and 3-5Cu/Co_6Al_2.

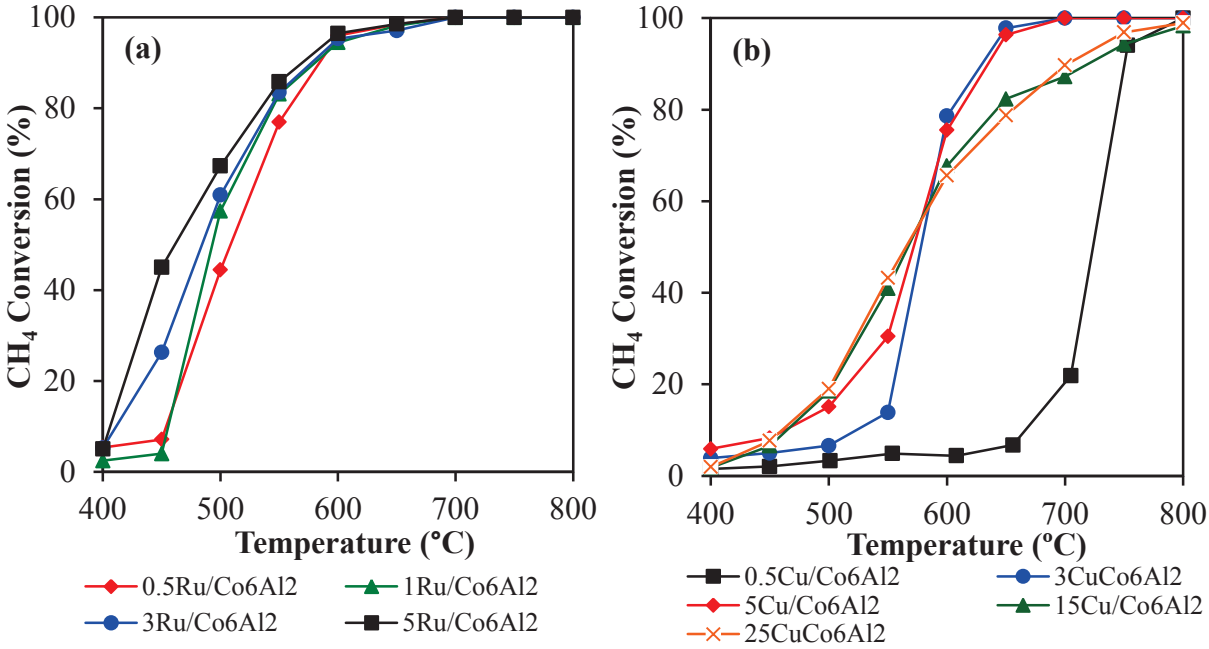

Figure 3.14 Methane conversion (%) over a) *y*Ru/Co_6Al_2 and b) *z*Cu/Co_6Al_2 catalysts calcined at 500°C

Hydrogen molar composition and CO and CO_2 selectivities at 800°C for yRu/Co_6Al_2 and zCu/Co_6Al_2 catalysts are shown in figures 3.15 and 3.16. For yRu/Co_6Al_2 catalysts, very close hydrogen molar compositions are obtained starting from 500°C with metal loadings≥ 1wt.%. At 450°C, more hydrogen is produced in the case of 5Ru/Co_6Al_2. In parallel, CO and CO_2 selectivities for these catalysts at 800°C show that 1Ru/Co_6Al_2 presents the lowest CO and highest CO_2 selectivity among the other catalysts.

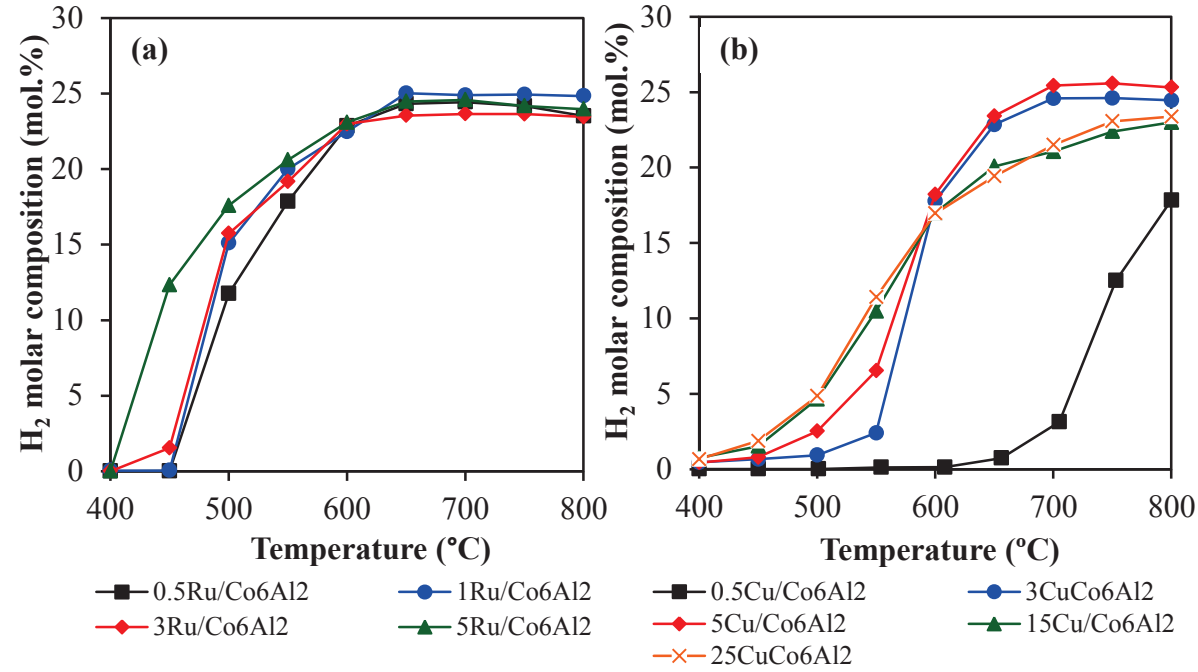

Figure 3.15 Hydrogen molar concentration (molar %) over a) *y*Ru/Co_6Al_2 and b) *z*Cu/Co_6Al_2 catalysts

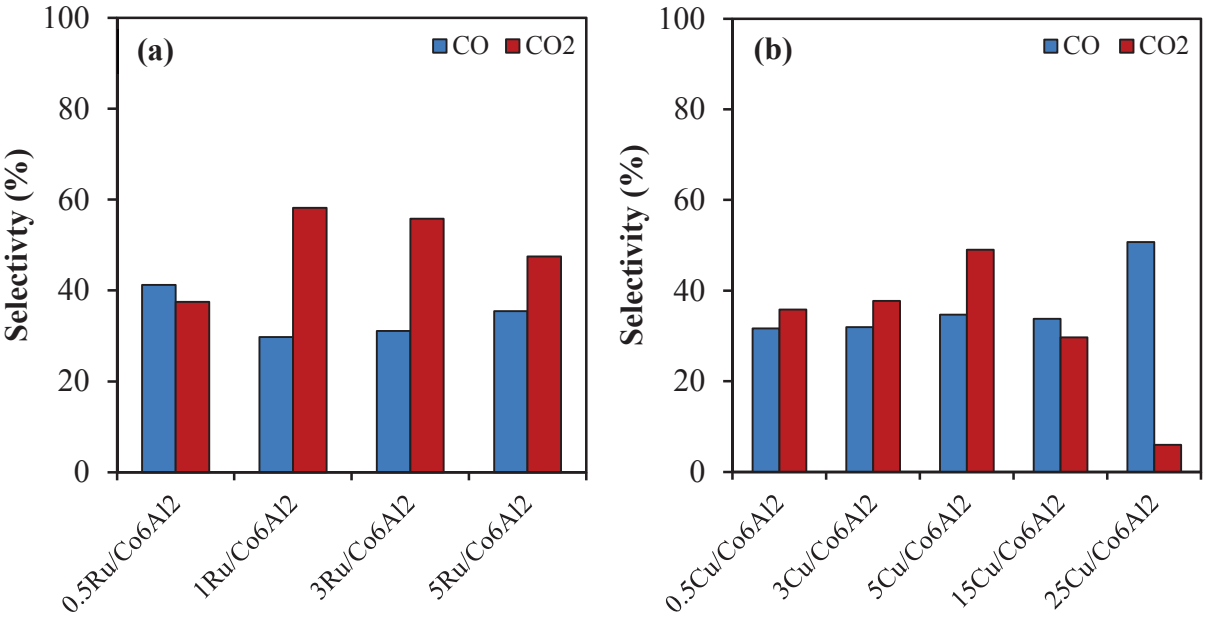

Figure 3.16 CO and CO_2 selectivities (%) over a) *y*Ru/Co_6Al_2 and b) *z*Cu/Co_6Al_2 catalysts at 800°C

For copper-based catalysts, it is noticed that 15Cu/Co_6Al_2 and 25Cu/Co_6Al_2 display greater H_2 production at lower temperatures, whereas 3Cu/Co_6Al_2 and

5Cu/Co_6Al_2 show higher H_2 amount at higher temperatures. However, CO_2 selectivities of these catalysts indicate that 5Cu/Co_6Al_2 presents the highest CO_2 selectivity and almost equal amount of CO compared to 0.5-3-15Cu/Co_6Al_2 catalysts.

In fact, to explain the above observations, it must be noted that higher metal loadings would decrease the catalytic activity because the hydrothermal atmosphere at high temperature can result in sintering of Ru or Cu clusters dispersed on the catalyst and reducing the dispersion of the active metal [206]. Therefore, a high content of the active phase would in turn lead to a decrease in the overall efficiency of the catalytic system.

In addition, there is a clear correlation between active phase dispersion and methane conversion [96, 207]. As seen in the XRD results in section 2.4.3, Ru and Cu agglomerates are present with high metal loadings indicating that the active phase is not well dispersed at the surface of Co_6Al_2 support leading to a decline in the catalytic activity. Ishihara et al. showed that the addition of 3 wt.% ruthenium to Ni/Al_2O_3 catalyst, reduced the catalytic performance towards hydrocarbons conversion in the steam reforming of m-cresol [206].

The higher H_2 production and CH_4 conversion at lower temperatures for 5Ru/Co_6Al_2, 15Cu/Co_6Al_2 and 25Cu/Co_6Al_2 can be explained by the fact that the presence of more active site species can enhance the methane decomposition and methane steam reforming reactions. But at the same time, the high CO and low CO_2 selectivities can confirm that water-gas shift reaction is not favored in this case.

From these results, it is concluded that 1wt.% Ru and 5wt.% Cu are the best metal loadings to be used, as the best catalytic system is the one with the minimum amount of active phase and yielding high amount of the desired products.

3.3.6 Influence of the H_2O/CH_4 Ratio

In the literature, methane steam reforming process suffers from coke and carbonaceous products deposition especially at low H_2O/CH_4 ratios in the feed, blocking the active sites and leading to catalyst deactivation. A higher H_2O/CH_4 ratio in the feed favors high methane conversions and hydrogen production and minimizes carbon accumulation [65]. Under oxidizing conditions, the rate of the carbon oxidation reaction by water vapor is higher than those leading to its formation on the metal surface, limiting coke deposition [208]. However, unnecessary generation of steam more than the reaction stoichiometry represents an extra energy consumption, which means a higher cost for the process [53, 94].

In order to optimize the steam/methane ratio to obtain suitable conversion results in the methane steam reforming reaction, the variation of the ratio was studied in the presence of $1Ru/Co_6Al_2$ catalyst. The ratio of the reactants (H_2O/CH_4) varied from 1 to 4 (by varying H_2O and fixing CH_4 flow rate). Catalytic tests were realized in the temperature range between 400°C and 800°C under a total volume of 50 $mL.min^{-1}$ with a GHSV equal to 15000 $mL.g^{-1}.h^{-1}$. It should be noted that H_2O/CH_4 equal to 1 is the theoretical required stoichiometry for the reaction.

Figure 3.17 represents the effect of the feed H_2O/CH_4 ratio on the methane conversion as a function of the temperature. Methane conversion curves are similar for $H_2O/CH_4 > 1$, whereas for $H_2O/CH_4 = 1$ the curve goes below the others at temperatures $\geq$ 550°C. This can be explained by the fact that under these operating conditions (low H_2O/CH_4 ratio leading to less oxidizing conditions), water gas shift is less favored limiting the produced hydrogen amount in the gaseous mixture and consequently leading to difficulties in the formation of metallic active sites. The high methane conversion observed between 550°C and 700C°C for $H_2O/CH_4 > 1$ is

explained by the easily formed metallic active sites generated by the produced hydrogen from the water gas shift and methane steam reforming reactions. Thus, the addition of excess water to the reaction mixture promotes these reactions justifying this higher activity with greater steam to carbon ratios. Experimental methane conversion below 450°C and 500°C for S/C= 1 and 3 are lower than theoretical one which means that the reaction is occurring below the thermodynamic equilibrium. Higher than 500°C, experimental methane conversion is very close to theoretical one for a S/C= 3. Whereas after 450°C for a S/C= 1, experimental conversion is much higher than theoretical one. This can be explained by the presence of side reactions like CH_4 decomposition reaction (equation 3.5) leading to higher amount of methane converted.

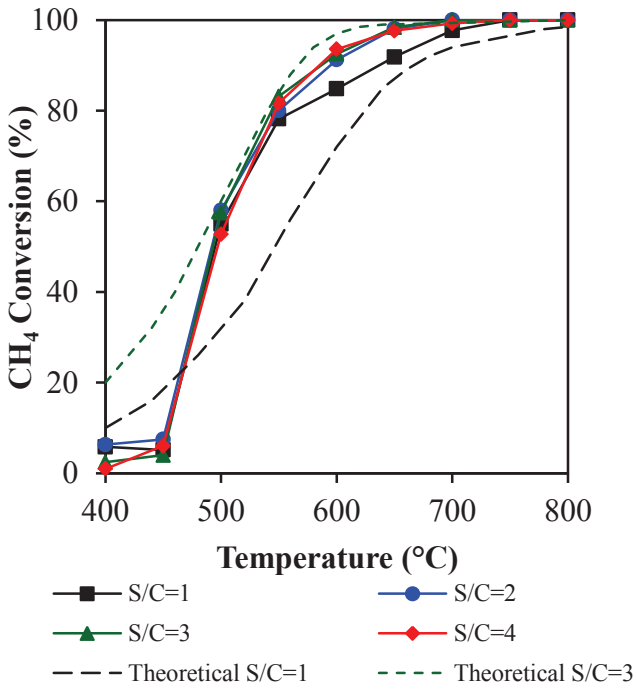

Figure 3.17 Effect of the H_2O/CH_4 feed ratio on the methane conversion (%) over 1Ru/Co_6Al_2 catalyst calcined at 500°C

The evolution of CO selectivity (%) and H_2/CO molar ratio are represented in figure 3.18. The increase in the CO concentration with temperature should be expected as a result of the thermodynamic equilibrium of the methane steam reforming and the reverse water-gas shift reactions (Figure 3.1) where raising of temperature would not favor the WGS reaction and thus causing more CO formation [205]. Carbon monoxide formation appears from 500°C, this is the reason why H_2/CO ratios are represented in the temperature range between 500°C and 800°C. It can be seen that for a ratio H_2O/CH_4= 3, the lowest CO selectivity and the highest H_2/CO molar ratio are obtained.

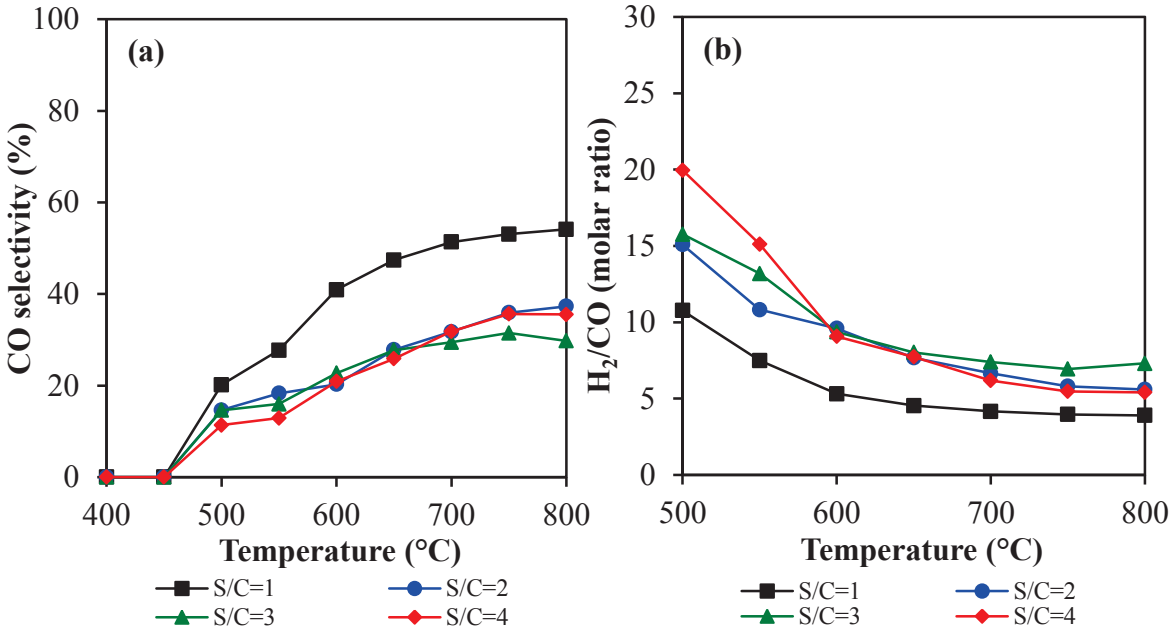

Figure 3.18 a) CO selectivity (%) and b) H_2/CO molar ratio over 1Ru/Co_6Al_2 calcined at 500°C as a function of the reaction temperature and S/C feed ratio

From the above observations, it is concluded that H_2/CO increases and CO selectivity decreases above a H_2O/CH_4 equal to 1. In fact, high H_2O/CH_4 ratios favor the water gas shift reaction leading to less CO formation and higher H_2/CO ratios. It is reported in the literature that the addition of steam (H_2O/CH_4 ratios of 3-5) will lead

to an increase in the H_2/CO molar ratio and hydrogen concentration [209, 210]. In addition, it is well-known that the formation of CO can delay CH_4 adsorption on the ruthenium surface leading to lower conversion. But, this inhibition is reduced at high temperatures (≥ 700°C) [65]. This explains the lower activity for H_2O/CH_4= 1 below 700°C.

The above results show the influence of H_2O/CH_4 ratio on the catalytic performance, and H_2O/CH_4 ratio equal to 3 is the best ratio compared to the others. It should be noted that the same analysis was achieved on $5Cu/Co_6Al_2$ and similar results and conclusions were obtained (see Appendix B).

3.3.7 Influence of the Gas Hourly Space Velocity on the Catalytic Activity

The influence of the GHSV on the catalytic behavior of $1Ru/Co_6Al_2$ catalyst in the temperature range between 400°C and 800°C is investigated with a total flow of 50 $mL.min^{-1}$ and a mass ranging from 25 mg to 300 mg according to the desired GHSV values (see section 3.1.4.3 for GHSV calculations).

Figure 3.19 shows the methane conversion (%) as a function of the temperature for four different GHSV 15000, 30000, 60000 and 120000 $mL.g^{-1}.h^{-1}$ was observed. A remarkable decrease in the catalytic performance with the increase of the GHSV values from 15000 $mL.g^{-1}.h^{-1}$ to 120000 $mL.g^{-1}.h^{-1}$. Intermediate GHSV values (30000 $mL.g^{-1}.h^{-1}$ and 60000 $mL.g^{-1}.h^{-1}$) show lower CH_4 conversions in the temperature range from 550°C to 650°C compared to 15000 $mL.g^{-1}.h^{-1}$. This result is similar to those obtained in the literature indicating that a decrease in the GHSV values will lead to an enhancement of the methane conversion [35, 210, 211]. This can be explained by the increase of the contact time (or residence time) between the

reactant feed and the catalyst contributing to an enhanced heat transfer through the catalyst and facilitating the reaction to proceed [193, 194, 211].

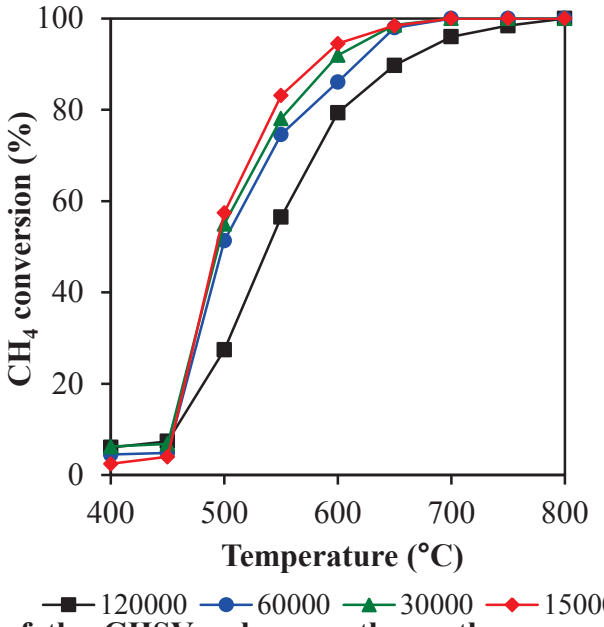

Figure 3.19 Effect of the GHSV values on the methane conversion (%) as a function of the temperature over 1Ru/Co_6Al_2 catalyst calcined at 500°C

CO and CO_2 selectivities (%) and H_2/CO molar ratio are displayed in figures 3.20 and 3.21.

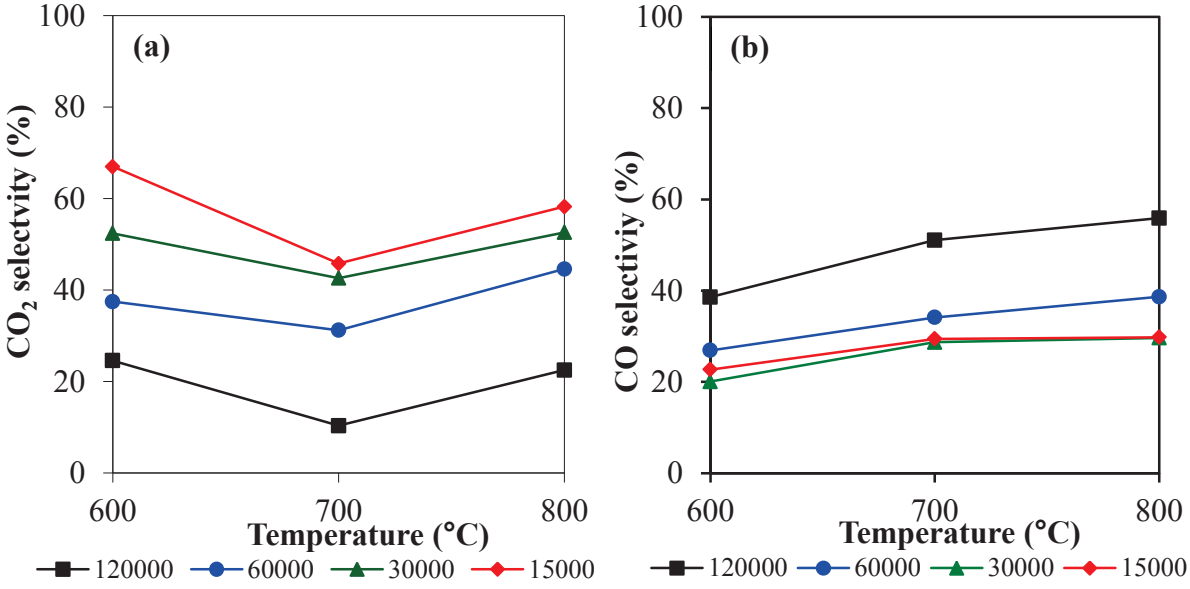

Figure 3.20 a) CO and b) CO_2 selectivities (%) over 1Ru/Co_6Al_2 calcined at 500°C catalyst as a function of the GHSV values

The CO selectivity is the highest (56% at 800°C) for a GHSV equal to 120000 $mL.g^{-1}.h^{-1}$, whereas it is only 29% for GHSV equal to 15000 $mL.g^{-1}.h^{-1}$ and 30000 $mL.g^{-1}.h^{-1}$. The highest CO_2 selectivity amount is obtained for the lowest GHSV (15000 $mL.g^{-1}.h^{-1}$). This points out that lower GHSV values enhance the water-gas shift reaction.

In parallel, figure 3.21 reveals that higher GHSV values correspond to the lowest H_2/CO ratios.

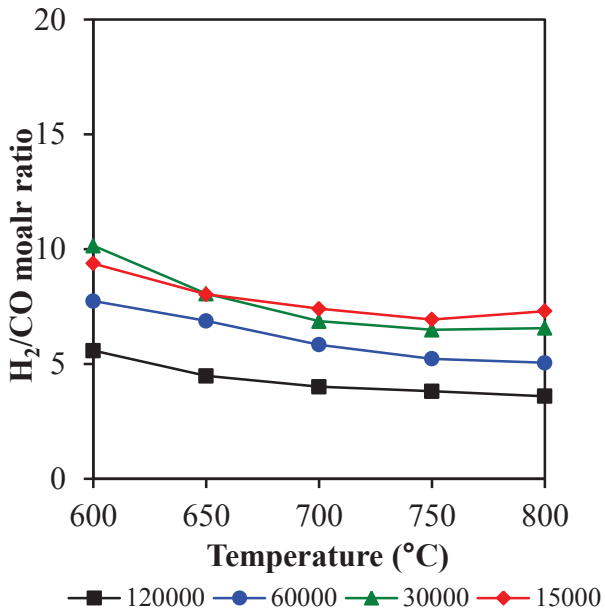

Figure 3.21 H_2/CO molar ratios over 1Ru/Co_6Al_2 calcined at 500°C catalyst as a function of the GHSV values

The highest ratio is obtained for GHSV= 15000 $mL.g^{-1}.h^{-1}$ which is slightly higher than GHSV= 30000 $mL.g^{-1}.h^{-1}$ confirming the enhancement of the WGS reaction with the decrease in the GHSV values. An intermediate behavior is seen for GHSV=60000 $mL.g^{-1}.h^{-1}$. It is observed that a catalyst is not much active when working with high space velocities due to the low methane conversion, high CO selectivity and low H_2/CO molar ratio compared to the results obtained for lower

GHSV values. In fact, for highly endothermic reactions, the problem of maintaining the temperature (or improper heat management) in the catalyst bed is more difficult with important space velocities [211]. A good thermal conductivity of the catalyst must be present to minimize the phenomena of the loss of temperature across the catalytic bed.

Catalytic performance of the copper based catalysts with the variation of the GHSV values is not presented due to similarities in the obtained results (see Appendix B).

3.4 Catalyst Stability Testing

The development of stable catalysts is one of the most important issues in catalysis. CH_4 decomposition, Boudouard and CO reduction reactions are the major source for carbon production. In addition to carbon formation, the catalytic activity can be altered by different conditions: the change of the catalyst oxidation state, or the support oxidation state and sintering or aggregation of the particles at high temperatures [65, 212].

In order to test the stability of the best catalytic system $1Ru/Co_6Al_2$, ten successive cycles were performed in the methane steam reforming reaction using the following conditions: H_2O/CH_4 ratio equal to 1:1 and 50 mg of the catalyst diluted with 150 mg of carborundum (SiC). The low molar steam/methane ratio is adopted because it can increase coke deposition. Each cycle consists of a reaction from 400°C to 800°C under the gaseous mixture (Ar, CH_4 and H_2O with a total volume of 50 $mL.min^{-1}$) and then they were cooled in the absence of the gaseous mixture. Results are illustrated in figure 3.22.

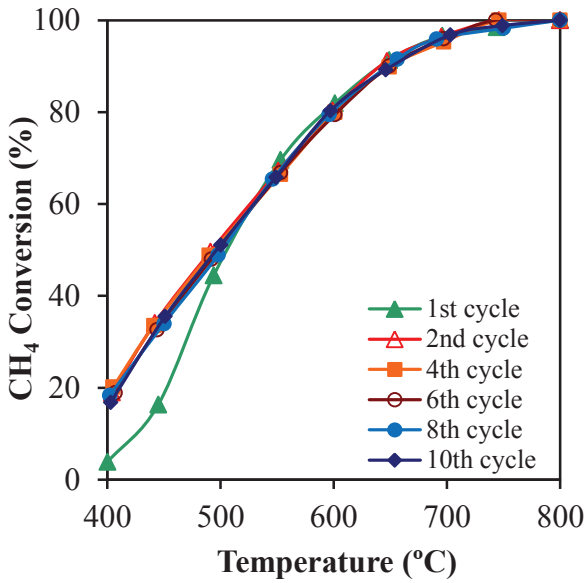

Figure 3.22 Evolution of the methane conversion (%) over 1Ru/Co_6Al_2 catalyst as a function of the reaction temperature during 10 successive cycles

The catalyst displayed a constant stability during the 10 cycles and with no observable deactivation. It can be noticed a difference in the beginning of the first cycle compared to the other 9 cycles. For the second cycle, CH_4 conversion was equal to 20% and 36% instead of 4% and 16% at 400°C and 450°C respectively. It can be considered that the hydrogen produced from the reaction after the 1st cycle (produced by the methane steam reforming, water gas shift and methane decomposition reactions) initiates an in-situ reduction of the catalyst leading to the amelioration of its activity at low temperatures which is clearly seen in the second cycle.

The same catalyst was tested also for its stability over time at a constant temperature of 550°C for a period of 100 hours (Figure 3.23). The used molar steam/methane ratio is equal to 1:1, and 10 mg of the catalyst were diluted in 190 mg SiC. This lower temperature was chosen because at higher temperatures, thermal effects can dominate on the catalytic ones. As can be seen, the result clearly shows that CH_4 conversion remains approximately constant during the reaction time.

Therefore, the activity remains stable at about 70% during the reaction time where no deactivation is observed during 100 hours of reaction. Thus the catalytic stability of $1Ru/Co_6Al_2$ was proven during methane steam reforming reaction in water-deficient conditions and low amount of the catalyst.

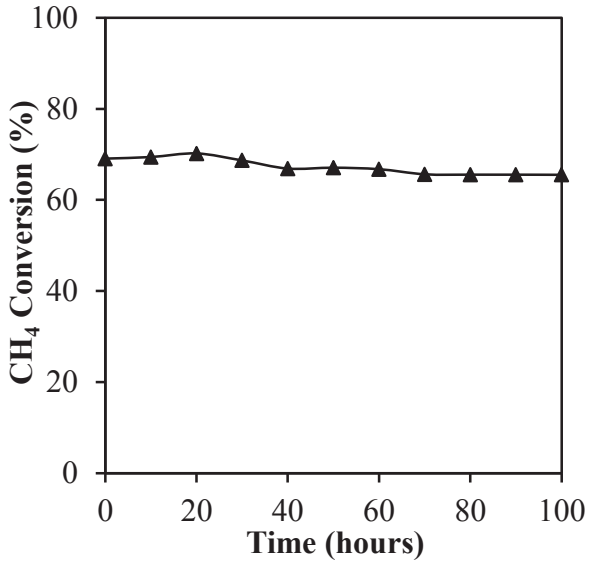

Figure 3.23 Evolution of the methane conversion (%) for $1Ru/Co_6Al_2$ catalyst as a function of time (100 h at 550°C) using a H_2O/CH_4= 1 and a total volume of 50 $mL.min^{-1}$

3.5 Comparison Between Prepared and Industrial Catalyst

In order to rank the prepared catalysts with the industrial ones, a widely used industrial catalyst $5Ru/Al_2O_3$ (Sigma-Aldrich) is chosen. Catalytic test performed on this catalyst was performed under the same conditions (GHSV= 15000 $mL.g^{-1}.h^{-1}$ and S/C= 3). Figure 3.24 shows methane conversion (%) for the prepared ($1Ru/Co_6Al_2$) and industrial catalyst ($5Ru/Al_2O_3$). The commercial catalyst presents a lower CH_4 conversion compared to the $1Ru/Co_6Al_2$ catalyst even though it has the greater amount of active phase. For example, at 600°C, methane conversion for the industrial catalyst was 83% whereas it is 93% for $1Ru/Co_6Al_2$. This lower activity for the

industrial catalyst is due to the formation of RuO_2 agglomerates on the calcined catalyst before test and the formation of coke (detected by TPO) during the catalytic reaction [53].

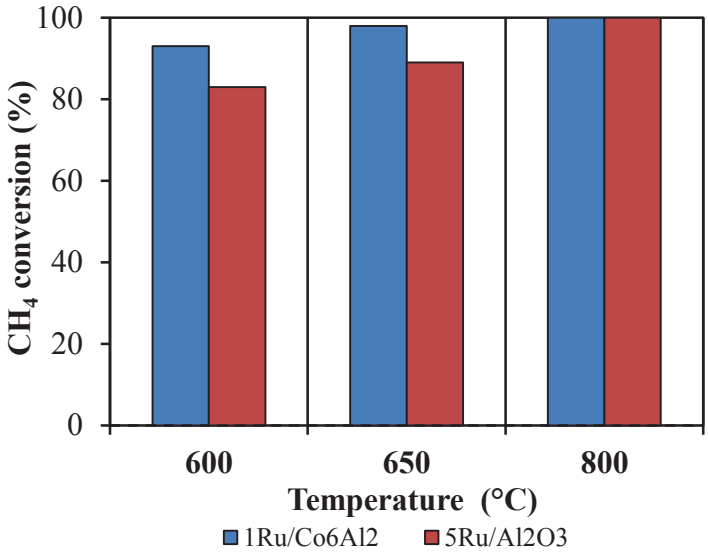

Figure 3.24 Methane conversion (%) in the presence of $1Ru/Co_6Al_2$ and the industrial catalyst $5Ru/Al_2O_3$

Table 3.1 summarizes some of previous works in literature over ruthenium-based catalysts in the methane steam reforming reaction with the adopted conditions and obtained results. It can be noticed that the best prepared catalyst $1Ru/Co_6Al_2$ in this study has a catalytic performance comparable and even better to those obtained in literature.

Table 3.1 Literature overview on some ruthenium-based catalysts used in the methane steam reforming reaction

Ru Weight percentage (%)	Support Nature	H_2O/CH_4	GHSV	Treatment	CH_4 conversion	Coke	Reference
0.5	Al_2O_3 CeO_2 ZrO_2	0.7	25000 h^{-1} - 10000 h^{-1}	-	20-40% at 800°C	Not mentioned	[213]
1	La_2O_3 $SrCO_3$	0.1	325000 $mL.h^{-1}.g^{-1}$	+	Oscillating behavior	+	[203]
4	SiO_2 ZrO_2 La_2O_3	1	200000 $mL.h^{-1}.g^{-1}$	+	~101.6 µmol/s.g_{cat} at 550°C	+	[214]
1	MgO Al_2O_3	2	Not mentioned	+	10-28% at 650°C	+	[198]
0.05	Al_2O_3	3	157000 $mL.h^{-1}.g^{-1}$	+	97% at 700°C	Not mentioned	[8]
0.1	Ni/Mg(Al)O	2	360000 $mL.h^{-1}.g^{-1}$	+	95% at 700°C	+	[48]
2	Al_2O_3	3	16000 h^{-1}	-	78-94% at 600-700°C	Not mentioned	[211]

3.6 Characterization of $1Ru/Co_6Al_2$ and $5Cu/Co_6Al_2$ After the Catalytic Test

The formation and removal of coke continues to be a subject of interest. Minimizing coke formation is one of the major factors controlling the industrial application of steam reforming especially that thermodynamically speaking, at high temperatures, coke formation is favored and cannot be avoided unless some operating

conditions can be chosen to minimize its formation [191, 192]. Therefore, in order to check for any carbonaceous deposits and check the oxidation state of the different species, XRD, TPO, DSC/TG and EPR analysis were carried out after test.

3.6.1 XRD Analysis for 1Ru/Co_6Al_2 and 5Cu/Co_6Al_2 After Methane Steam Reforming Reaction

XRD patterns for 1Ru/Co_6Al_2 calcined at 500°C and 800°C before and after the methane steam reforming reaction are displayed in figure 3.25.

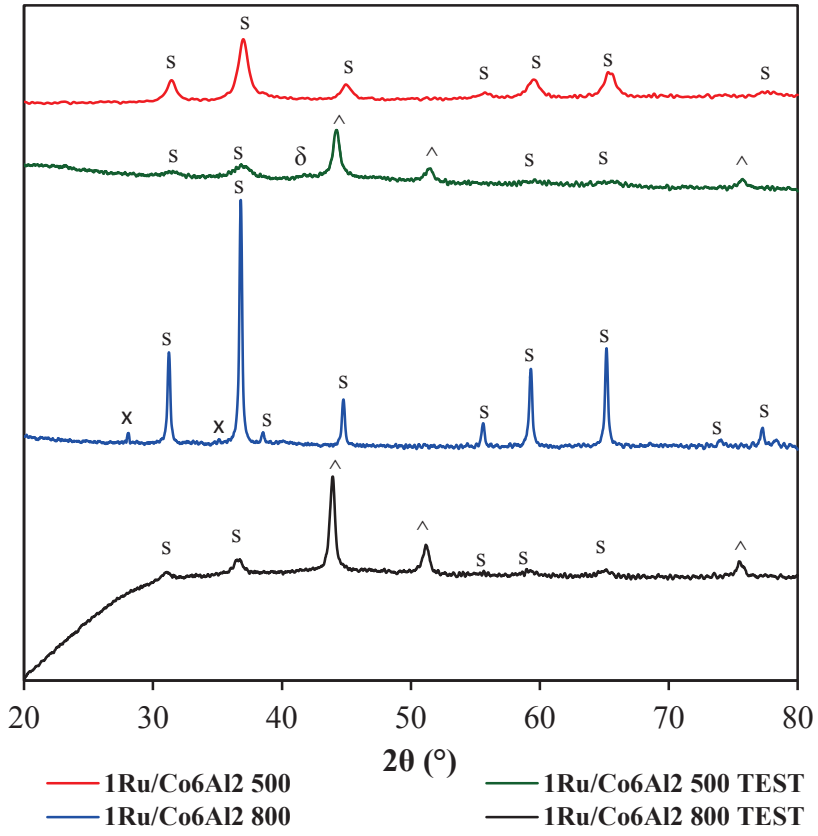

Figure 3.25 XRD analysis for 1Ru/Co_6Al_2 at 500°C and 800°C before and after MSR. "S" spinel Co_3O_4 (JCPDS N°42-1467) $CoAl_2O_4$ (JCPDS N°44-0160) Co_2AlO_4 (JCPDS N°38-0814), "^" metallic Co (JCPDS N°15-0806), "δ" metallic Ru (JCPDS N°06-0663) and "x" tetragonal RuO_2 (JCPDS N°40-1290)

Metallic Ru and Co were formed during the methane steam reforming reaction in the presence of $1Ru/Co_6Al_2$ catalysts. In fact, diffraction lines attributed to metallic Ru (JCPDS N°06-0663) were slightly observed (because of the low Ru content) showing that Ru particles were reduced during the reaction. Intense diffraction lines attributed to metallic Co (JCPDS N°15-0806) and cobalt oxide spinel phase (JCPDS N°42-1467, 44-0160 and 38-0814) were identified indicating that a major part of the cobalt oxide species was reduced. No diffraction lines due to graphitic carbon were observed in the XRD analysis.

Figure 3.26 shows the XRD patterns corresponding to the $5Cu/Co_6Al_2$ catalyst calcined at 500°C and 800°C before and after its use in the methane steam reforming reaction. The diffraction patterns present lines attributed to metallic Cu (JCPDS N°04-0836). CuO diffraction lines were absent indicating that copper oxide species are reduced during the catalytic test. The cobalt oxide spinel phase diffraction lines were still present after test but their intensities were decreased. Intense diffraction lines attributed to metallic Co (JCPDS N°15-0806) were identified indicating that a part of the cobalt oxide species were reduced during the catalytic test. However, reflections corresponding to graphitic carbon (JCPDS N°75-1621) are not observed. The lattice oxygen attached to the active sites appears to contribute in the oxidation of CH_x fragments adsorbed on the catalyst leading to the suppression of inactive carbonaceous species formed during the reaction. In fact, mobile oxygen from the support migrates to the active sites hindering coke formation and the consumed lattice oxygen would be regenerated by steam [96, 207].

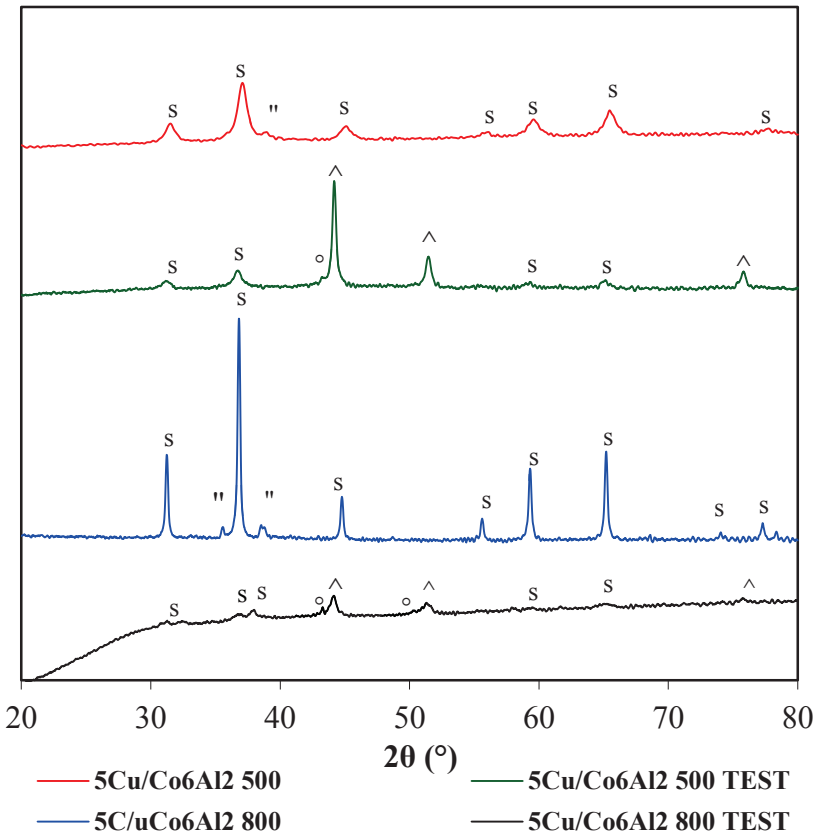

Figure 3.26 XRD analysis for 5Cu/Co_6Al_2 calcined at 500°C and 800°C before and after MSR. "'" CuO tenorite (JCPDS N°45-0937), "°" metallic Cu (JCPDS N°04-0836), "S" spinel Co_3O_4 (JCPDS N°42-1467) $CoAl_2O_4$ (JCPDS N°44-0160) Co_2AlO_4 (JCPDS N°38-0814) and "^" metallic Co (JCPDS N°15-0806)

Figure 3.27 shows XRD patterns of 1Ru/$Co_xMg_{6-x}Al_2$ after methane steam reforming reaction. 1Ru/Co_6Al_2 as discussed above represents lines that correspond to metallic ruthenium and cobalt that were reduced during the reaction. The spinel phase is present indicating that not all cobalt species were reduced. With the increase of the magnesium content, metallic ruthenium is not seen and the intensity of the metallic cobalt decreases for 1Ru/$Co_4Mg_2Al_2$. 1Ru/$Co_2Mg_4Al_2$ and 1Ru/Mg_6Al_2 display

different behavior: metallic cobalt and ruthenium are absent, and the hydrotalcite phase (JCPDS N°22-0700) reappears after the reaction as a consequence of the high affinity of magnesium to water leading to the reconstruction of the hydrotalcite phase. Other phases are present too for $1Ru/Co_2Mg_4Al_2$ and $1Ru/Mg_6Al_2$ catalysts: MgO (JCPDS N°45-0946), $MgAl_2O_4$ (JCPDS N°73-1959), RuO_2 (JCPDS N°40-1290) and cobalt oxide spinel phases (JCPDS N°42-1467, 44-0160 and 38-0814).

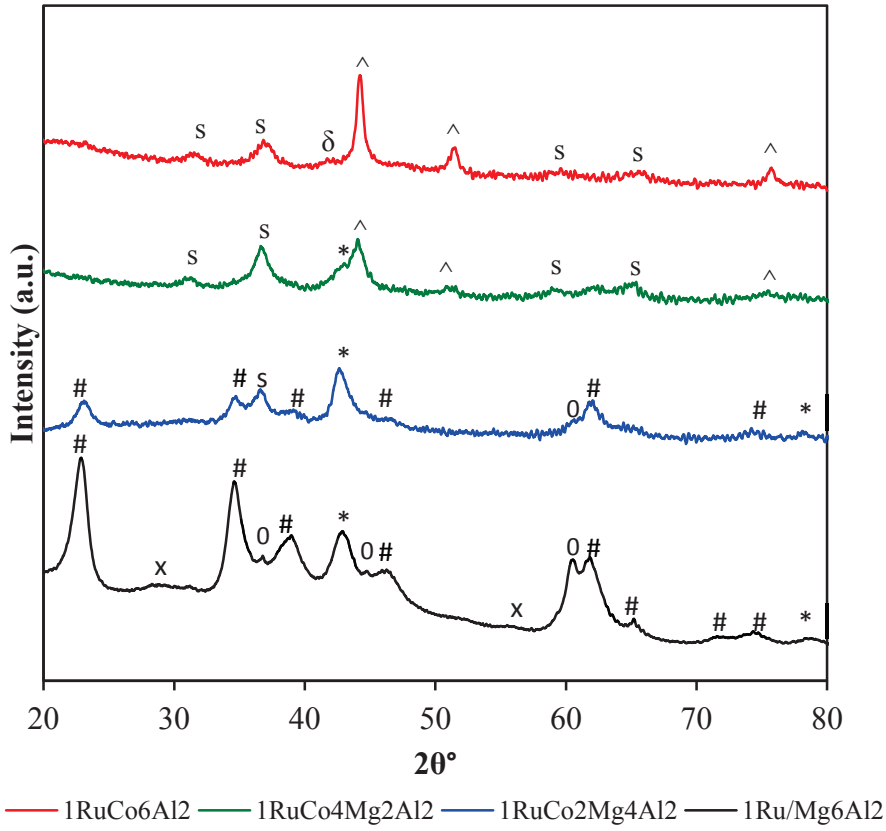

Figure 3.27 XRD analysis for $1Ru/Co_xMg_{6-x}Al_2$ calcined at 500°C after MSR reaction. "S" spinel Co_3O_4 (JCPDS N°42-1467) $CoAl_2O_4$ (JCPDS N°44-0160) Co_2AlO_4 (JCPDS N°38-0814), "^" metallic Co (JCPDS N°15-0806), "δ" metallic Ru (JCPDS N°06-0663), "x" tetragonal RuO_2 (JCPDS N°40-1290), "0" $MgAl_2O_4$ spinel (JCPDS N°73-1959), "#" MgO periclase (JCPDS N°45-0946) and "*" hydrotalcite phase (JCPDS N°22-0700)

3.6.2 TPO Analysis for 1Ru/Co_6Al_2 and 5Cu/Co_6Al_2 After Methane Steam Reforming Reaction

Oxygen consumption of 1Ru/$Co_xMg_{6-x}Al_2$ catalysts after the catalytic test is shown on figure 3.28a. Two oxidation peaks at 115°C and 219°C related to the oxidation of metallic ruthenium and cobalt respectively are present for 1Ru/Co_6Al_2. Their intensities decrease with the increase of the magnesium content until they disappear for 1Ru/Mg_6Al_2. These results correlate well with the obtained XRD patterns that show the present of reduced Co and Ru for higher cobalt content (Figure 3.27).

Figure 3.28b represents oxygen consumption of 1Ru/Co_6Al_2 and 5Cu/Co_6Al_2 calcined at 500°C and 800°C after catalytic test. 5Cu/Co_6Al_2 calcined at 500°C exhibits a similar behavior as 1Ru/Co_6Al_2 calcined at 500°C where two oxidation peaks at 150°C and 295°C attributed to the oxidation of metallic copper and cobalt are present. However, in the case of 1Ru/Co_6Al_2 calcined at 800°C, only one oxidation peak is present at 300°C. In fact, XRD patterns of this latter did not show the lines corresponding to metallic ruthenium whereas the same catalyst calcined at 500°C clearly presents this reduced metallic species. In a previous study done on Ru/CeO_2 catalyst, it is reported that above 700°C, RuO_2 may be converted to some volatile ruthenium oxides RuO_3 and RuO_4 [47, 215]. In addition, it must be noted that the oxidation peak for this catalyst occurs at a temperature higher than the ones for the same catalyst calcined at 500°C. This means that the interaction between the active phase and cobalt species is weakened at higher calcination temperature (as seen in figures 2.9 and 2.15) justifying the lower catalytic performance.

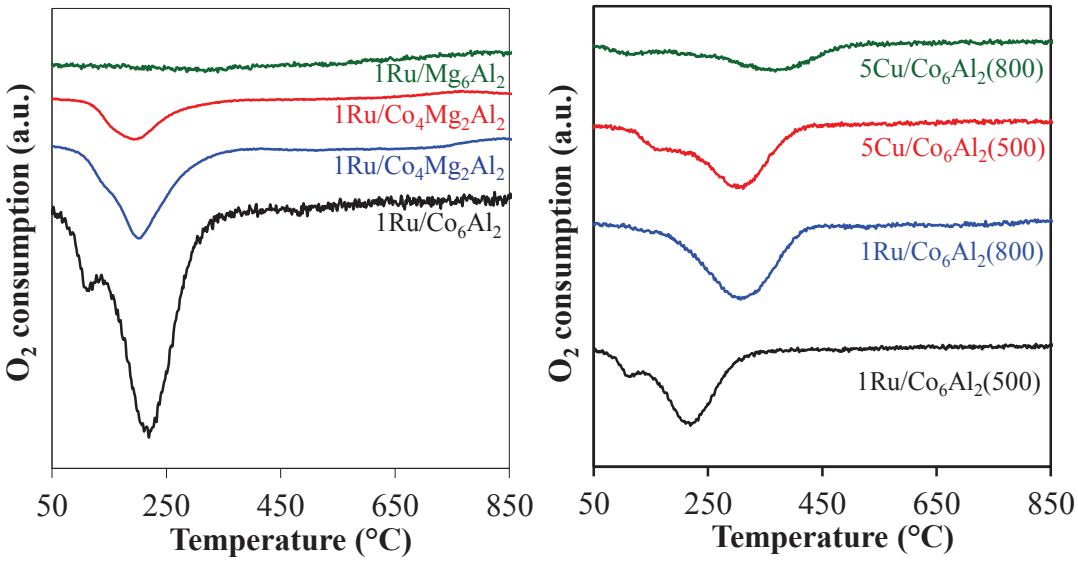

Figure 3.28 Oxygen consumption for a) 1Ru/$Co_xMg_{6-x}Al_2$, b) 1Ru/Co_6Al_2 and 5Cu/Co_6Al_2 calcined at 500°C and 800°C after catalytic reaction

5Cu/Co_6Al_2 calcined at 800°C shows a small peak at lower temperature and a second one at 360°C. It can be seen that oxygen consumption is decreased with the higher calcination temperature because crystallized species are harder to be oxidized. No oxygen consumption peak corresponding to coke oxidation was observed indicating the absence of coke formation on the catalyst (coke oxidation occurs mainly in the temperature range 400-550°C).

3.6.3 DSC/TG Analysis for 1Ru/Co_6Al_2 and 5Cu/Co_6Al_2 After the Catalytic Test

Figure 3.29 represents the DSC/TG curves obtained for 1Ru/$Co_xMg_{6-x}Al_2$ catalysts after methane steam reforming reaction. In correlation with the TPO and XRD analyses, 1Ru/Co_6Al_2 and 1Ru/$Co_4Mg_2Al_2$ catalysts showed a mass gain and 2 exothermic peaks at 116°C and 186°C due to the re-oxidation of the reduced species during the reaction. 1Ru/Mg_6Al_2 and 1Ru/$Co_2Mg_4Al_2$ revealed endothermic peaks and

an important mass loss attributed to the destruction of the hydrotalcite structure that was reconstructed during the reaction as shown in the XRD results (Figure 3.27).

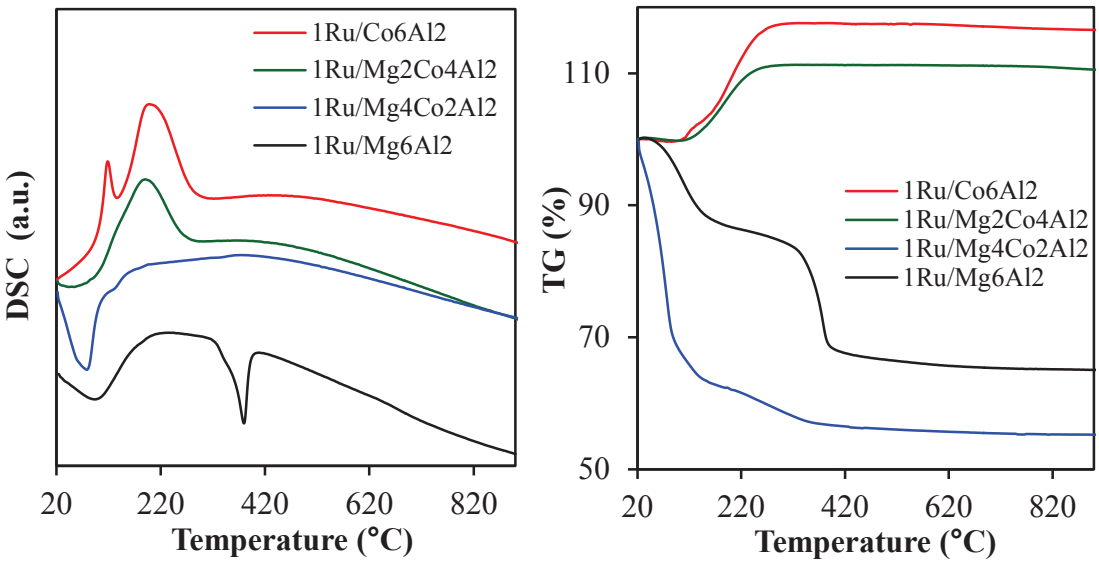

Figure 3.29 a) DSC b) TG curves obtained during the oxidation of 1Ru/$Co_xMg_{6-x}Al_2$ catalysts calcined at 500°C after methane steam reforming

3.6.4 EPR Analysis of Ruthenium and Copper-Based Catalysts After Methane Steam Reforming Reaction

Many studies examined the structure of carbonaceous materials and coke presence using the electron paramagnetic resonance technique [47, 216-218].

In order to study these carbonaceous materials formed during the test, isothermal methane steam reforming tests were performed at the desired temperature for 3 hours (from 400°C to 850°C). Then, the catalysts are recuperated and characterized by EPR technique. All the EPR spectra obtained for the cobalt containing catalysts (Ru or Cu based catalysts) revealed a large EPR signal.

EPR signal of 1Ru/Co_6Al_2 catalyst after isothermal test at 800°C is represented in figure 3.30. This large signal is attributed to the presence of an important quantity of paramagnetic cobalt species. However, EPR study of cobalt is

very difficult to interpret. It should be noted that EPR spectrum of $1Ru/Co_6Al_2$ after the methane steam reforming test at 400°C did not show any signal. It only appears for catalysts recuperated following isotherms at temperatures above 400°C. Its intensity increases with the increase of the temperature.

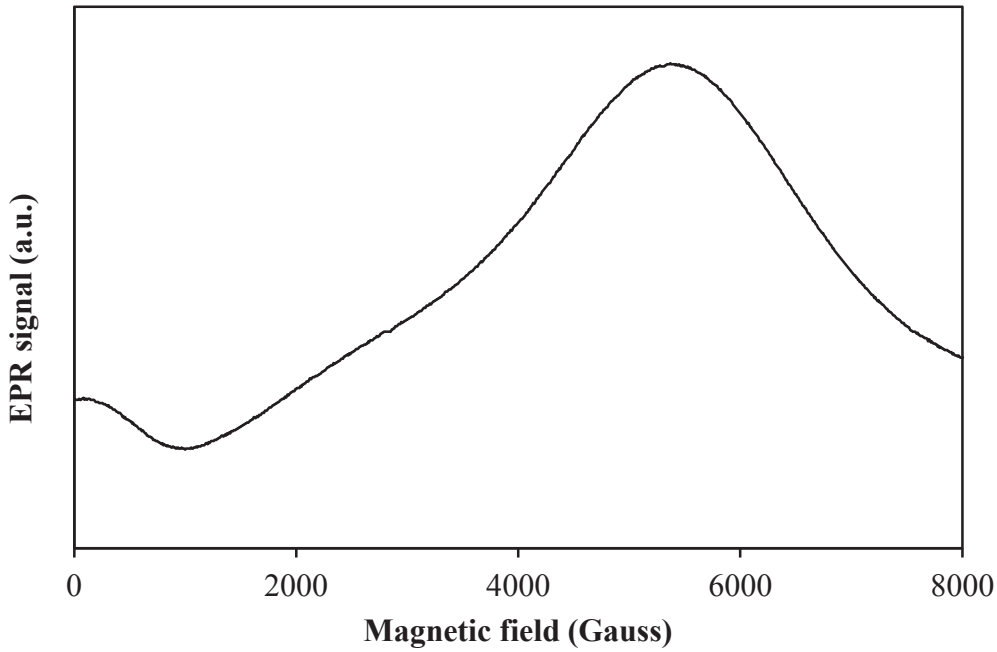

Figure 3.30 EPR spectra for $1Ru/Co_6Al_2$ recorded at ambient temperature after methane steam reforming catalytic test at 800°C

In literature, it is known that carbides could be formed on cobalt in the methane steam reforming reaction [219, 220]. But they are formed in the temperature range between 200°C and 400°C [221] and they are not stable above these temperatures [219], therefore, this signal cannot be attributed to the formation of carbides. Therefore, it may be attributed to the increase in the conductivity of our solids due to cobalt species reduction, leading to the formation to a large EPR signal.

The cobalt free $1Ru/Mg_6Al_2$ catalyst represents a different behavior. Figure 3.31 shows EPR spectra recorded at ambient temperature after isothermal methane steam reforming test (over a period of 3 hours) from 600°C to 850°C over

1Ru/Mg_6Al_2. An isotropic signal (S3) centered at g= 2.0029 was recorded in the magnetic field range of 3475-3495 Gauss for isothermal tests above 600°C. It can be attributed to the presence of carbon species formed at the surface of the catalyst that were detected by EPR due the high sensitivity of this technique towards traces of paramagnetic species [222]. The intensity of this signal increases gradually with the increase of the temperature. At 750°C, the formation of the largest quantity of carbon is obtained yielding the most intense and largest EPR signal. At 800°C, an additional signal (S4) centered at g= 2.0032 Gauss was observed that may be attributed to the presence of coke produced during the reaction.

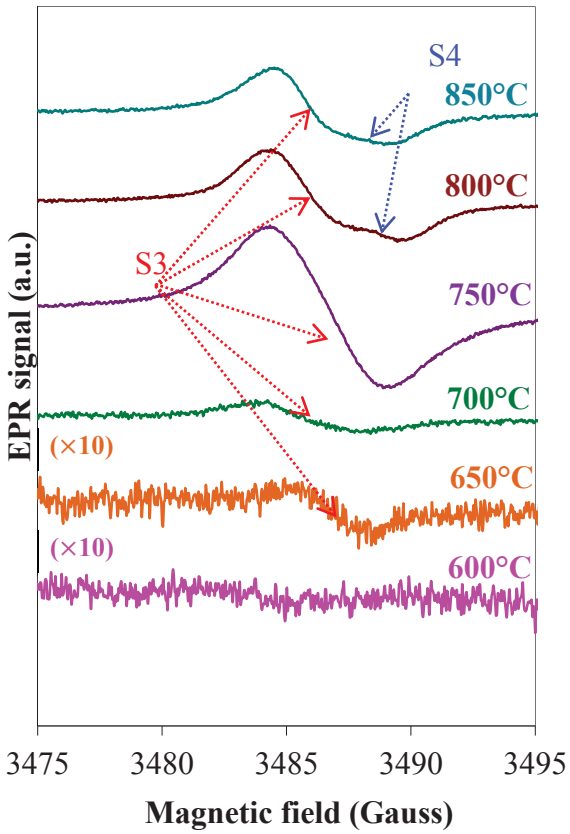

Figure 3.31 EPR spectra for 1Ru/Mg_6Al_2 recorded at ambient temperature after static methane steam reforming catalytic test

The two signals S3 and S4 correspond to two different paramagnetic species: carbon and coke. In fact, carbon is usually the product of CO disproportionation reaction (or Boudouard reaction) during the MSR reaction (Equation 3.4) which is thermodynamically favored above 600°C while coke is produced by the decomposition, cracking or condensation of hydrocarbons on the catalyst surface formed at high temperature (≥ 800°C) [223]. Coke consists of polymerized hydrocarbons or mainly carbon such as graphite. Carbon and coke structure varies with the reaction type, catalyst type and reaction conditions [221].

However, inspite of the detection of these carbon and coke species at the surface of the catalyst, the stability and the activity of the catalyst is not affected. Sometimes, carbon filaments formed would not necessarily cause a loss of the catalytic activity unless they are formed in a sufficient quantity that can plug the pores of the active metal [224]. In addition, Menon suggested that catalytic reactions accompanied by carbon or coke formation can be broadly categorized in two classifications: coke-sensitive or coke-insensitive reactions. In the coke-sensitive reactions, coke is deposited on active sites leading to a decline in the activity, while in coke-insensitive reactions, coke formed on the active sites can be readily removed by hydrogen (or other gasifying agents). Therefore, some forms of carbon and coke do not result in the loss of the catalytic activity [225].

On the basis of this classification, Menon reasoned that the structure and location of coke are more important than its quantity in affecting the catalytic performance. In the above studied case, the nature of the carbon formed on the catalyst is probably carbon filaments or whiskers. They are formed by decomposition of CO on the active site in the temperature range between 300°C and 1000°C, and

they can react with hydrogen in the temperature range between 400°C and 600°C [225].

The mechanism of carbon deposition (C_α) from carbon monoxide dissociation can be summarized in the following equations [224] ("a" and "g" refer to adsorbed and gaseous states respectively):

$$CO\ (a) \rightarrow C_\alpha\ (a) + O\ (a) \qquad \text{(Equation 3.9)}$$

$$C_\alpha\ (a) \rightarrow C\ \text{in metal} \rightarrow C_v \qquad \text{(Equation 3.10)}$$

$$C_\alpha\ (a) \xrightarrow{4H} CH_4\ (g) \qquad \text{(Equation 3.11)}$$

CO dissociates on metals to form C_α which is an adsorbed atomic carbon, and then, carbon filaments or whiskers C_v are formed by precipitation of dissolved carbon at the rear side of metal crystallites causing the metal particles to grow away from the support [226]. Filament growth stops and the encapsulation of the metal particles do not occur if H_2O/hydrocarbon ratios are sufficiently high [224].

In literature, it is reported that whisker carbon does not affect the catalytic performance, but it results in a pressure drop due to reactor blockage [219, 221]. Carbon formation risk is more important with higher hydrocarbons in the gas feed.

In the case of coke, the following equations summarized the formation and transformation of coke on the metal surface (where "a", "g" and "s" refer to adsorbed, gaseous and solid states respectively) [224]:

$$C_nH_m\ (a) \rightarrow C_\alpha\ (a) + H\ (a) + CH_x\ (a) + C_2H_y\ (a) + \ldots + C_nH_z\ (a) \qquad \text{(Equation 3.12)}$$

$$C_\alpha\ (a) \xrightarrow{4H\ (a)} CH_4\ (a) \rightarrow CH_4\ (g) \qquad \text{(Equation 3.13)}$$

$$2H\ (a) \rightarrow H_2\ (a) \rightarrow H_2\ (g) \qquad \text{(Equation 3.14)}$$

$$CH_x \xrightarrow{+(4-x)H\ (a)} CH_4\ (a) \rightarrow CH_4\ (g) \qquad \text{(Equation 3.15)}$$

$CH_x \rightarrow$ condensed HC (a) $\rightarrow C_\alpha, C_\beta, C_c$ (s) + $H_{2\,(g)}$ (Equation 3.16)

(coke) (carbon)

The designation C_α, C_β and C_c are adsorbed atomic carbon, polymeric or amorphous films or filaments and graphitic carbon respectively. In our case, at high temperatures (above 750°C) we are forming another source of carbon coming from the condensed adsorbed hydrocarbons (or coke) as seen in equation 3.16. It seems that graphitic carbons C_c are formed because they are the only type of carbons formed at high temperatures (up to 850°C) compared to the remaining carbon type which are produced at lower temperatures [224].

EPR spectrum recorded at the temperature of liquid nitrogen for 5Cu/Mg_6Al_2 after catalytic test is shown in figure 3.32.

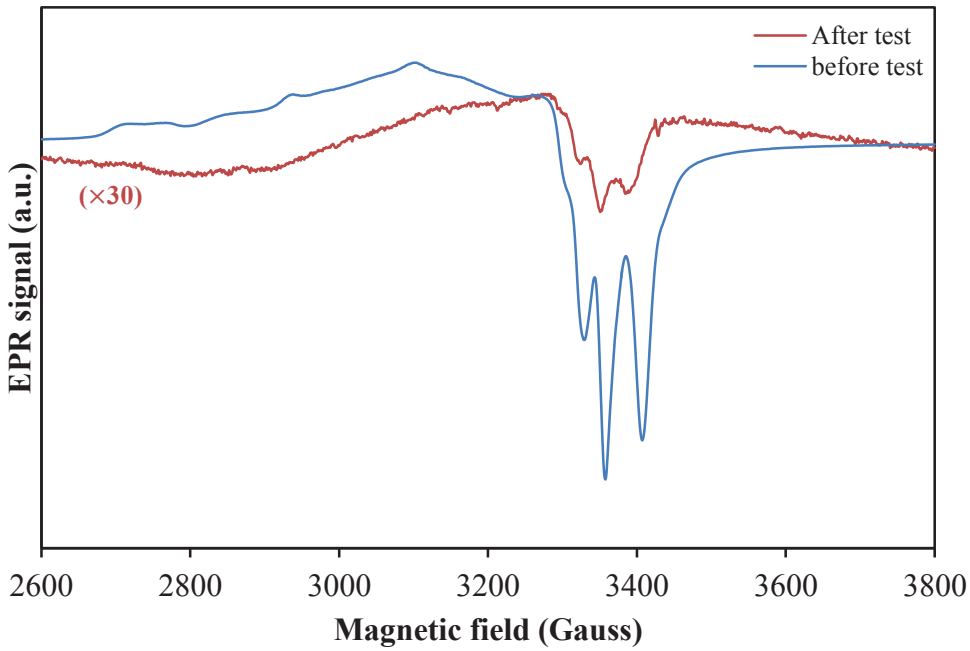

Figure 3.32 EPR spectra for 5Cu/Mg_6Al_2 recorded at 77 K before and after methane steam reforming reaction

It is shown that the intensity of the signal decreases in a remarkable way indicating the diminution of isolated Cu^{2+} species as the result of their reduction. Nevertheless, the formation of CuO agglomerates can also reduce the intensity of the signal of the isolated Cu^{2+} [227].

3.6.5 Condensate Analysis

After each isothermal reaction, the condensates are recuperated and qualitatively analyzed in a HS-CPG-FID technique. Methanol, formaldehyde (methanal), formic acid (methanoic acid) and methyl formate (methyl methanoate) were detected as secondary by-products of the methane steam reforming reaction.

3.7 Conclusion

Hydrogen production from methane steam reforming was studied in the presence of ruthenium and copper-based catalysts supported on $Co_xMg_{6-x}Al_2$ oxides. The influence of different parameters was presented (influence of the nature of the support, influence of the active phase and its content, GHSV, H_2O/CH_4…). It was observed that methane conversion increases with the increase the H_2O/CH_4 ratio and the temperature. Consequently the experimental parameters were optimized. The optimum metal content for the ruthenium and copper active phases were 1wt.% and 5wt.% respectively. With the increase of the active metal content, problems of agglomerate formation may be induced. Furthermore, it was demonstrated that the catalytic performance was higher with the increase of the cobalt content. $1Ru/Co_6Al_2$ catalyst had the best catalytic activity among all the other prepared catalysts. It exhibits a constant stability with no deactivation even after 100 hours and under low

H_2O/CH_4 ratio. Moreover, supports showed an important role by interacting with water molecules and dissociating them which is the case of $1Ru/Co_xMg_{6-x}Al_2$ and $5Cu/Co_xMg_{6-x}Al_2$ whereas Co_6Al_2 support facilitated the oxidation of carbon monoxide to carbon dioxide. In parallel, higher metal content presented higher H_2 production and CH_4 conversion indicating that the presence of more active site species can enhance the methane decomposition and methane steam reforming reactions. Therefore, a proposed mechanism that can be elucidated is very similar to the one presented in chapter 1 where steam is dissociatively adsorbed on the support sites, and methane is dissociatively adsorbed on the Ru active sites. In addition, higher reactivity was observed for the prepared catalysts compared to the industrial one tested under the same operating conditions. TPO, XRD, DSC/TG did not reveal the presence of carbonaceous species formed during the reaction, but they showed the presence of reduced metallic species formed during the reaction. Finally, EPR technique was able to detect the presence of carbon formed during Boudouard reaction and coke formed during the methane decomposition reaction due to the high sensitivity of this technique.

CHAPTER 4

CATALYTIC STEAM REFORMING OF ETHANOL OVER $Co_xMg_{6-x}Al_2$, $Ru/Co_xMg_{6-x}Al_2$ AND $Cu/Co_xMg_{6-x}Al_2$ SOLIDS

4.1 Steam Reforming of Ethanol

4.1.1 Introduction

Hydrogen production from the "in-situ" steam reforming of alcohols favors its use as an alternative fuel, removing the difficulty of its storage and distribution [66-68]. From an environmental point of view, the use of ethanol is preferred among other alcohols because of being not toxic and it is considered as a renewable raw material that is easily obtained from biomass [11, 68, 228]. However, ethanol steam reforming reaction suffers from by-products formation especially ethylene that can be easily transformed to carbon that leads to catalyst poisoning [69]. Therefore, the use of a suitable catalyst can avoid the formation of by-products or reform them.

In the first section of this chapter, a thermodynamic study of the above reaction with some of its side reactions is displayed. Then, the procedure with the operating catalytic test conditions are described.

In the second section, ethanol steam reforming reaction is studied in the absence and in the presence of an active phase. Additionally, the influence of some parameters such as the nature of the support, the nature of the active phase and its content, and the steam-to-ethanol ratio is discussed.

In the third section, DSC/TG, XRD and EPR analysis were performed on the used catalysts to see if there was formation of carbon during the reaction, and to assess the state of the catalysts after the catalytic reaction.

4.1.2 The Thermodynamics of the Reaction

The theoretical converion of ethanol (%) as a function of the temperature for a S/C= 1.5 (or steam/ethanol= 3) and under atmospheric pressure is represented in figure 4.1. Total conversion of ethanol occurs at a temperature greater than 400°C.

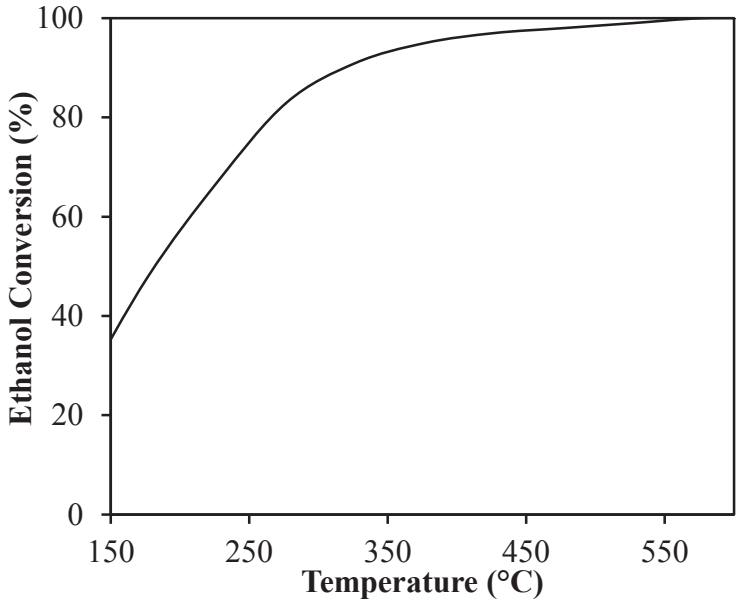

Figure 4.1 Theoretical ethanol conversion (%) versus temperature (S/C= 1.5)

Table 4.1 represents ΔG ($kJ.mol^{-1}$) values as function of the temperature (°C) at 1 atm for all the reactions involved in ethanol steam reforming reaction. Their equations are summarized below (Equations 4.1-4.23):

- Ethanol steam reforming reaction with sufficient steam supply:

$CH_3CH_2OH + 3\ H_2O \leftrightarrow 6\ H_2 + 2\ CO_2$ $\Delta H° = 173\ kJ.mol^{-1}$ (Equation 4.1)

- Ethanol steam reforming reaction with insufficient steam supply:

$CH_3CH_2OH + H_2O \leftrightarrow 2\ CO + 4\ H_2$ $\Delta H° = 256\ kJ.mol^{-1}$ (Equation 4.2)

- Water-gas shift reaction:

$CO + H_2O \leftrightarrow CO_2 + H_2$ $\Delta H° = -41\ kJ.mol^{-1}$ (Equation 4.3)

- Ethanol dehydrogenation (acetaldehyde formation):

$CH_3CH_2OH \leftrightarrow H_2 + CH_3CHO$ $\Delta H° = 69\ kJ.mol^{-1}$ (Equation 4.4)

- Acetaldehyde decomposition:

$CH_3CHO \leftrightarrow CH_4 + CO$ $\Delta H° = -19\ kJ.mol^{-1}$ (Equation 4.5)

- Acetaldehyde steam reforming (1):

$CH_3CHO + H_2O \leftrightarrow 3\ H_2 + 2\ CO$ $\Delta H° = 187\ kJ.mol^{-1}$ (Equation 4.6)

- Acetaldehyde steam reforming (2):

$CH_3CHO + H_2O \leftrightarrow H_2 + CO_2 + CH_4$ $\Delta H° = -60\ kJ.mol^{-1}$ (Equation 4.7)

- Ethanol decomposition (1):

$CH_3CH_2OH \leftrightarrow CO + CH_4 + H_2$ $\Delta H° = 50\ kJ.mol^{-1}$ (Equation 4.8)

- Ethanol decomposition (2):

$2\ CH_3CH_2OH \leftrightarrow CH_3COCH_3 + CO + 3\ H_2$ $\Delta H° = 142\ kJ.mol^{-1}$ (Equation 4.9)

- Ethanol decomposition (3):

$CH_3CH_2OH \leftrightarrow 0.5\ CO_2 + 1.5\ CH_4$ $\Delta H° = -74\ kJ.mol^{-1}$ (Equation 4.10)

- Ethanol dehydration (ethylene formation):

$CH_3CH_2OH \leftrightarrow CH_2CH_2 + H_2O$ $\Delta H° = 45\ kJ.mol^{-1}$ (Equation 4.11)

- Steam reforming of ethylene:

$CH_2CH_2 + 2\ H_2O \leftrightarrow 2\ CO + 4\ H_2$ $\Delta H° = 211\ kJ.mol^{-1}$ (Equation 4.12)

- Ethylene hydrogenation (ethane formation):

$CH_2CH_2 + H_2 \leftrightarrow CH_3CH_3$ $\Delta H° = -137\ kJ.mol^{-1}$ (Equation 4.13)

- Methane decompostion:

$CH_4 \leftrightarrow 2\ H_2 + C$ $\Delta H° = 75\ kJ.mol^{-1}$ (Equation 4.14)

- Boudouard reaction:

$2\ CO \leftrightarrow CO_2 + C$ $\Delta H° = -173\ kJ.mol^{-1}$ (Equation 4.15)

- CO reduction:

$CO + H_2 \leftrightarrow H_2O + C$ $\Delta H° = -131\ kJ.mol^{-1}$ (Equation 4.16)

- CO_2 reduction:

$CO_2 + 2\ H_2 \leftrightarrow 2\ H_2O + C$ $\Delta H° = -90\ kJ.mol^{-1}$ (Equation 4.17)

- Coke formation from ethylene:

$CH_2CH_2 \leftrightarrow 2\ C + 2\ H_2$ $\Delta H° = -52\ kJ.mol^{-1}$ (Equation 4.18)

- Coke formation from ethane:

$CH_3CH_3 \leftrightarrow 2\ C + 3\ H_2$ $\Delta H° = 84\ kJ.mol^{-1}$ (Equation 4.19)

- Methanation (1):

$CO + 3\ H_2 \leftrightarrow CH_4 + H_2O$ $\Delta H° = -206\ kJ.mol^{-1}$ (Equation 4.20)

- Methanation (2):

$CO_2 + 4\ H_2 \leftrightarrow CH_4 + 2\ H_2O$ $\Delta H° = -165\ kJ.mol^{-1}$ (Equation 4.21)

- Acetone formation:

$2CH_3CH_2OH+H_2O \leftrightarrow CH_3COCH_3+CO_2+4H_2$ $\Delta H° = 101 kJ.mol^{-1}$ (Equation 4.22)

- Acetic acid formation:

$CH_3CH_2OH + H_2O \leftrightarrow CH_3COOH + 2\ H_2$ $\Delta H° = 44\ kJ.mol^{-1}$ (Equation 4.23)

Table 4.1 ΔG (kJ.mol^{-1}) values as function of the temperature (°C) at 1 atm for all the reactions involved in ethanol steam reforming reaction

T (°C)	ESR Sufficient Steam	ESR Insufficient Steam	WGS	Ethanol Dehydrogenation	Acetaldehyde Decomposition	Acetaldehyde Steam Reforming 1	Acetaldehyde Steam Reforming 2	Ethanol Decomposition 1	Ethanol Decomposition 2	Ethanol Decomposition 3	Ethanol Dehydration	Steam Reforming Of Ethylene
25	64.9	122.1	-28.6	34.9	-54.8	87.2	-83.4	-19.8	46.1	-105.1	7.6	114.5
125	64.2	121.3	-28.5	34.7	-55.1	86.5	-83.5	-20.2	45.3	-105.3	7.4	113.9
225	26.6	75.4	-24.4	23.2	-67.1	52.2	-91.6	-43.9	12.3	-115.8	-5.3	80.8
325	-12.8	28.1	-20.4	11.2	-79.4	16.8	-99.8	-68.1	-21.9	-126.4	-18.3	46.4
425	-53.6	-20.3	-16.7	-0.9	-91.6	-19.3	-108.2	-92.5	-56.9	-136.9	-31.3	11.1
525	-95.3	-69.2	-13.1	-13.2	-103.7	-55.9	-116.8	-117.1	-92.4	-147.4	-44.3	-24.8
625	-137.6	-118.4	-9.6	-25.6	-115.8	-92.8	-125.4	-141.4	-127.9	-157.7	-57.3	-61.1
725	-180.3	-167.9	-6.2	-38.1	-127.9	-129.9	-134.1	-165.9	-163.8	-168.1	-70.2	-97.7
825	-223.5	-217.5	-3.1	-50.4	-139.9	-167.1	-142.9	-190.3	-199.6	-178.2	-83.1	-134.4

T (°C)	Ethylene Hydrogenation	CH_4 Decomposition	Boudouard Reaction	CO Reduction	CO_2 Reduction	Coke From Ethylene	Coke From Ethane	Methanation 1	Methanation 2	Acetone Formation	Acetic Acid Formation
25	-100.4	50.5	-120.1	-91.4	-62.8	-68.4	32.1	-141.9	-113.3	17.3	22.2
125	-100.1	50.4	-119.7	-91.2	-62.6	-68.4	31.7	-141.5	-113.1	16.8	22.1
225	-87.8	41.8	-102.1	-77.5	-53.1	-74.3	13.5	-119.4	-95.1	-12.1	14.3
325	-75.1	32.5	-84.1	-63.6	-43.2	-80.9	-6.1	-96.1	-75.7	-42.3	5.9
425	-61.9	22.7	-66.1	-49.5	-32.9	-88.1	-26.1	-72.2	-55.5	-73.5	-2.9
525	-48.6	12.5	-48.3	-35.3	-22.2	-95.4	-46.8	-47.8	-34.7	-105.5	-12.1
625	-35.2	2.1	-30.6	-21.1	-11.4	-103.1	-67.9	-23.1	-13.4	-137.5	-21.4
725	-21.9	-8.7	-12.9	-6.7	-0.4	-111.1	-89.2	2.1	8.2	-170.1	-31.1
825	-8.3	-19.4	4.7	7.7	10.7	-119.1	-110.7	27.1	30.1	-202.6	-41.1

Figure 4.2 shows the variation of the equilibrium constants of the main reactions that occur during the ethanol steam reforming reaction as function of temperature. Thermodynamic calculations indicate that the ethanol steam reforming reactions with sufficient and insufficient steam are spontaneous above 125°C and 225°C ($\Delta G < 0$) respectively. Whereas for the water-gas shift reaction, it is favored below 625°C. Ethanol dehydrogenation and acetic acid formation are thermodynamically favored above 325°C. And finally, acetone formation and ethanol dehydration are favored over 125-825°C temperature range.

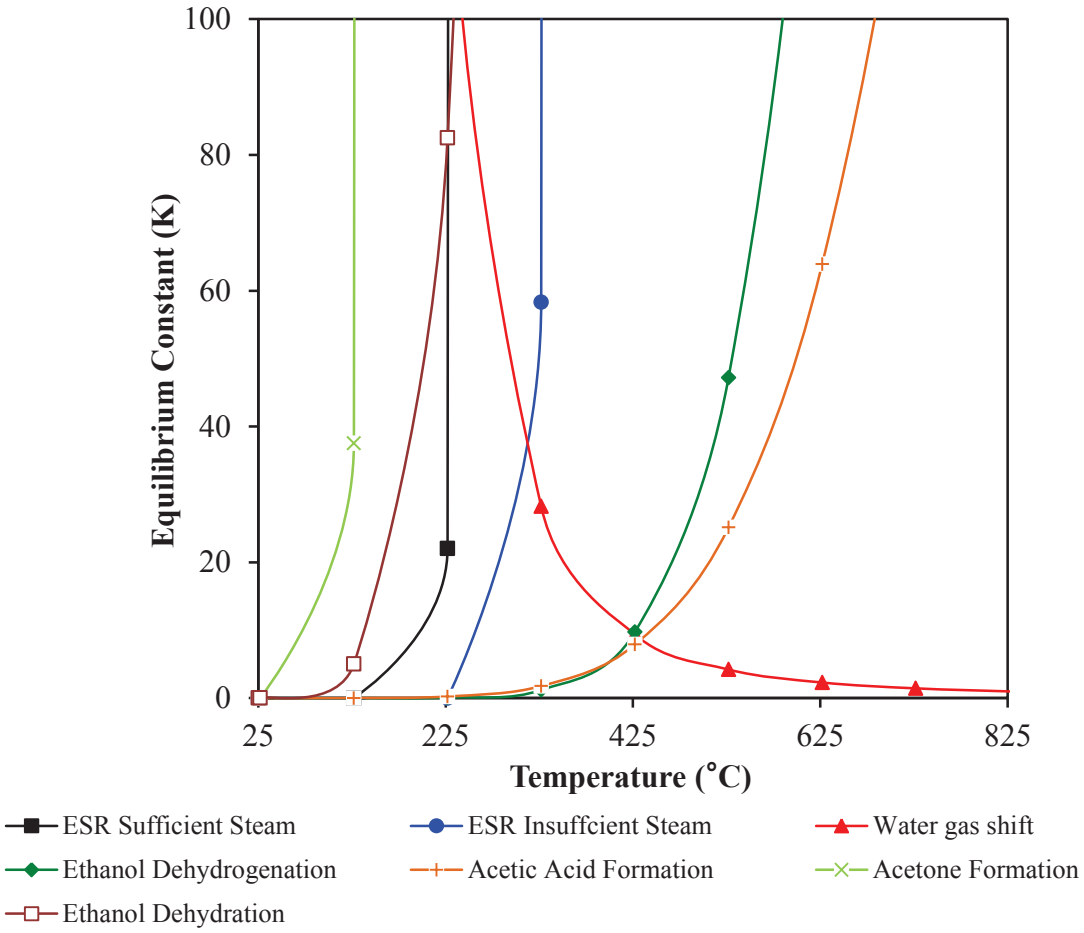

Figure 4.2 Equilibrium constants for the main reactions occurring during the ethanol steam reforming reaction

4.1.3 Experimental Procedure

Catalysts reactivities in the ethanol steam reforming reaction were evaluated under atmospheric pressure in a fixed catalytic bed reactor. The experimental setup is shown in figure 4.3.

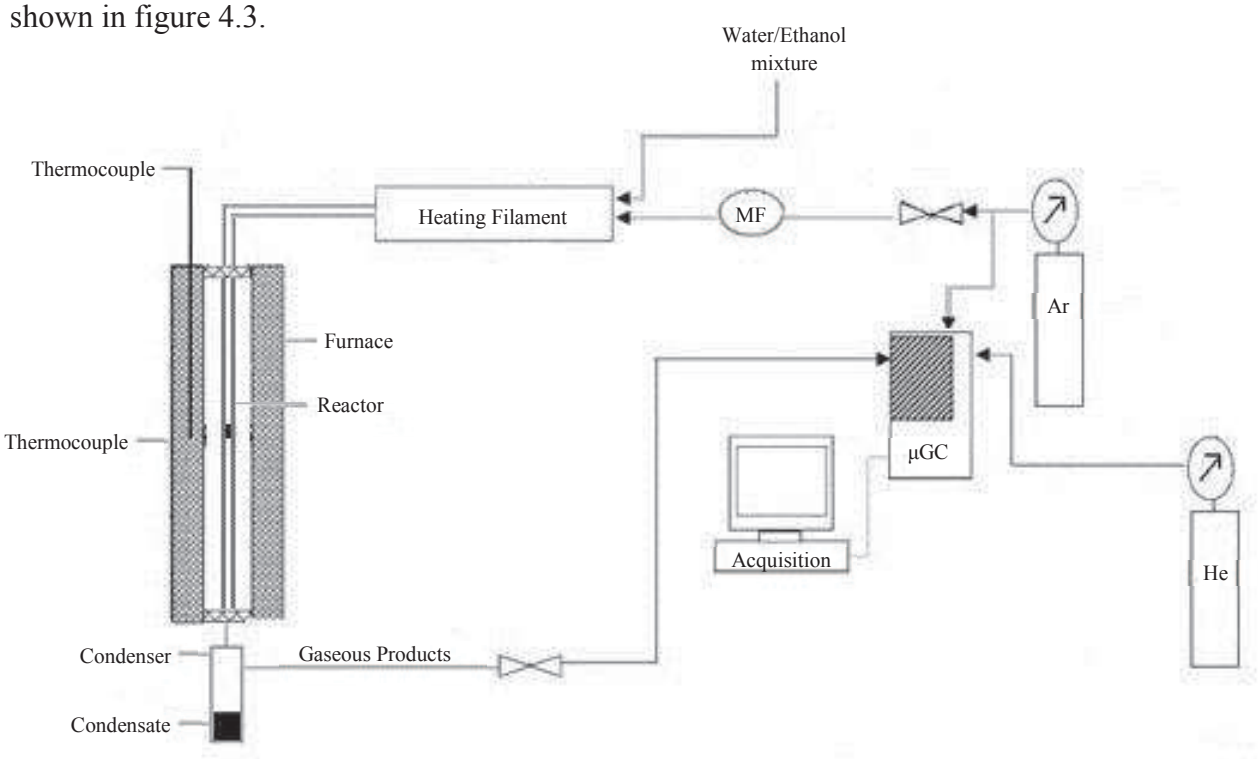

Figure 4.3 Schematic diagram of the experimental apparatus used for the ethanol steam reforming reaction

An adequate quantity (0.1 $mL.min^{-1}$) of an ethanol/water mixture is injected in a heated section (150°C) and carried along using an argon flow. The gaseous mixture enters the reactor which is placed inside a temperature programmed electrical furnace. The catalytic bed temperature is monitored with a thermocouple positioned at the level of the catalyst.

The gaseous products leave the reactor and enter a condenser located at its outlet and immersed in a salty ice bath. At the end of each test, the condensate is recuperated and analysed in a GC-FID (Agilent 7890A) apparatus in order to identify

the by-products formed during the reaction and the extent of ethanol conversion. Non condensed products are automatically injected in a micro-GC (Agilent 3000A) equipped with two analysis modules: a molecular sieve column that separates CH_4, H_2 and CO using argon as a carrier gas, and a Plot U column separating CO_2 and with helium as a carrier gas. The detection of these products was done using a thermal conductivity detectore (TCD).

Ethanol steam reforming reaction was studied under the following conditions:

- Steam/carbon (S/C) ratios of 0.75, 1.5 and 3 and a GHSV= 10000 $mL.g^{-1}.h^{-1}$
- A pelletized catalyst with a mass of 150 mg
- Temperature ranging from 300°C up to 600°C

4.1.4 Calculations of Ethanol/H_2O Ratio

A sample calculation for the preparation of a volume of 200 mL of water/ethanol mixture is established in table 4.2. For example, to prepare water/ethanol mixture with a ratio equal to three, the molecular weight of water is multiplied by three and that of ethanol by one (molar fraction of water and ethanol). Therefore, the steam-to-carbon ratio will be 3/2= 1.5. The volume is obtained by dividing this mass by the density of the corresponding liquid. A volume fraction is obtained and used to calculate the volume of each liquid. From this volume, the mass of water and ethanol are calculated. Liquids will be weighed and then mixed together. The mass measurement is preferred over the volumeric measurement which is less accurate.

Table 4.2 Example for the preparation of a water/ethanol mixture = 3 (S/C=1.5) with a total volume of 200 mL

	EtOH	H_2O
Steam/Carbon	2	3
Total Volume (mL)	200	
Molar Mass ($g.mol^{-1}$)	46.068	18.015
Density	0.788	1
Molar Fraction	1	3
Mass	46.068	54.045
Volume	58.387	54.045
Volume Fraction	0.519	0.481
Volume (mL)	103.8	96.2
Mass (g)	81.794	96.2
Number of Moles (mol)	1.775	5.344

4.1.5 Productivity Calculations

Productivity ($mmol.h^{-1}.g^{-1}cata$) = $\frac{60PV}{mRT}$

Where: P is the atmospheric pressure (1 atm)

V is the volume of each gaseous product (H_2, CO_2, CO) in L

m is the mass of the catalyst in g

R= 0.08206 $L.atm.mol^{-1}.k^{-1}$

T= 293 K

4.1.6 Ethanol Conversion

Ethanol conversion (X_{EtOH}) is calculated as follows:

$$X_{EtOH} = \frac{n_i EtOH - n_f EtOH}{n_i EtOH} \times 100$$

Where n_iEtOH is the number of moles injected of ethanol and n_fEtOH is the number of moles of ethanol recuperated in the condensate.

4.2 Evaluation of ESR in the Absence of a Catalyst

A blank ethanol steam reforming test using carborundum (SiC) loaded in the reactor is done as a reference to study the reaction in the absence of a catalyst. H_2, CO_2, CH_4 and CO productivities from 300°C to 600°C for the uncatalyzed reaction using carborundum (SiC) are represented in figure 4.4 using a stoichiometric steam-to-carbon ratio equal to 1.5. Five injections were made at each temperature. Their average are represented only for all this chapter.

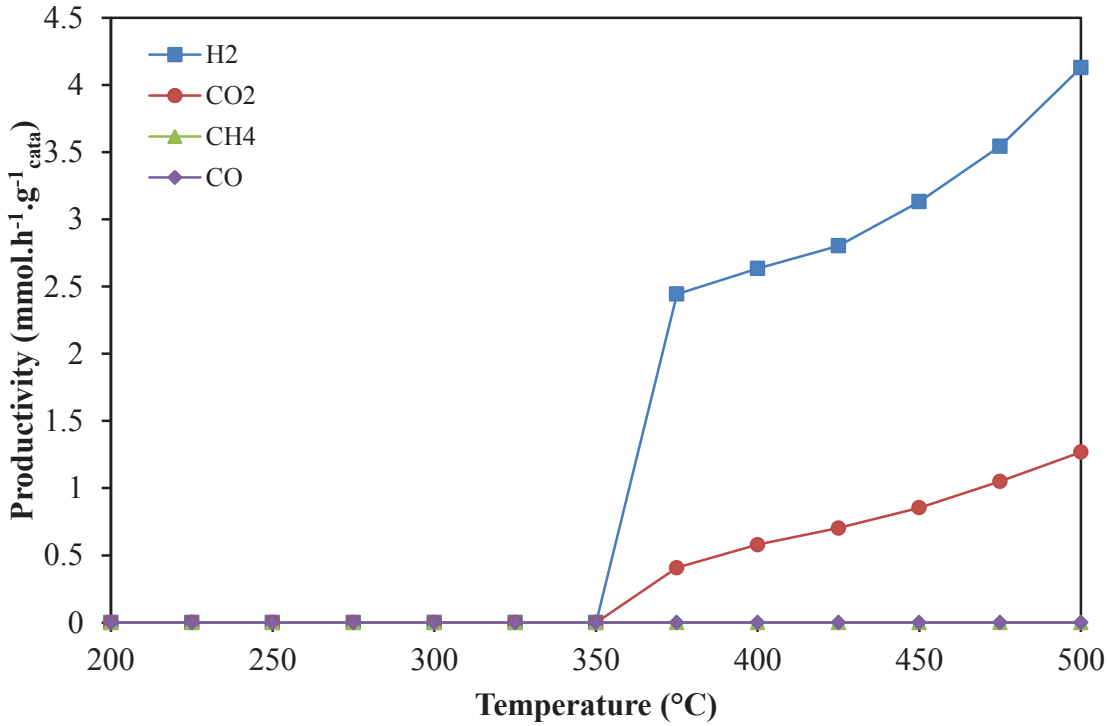

Figure 4.4 H_2, CO_2, CH_4 and CO productivity (mmol.h^{-1}.g^{-1}_{cata}) from 300°C to 600°C for the uncatalyzed reaction using carborundum (SiC) under a S/C=1.5

Very small H_2 and CO_2 quantities are produced over the studied temperature range in the case of the uncatalyzed reaction. No CH_4 and CO are detected as the reaction is slightly occuring.

4.3 Evaluation of the Performance of the Catalysts in ESR

4.3.1 Catalytic Performance of $Co_xMg_{6-x}Al_2$ Supports

H_2, CO_2, CH_4 and CO productivities from 300°C to 500°C for Co_6Al_2, $Co_4Mg_2Al_2$, $Co_2Mg_4Al_2$ and Mg_6Al_2 supports calcined at 500°C are represented in figure 4.5 using a stoichiometric steam-to-carbon ratio equal to 1.5.

Only H_2, CO_2, CH_4 and negligible amount of CO are detected. The insignificant amount of CO produced in the gaseous mixture can be due to the water gas shift reaction (Equation 4.3) that reforms CO into CO_2 and H_2.

On the other hand, no ethane and ethylene are seen, nevertheless we cannot confirm that they are not produced during the process, because they may be produced in the studied temperature range but directly reformed by the reaction with water (Equation 4.12) [229]. It can be seen that as the temperature increases from 300°C to 500°C, H_2, CO_2 and CH_4 productivities increase. The nature of the support strongly affects the product composition. With the increase of cobalt content, higher hydrogen and carbon dioxide productivities are detected and particularly for Co_6Al_2 support. In literature, catalysts containing cobalt showed the highest activity and selectivity to hydrogen [13, 71, 91, 95, 228, 231-233]. In addition, the qualitative condensate analysis at 450°C reveals the presence of unreacted ethanol, acetone and acetaldehyde for cobalt containing support while only ethanol and acetaldehyde are identified in the case of Mg_6Al_2. In fact, it is well known that the presence of MgO favors ethanol dehydrogenation -acetaldehyde formation- (Equation 4.4) and inhibit dehydration -ethylene formation- (Equation 4.11) due to its basic character [11, 233, 234] and it is stated that acetone formation is seen for cobalt-based catalysts [235].

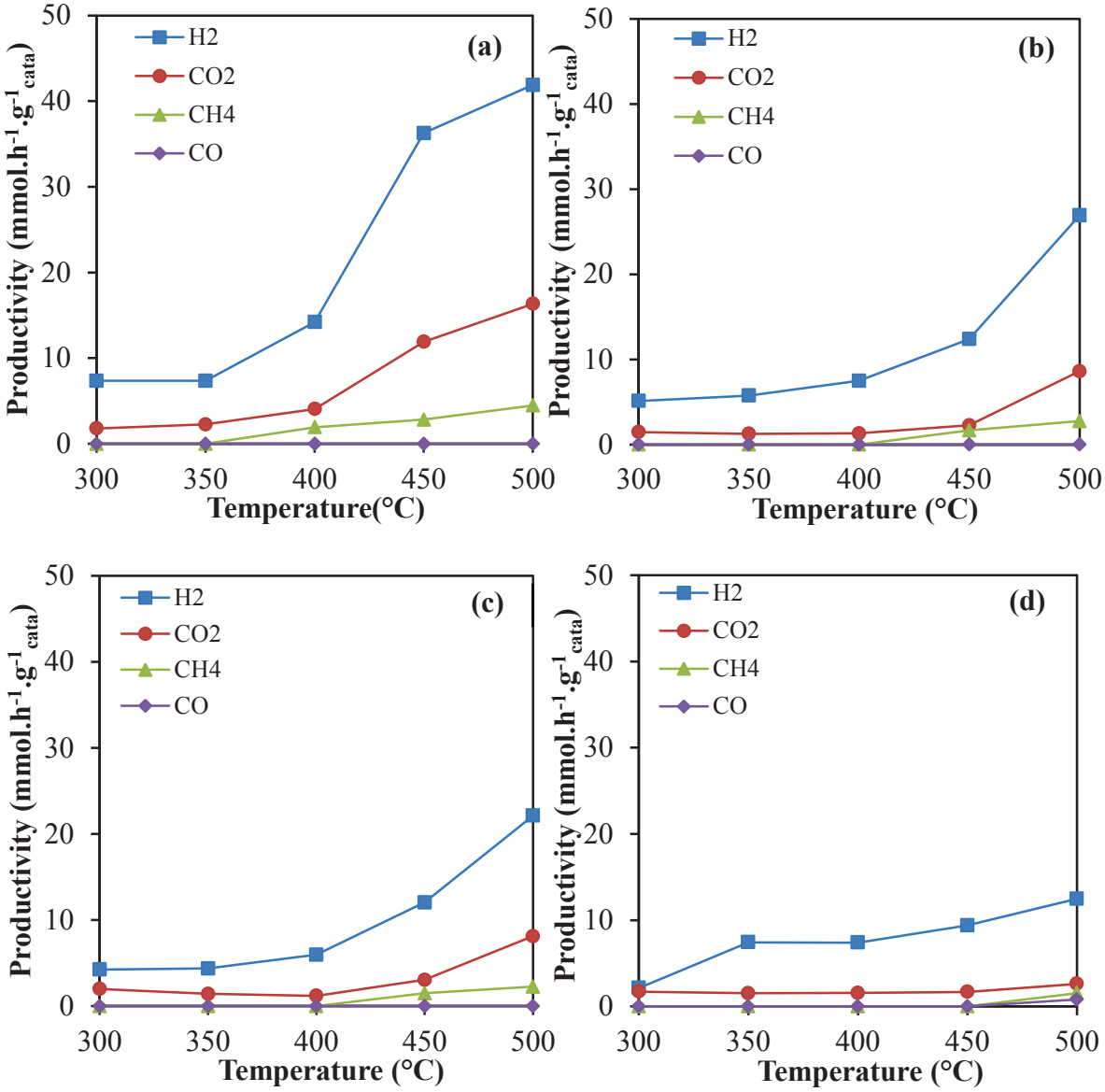

Figure 4.5 H_2, CO_2, CH_4 and CO productivity (mmol.h^{-1}.g^{-1}_{cata}) from 300°C to 500°C in the presence of (a) Co_6Al_2 (b) $Co_4Mg_2Al_2$ (c) $Co_2Mg_4Al_2$ (d) Mg_6Al_2 calcined supports

It must be noted that with the increase of temperature from 300°C to 500°C in the presence of supports, the presence of ethanol is seen indicating that ethanol is not totally converted. For example, at 450°C, the ethanol conversion was the following: 25%, 50%, 62% and 76% for Mg_6Al_2, $Co_2Mg_4Al_2$, $Co_4Mg_2Al_2$ and Co_6Al_2 respectively which is lower than the theoretical conversion (98% at 450°C). In

literature, it was found that at 450°C and under a S/C ratio equal to 2, 30% of ethanol was converted in the presence of $Co_2Mg_4Al_2$ [236].

4.3.2 Catalytic Performance of $Cu/Co_xMg_{6-x}Al_2$ and $Ru/Co_xMg_{6-x}Al_2$

4.3.2.1 Activity of $5Cu/Co_6Al_2$ from 300°C to 500°C in ESR

Co_6Al_2 is found to be the best support among the other Co-Mg-Al oxides. Therefore, in this section, 5wt.% Cu is impregnated on Co_6Al_2 support and tested in the temperature range of 300-500°C to choose the optimum temperature at which high H_2-CO_2 and low CH_4-CO quantities are obtained.

H_2, CO_2, CH_4 and CO productivities (in $mmol.h^{-1}.g^{-1}_{cata}$) for $5Cu/Co_6Al_2$ from 300°C to 500°C are displayed in figure 4.6 using a S/C= 1.5. By comparing these resuslts to the ones obtained for Co_6Al_2 support, it can be seen that the addition of copper improves the activity and the productivity of hydrogen and carbon dioxide. In fact, copper is known as a good active agent in the ESR [237-239]. CO is also found in traces which can be explained by the fact that copper is known for its activity in the WGS reaction [240, 241]. In general, transition-metal catalysts are known to be active for the CO hydrogenation or methanation (Equation 4.20). Therefore, a part of methane observed at 500°C is thought to be formed by hydrogenation of CO that begins to be thermodynamically favored starting from this temperature. In literature, it was found that Ni/TiO_2 catalyst calcined at 500°C and using water/ethanol ratio equal to 3, exhibited 82% conversion of ethanol with a hydrogen productivity of 12.6 $mmol.h^{-1}.g^{-1}_{cata}$ at 500°C eventhough it was reduced under H_2 before the reaction [242]. Whereas, $5Cu/Co_6Al_2$ catalyst showed 100% conversion of ethanol with 50 $mmol.h^{-1}.g^{-1}_{cata}$ even without any catalyst treatment.

Moreover, it can be noticed that with the increase of temperature, gaseous productivity increases up to 450°C, then it falls down at 500°C. The decrease of the productivity at 500°C may be due to coke formation that can deactivate the catalyst (Equations 4.15, 4.16, 4.17). E. Ozdogan found that copper based catalysts showed also a decrease in the catalytic performance due to coke formation from 400°C to 450°C under a S/C=1.5 [243].

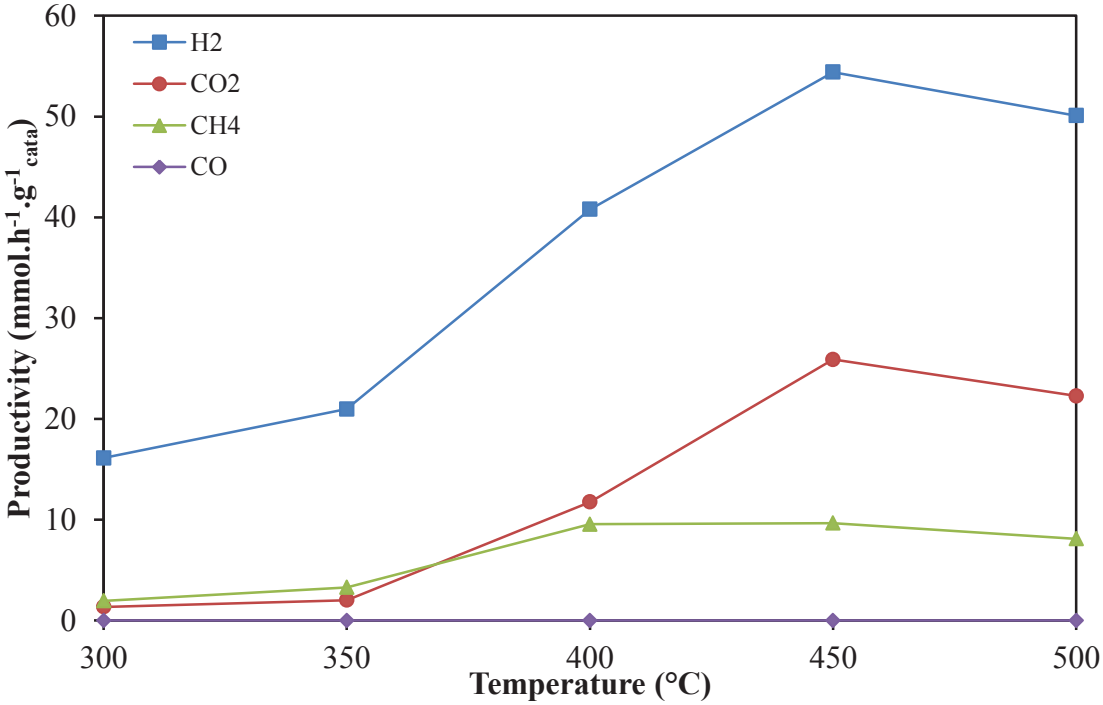

Figure 4.6 H_2, CO_2, CH_4 and CO productivity (mmol.h^{-1}.g^{-1}_{cata}) from 300°C to 500°C in the presence of 5Cu/Co_6Al_2 calcined catalyst (S/C= 1.5)

In parallel, the analysis of the condensates shows the presence of acetic acid, acetaldehyde, ethyl acetate and unreacted ethanol starting from 350°C. At 450°C and 500°C, ethanol is found as traces and is almost 100% converted and the other by-products are detected but in negligible quantities. Iwasa and Takezawa have reported that ethyl acetate, acetic acid and C4 species are produced over Cu-based catalysts [244]. Also, copper is known to favor the dehydrogenation reaction -producing

acetaldehyde- (Equation 4.4) over the dehydration reaction -producing ethylene then ethane- (Equations 4.11 and 4.13) [77, 237, 238, 245-248].

From these experimental results, it is concluded that the presence of copper improves hydrogen productivity and ethanol conversion compared to supports alone. Furthermore, the best result is obtained at 450°C because ethanol is almost completely converted with a maximum of hydrogen productivity reached, and only traces of CO and by-products are detected. In fact, ESR should work at temperatures as low as possible in order to promote WGS reaction that consumes CO to produce hydrogen. Therefore, this temperature will be considered for the rest of the catalytic tests.

4.3.2.2 Activity of $5Cu/Co_xMg_{6-x}Al_2$ at 450°C in ESR

H_2, CO_2, CH_4 and CO productivities for $5Cu/Co_xMg_{6-x}Al_2$ are represented in figure 4.7 at a temperature of 450°C during 4 hours and S/C= 1.5.

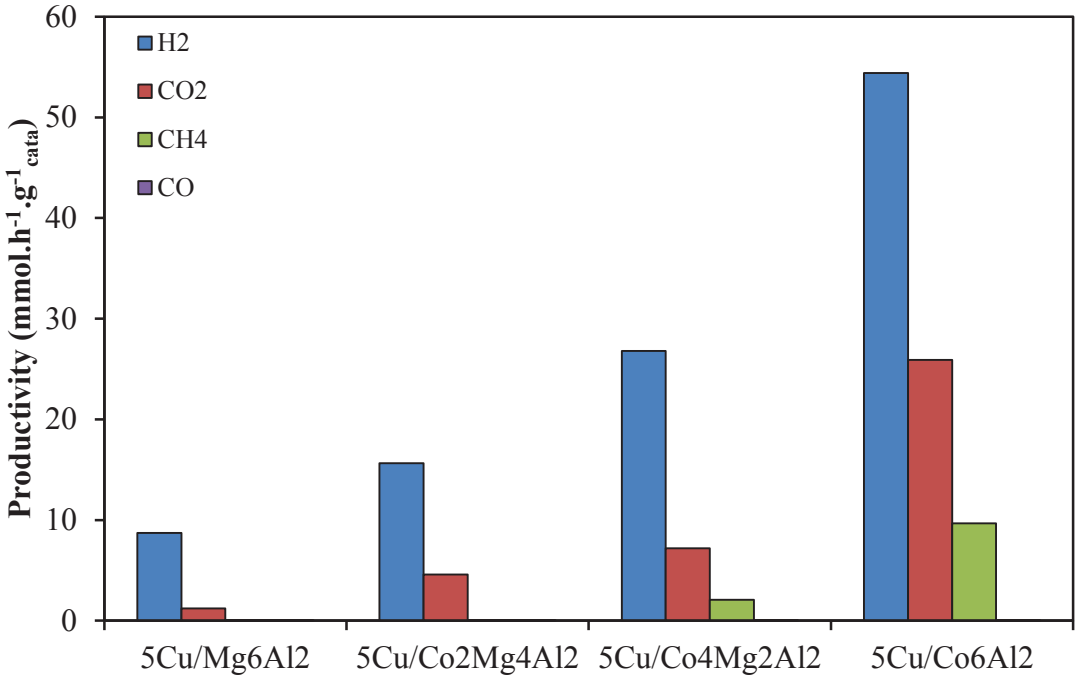

Figure 4.7 H_2, CO_2, CH_4 and CO productivity ($mmol.h^{-1}.g^{-1}_{cata}$) at 450°C in the presence of (a) $5Cu/Co_6Al_2$ (b) $5Cu/Co_4Mg_2Al_2$ (c) $5Cu/Co_2Mg_4Al_2$ (d) $5Cu/Mg_6Al_2$ calcined catalysts (S/C= 1.5)

First, hydrogen and carbon dioxide productivities are more important than in the case of supports alone due to the presence of the active phase. And as seen before (section 4.3.1), hydrogen and carbon dioxide productivities increase with the cobalt content. The obtained methane may be produced from acetaldehyde decomposition and steam reforming (Equations 4.5 and 4.7) and from ethanol decomposition reaction (Equation 4.8 and 4.10). The negligible amount of CO produced can be due to the water gas shift reaction (Equation 4.3) that reforms CO to CO_2 and H_2.

Many by-products are identified in the analysis of the condensates: acetic acid, acetone, acetaldehyde, ethyl acetate, and unreacted ethanol. It must be mentioned that ethyl acetate may be produced from the esterification reaction between unreacted ethanol and acetic acid produced from equations 4.9 and 4.22. Among the four catalysts, only $5Cu/Co_6Al_2$ exhibits nearly a total conversion of ethanol with the highest hydrogen productivity (54 $mmol.h^{-1}.g^{-1}_{cata}$) at 450°C.

4.3.2.3 Activity of $1Ru/Co_xMg_{6-x}Al_2$ at 450°C in ESR

H_2, CO_2, CH_4 and CO productivities for $1Ru/Co_xMg_{6-x}Al_2$ are represented in figure 4.8 at a temperature of 450°C during 4 hours and a steam/carbon of 1.5. In the presence of ruthenium as an active phase, hydrogen productivity is also higher than that obtained for supports alone. By comparing the results to the copper-based catalysts, it can be seen that H_2, CO_2 and CH_4 productivities for $1Ru/Co_4Mg_2Al_2$ and $1Ru/Co_2Mg_4Al_2$ are higher than the ones obtained in the presence $5Cu/Co_4Mg_2Al_2$ and $5Cu/Co_2Mg_4Al_2$. However, $5Cu/Co_6Al_2$ catalyst remains the best catalyst among the prepared ones because it presents the highest H_2.

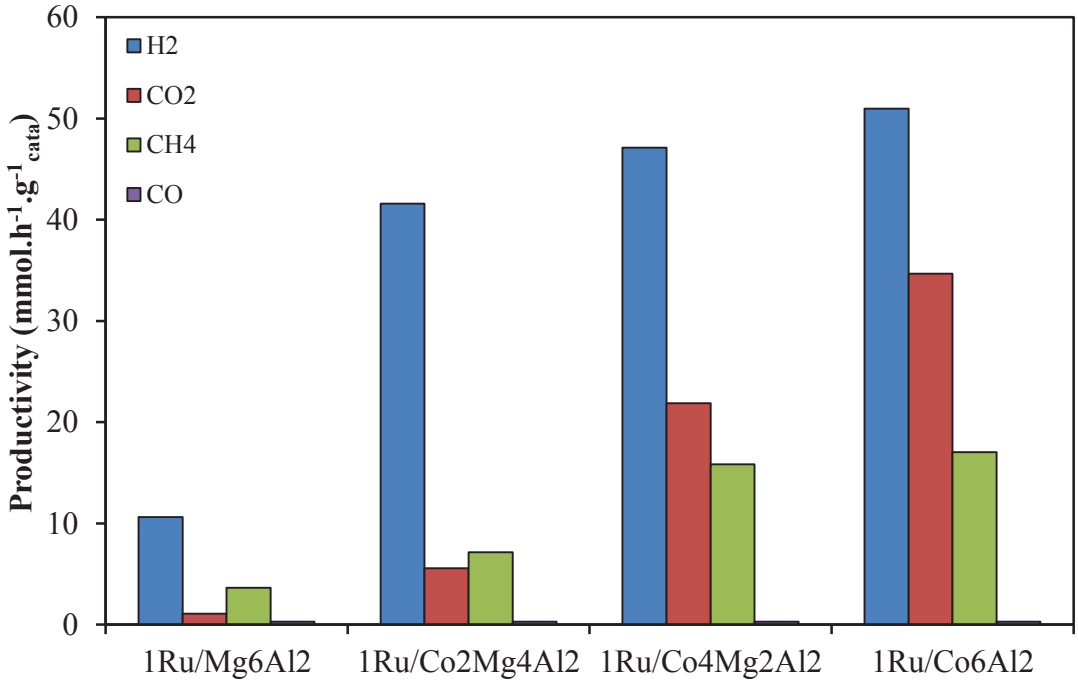

Figure 4.8 H_2, CO_2, CH_4 and CO productivity (mmol.h^{-1}.g$^{-1}_{cata}$) at 450°C in the presence of (a) 1Ru/Co_6Al_2 (b) 1Ru/$Co_4Mg_2Al_2$ (c) 1Ru/$Co_2Mg_4Al_2$ (d) 1Ru/Mg_6Al_2 calcined catalysts (S/C= 1.5)

The condensates analysis for 1Ru/$Co_xMg_{6-x}Al_2$ catalysts shows that acetic acid, acetone, acetaldehyde and unreacted ethanol are the main by-products. Acetic acid is absent for 1Ru/Mg_6Al_2 while it is present for all cobalt-containing catalysts. Ethanol is totally converted for 1Ru/Co_6Al_2 and 1Ru/$Co_4Mg_2Al_2$ whereas it is around 85% converted for the 2 other catalysts. By comapring the ruthenium-based catalysts result to that found in literature in the presence of 1Ru/Al_2O_3 catalyst, higher ethanol conversion was obtained in the presence of the hydrotalcite supports. In fact, 1Ru/Al_2O_3 showed at 800°C and under a S/C= 1.5, 42% conversion of ethanol [11, 73].

4.3.3 Influence of the Steam/Carbon Ratio

In general, it is known that the increase of the steam/carbon ratio is beneficial to increase hydrogen productivity and decrease coke and by-products formation [11, 22, 249, 250]. Therefore, two more steam/carbon ratios are used in order to study the influence of this ratio on the catalytic performance of $5Cu/Co_6Al_2$: 0.75 and 3. Results are illustrated in figure 4.9.

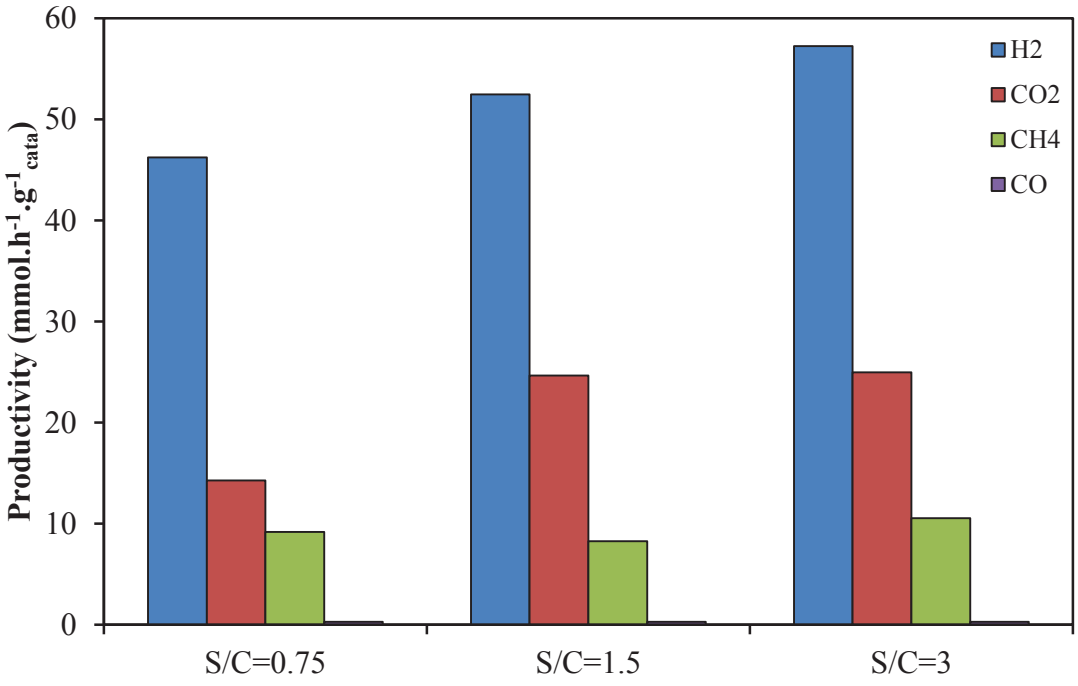

Figure 4.9 H_2, CO_2, CH_4 and CO productivity ($mmol.h^{-1}.g^{-1}_{cata}$) at 450°C in the presence of $5Cu/Co_6Al_2$ under S/C ratios of 0.75, 1.5 and 3

Higher amount of hydrogen and carbon dioxide are obtained with the increase of the steam/carbon ratio. Methane productivity is almost the same with the three different ratios and CO is produced in negligible quantities. These performances can be attributed to the WGS as it strongly moves towards the CO_2 and H_2 formation as a consequent of the presence of higher amount of H_2O leading to the decrease of the CO concentration in the outlet stream. On the other hand, whatever the amount of

water introduced, ethanol is completely converted, and traces of intermedate products are detected. Furthermore, Ting Dong et al. reported that above a steam/carbon equal to 4, no distinct influence on the selectivity was observed [250].

4.3.4 Influence of the Active Phase Content

In order to see the effect of metal loading on the catalytic performance, different copper loadings of 0.5, 3, 5, 15 and 25 wt.% are impregnated on Co_6Al_2 and tested in the ESR reaction under a stoichiometric steam/carbon ratio of 1.5 at 450°C during 4 hours. Results are shown in figure 4.10.

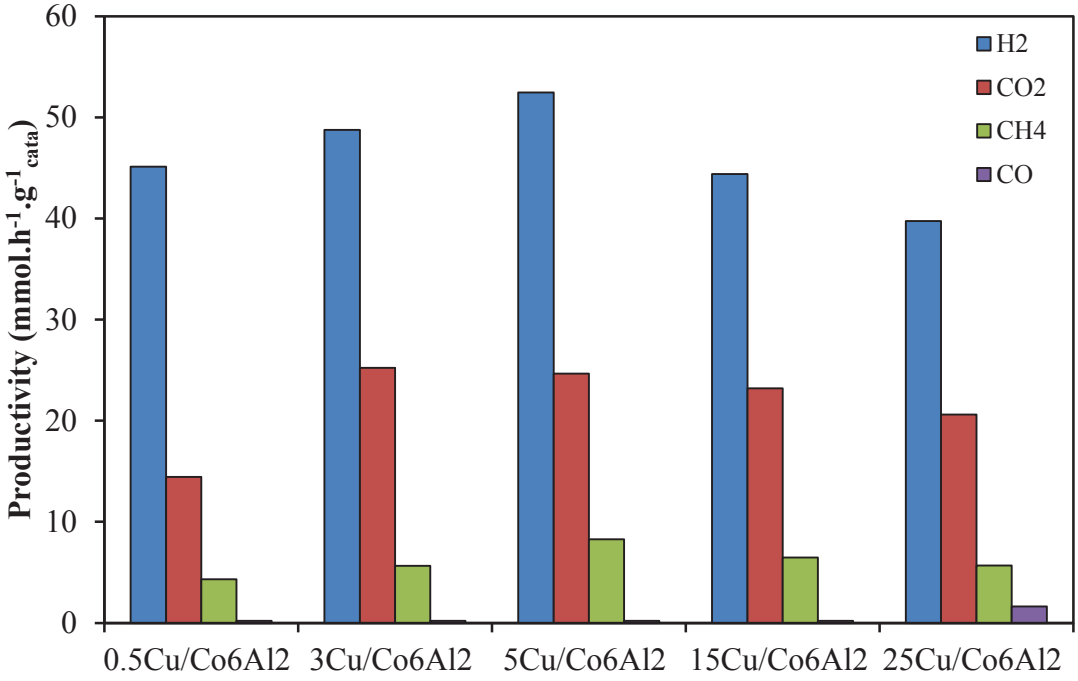

Figure 4.10 H_2, CO_2, CH_4 and CO productivity (mmol.h^{-1}.g$^{-1}_{cata}$) at 450°C in the presence of Cu/Co_6Al_2 with different copper loadings of 0.5, 3, 5, 15 and 25 wt.% (S/C= 1.5)

First of all, hydrogen productivity increases with the increase of metal content up to 5%, then it falls with higher contents. Produced carbon dioxide displays the same trend except for $5Cu/Co_6Al_2$ and $3Cu/Co_6Al_2$ that exhibit similar CO_2 amount.

Methane obtained is almost equal for all the catalysts except for 5Cu/Co_6Al_2 that shows higher amount. It must be noted that 25Cu/Co_6Al_2 presents the highest amount of CO compared to all other catalysts. The decrease in the catalytic performance with the increase of metal loadings is due to copper agglomerates present for 15Cu/Co_6Al_2 and 25Cu/Co_6Al_2 catalysts (section 2.4.3).

In literature, it is known that an increase in copper loading can improve ethanol dehydrogenation in detriment of its dehydration to a certain extent; and higher copper content reduces ethanol conversions, which may be due to a reduction in total surface area making the catalyst less active [69]. Concerning condensates analysis, 100% of ethanol is converted for all the catalysts that present traces of acetaldehyde except 0.5Cu/Co_6Al_2 that shows important amount of acetaldehyde and acetone.

It is concluded that 5wt.% Cu loading is the optimal metal loading due to the high hydrogen productivity and ethanol conversion.

4.3.5 Catalyst stability testing

The activity and stability of 5Cu/Co_6Al_2 and 5Cu/$Co_2Mg_4Al_2$ catalysts are examined for a period of 50 h at 450°C under a S/C=1.5 (figure 4.11 and 4.12 respectively). 5Cu/Co_6Al_2 catalyst deactivates after 20 hours whereas 5Cu/$Co_2Mg_4Al_2$ shows a higher stability over the desired period eventhough a decrease in the productivity of H_2 is visibly seen for this later. A possible reason for the deactivation could be the loss of active phase area due to the blocking of the metal surface sites by carbonaceous deposits. Whereas lower amount of these deposits may be formed in the case of 5Cu/$Co_2Mg_4Al_2$ because of the basic character of the catalyst leading to a higher resistance to deactivation. It must be noted that 5Cu/Co_6Al_2 catalyst that showed 100% ethanol conversion in the test operating at 450°C for 3 hours, presents

only 86% of ethanol conversion after 50 hours of the reaction. This is due to the deactivation that decreases ethanol conversion during the reaction.

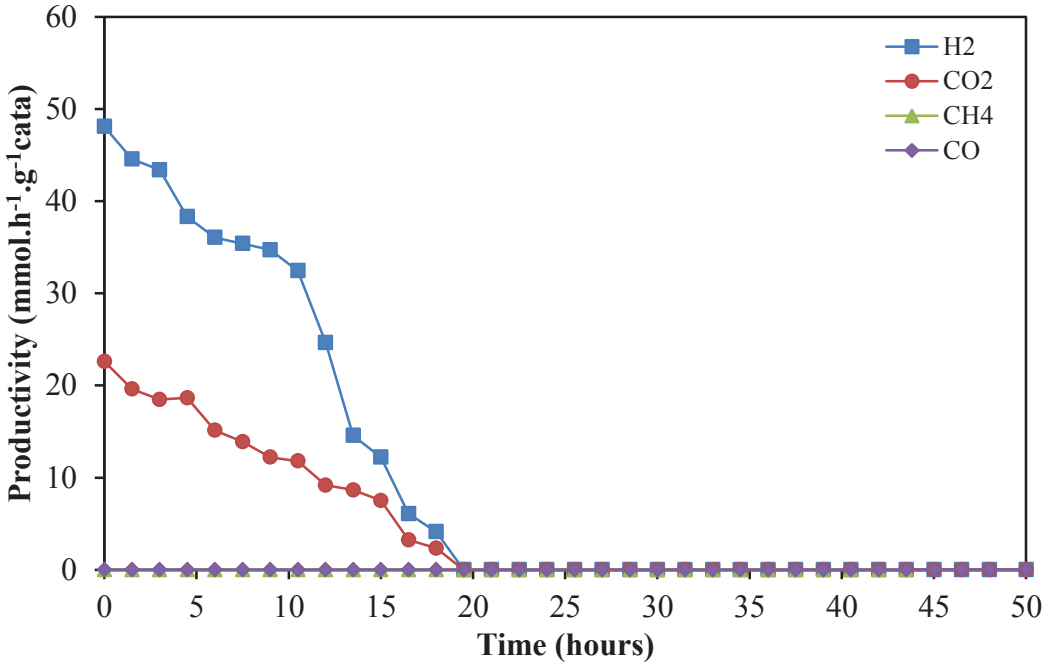

Figure 4.11 Evolution of H_2, CO_2, CH_4 and CO productivity (mmol.h^{-1}.g^{-1}_{cata}) in the presence of 5Cu/Co_6Al_2 as a function of time (50 h at 450°C) using a S/C= 1.5

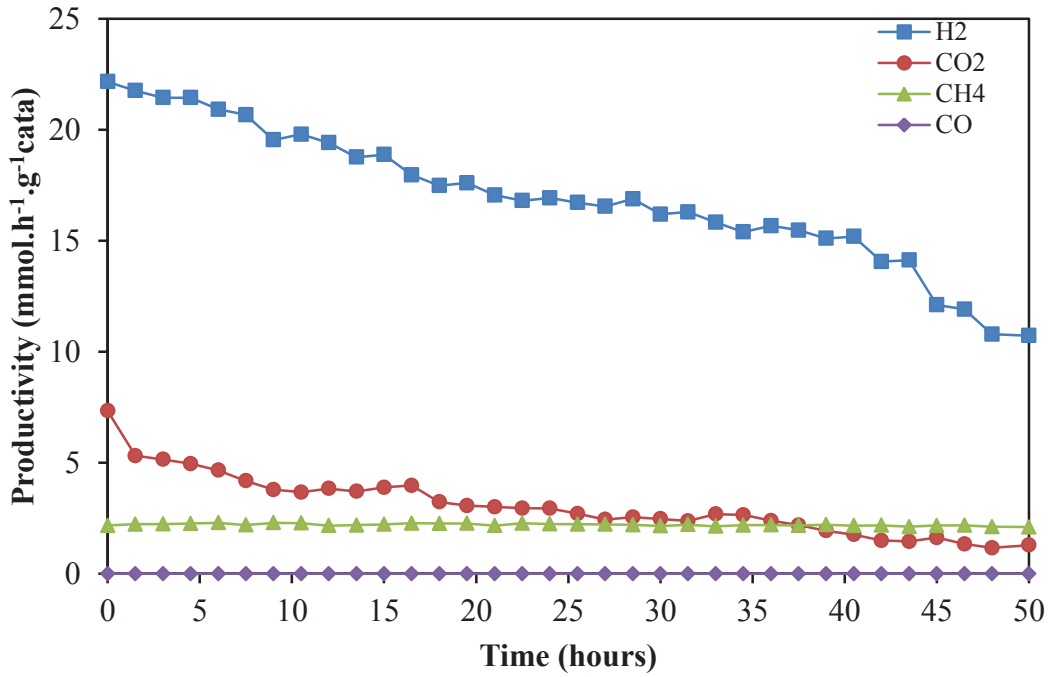

Figure 4.12 Evolution of H_2, CO_2, CH_4 and CO productivity (mmol.h^{-1}.g^{-1}_{cata}) in the presence of 5Cu/$Co_2Mg_4Al_2$ as a function of time (50 h at 450°C) using a S/C= 1.5

4.4 Charaterization of the Used Solids

In general, the following issues need to be taken into consideration during the ethanol steam reforming reaction: (1) reforming should preferably be carried out at low temperatures and atmospheric pressures to reduce the operating costs and enhance the WGS reaction; (2) the catalyst should provide high selectivity to hydrogen and inhibit carbon monoxide formation and the formation of by-products should be as minimum as possible; (3) the catalyst must resist to coke formation which deactivates the catalyst by reducing the number of active sites and hence the reaction rates. In order to check the oxidation states of the active species and the formation of coke during the reaction, DSC/TG, XRD and EPR characterization techniques were carried out on used samples.

4.4.1 DSC/TG Analysis for 1Ru/Co_6Al_2, 5Cu/Co_6Al_2 and 5Cu/$Co_2Mg_4Al_2$ After Ethanol Steam Reforming Reaction

Figures 4.13a and 4.13b represent the DSC/TG analysis obtained for 5Cu/Co_6Al_2 and 5Cu/$Co_2Mg_4Al_2$ catalysts after an aging test for 50 hours at 450°C. Whereas figures 4.13c and 4.13d showed the DSC/TG curves for 5Cu/Co_6Al_2 and 1Ru/Co_6Al_2 catalysts after a test at 450°C for 3 hours.

First, the catalysts based on Co_6Al_2 support shows an exothermic peak and a weight gain around 200°C. This is due to the re-oxidation of the reduced species during the reaction. Two other exothermic peaks with a corresponding weight loss at higher temperatures (between 300°C and 360°C) are noticed for the catalysts after the aging test These peaks are due to a two-stage oxidation of graphitic carbon deposited on different environment of the catalyst during the reaction. In fact, the first exothernic peak is associated to a fast oxidation of carbon present at the surface of the

catalyst while the second corresponds to a slow oxidation process due to some difficulties for oxygen to penetrate into the catalyst [47, 251, 252] because a part of the graphitic carbon are located inside the catalyst (in the bulk).

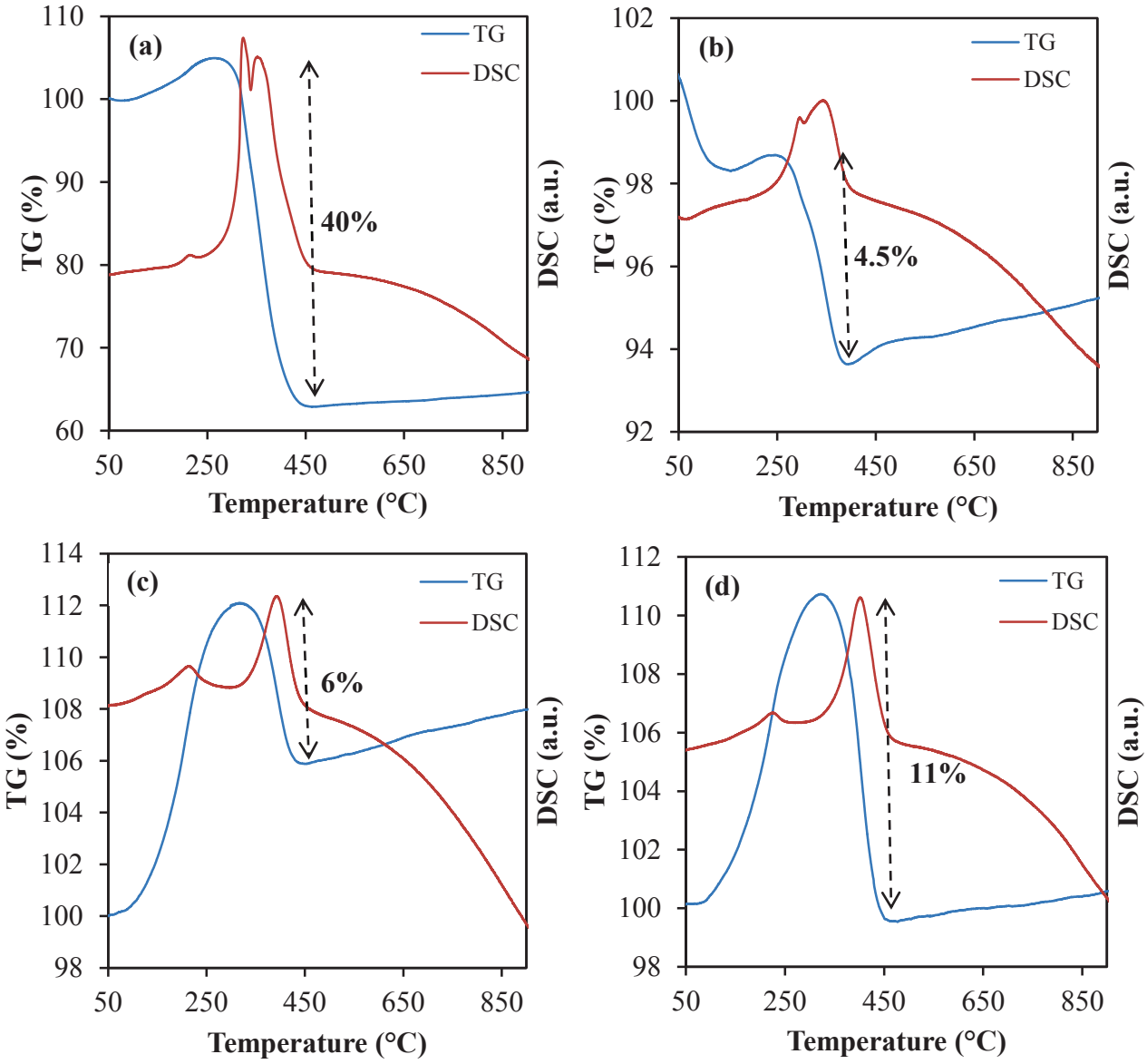

Figure 4.13 DSC/TG curves obtained during the oxidation of (a) 5Cu/Co_6Al_2 (b) 5Cu/$Co_2Mg_4Al_2$ after aging test at 450°C and (c) 5Cu/Co_6Al_2 (d) 1Ru/Co_6Al_2 after test at 450°C for 3 hours

However, only one peak is seen in the case of the two other ordinary tests. It must be noted that an important difference is seen in the weight loss between $5Cu/Co_6Al_2$ (40%) and $5Cu/Co_2Mg_4Al_2$ (4.5%) after aging test (figures 4.13a,b). Therefore, the amount of coke deposited on $5Cu/Co_6Al_2$ is much more higher than that formed on $5Cu/Co_2Mg_4Al_2$. This big quantity of coke can explain the reason for the deactivation of $5Cu/Co_6Al_2$ after only 20 hours of the test. On the other hand, $5Cu/Co_2Mg_4Al_2$ that did not show an important amount of carbon species or a deactivation even after 50 hours, contains MgO and $MgAl_2O_4$. These magnesium oxides are well-known for their basic properties [195]. Their presence allows CO_2 adsorption on the catalyst and hence, decreases carbon deposit.

As suggested in literature [195], carbon deposit can be attenuated or removed if the metal responsible for the catalytic activity is supported on an oxide showing strong basic sites. In addition, it can be seen that the amount of carbon species formed in the case of $1Ru/Co_6Al_2$ (6%) is lower than that of $5Cu/Co_6Al_2$ (11%) during the 3 hours reaction (figures 4.13c, d) indicating a better resistance to carbon deposition in the case of Ru compared to Cu.

4.4.2 XRD Analysis for Mg_6Al_2, $5Cu/Mg_6Al_2$ and $1Ru/Mg_6Al_2$ After Ethanol Steam Reforming Reaction

XRD patterns for Mg_6Al_2, $5Cu/Mg_6Al_2$ and $1Ru/Mg_6Al_2$ after ethanol steam reforming reaction at 450°C are illustrated in figure 4.14.

First, it can be noticed that no lines attributed to metallic copper or ruthenium are seen which can be due to small reduced quantity formed during the reaction not detected by XRD. Moreover, intense lines attributed to MgO (JCPDS N°45-0946), $MgAl_2O_4$ (JCPDS N°73-1959) phases are still present after the reaction and

reflections corresponding to graphitic carbon (JCPDS N°75-1621) are detected for the three solids. Finally, hydrotalcite structure reappears after the reaction indicating that it was reconstructed during the ethanol steam reforming reaction. As seen in literature, the reconstruction or “memory effect” is more important for supports with high Mg content [111].

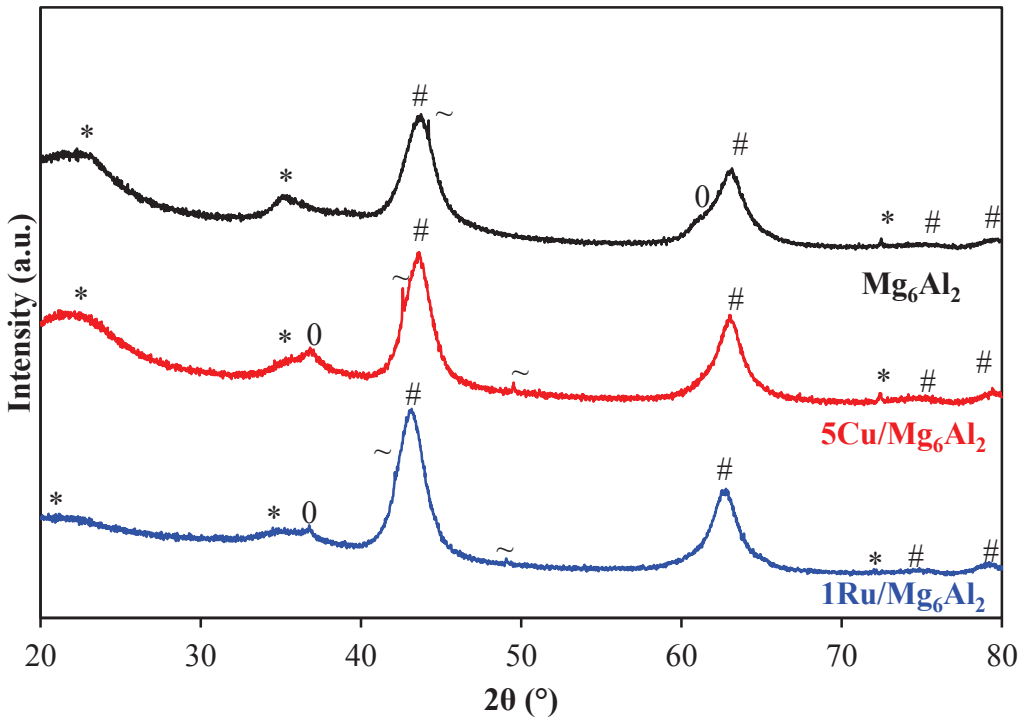

Figure 4.14 XRD analysis for Mg_6Al_2, 5Cu/Mg_6Al_2 and 1Ru/Mg_6Al_2 catalysts after ethanol steam reforming test at 450°C. “*” Hydrotalcite phase (JCPDS N°22-0700), “#” MgO periclase (JCPDS N°45-0946), “0” $MgAl_2O_4$ spinel (JCPDS N°73-1959) and "~ " graphitic carbon (JCPDS N°75-1621)

4.4.3 EPR Analysis of Ruthenium and Copper-Based Catalysts After Ethanol Steam Reforming Reaction

EPR spectra recorded at ambient temperature after ethanol steam reforming reaction at 450°C (for 3 hours and S/C=1.5) in the presence of magnesium containing solids (Mg_6Al_2, $5Cu/Mg_6Al_2$ and $1Ru/Mg_6Al_2$) are displayed in figure 4.15.

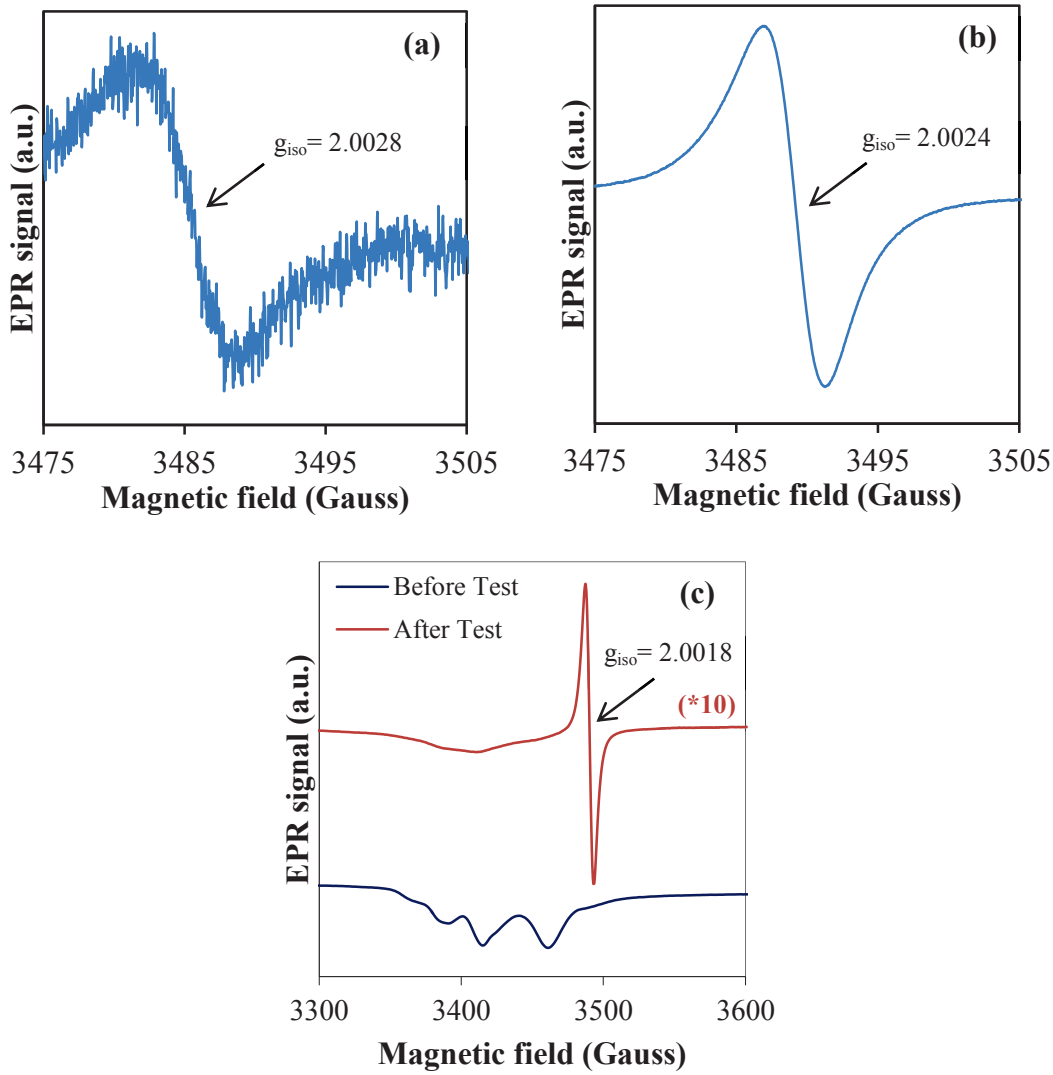

Figure 4.15 EPR spectra for (a) Mg_6Al_2 (b) $1Ru/Mg_6Al_2$ (c) $5Cu/Mg_6Al_2$ recorded at ambient temperature after ethanol steam reforming reaction at 450°C for 3 hours

An isotropic signal centered at g= 2.0028, 2.0024 and 2.0018 for Mg_6Al_2, $1Ru/Mg_6Al_2$ and $5Cu/Mg_6Al_2$ respectively is recorded. It can be attributed to the presence of carbon species formed at the surface of the catalyst during the reaction confirming the results obtained in the XRD analysis (section 4.4.2). In addition, the intensity of Cu^{2+} species decreases after the reaction indicating the decrease of the number of Cu^{2+} species due to the reduction of Cu^{2+} to Cu^{+} and Cu^{0}.

4.5 Conclusion

Ethanol steam reforming reaction was studied in the presence of ruthenium and copper-based catalysts supported on $Co_{6-x}Mg_xAl_2$ oxides. The influence of some parameters was presented (influence of the nature of the support, influence of the nature of active phase and its content, steam/carbon ratio, stability over time). The best catalyst among the prepared solids was $5Cu/Co_6Al_2$ due to the complete ethanol conversion (at 450°C) and the highest hydrogen and carbon dioxide productivities. It showed a better activity than the ruthenium-based catalysts. However, an aging test for 50 hours deactivated this catalyst due to the formation of high amount of carbonaceous products seen by the DSC/TG technique. On the other hand, $5Cu/Co_2Mg_4Al_2$ showed a much lower quantity of carbon species instead of deactivating during the aging test due to the basic character of the magnesium oxide phase detected by XRD. But at the same time, lower hydrogen amount is produced in the case of this catalyst.

GENERAL CONCLUSION

In the present study, Co/Mg/Al hydrotalcites have been investigated as supports on which copper or ruthenium active metals are impregnated and tested in methane and ethanol steam reforming reactions.

First, it was demonstrated that a partial reconstruction of the hydrotalcite structure during the impregnation step of the active phase is detected especially for solids with high Mg amount due to the basic properties of the support. In addition, the analyses of the specific surface area showed an increase in the S_{sp} after calcination due to the destruction of the hydrotalcite phase.

XRD and TPR analyses revealed an interaction between the active phase and supports rich in cobalt. The presence of copper and ruthenium oxides decreases the reduction temperature of $Co_xMg_{6-x}Al_2$ solids due to the incorporation of metals enhancing the reducibility of the cobalt ions. Also, these analyses showed two kinds of active phase: agglomerates and dispersed species in interaction with the support. The formation of agglomerates was observed for higher ruthenium and copper content leading to a decrease in the specific surface area. The higher calcination temperature led to a weakness of the interaction between Co and active phase.

EPR analysis showed the formation of Ru^+ species that were easily reduced in the case of $1Ru/Mg_6Al_2$. Two types of isolated copper (II) species are detected for $5Cu/Mg_6Al_2$: the first one is located in the bulk in octahedral sites that is not easily reduced and the other at the surface in tetrahedral sites that is primarily reduced.

The influence of different parameters was reported in the methane steam reforming reaction: influence of the nature of the support, influence of the active phase and its content, calcination temperature, treatment, GHSV, H_2O/CH_4. A H_2O/CH_4 ratio higher than the stoichiometry seems to be necessary to enhance the methane conversion. The optimum metal content for the ruthenium and copper active phases were 1wt.% and 5wt.%

respectively as higher metal loadings caused the problem of agglomerate formation. Furthermore, it was demonstrated that the catalytic performance was higher with the increase of the cobalt content and $1Ru/Co_6Al_2$ catalyst had the best catalytic activity among all the other prepared catalysts even with no hydrogen pretreatment. Reduced ruthenium and cobalt were observed after the reaction. $1Ru/Co_6Al_2$ also exhibits a constant stability during 100 hours under extreme conditions. In addition, high reactivity was observed for the prepared catalysts compared to the industrial one tested under the same operating conditions. The presence of coke was not observed using TPO, XRD, DSC/TG due to its presence in low quantities undetectable in the range of these techniques. However, EPR was able to detect and differentiate between two kinds of carbonaceous species: carbon formed during Boudouard reaction and coke formed during the methane decomposition reaction.

Concerning ethanol steam reforming reaction, $5Cu/Co_6Al_2$ catalysts presented the highest produced amount of hydrogen and carbon dioxide among all the other catalysts. However, it directly deactivated after 20 hours aging test due to the high amount of carbonaceous products seen by the DSC/TG technique. On the other hand, $5Cu/Co_2Mg_4Al_2$ showed a much lower quantity and it did not deactivate during the aging test due to the basic character of the magnesium oxide phase detected by XRD but it produced lower hydrogen amount than $5Cu/Co_6Al_2$. Therefore, $5Cu/Co_4Mg_2Al_2$ catalyst could be a good compromise between a high activity and low carbonaceous deposition. In addition, undesirable products detected from the condensate analysis interfered in the process of ESR for all the studied catalysts like the formation of acetone, acetaldehyde, acetic acid and ethyl acetate. Consequently, the development of a catalyst which could operate at lower temperatures and avoid the formation of by-products and carbon is a current goal of research.

Finally, some suggestions presented below would contribute to the improvement of this study. First, a partial oxidation reaction and a kinetic study could be achieved on both reactions. In addition, it would be necessary to perform measurements on the studied samples to evaluate their acid-base sites, and chemisorption studies to determine the dispersion of the active species.

LIST OF REFERENCES

[1] C. Baird, M. Cann (2008). Environmental Chemistry. New York: W.H. Freeman and Company

[2] S.M. Kotay, D. Das, Biohydrogen as a renewable energy resource-prospects and potentials, International Journal of Hydrogen Energy, 33 (2008) 258-263

[3] V. Palma, F. Castaldo, P. Ciambelli, G. Iaquaniello, (2012), Sustainable hydrogen production by catalytic bio-ethanol steam reforming, Retrieved from http://www.intechopen.com/books/greenhouse-gases-capturing-utilization-and-reduction/sustainable hydrogen-production-by-catalytic-bio-ethanol-steam-reforming

[4] A. Fonseca, E.M. Assaf, Production of the hydrogen by methane steam reforming over nickel catalysts prepared from hydrotalcite precursors, Journal of Power Sources, 142 (2005) 154-159

[5] S. Rasi, A. Veijanen, J. Rintala, Trace compounds of biogas from different biogas production plants, Energy, 32 (2007) 1375-1380

[6] R.B. Gupta (2009). Production of Hydrogen from Hydrocarbons, in Hydrogen Fuel: Production, Transport and Storage, Boca Raton: CRC Press

[7] R.P.J.M. Raven, K.H. Gregersen, Biogas plants in Denmark: successes and setbacks, Renewable and Sustainable Energy Reviews, 11 (2007) 116-132

[8] A. Denis, W. Grzegorczyk, W. Gac, A. Machocki, Steam reforming of ethanol over Ni/support catalysts for generation of hydrogen for fuel cell applications, Catalysis Today, 137 (2008) 453-459

[9] M. Constant, H. Naveau, G.L. Ferrero, E.J. Nyns, (1989). Biogas: End Use in the European Community. New York: Elsevier Science Publishing Co

[10] T. Caillot, P. Gelin, J. Dailly, G. Gauthier, C. Cayron, J. Laurencin, Catalytic steam reforming of methane over $La_{0.8}Sr_{0.2}CrO_3$ based Ru catalysts, Catalysis Today, 128 (2007) 264-268

[11] L. Zhou, Y. Guo, Q. Zhang, M. Yagi, H.B. Li, J. Chen, Self-activation and self-regenerative activity of trace Ru-doped plate-type anodic alumina supported nickel catalysts in steam reforming of methane, Catalysis Communication, 10 (2008) 325-329

[12] J.G. Jakobsen (2010). Noble metal catalysts for methane steam reforming. Technical University of Denmark

[13] S. Cavallaro, S. Freni, Ethanol steam reforming in a molten carbonate fuel cell. A preliminary kinetic investigation, International Journal of Hydrogen Energy, 21 (1996) 465-469

[14] M. Ni, D.Y.C. Leung, M.K.H. Leung, A review on reforming bio-ethanol for hydrogen production, International Journal of Hydrogen Energy, 32 (2007) 3238-3247

[15] Y. Zhan, D. Li, K. Nishida, T. Shishido, Y. Oumi, T. Sano, K. Takehira, Preparation of “intelligent” Pt/Ni/Mg(Al)O catalysts starting from commercial Mg-Al LDHs for daily start-up and shut-down steam reforming of methane, Applied Clay Science, 45 (2009) 147-154

[16] G. Busca, U. Costantino, T. Montanari, G. Ramis, C. Resini, M. Sisani, Nickel versus cobalt catalysts for hydrogen production by ethanol steam reforming: Ni-Co-Zn-Al catalysts from hydrotalcite-like precursors, International Journal of Hydrogen Energy, 35 (2010) 5356-5366

[17] F. Aupretre, C. Descorme, D. Duprez., Bio-ethanol catalytic steam reforming over supported metal catalysts, Catalysis Communications, 3 (2002) 263-267

[18] A.B. Stambouli, E. Traversa, Fuel cells, an alternative to standard sources of energy, Renewable and Sustainable Energy Reviews, 6 (2002) 295-304

[19] M.S. Batista, R.K.S. Santos, E.M. Assaf, J.M. Assaf, E.A. Ticianelli, Characterization of the activity and stability of supported cobalt catalysts for the steam reforming of ethanol, Journal of Power Sources, 124 (2003) 99-103

[20] J. Wee, Applications of proton exchange membrane fuel cell systems, Renewable and Sustainable Energy Reviews, 11 (2007) 1720-1738

[21] M. Momirlan, T.N. Veziroglu, The properties of hydrogen as fuel tomorrow in sustainable energy system for a cleaner planet, International Journal of Hydrogen Energy, 30 (2005) 795-802

[22] C-B. Wang, C-C. Lee, J-L. Bi, J-Y. Siang, J-Y. Liu, C-T. Yeh, Study on the steam reforming of ethanol over cobalt oxides, Catalysis Today, 146 (2009) 76-81

[23] A.N. Fatsikostas, X.E. Verykios, Reaction network of steam reforming of ethanol over Ni-based catalysts, Journal of Catalysis, 225 (2004) 439-452

[24] J. Xuan, M.K.H. Leung, D.Y.C. Leung, M. Ni, A review of biomass-derived fuel processors for fuel cell systems, Renewable and Sustainable Energy Reviews, 13 (2009) 1301-1313

[25] H. Katuwal, A.K. Bohara, Biogas: A promising renewable technology and its impact on rural households in Nepal, Renewable and Sustainable Energy Reviews, 13 (2009) 2668-2674

[26] P. Sabatier, J.B. Senderens, Comptes Rendues Academe des Sciences, 134 (1902) 514

[27] B. Neumann, K. Jacob, Z. Electrochem., 30 (1924) 557

[28] S. Freni, G. Calogero, S. Cavallaro, Hydrogen production from methane through catalytic partial oxidation reactions, Journal of Power Sources, 87 (2000) 28-38

[29] T. Rostrup-Nielsen, Manufacture of hydrogen, Catalysis Today, 106 (2005) 293-296

[30] Q. Zhu, X. Zhao, Y. Deng, Advances in the partial oxidation of methane to synthesis gas, Journal of Natural Gas Chemistry, 13 (2004) 191-203

[31] J.R. Rostrup-Nielsen, Activity of nickel catalysts for steam reforming of hydrocarbons, Journal of Catalysis, 31 (1973) 173-199

[32] Q. Zhuang, Y. Qin, L. Chang, Promoting effect of cerium oxide in supported nickel catalyst for hydrocarbon steam-reforming, Applied Catalysis, 70 (1991) 1-8

[33] P.A.A. Adesina, D.L. Trimm, N.W. Cant, Kinetic study of iso-octane steam reforming over a nickel-based catalyst, Chemical Engineering Journal, 99 (2004) 131-136

[34] C. Pistonesi, A. Juan, B. Irigoyen, N. Amadeo, Theoretical and experimental study of methane steam reforming reactions over nickel catalyst, Applied Surface Science, 253 (2007) 4427-4437

[35] X. Zhai, S. Ding, Z. Liu., Y. Jin, Y. Cheng, Catalytic performance of Ni catalysts for steam reforming of methane at high space velocity, International Journal of Hydrogen Energy, 36 (2011) 482-489

[36] S.M. Hashemnejad, M. Parvari, Deactivation and regeneration of nickel-based catalysts for steam methane reforming, Chinese Journal of Catalysis, 32 (2011) 273-279

[37] K. Kusakabe, K.I. Sotowa, T. Eda, Y. Iwamoto, Methane steam reforming over Ce-ZrO_2-supported noble metal catalysts at low temperature, Fuel Processing Technology, 86 (2004) 319-326

[38] W. Shan, M. Fleys, F. Lapicque, D. Swierczynski, A. Kiennemann, Y. Simon, P.M. Marquaire, Syngas production from partial oxidation of methane over $Ce_{1-x}Ni_xO_y$ catalysts prepared by complexation-combustion method, Applied Catalysis A: General, 311 (2006) 24-33

[39] T. Ohi, T. Miyata, D. Shishido, T. Li, T. Kawabata, T. Sano, K. Takehira, Sustainability of Ni loaded Mg-Al mixed oxide catalyst in daily startup and shut down operations of CH_4 steam reforming, Applied Catalysis A: General, 308 (2006) 194-203

[40] J. Rostrup-Nielsen, J.B. Hansen, CO_2 reforming of methane over transition metals, Journal of Catalysis, 144 (1993) 38-49

[41] T. Mizuno, T. Nakajima, A stable catalyst for hydrogen production by steam reforming of 2-propanol: Rh/Al_2O_3, Journal of Chemical Engineering of Japan, 35 (2002) 485-488

[42] E. Kikuchi, S. Tanaka, Y. Yamazaki, Y. Morita, Bulletin of the Japan Petroleum Institute, (1974) 95-98

[43] D. Qin, J. Lapszewicz, Study of mixed steam and CO_2 reforming of CH_4 to syngas on MgO-supported metals, Catalysis Today, 21 (1994) 551-560

[44] H. Al-Qahtani, Effect of aging on a steam reforming catalyst, Chemical Engineering Journal, 66 (1997) 51-56

[45] A. Berman, R.K. Karn, M. Epstein, Kinetics of steam reforming of methane on Ru/Al_2O_3 catalyst promoted with Mn oxides, Applied Catalysis A: General, 282 (2005) 73-83

[46] A.C. Basagiannis, X.E. Verykios, Influence of the carrier on steam reforming of acetic acid over Ru-based catalysts, Applied Catalysis B: Environmental, 82 (2008) 77-88

[47] S. Aouad (2007). Etudes des propriétés physico-chimiques et catalytiques des solides à base de ruthénium. Unpublished doctoral dissertation, Université du Littoral Côte d'Opale, Dunkerque

[48] D. Li, I. Atakea, T. Shishido, Y. Oumi, T. Sano, K. Takehira, Self-regenerative activity of Ni/Mg(Al)O catalysts with trace Ru during daily start-up and shut-down operation of CH_4 steam reforming, Journal of Catalysis 250 (2007) 299-312

[49] J.H. Jeong, J.W. Lee, D.J. Seo, Y. Seo, W.L. Yoon, D.K. Lee, D.H. Kim, Ru-doped Ni catalysts effective for the steam reforming of methane without the pre-reduction treatment with H_2, Applied Catalysis A: General, 302 (2006) 151-156

[50] R. Lanza, P. Canu, S.G. Jaras, Methane partial oxidation over Pt-Ru catalyst: An investigation on the mechanism, Applied Catalysis A: General, 375 (2010) 92-100

[51] V. Choque, N. Homs, R. Cicha-Szot, P. Ramirez de la Piscina, Study of ruthenium supported on Ta_2O_5-ZrO_2 and Nb_2O_5-ZrO_2 as catalysts for the partial oxidation of methane, Catalysis Today, 142 (2009) 308-313

[52] M. Safariamin (2010). Valorisation catalytique du biogaz (CH_4 + CO_2) par reformage à sec: étude des propriétés physico-chimiques et catalytiques de solides à base de ruthénium et cuivre. Unpublished doctoral dissertation, Université du Littoral Côte d'Opale, Dunkerque

[53] A.M. Rakib (2012). Valorisation du méthane en hydrogène par reformage catalytique. Unpublished doctoral dissertation, Université du Littoral Côte d'Opale, Dunkerque

[54] S. Saa, H. Silva, L. Brandaoa, J.M. Sousaa, A. Mendes, Catalysts for methanol steam reforming-A review, Applied Catalysis B: Environmental, 99 (2010) 43-57

[55] A. Bshish, Z. Yaakob, B. Narayanan, R. Ramakrishnan, A. Ebshish, Steam-reforming of ethanol for hydrogen production, Chemical Papers, 65 (2011) 251-266

[56] H. Laversin, D. Courcot, E.A. Zhilinskaya, R. Cousin, A. Aboukaïs, Study of active species of Cu-K/ZrO catalysts involved in the oxidation of soot, Journal of Catalysis, 241 (2006) 456-464

[57] N. Tien-Thao, H. Alamdari, M.H. Zahedi-Niaki, S. Kaliaguine, $LaCo_{1-x}Cu_xO_{3-\delta}$ perovskite catalysts for higher alcohol synthesis, Applied Catalysis A: General, 311 (2006) 204-212

[58] T.V. Reshetenko, L.B. Avdeeva, Z.R. Ismagilov, A.L. Chuvilin, V.A. Ushakov, Carbon capacious Ni-Cu-Al_2O_3 catalysts for high-temperature methane decomposition, Applied Catalysis A: General, 247 (2003) 51-63

[59] T.J. Huang, T.C. Yu, S.Y. Jhao, Weighting variation of water-gas shift in steam reforming of methane over supported Ni and Ni-Cu catalysts, Industrial & Engineering Chemistry Research, 45 (2006) 150-156

[60] J. Knudsen, A.U. Nilekar, R.T. Vang, J. Schnadt, E.L. Kunkes, J.A. Dumesic, M. Mavrikakis, F. Besenbacher, A Cu/Pt near-surface alloy for water-gas shift catalysis, Journal of the American Chemistry Society, 129 (2007) 6485-6490

[61] G.R. Morado, F. Khosravian, M. Rahmanzadeh, Effects of partial substitution of Ni by Cu in $LaNiO_3$ perovskite catalyst for dry methane reforming, Chinese Journal of Catalysis, 33 (2012) 797-801

[62] F.S. Toniolo, R.N.S.H. Magalhaes, C.A.C. Perez, M. Schmal, Structural investigation of $LaCoO_3$ and $LaCoCuO_3$ perovskite-type oxides and the effect of Cu on coke deposition in the partial oxidation of methane, Applied Catalysis B: Environmental, 117-118 (2012) 156-166

[63] J.R. Rostrup-Nielsen, J. Schested, Hydrogen and synthesis gas by steam and CO_2 reforming, Advances in Catalysis, 47 (2002) 65-139

[64] F. Melo, N. Morlanes, Synthesis, characterization and catalytic behaviour of NiMgAl mixed oxides as catalysts for hydrogen production by naphtha steam reforming, Catalysis Today, 133-135 (2008) 383-393

[65] M.H. Halabi, M.H.J.M. de Croon, J. Van der Schaaf, P.D. Cobden, J.C. Schouten, Low temperature catalytic methane steam reforming over ceria-zirconia supported rhodium, Applied Catalysis A: General, 389 (2010) 68-79

[66] J. Sun, X. Qiu, F. Wu, W. Zhu, W. Wang, S. Hao, Hydrogen from steam reforming of ethanol in low and middle temperature range for fuel cell application, International Journal of Hydrogen Energy, 29 (2004) 1075-1081

[67] Y. Yang, J. Ma, F. Wu, Production of hydrogen by steam reforming of ethanol over a Ni/ZnO catalyst, International Journal of Hydrogen Energy, 31 (2006) 877-882

[68] M. Benito, J.L. Sanz, R. Isabel, R. Padilla, R. Arjona, L. Daza, Bio-ethanol steam reforming: Insights on the mechanism for hydrogen production, Journal of Power Sources, 151 (2005) 11-17

[69] A.J. Vizcaino, A. Carrero, J.A. Calles, Hydrogen production by ethanol steam reforming over Cu-Ni supported catalysts, International Journal of Hydrogen Energy, 32 (2007) 1450-1461

[70] P.D. Vaidya, A.E. Rodrigues, Insight into steam reforming of ethanol to produce hydrogen for fuel cells, Chemical Engineering Journal, 117 (2006) 39-49

[71] J.S. Moura, M.O.G. Souza, J.A. Bellido, E.M. Assaf, M. Opportus, P. Reyes, M.C. Rangel, Ethanol steam reforming over rhodium and cobalt-based catalysts: Effect of the support, International Journal of Hydrogen Energy, 37 (2012) 3213-3224

[72] J.S. Lisboa, D.C.R.M. Santos, F.B. Passos, F.B. Noronha, Influence of the addition of promoters to steam reforming catalysts, Catalysis Today, 101 (2005) 15-21

[73] D.K. Liguras, D.I. Kondarides, X.E. Verykios, Production of hydrogen for fuel cells by steam reforming of ethanol over supported noble metal catalysts, Applied Catalysis B: Environmental, 43 (2003) 345-354

[74] A.C.W. Koh, W.K. Leong, L.W. Chen, T.P. Ang, J. Lin, B.F.G. Johnson, Highly efficient ruthenium and ruthenium-platinum cluster-derived nanocatalysts for hydrogen production via ethanol steam reforming, Catalysis Communications, 9 (2008) 170-175

[75] A.C.W. Koha, L. Chenb, W.K. Leong, T.P. Ang, B.F.G. Johnson, T. Khimyak, J. Lin, Ethanol steam reforming over supported ruthenium and ruthenium-platinum catalysts: Comparison of organometallic clusters and inorganic salts as catalyst precursors, International Journal of Hydrogen Energy, 34 (2009) 5691-5703

[76] B.A. Raich, H.C. Foley, Ethanol dehydrogenation with a palladium membrane reactor: an alternative to wacker chemistry, Industrial and Engineering Chemistry Research, 37 (1998) 3888-3895

[77] F. Marino, G. Baronetti, M. Jobbagy, M. Laborde, Cu-Ni-K/γ-Al_2O_3 supported catalysts for ethanol steam reforming: Formation of hydrotalcite-type compounds as a result of metal-support interaction, Applied Catalysis A: General, 238 (2003) 41-54

[78] S. Velu, K. Suzuki, M. Vijayaraj, S. Barman, C.S. Gopinath, In situ XPS investigations of $Cu_{1-x}Ni_xZnAl$ mixed metal oxide catalysts used in the oxidative steam reforming of bio-ethanol, Applied Catalysis B: Environmental, 55 (2005) 287-299

[79] S. Freni, N. Mondello, S. Cavallaro, G. Cacciola, V.N. Parmon, V.A. Sobyanin, Hydrogen production by steam reforming of ethanol: a two Step process, reaction kinetics and catalysis letters, 71 (2000) 143-152

[80] A. Vaccari, Clays and catalysis: a promising future, Applied Clay Science, 14 (1999) 161-198

[81] C. Klein, C.S. Hurlbut, (1993). Manual of Mineralogy. NewYork: JohnWiley & Sons, Inc.

[82] Z.P. Xu, H.C. Zeng, A new approach for design and synthesis of Co II and Co II,III hydroxide materials, The International Journal of Inorganic Materials, 2 (2000) 187-196

[83] H. Tamura, J. Chiba, M. Ito, T. Takeda, S. Kikkawa, Y. Mawatari, M. Tabata, Formation of hydrotalcite in aqueous solutions and intercalation of ATP by anion exchange, Journal of Colloid and Interface Sciences, 300 (2006) 648-654

[84] V. Rives, Characterization of layered double hydroxides and their decomposition products, Materials Chemistry and physics, 75 (2002) 19-25

[85] J. Carpentier, J-F. Lamonier, S. Siffert, E. Zhilinskaya, A. Aboukaïs, Characterization of Mg/Al hydrotalcite with interlayer palladium complex for catalytic oxidation of toluene, Applied catalysis A: general, 234 (2002) 91-101

[86] F. Cavani, F. Trifiro, A. Vaccari, Hydrotalcites-type anionic clays: preparation, properties and applications, Catalysis Today, 11 (1991) 173-301

[87] D.L. Bish, G.W. Brindley, A reinvestigation of takovite, a nickel-aluminium hydroxy-carbonate of the pyroaurite group, American Mineralogist, 62 (1977) 458-464

[88] C. Gennequin, S. Kouassi, L. Tidahy, R. Cousin, J-F. Lamonier, G. Garcon, P. Shirali, F. Cazier, A. Aboukaïs, S. Siffert, Co-Mg-Al oxides issued of hydrotalcite precursors for total oxidation of volatile organic compounds. Identification and toxicological impact of the by-products, Comptes Rendus Chimie, 13 (2010) 494-501

[89] J.C.A.A. Roelofs, D.J. Lensveld, A.V. Dillen, K.P. De Jong, On the structure of activated hydrotalcites as solid base catalysts for liquid-phase aldol condensation, Journal of catalysis, 203 (2001) 184-191

[90] S. Wang, G.Q. Lu, CO_2 reforming of methane on Ni catalysts: effect of the support phase and preparation technique, Applied Catalysis B: Environmental, 16 (1998) 269-277

[91] M.S. Batista, R.K.S. Santos, E.M. Assaf, J.M. Assaf, E.A. Ticianelli, High efficiency steam reforming of ethanol by cobalt-based catalysts, Journal of Power Sources, 134 (2004) 27-32

[92] J.R.H. Ross, Natural gas reforming and CO_2 mitigation, Catalysis Today, 100 (2005) 151-158

[93] M. Johns, P. Collier, M.S. Spencer, T. Alderson, G.J. Hutchings, Combined steam reforming of methane and Fischer-Tropsch synthesis for the formation of hydrocarbons: a proof of concept study, Catalysis Letters, 90 (2003) 187-94

[94] A.F. Lucredio, E.M. Assaf, Cobalt catalysts prepared from hydrotalcite precursors and tested in methane steam reforming, Journal of Power Sources, 159 (2006) 667-672

[95] R. Guil-Lopez, R.M. Navarro, M.A. Pena, J.L.G. Fierro, Hydrogen production by oxidative ethanol reforming on Co, Ni and Cu ex-hydrotalcite catalysts, International Journal of Hydrogen Energy, 36 (2011) 1512-1523

[96] K. Urasaki, Y. Sekine, S. Kawabe, E. Kikuchi, M. Matsukata, Catalytic activities and coking resistance of Ni/perovskites in steam reforming of methane, Applied Catalysis A: General, 286 (2005) 23-29

[97] F. Frusteri, S. Freni, L. Spadaro, V. Chiodo, G. Bonura, S. Donato, S. Cavallaro, H_2 production for MC fuel cell by steam reforming of ethanol over MgO supported Pd, Rh, Ni and Co catalysts, Catalysis Communications, 5 (2004) 611-615

[98] S. Cavallaro, N. Mondello, S. Freni, Hydrogen produced from ethanol for internal reforming molten carbonate fuel cell, Journal of Power Sources, 102 (2001) 198-204

[99] J.P. Breen, R. Burch, H.M. Coleman, Metal-catalyzed steam reforming of ethanol in the production of hydrogen for fuel cell applications, Applied Catalysis B: Environmental, 39 (2002) 65-74

[100] P. Forzatti, L. Lietti, Catalyst deactivation, Catalysis Today, 52 (1999) 165-181

[101] J.A. Moulijn, A.E. Diepen, F. Kapteijn Catalyst deactivation: is it predictable? What to do?, Applied Catalysis A: General, 212 (2001) 3-16

[102] W.T. Reichle, Catalytic reactions by thermally activated, synthetic, anionic clay minerals, Journal of Catalysis, 94 (1985) 547-557

[103] W.T. Reichle, Synthesis of anionic clay minerals (mixed metal hydroxides, hydrotalcite), Solid States Ionics, 22 (1986) 135-141

[104] M.N. Bennani, D. Tichit, F. Figueras, S. Abouarnaddase, Synthèse et caractérisation d'hydrotalcite Mg-Al. Application à l'éldolisation de l'acétone, Journal de Chimie Physique, 96 (1999) 498-509

[105] W. Yang, Y. Kim, P.K.T. Liu, M. Sahimi, T.T. Tsotsis, A study by insitu techniques of the thermal evolution of the structure of Mg-Al-CO_3 layered double hydroxide, Chemical Engineering Science, 57 (2002), 2945-2953

[106] M. Bellotto, B. Rebours, O. Clause, J. Lynch, D. Bazin, E. Elkaim, Hydrotalcite decomposition mechanism: A clue to the structure and reactivity of spinel-like mixed oxides, Journal of Physical Chemistry, 100 (1996) 8535-8542

[107] T. Hibino, A. Tsunashima, Formation of spinel from a hydrotalcite-like compound at low temperature: reaction between edges of crystallites, Clays and Clay Minerals, 45 (1997) 842-853

[108] T. Stanimirova, G. Kirov, Thermal "structural memory" of hydrotalcite metaphase, Annual of University of Sofia, Geology, 92 (2000) 121-130

[109] J. Perez-Ramirez, G. Mul, F. Kapteijn, J.A. Moulijn, On the stability of the thermally decomposed Co-Al hydrotalcite against retrotopotactic transformation, Materials Research Bulletin, 36 (2001) 1767-1775

[110] J. Perez-Ramirez, G. Mul, F. Kapteijn, J. A. Moulijn, A spectroscopic study of the effect of the trivalent cation on the thermal decomposition behaviour Co-based hydrotalcites, Journal of Materials Chemsitry, 11 (2001) 2529-2536

[111] Y-J. Lin, D-Q. Li, D. G. Evans, X. Duan, Modulating effect of Mg-Al-CO_3 layered double hydroxides on the thermal stability of PVC resin, Polymer Degradation and Stability, 88 (2005) 286-293

[112] S. Issa (2009). Production of hydrogen by dry reforming of methane in the presence of mixed oxides Co-Mg-Al-O and the effect of adding Ru on the catalytic properties of these oxides. M2 Internship Report at the University of Balamand, Faculty of Sciences

[113] J. Perez-Ramirez, G. Mul, F. Kapteijn, J. A. Moulijn, Comments on "Infrared emission spectroscopic studies of the thermal transformation of Mg, Ni, and Co hydrotalcite catalysts", Applied Catalysis A: General, 204 (2000) 265-267

[114] A. Vaccari, M. Gazzano, Hydrotalcite-type anionic clays as precursors of high-surface-area Ni/Mg/Al mixed oxides, Studies in Surface Science and Catalysis, 91 (1995) 893-902

[115] S. Ribet, D. Tichit, B. Coq, B. Ducourant, F. Morato, Synthesis and activation of Co-Mg-Al layered double hydroxides, Journal of Solid State Chemistry, 142 (1999) 382-392

[116] K.K. Rao, M. Gravelle, J.S. Valente, F. Figueras, Activation of Mg-Al hydrotalcites catalysts for aldol condensation, Journal of Catalysis, 173 (1998) 115-121

[117] Y. Xi, R.J. Davis, Influence of water on the activity and stability of activated Mg-Al hydrotalcites for the transesterification of tributyrin with methanol, Journal of Catalysis, 254 (2008) 190-197

[118] A.J. Marchi, C.R. Apesteguia, Impregnation induced memory effect of thermally activated layered double hydroxides, Applied Clay Science, 13 (1998) 35-48

[119] A.E. Palomeras, J.G. Prato, F. Rey, A. Corma, Using the “memory effect” of hydrotalcites for improving the catalytic reduction of nitrates in water, Journal of Catalysis, 221 (2004) 62-66

[120] F. Delorme, A. Seron, M. Bizi, V. Jean-Prost, D. Martineau, Effect of time on the reconstruction of the $Mg_4Al_2(OH)_{12}CO_3.3H_2O$ layered double hydroxide in Na_2CO_3 solution, Journal of Materials Science, 41 (2006) 4875-4882

[121] M. Labaki (2002). Etude de l'oxydation totale du propène sur des catalyseurs à base de zirconium modifiés par l'ajout du cuivre et/ou de l'yttrium. Unpublished doctoral dissertation, Université du Littorale Côte d'Opale, Dunkerque

[122] K. Takehira, T. Kawabata, T. Shishido, K. Murakami, T. Ohi, D. Shoro, M. Honda, K. Tabaki, Mechanism of reconstitution of hydrotalcite leading to eggshell-type Ni loading on Mg-Al mixed oxides, Journal of Catalysis, 231 (2005) 92-104

[123] K. Takehira, T. Shishido, D. Shouro, K. Murakami, M. Honda, T. Kawabata, K. Takaki, Novel and effective surface enrichment of active species in Ni-loaded catalyst prepared from Mg-Al hydrotalcite-type anionic clay, Applied Catalysis A: General, 279 (2005) 41-51

[124] C. Gennequin (2008). Etude catalytique d'oxydes mixtes à base de cobalt, magnésium et aluminium dérivés de précurseurs de type hydrotalcite pour l'oxydation totale des composés organiques volatiles. Unpublished doctoral dissertation, Université du Littorale Côte d'Opale, Dunkerque

[125] T. Sato, U. Fujita, T. Endo, M. Shimada, A. Tsunashima, Synthesis of hydrotalcite-like compounds and their physico-chemical properties, Reactivity of Solids, 5 (1988) 219-228

[126] C. Gennequin, R. Cousin, J-F. Lamonier, S. Siffert, A. Aboukaïs, Toluene total oxidation over Co Supported catalysts synthesized using « memory effect » of Mg-Al hydrotalcite, Catalysis Communications, 9 (2008) 1639-1643

[127] C. Gennequin, T. Barakat, H.L. Tidahy, R. Cousin, J-F. Lamonier, A. Aboukaïs, S. Siffert, Use and observation of the hydrotalcite « memory effect » for VOC oxidation, Catalysis Today, 157 (2010) 191-197

[128] W. Xie, H. Peng, L. Chen, Calcined Mg-Al hydrotalcites as solid base catalysts for methanolysis of soybean oil, Journal of Molecular Catalysis A-Chemical, 246 (2006) 24-32

[129] H.Y. Wang, E. Ruckenstein, Conversion of methane to syngas over Co/Al_2O_3, Catalysis Letters, 75 (2001) 13-18

[130] W.T. Reichle, S.Y. Kang D.S. Everhardt, The nature of the thermal decomposition of a catalytically active anionic clay mineral, Journal of Catalysis, 101 (1986) 352-359

[131] T. Stanimirova, N. Petrova, I. Vergilov, G. Kirov, Thermal decomposition products of hydrotalcite-like compounds: low temperature metaphases, Journal of Materials Science, 34 (1999) 4153-4161

[132] E. Genty (2010), Synthèse et caractérisation physico-chimique des matériaux catalytiques à base de métaux précieux. Applications pour des réactions de dépollutions atmosphériques. M1 Internship Report realized at the University of Littoral-Cote d'Opale, France

[133] A. Aoun, S. Aouad, B. El-Khoury, H. El-Nakat, E. Abi-Aad, A. Aboukaïs, Catalytic oxidation of carbon black over $Ru/Mg_xCo_yAl_z$ catalysts, Physics Procedia, 21 (2011) 1-5

[134] P. Arnoldy, J.A. Moulijn, Temperature programmed reduction of $CoOAl_2O_3$ catalysts, Journal of Catalysis, 93 (1985) 38-54

[135] B.A. Sexton, A.E. Hughes, An XPS and TPR study of the reduction promoted cobalt-kieselguhr Fischer-Tropsch catalysts, Journal of Catalysis, 97 (1986) 390-406

[136] Z. Wang, Z. Jiang, W. Shangguan, Simultaneous catalytic removal of NO_x and soot particulate over Co-Al mixed oxide catalysts derived from hydrotalcites, Catalysis Communications, 8 (2007) 1659-1664

[137] A. Böttcher, H. Conrad, H. Niehus, Reactivity of oxygen phases created by the high temperature of oxidation of Ru, Surface Science, 452 (2000) 125- 132

[138] V. Mazzieri, F. Coloma-Pascual, A. Arcoya, P.C. L'Argentière, N.S. Figoli, XPS, FTIR, and TPR characterization of Ru/Al_2O_3 catalysts, Applied Surface Science, 210 (2003) 222-230

[139] J. Dulac, Deformed spinel structures in system $NiRh_2O_4$-$CuRh_2O_4$, Bulletin de la Societe Française de Mineralogie et de Crystallographie, 92 (1969) 487

[140] E. Iglesia, S.L. Soled, R.A. Fiato, G.H. Via, Bimetallic synergy in cobalt ruthenium Fischer-Tropsch synthesis catalysts, Journal of Catalysis, 143 (1993) 345-368

[141] Y. Liu, F.Y. Huang, J.M. Li, W.Z. Weng, C.R. Luo, M.L. Wang, In situ Raman study on the partial oxidation of methane to synthesis gas over Rh/Al_2O_3 and Ru/Al_2O_3 catalysts, Journal of Catalysis, 256 (2008)192-203

[142] W. Wang, R. Ran, Z. Shao, Combustion-synthesized Ru-Al_2O_3 composites as anode catalyst layer of a solid oxide fuel cell operating on methane, International Journal of Hydrogen Energy, 36 (2011) 755-764

[143] S. Hosokawa, H. Kanai, K. Utani, Y. Taniguchi, Y. Saito, S. Imamura, State of Ru on CeO_2 and its catalytic activity on wet oxidation of acetic acid, Applied Catalysis B: Environmental, 45 (2003) 181-187

[144] M. Labaki, J-F. Lamonier, S. Siffert, A. Aboukaïs, Therrnal analysis and temperature-programmed reduction studies of copper-zirconium and copper zirconium-yttrium compounds, Thermochimica Acta, 427 (2005) 193-200

[145] F. Kovanda, K. Jiratova, J. Rymes, D. Kolousek, Characterization of activated Cu/Mg/Al hydrotalcites and their catalytic activity in toluene combustion, Applied Clay Science, 18 (2001) 71–80

[146] J. Chen, J. Zhu, Y. Zhan, X. Lin, G. Cai, K. Wei, Q. Zheng, Characterization and catalytic performance of Cu/CeO_2 and Cu/MgO-CeO_2 catalysts for NO reduction by CO, Applied Catalysis A: General, 363 (2009) 208–215

[147] Z. Wang, Z. Jiang, W. Shangguan, Simultaneous catalytic removal of NOx and soot particulate over Co- Al mixed oxide derived from hydrotalcite, Catalysis Communications, 8 (2007) 1659-1664

[148] F. Millange, R.I. Walton, D. O'Hare, Time-resolved in situ X-ray diffraction study of the liquid-phase reconstruction of Mg-Al-carbonate hydrotalcite-like compounds, Journal of Materials Chemistry, 10 (2000) 1713-1720

[149] M.J. Hernadez-Moreno, M.A. Ulibarri, J.L. Rendon, C.J. Serna, IR characteristics of hydrotalcite like compounds, Phyics and Chemistry of Minerals, 12 (1985) 34-38

[150] J. Perez-Ramirez, G. Mul, F. Kapteijn, J. A. Moulijn, In situ Fourier Transform infrared and Raman spectroscopic study on the thermal decomposition of Co-Al and Ni-Al hydrotalcites, Vibrational Spectroscopy, 27 (2001) 75-88

[151] T. Mokkelbost, I. Kaus, T. Grande, M.A. Einarsrud, Combustion synthesis and characterization of nanocrystalline CeO_2-based powders, Chemistry of Materials, 16 (2004) 5489-5494

[152] G. Busca, V. Lorenzelli, Infrared spectroscopic identification of species arising from reactive adsorption of carbon oxides on metal oxide surfaces, Journal of Materials Chemistry, 7 (1982) 89-126

[153] C. Binet, M. Daturi, J-C. Lavalley, IR study of polycrystalline ceria properties in oxidized and reduced state, Catalysis Today, 50 (1999) 207-225

[154] X. Jiaoxing, L. Guangshe, L. Liping, CeO_2 nanocrystals: Seed-mediated synthesis and size control, Materials Research Bulletin, 43 (2008) 990-995

[155] J.T. Kloprogge, R.L. Frost, Infrared emission spectroscopic study of the thermal transformation of Mg, Ni and Co hydrotalcite catalysts, Applied Catalysis A: general, 184 (1999) 61-71

[156] J.T. Kloprogge, R.L. Frost, Fourier Transform Infrared and Raman spectroscopic study of the local structure of Mg, Ni and Co hydrotalcites, Journal of Solid State Chemistry, 146 (1999) 506-515

[157] M.J. Holgado, V. Rives, M.S. San Roman, Characterization of Ni-Mg-Al mixed oxides and their catalytic activity in oxidative dehydrogenation of n-butane and propene, Applied Catalysis A: General, 214 (2001) 219-228

[158] M.L. Bailly, C. Chizallet, G. Costentin, J.M. Krafft, H. Lauron-Pernot, M. Che, A spectroscopy and catalysis study of the nature of active sites of MgO catalysts: Thermodynamic Bronsted basicity versus reactivity of basic sites, Journal of Catalysis, 235 (2005) 413-422

[159] J.T. Kloprogge, D. Wharton, L. Hickey, R.L. Frost, Infrared and Raman study of interlayer anions CO_3^{2-}, NO_3^-, SO_4^{2-} and ClO_4^- in Mg/Al hydrotalcite, American Mineralogist, 87 (2002) 623-629

[160] J. Preudhomme, P. Tarte, Infrared studies of spinel-III. The normal II-III spinels, Spectrochimica Acta A- Molecular and Biomolecular Spectroscopy, 27 (1971) 1817-1835

[161] S. Musie, S. Popovie, M. Maljkovie, A. Sarie, Synthesis and Characterization of nanocrystalline RuO_2 powders, Materials Letters, 58 (2004) 1431-1436

[162] P.G.M. Brown, Nitro complexes of nitrosyl ruthenium, Journal of Inorganic and Nuclear Chemistry, 13 (1960) 73-83

[163] K. Hadjiivanov, J.C. Lavalley, J. Lamotte, F. Maugé, J. Saint-Just, M. Che, FTIR study of CO interaction with Ru/TiO_2 catalysts, Journal of Catalysis, 176 (1998) 415-425

[164] E. Guglielminotti, F. Boccuzzi, M. Manzoli, F. Pinna, M. Scarpa, Ru/ZrO_2 catalysts, O_2, CO, NO adsorption and reactivity, Journal of Catalysis, 192 (2000) 149-157

[165] S. Hosokawa, S. Nogawa, K. Taniguchi, K. Utani, H. Kanai, S. Imamura, Oxidation characteristics of Ru/CeO_2 catalysts, Applied Catalysis A: General, 288 (2005) 67-73

[166] Z. Wang, E. Wang, L. Gao, L. Xu, Synthesis and properties of Mg_2Al layered double hydroxides containing 5-fluorouracil, Journal of Solid State Chemistry, 178 (2005) 736-741

[167] C. Gennequin, S. Siffert, R. Cousin, A. Aboukaïs, Co-Mg-Al hydrotalcite precursors for catalytic total oxidation of volatile organic compounds, Topics in Catalysis, 52 (2009) 482-491

[168] K.S.W. Sing, D.H. Everett, R.A.W. Haul, L. Moscou, R.A. Pierotti, J. Rouquerol, T. Siemieniewska, Reporting physisorption data for gas/solid systems with special reference to the determination of surface area and porosity, Pure and Applied Chemistry, 57 (1985) 603-619

[169] M. Thommes, Physical adsorption characterization of nanoporous materials, Chemical Engineering and Technology, 82 (2010) 1059-1071

[170] G.I. Pilipenko, A.A. Sabirzyanov, V.G. Stepanov, D.V. Oparin, V.V. Izotov, F.F. Gavrilov, Quasidynamical Jahn-Teller effect in the electron paramagnetic resonance spectra of Ru^{+} ions in lithium hydride and deuteride, Journal of Physics: Condensed Matter, 4 (1992) 4047-4054

[171] G.I. Pilipenko, A.A. Sabirzyanov, D.V. Oparin, V.G. Stepanov, F.F. Gavrilov, Photostimulated processes in the Jahn-Teller system LiH(D):Ru, Journal of Physics: Condensed Matter, 4 (1992) 4055-4062

[172] P. Castillo-Villalon, J. Ramirez, Spectroscopic study of the electronic interactions in Ru/TiO_2 HDS catalysts, Journal of Catalysis, 268 (2009) 39-48

[173] H. Laversin (2002), Etude d'hydrotalcite à base de Co, Fe et Cu comme précurseurs de catalyseurs pour la réaction d'oxydation de propène. M2 Internship Report realized at the University of Littoral - Côte d'Opale, France

[174] A. Aboukaïs, A. Bennani, C. Lamonier-Dulongpont, E. Abi-Aad, G. Wrobel, Redox behaviour of copper(II) species on CuCe oxide catalysts: electron paramagnetic resonance (EPR) study, Colloids and Surfaces A: Physicochemical and Engineering Aspects ,115 (1996) 171-177

[175] H. Tominaga, Y. Ono, T. Keii, Spectroscopic study of Cu(II) ions supported on silica gel by cation exchange method, Journal of Catalysis, 40 (1975) 197-202

[176] G. Scholz, R. Luck, R. Stober, H.J. Lunk , F. Ritschl, Copper-oxygen coordination in Cu^{II} heteropolyanion compounds: electron paramagnetic resonance studies, Journal of the Chemical Society, Faraday Transactions, 87 (1991) 717-725

[177] E. Crusson-Blouet. A. Aboukaïs, F.C. Aissi, M. Guelton, Behavior of copper(II) ion pairs in copper molybdovanadophosphate hydrate catalyst, Chemistry of Materials, 4 (1992) 1129-1131

[178] G. Verquin, G. Fontaine, E. Abi-Aad, E. Zhilinskaya, A. Aboukaïs , J-L. Bernier, EPR study of copper (II) complexes of hydroxysalen derivatives in order to be used in the DNA cleavage, Journal of Photochemistry and Photobiology B: Biology, 86 (2007) 272-278

[179] R.G. Lemus, J.M.M. Duart, Updated hydrogen production costs and parities for conventional and renewable technologies, International Journal of Hydrogen Energy, 35 (2010) 3929-3936

[180] A. Tanksale, J.N. Beltramini, G.M. Lu, A review of catalytic hydrogen production processes from biomass, Renewable and Sustainable Energy Reviews, 14 (2010) 166-182

[181] J.R. Rostrup Nielsen, J.H.B. Hansen, CO_2-reforming of methane over transition metals, Journal of Catalysis, 144 (1993) 38-49

[182] T-J. Huang, S-Y. Jhao, Ni-Cu/samaria doped ceria catalysts for steam reforming of methane in the presence of cabron dioxide, Applied Catalysis A:General, 302 (2006) 325-332

[183] J.H. Jeong, J.W. Lee, D.J. Seo, Y. Seo, W.L. Yoon, D.K. Lee, D.H. Kim, Ru-doped Ni catalysts effective for the steam reforming of methane without the pre-reduction treatment with H_2, Applied Catalyis A:General, 302 (2006) 151-156

[184] A. Djaidja, A. Kiennemann, A. Barama, Effect of Fe or Cu addition on Ni/Mg-Al and Ni/MgO catalysts in the steam-reforming of methane, Studies in Surface Science and Catalysis, 162 (2006) 945-952

[185] G. Jones, J.G. Jakobsen, S.S. Shim, J. Kleis, M.P. Andersson, J. Rossmeisl, F. Abild-Pedersen, T. Bligaard, S. Helveg, B. Hinnemann, J.R. Rostrup Nielsen, I. Chorkendorff, J. Sehested, J.K.Norskov, First principles calculations and experimental insight into methane steam reforming over transition metal catalysts, Journal of Catalysis, 259 (2008) 147-160

[186] K.Y. Koo, H.S. Roh, Y.T. Seo, D.J.Seo, W.L. Yoon, S.B. Park, Coke study on MgO-promoted Ni/Al_2O_3 catalyst in combined H_2O and CO_2 reforming of methane for gas to liquid (GTL) process, Applied Catalysis A: General, 340 (2008) 183-190

[187] K-S. Cha, H-S. Kim, B-K. Yoo, Y-S. Lee, K-S. Kang, C-S. Park, Y-H. Kim, Reaction characteristics of two-step methane reforming over a Cu-ferrite/Ce-ZrO_2 medium, International Journal of Hydrogen Energy, 34 (2009) 1801-1808

[188] B.C. Enger, R. Lodeng, A. Holmen, A review of catalytic partial oxidation of methane to synthesis gas with emphasison reaction mechanisms over transition metal catalysts, Applied Catalysis A: General, 346 (2008) 1-27

[189] T.V. Choudhary, D.W. Goodman, Methane activation on Ni and Ru model catalysts, Journal of Molecular Catalysis A: Chemical, 163 (2000) 9-18

[190] G.W. Bridger, G.C. Chinchen, Hydrocarbon-reforming catalysts (chapter 5), catalyst handbook-with special reference to unit processes in ammonia and hydrogen manufacture, 1970

[191] J.R. Rostrup-Nielsen, Steam reforming catalysts, Teknisk Forlag A/S (Danish Technical Press Inc.), Copenhagen, 1975

[192] M.V. Twigg, Catalyst Handbook, 2nd edition, Manson. Publishing, London, 1996

[193] V.R. Choudhary, A.M. Rajput, Simultaneous Carbon Dioxide and Steam Reforming of Methane to Syngas over NiO-CaO Catalyst, Industrial & Engineering Chemistry Research, 35 (1996) 3934-3939

[194] X-Y. Quek, D. Liu, W.N.E. Cheo, H. Wang, Y. Chen, Y. Yang, Nickel-grafted TUD mesoporous catalysts for carbon dioxide reforming of methane, Applied Catalysis B: Environmental, 95 (2010) 374-382

[195] C. Gennequin, M. Safariamin, S. Siffert, A. Aboukaïs, E. Abi-Aad, CO_2 reforming of CH_4 over Co-Mg-Al mixed oxides prepared via hydrotalcite like precursors, Catalysis Today, 176 (2011) 139-143

[196] L.P.R. Profeti, E.A. Ticianelli, E.M. Assaf, Co/Al_2O_3 catalysts promoted with noble metals for production of hydrogen by methane steam reforming, Fuel, 87 (2008) 2076-2081

[197] S.S. Maluf, P.A.P. Nascente, E.M. Assaf, CuO and CuO-ZnO catalysts supported on CeO_2 and CeO_2-LaO_3 for low temperature water-gas shift reaction, Fuel Processing Technology, 91 (2010) 1438-1445

[198] L.S. Carvalho, A.R. Martins, P. Reyes, M. Oportus, A. Albonoz, V. Vicentini, M.C. Rangel, Preparation and characterization of $Ru/MgO-Al_2O_3$ catalysts for methane steam reforming, Catalysis Today, 142 (2009) 52-60

[199] G.S. Gallego, F. Mondragon, J. Barrault, J.M. Tatibouet, C.B. Batiot-Dupeyrat, CO_2 reforming of CH_4 over La-Ni based perovskite precursors, Applied Catalysis A: General, 311 (2006) 164-171

[200] M. Safariamin, L.H. Tidahy, E. Abi-Aad, S. Siffert, A. Aboukaïs, Dry reforming of methane in the presence of ruthenium-based catalysts, Comptes Rendus Chimie, 12 (2009) 748-753

[201] S. Li, Y. Lu, L. Guo, X. Zhang, Hydrogen production by biomass gasification in supercritical water with bimetallic Ni-M/γ-Al_2O_3 catalysts, International Journal of Hydrogen Energy, 36 (2011) 14391-14400

[202] J. Knudsen, A.U. Nilekar, R.T. Vang, J. Schnadt, E.L. Kunkes, J.A. Dumesic, M. Mavrikakis, F. Besenbacher, A Cu/Pt near-surface alloy for water-gas shift catalysis, Journal of the American Chemistry Society, 129 (2007) 6485-6490

[203] T. Caillot, G. Gauthier, P. Delichere, C. Cayron, F.J. Cadete, Evidence of anti-coking behavior of $La_{0.8}Sr_{0.2}Cr_{0.98}Ru_{0.02}O_3$ as potential anode material for solid oxide fuel cells directly fed under methane, Journal of Catalysis, 290 (2012) 158-164

[204] D. Li, N. Ichikuni, S. Shimazu, T. Uematsu, Catalytic properties of sprayed Ru/Al_2O_3 and promoter effects of alkali metals in CO_2 hydrogenation, Applied Catalysis A: General, 172 (1998) 351-358

[205] V.R. Choudhary, B.S. Uphade, A.S. Mamman, Simultaneous steam and CO_2 reforming of methane to syngas over Ni/MgO/SA-5205 in presence and absence of oxygen, Applied Catalysis A: General, 168 (1998) 33-46

[206] A. Ishihara, E.W. Qian, I.N. Finahari, I.P. Sutrisna, T. Kabe, Addition effect of ruthenium on nickel steam reforming catalysts, Fuel, 84 (2005) 1462-1468

[207] R. Craciun, W. Daniell, H. Knozinger, The Effect of CeO_2 structure on the activity of supported Pd catalysts used for methane steam reforming, Applied Catalysis A: General, 230 (2002) 153-161

[208] P. Leroi, B. Madani, C. Pham-Huu, M.J. Ledoux, S. Savin-Poncet, J.L. Bousquet, Ni/SiC: a stable and active catalyst for catalytic partial oxidation of methane, Catalysis Today, 91 (2004) 53-58

[209] N. Muradov, F. Smith, A.T. Raissi, Hydrogen production by catalytic processing of renewable methane-rich gases, International Journal of Hydrogen Energy, 33 (2008) 2023-2035

[210] D.G. Avraama, T.I. Halkides, D.K. Liguras, O.A. Bereketidoub, M.A. Goula, An experimental and theoretical approach for the biogas steam reforming reaction, International Journal of Hydrogen Energy, 35 (2010) 9818-9827

[211] H.C. Lee, Y. Potapova, D. Lee, A core-shell structured, metal-ceramic Composite-Supported Ru Catalyst for methane steam reforming, Journal of Power Sources, 216 (2012) 256-260

[212] Y. Sakai, H. Saito, T. Sodesawa, F. Nozaki, Catalytic reactions of hydrocarbon with carbon dioxide over metallic catalysts, Reaction Kinetics and Catalysis Letters, 24 (1984) 253-257

[213] R. Lanza, P. Canu, S.G. Jaras, Methane partial oxidation over Pt–Ru catalyst: An investigation on the mechanism, Applied Catalysis A: General, 375 (2010) 92-100

[214] M.A. Soria, C. Mateos-Pedrero, I. Rodriguez-Ramosa, A. Guerrero-Ruiz, Catalytic steam reforming of methane under conditions of applicability with Pd membranes over supported Ru catalysts, Catalysis Today, 171 (2011) 126-131

[215] M. Dakhad, D. Fino, S. Rayalu, R. Kumar, A. Watanabe, H. Haneda, S. Devotta, T. Mitsuhashi N. Labhsetwar, Zirconia supported Ru-Co bimetallic catalysts for diesel soot oxidation, Topics in Catalysis, 42 (2007) 273-276

[216] I.A. Ikonnikov, V.E. Rudnik, A.Y. Loginov, Effect of high-temperature coke deposition coke deposition from methane upon the structure of Manganese-Yttrium oxides, Carbon, 35 (1997) 587-592

[217] M.F. Ottaviani, R. Mazzeo, EPR characterization of graphitized and activated micro- and meso-porous carbons, Microporous and Mesoporous Materials 141 (2011) 61-68

[218] E. Saab (2007). Etudes des performanes d'oxydes de cerium et d'aluminium dans l'oxydation totale du noir de carbone. Unpublished doctoral dissertation, Université du Littorale Côte d'Opale, Dunkerque

[219] D.L. Trimm, Coke formation and minimisation during steam reforming reactions, Catalysis Today, 37 (1997) 233-238

[220] B. Delmon, G.E Froment, Catalyst deactivation, Studies in Surface Science and Catalysis, vol. 34, Elsevier, Amsterdam, 1987

[221] C.H. Bartholomew, Mechanisms of catalyst deactivation, Applied Catalysis A: General, 212 (2001) 17-60

[222] W. Zhang, M. Dubois, K. Guerin, A. Hamwi, J. Giraudet, F. Masin, Solid-state NMR and EPR study of fluorinated carbon nanofibers, Journal of Solid State Chemistry, 181 (2008) 1915-1924

[223] P. Forzatti, L. Lietti, Catalyst deactivation, Catalysis Today, 52 (1999) 165-18

[224] C.H. Bartholomew, Carbon deposition in steam reforming and methanation, Catalysis Reviews- Science and Engineering, 24 (1982) 67-112

[225] P.G. Menon, Coke on catalysts harmful, harmless, invisible and beneficial types, Journal of Molecular Catalysis, 59 (1990) 207-220

[226] J.R. Rostrup-Nielsen, D.L. Trimm, Mechanisms of carbon formation on nickel-containing catalysts, Journal of Catalysis, 48 (1977) 155-165

[227] R. Cousin, S. Capelle, E. Abi-Aad, D. Courcot, A. Aboukaïs, Investigation of binary and ternary Cu-V-Ce oxides by X-ray diffraction, thermal analysis, and electron paramagnetic resonance, Chemical Materials, 13 (2001), 3862-3870

[228] J. Llorca, N. Homs, J. Sales, and P.R. de la Piscina, Efficient production of hydrogen over supported cobalt catalysts from ethanol steam reforming, Journal of Catalysis, 209 (2002) 306-317

[229] A. Chica, S. Sayas, Effective and stable bioethanol steam reforming catalyst based on Ni and Co supported on all-silica delaminated ITQ-2 zeolite, Catalysis Today, 146 (2009) 37-43

[230] L.C. Chen, S.D. Lin, The ethanol steam reforming over Cu-Ni/SiO_2 catalysts: Effect of Cu/Ni ratio, Applied Catalysis B: Environmental, 106 (2011) 639-649

[231] R. Padilla, M. Benito, L. Rodriguez, A. Serrano, G. Munoz, L.Daza, Nickel and cobalt as active phase on supported zirconia catalysts for bio-ethanol reforming: influence of the reaction mechanism on catalysts performance, International Journal of Hydrogen Energy, 35 (2010) 8921-8928

[232] F. Haga, T. Nakajima, K. Yamashita, S. Mishima, Effect of crystallite size on the catalysis of alumina-supported cobalt catalyst for steam reforming of ethanol, Reaction Kinetics and Catalysis Letters, 63 (1998) 253-259

[233] J. Llorca, P. Ramirez de la Piscina, J.A. Dalmon, J. Sales, N. Homs, CO-free hydrogen from steam-reforming of bioethanol over ZnO-supported cobalt catalysts: Effect of the metallic precursor, Applied Catalysis B: Environmental, 43 (2003) 355-369

[234] A. Casanovas, M. Roig, C. Leitenburg, A. Trovarelli, J. Llorca, Ethanol steam reforming and water gas shift over Co/ZnO catalytic honeycombs doped with Fe, Ni, Cu, Cr and Na, International Journal of Hydrogen Enegy, 35 (2010) 7690-7698

[235] H. Song, L. Zhang, R.B. Watson, D. Braden, U.S. Ozkan, Investigation of bio-ethanol steam reforming over cobalt-based catalysts, Catalysis Today, 129 (2007) 346-354

[236] R. Espinal, E. Taboada, E. Molins, R.J. Chimentao, F. Medina, J. Llorca, Cobalt hydrotalcites as catalysts for bioethanol steam reforming. The promoting effect of potassium on catalyst activity and long-term stability, Applied Catalysis B: Environmental, 127 (2012) 59- 67

[237] F. Marino, M. Boveri, G. Baronetti, M. Laborde, Hydrogen production from steam reforming of bioethanol using Cu/Ni/K/γ-Al_2O_3 catalysts: Effect of Ni, International Journal of Hydrogen Energy, 26 (2001) 665-668

[238] F. Marino, M. Boveri, G. Baronetti, M. Laborde, Hydrogen production via catalytic gasification of ethanol: a mechanism proposal over copper–nickel catalysts, International Journal of Hydrogen Energy, 29 (2004) 67-71

[239] W. Grzegorczyk, A. Denis, W. Gac, T. Ioannides and A. Machocki, Hydrogen Formation via Steam Reforming of Ethanol Over Cu/ZnO Catalyst Modified with Nickel, Cobalt and Manganese, Catalysis Letters,128 (2009) 443-448

[240] F. Aupretre, C. Descorme, D. Duprez, Bio-ethanol catalytic steam reforming over supported metal catalysts, Catalysis Communications, 3 (2002) 263-267

[241] P.D. Vaidya, A.E. Rodrigues, Insight into steam reforming of ethanol to produce hydrogen for fuel cells, Chemical Engineering Journal, 117 (2006) 39-49

[242] V. Nichele, M. Signoretto, F. Menegazzo, F. Pinna, I. Rossetti, C. Biffi, G. Cruciani, G. Cerrato. (2012). Ni/TiO_2 for ethanol steam reforming: which is the best synthetic approach? [Abstract]. International Congress on Catalysis. Retrieved from http://air.unimi.it/handle/2434/208467

[243] E. Ozdogan (2007). Steam reforming of ethanol for hydrogen production using Cu-MCM41 and Ni-MCM41 type mesoporous catalytic materials. Master report at the Middle East Technical University, Turkey

[244] N. Iwasa, N. Takezawa, Reforming of ethanol-dehydrogenation to ethyl acetate and steam reforming to acetic acid over copper-based catalysts, Bulletin of the Chemical Society of Japan, 64 (1991) 2619-2623

[245] B.A. Raich, H.C. Foley, Ethanol Dehydrogenation with a Palladium Membrane Reactor: An Alternative to Wacker Chemistry, Industrial and Engineering Chemistry Research, 37 (1998) 3888-3895

[246] Y.J. Tu, V.W. Chen, Effects of Alkaline-Earth Oxide Additives on Silica-Supported Copper Catalysts in Ethanol Dehydrogenation, Industrial and Engineering Chemistry Research, 37 (1998) 2618-2622

[247] F. Marino, E.G. Cerrella, S. Duhalde, M. Jobbagy, M.A. Laborde, Hydrogen from steam reforming of ethanol. Characterization and performance of copper-nickel supported catalysts, International Journal of Hydrogen Energy, 23 (1998) 1095-1101

[248] T. Nishiguchi, T. Matsumoto, H. Kanai, K. Utani, Y. Matsumura, W.J. Shen, Catalytic steam reforming of ethanol to produce hydrogen and acetone, Applied Catalysis A: General, 279 (2005) 273-277

[249] V. Klouz, V. Fierro, P. Denton, H. Katz, J.P. Lisse, S. Bouvot-Mauduit, C. Mirodatos, Ethanol reforming for hydrogen production in a hydrid electric vehicle: process optimization, Journal of Power Sources, 105 (2002) 26-34

[250] T. Dong, Z. Wang, L. Yuan, Y. Torimoto, M. Sadakata, Q. Li, Hydrogen production by ethanol steam reforming on potassium doped $12CaO.7Al_2O_3$ catalyst, Catalysis Letters, 119 (2007) 29-39

[251] J.P.A. Neeft, F. Hoorneart, M. Makkee, J. Moulijn, The effects of heat and mass transfer in thermogravimetrical analysis. A case study towards the catalytic oxidation of soot, Thermochimica Acta, 287 (1996) 261-278

[252] C. Decarne, E. Abi-Aad, B.G. Kostyuk, V.V. Lunin, A. Aboukaïs, Characterization of cerium and copper species in Cu-Ce-Al oxide systems by temperature programmed reduction and electron paramagnetic resonance, Journal of Materials Science, 39 (2004) 2349-2356

Appendix A: Structures

Spinel structure

Spinel has the general formula: $A^{2+}B_2^{3+}O_4^{2-}$ where the A^{2+} ions occupy tetrahedral sites and B^{3+} ions occupy octahedral sites (ex: $MgAl_2O_4$). Oxides ions are arranged in a cubic close-packed lattice. Figure I is a spinel structure schematic.

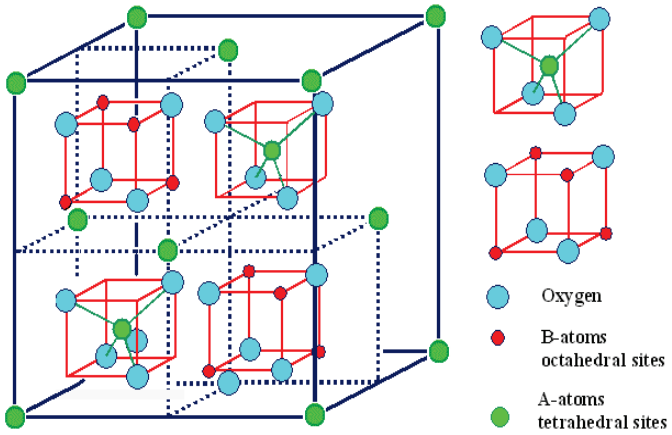

AB_2O_4 spinel The red cubes are also contained in the back half of the unit cell

Figure I Spinel structure

Periclase structure

The periclase structure (Figure II) is composed of a mono-oxide mineral of magnesium MgO. The crystal structure of periclase is composed of two interpenetrating face centered cubic lattice of cation and oxygen. Both cations and anions are in octahedral coordination.

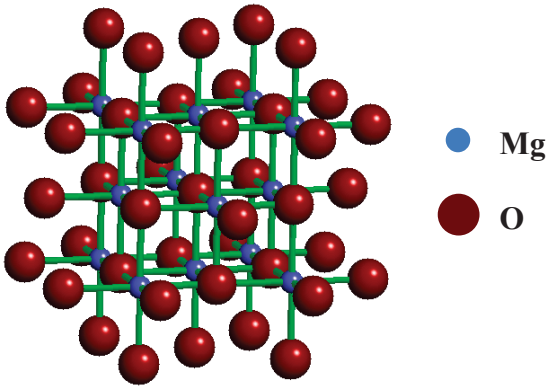

Figure II Periclase structure

Tenorite structure

Tenorite or CuO (Figure III) has an atomic arrangement unique among all compounds of formula type AB. The structure is characterized by a planar rectangular coordination of four oxygen atoms around copper and oxygen is surrounded by four copper atoms in the form of distorted tetrahedron.

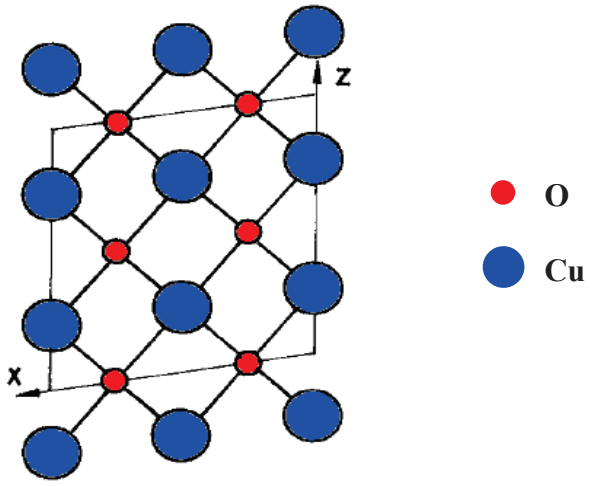

Figure III Tenorite structure

Tetragonal structure

RuO_2 belongs to the family of transition-metal oxide compounds with tetragonal rutile structure (Figure IV). The ruthenium cations have a co-ordination number of 6 meaning they are surrounded by an octahedron of 6 oxygen atoms. The oxygen anions have a co-ordination number of 3 resulting in a trigonal planar co-ordination.

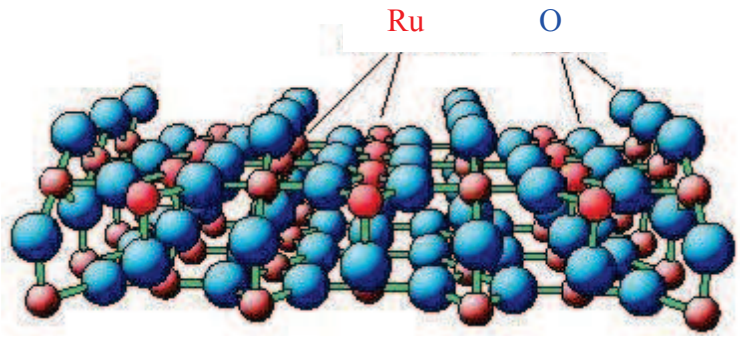

Figure IV Tetragonal rutile structure of RuO_2

Appendix B: Not Presented Results

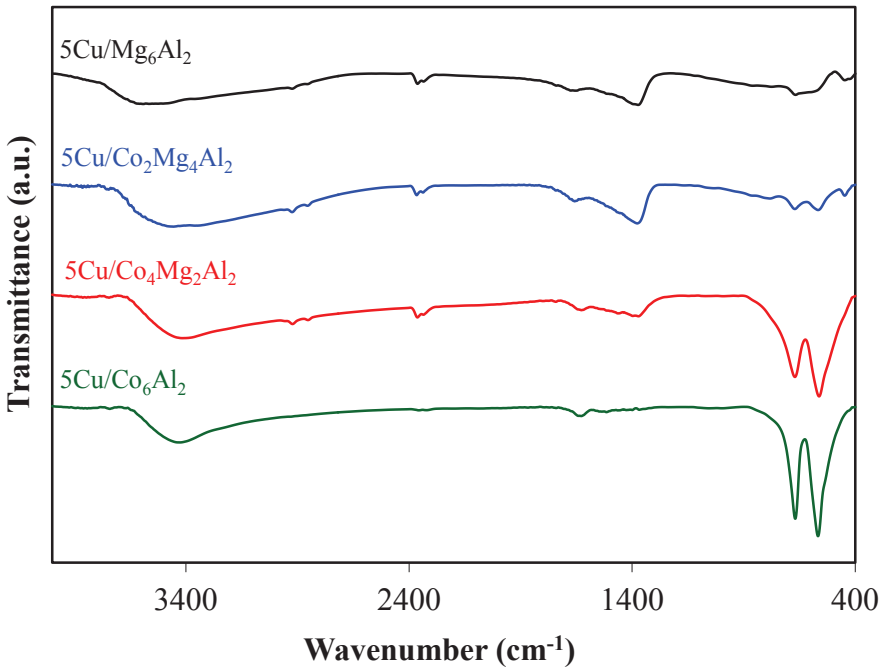

Figure V FTIR spectra of $5Cu/Co_xMg_{6-x}Al_2$ calcined at 500°C

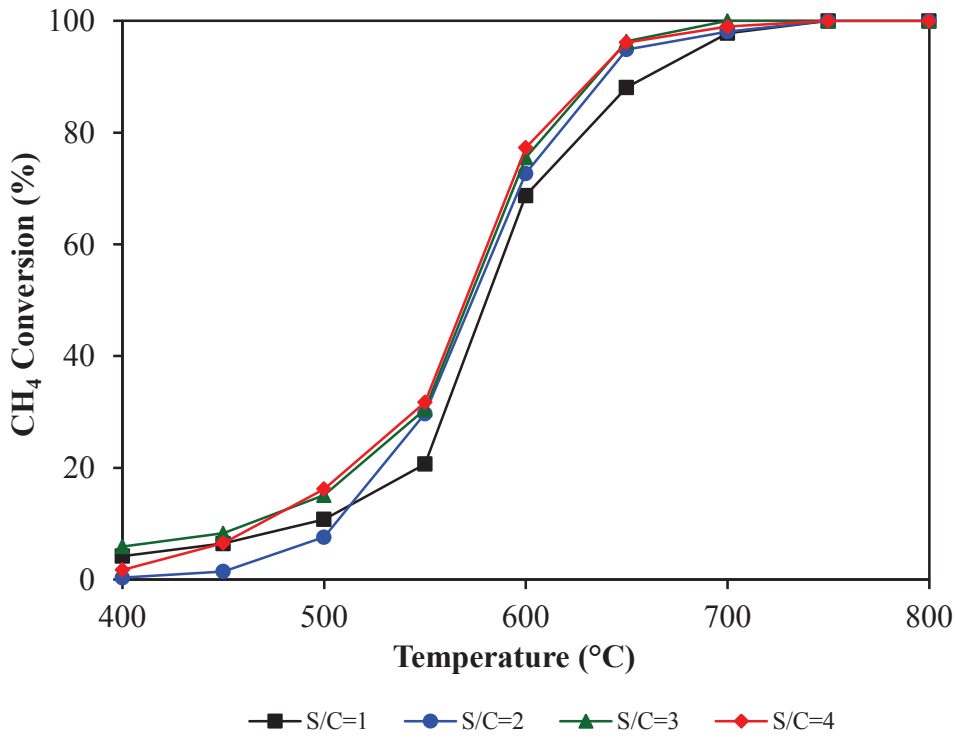

Figure VI Effect of the H_2O/CH_4 feed ratio on the methane conversion (%) over $5Cu/Co_6Al_2$ catalyst calcined at 500°C

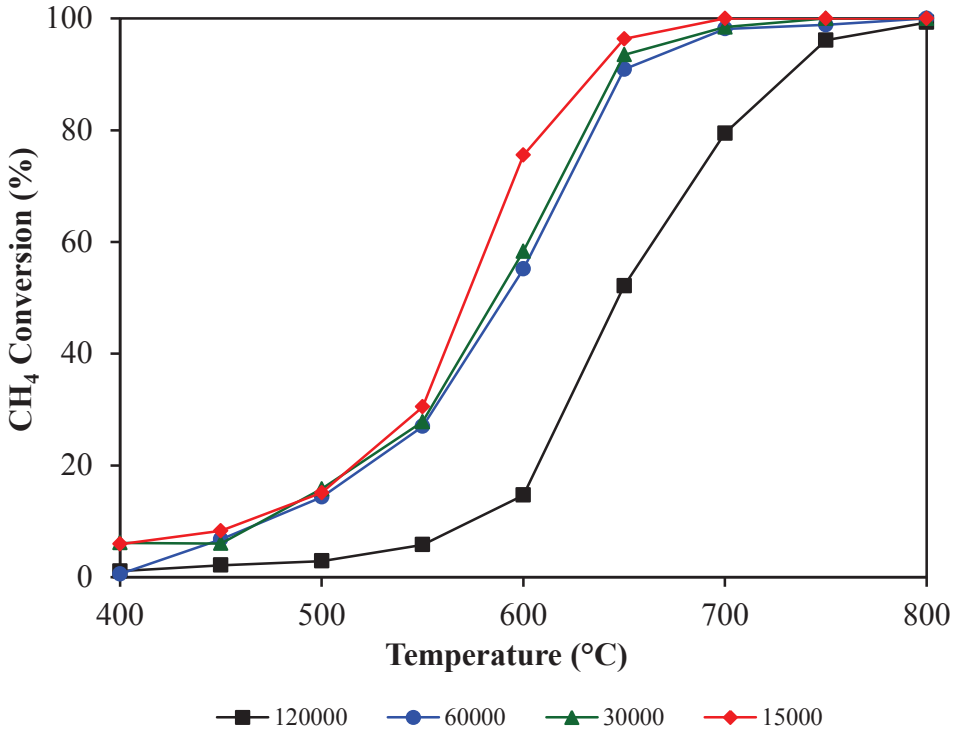

Figure VII Effect of the GHSV values on the methane conversion (%) as a function of the temperature over 5Cu/Co_6Al_2 catalyst calcined at 500°C

Appendix C: Porosimetry

When the gas comes into contact with a solid surface, molecules of the gas will adsorb on the surface. The measurement of the amount of gas adsorbed over a range of partial pressures at a single temperature results in a graph known as an adsorption isotherm. The interpretation of the isotherms is rich in information about the texture of the adsorbent. Six isotherm types proposed by the IUPAC are usually encountered depending on the type of adsorbate and adsorbent. They are illustrated in figure VIII. Isotherm of type I is observed for solids presenting microporous (< 2 nm) like activated carbon and zeolites. Type II and III are associated to adsorption on macroporous adsorbent (> 50 nm) with strong and weak adsorbate-adsorbent interactions respectively. Type IV and V represent adsorption isotherms with hysteresis corresponding to mesoporous adsorbent (2 nm < pore size < 50 nm) with strong and weak affinities respectively. Finally, type VI is stepwise multilayer adsorption on a uniform non-porous surface.

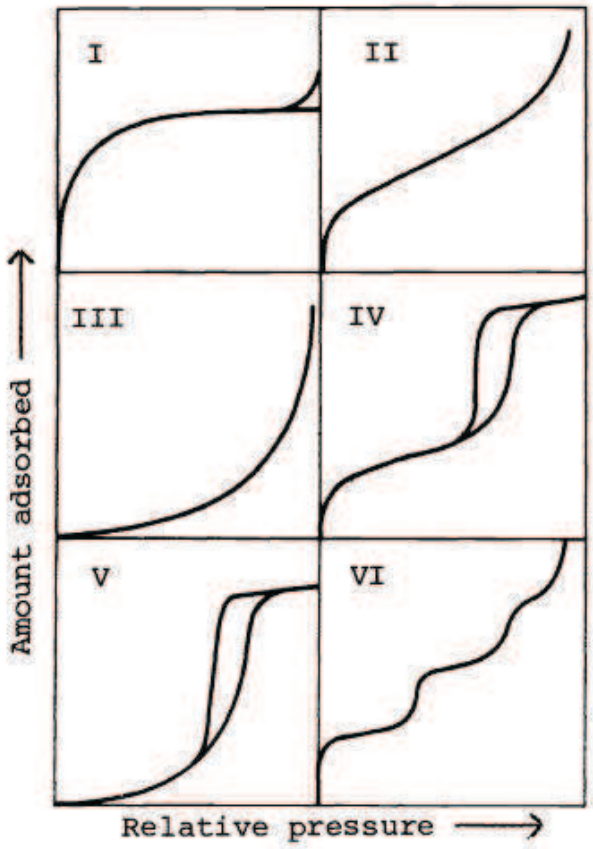

Figure VIII IUPAC classification for adsorption isotherm

At the same time, hysteresis loops that correspond to mesoporous systems are classified -according to their form- in four categories: H1, H2, H3 and H4. They are represented in figure VI. H1 type is associated to solids with agglomerates having narrow distributions of pore size. H2 type corresponds to porous solids whose size distribution and pore size are not uniform. H3 type is observed with aggregates of plate-like particles giving rise to slit-shaped pores. H4 type appears to be associated with narrow slit-like pores.

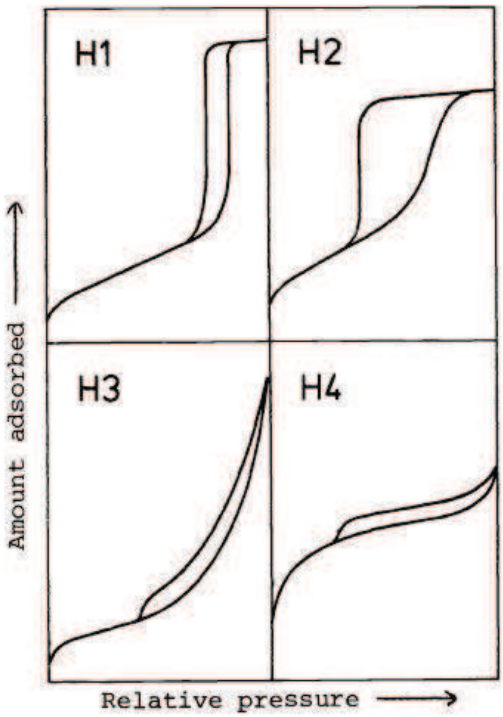

Figure IX Types of hysteresis loops

Appendix D: Thermodynamic Calculations

Thermodynamic calculation of the equilibrium constant *K* is carried out according to the following formula:

$$K = e^{-\frac{\Delta G_T}{R \times T}}$$

where: ΔG_T: Molar gibbs energy of the reaction at a given temperature ($J.mol^{-1}$)

R: Gas constant (8,314 $J.mol^{-1}.K^{-1}$)

T: Temperature (K)

ΔG_T is calculated according to the following formula:

$\Delta G_T = \Delta H_T - T\ \Delta S_T$

where: ΔH_T: Molar enthalpy at a given temperature ($J.mol^{-1}$)

ΔS_T: Molar entropy at a given temperature ($J.mol^{-1}.k^{-1}$)

ΔH_T and ΔS_T of the reactants or products at each temperature are taken from the "*CRC Handbook of Physics and Chemistry*".

Appendix E: Theoretical Conversion of Methane and Ethanol

Theoretical methane conversion in the methane steam reforming reaction is calculated according to the following steps:

MSR: $CH_4 + H_2O \leftrightarrow CO + 3\,H_2$

Initial:	n_{0CH_4}	n_{0H_2O}	0	0
Final:	$n_{0CH_4} - x$	$n_{0H_2O} - x$	x	$3x$

Therefore, the total number of moles is:

$$n_t = n_{f\,CH_4} + n_{f\,H_2O} + n_{f\,CO} + 3\,n_{f\,H_2} = (n_{0CH_4} - x) + (n_{0H_2O} - x) + x + 3x$$

where n_0 and n_t are the initial and total number of moles and $n_{f\,CH_4}$, $n_{f\,H_2O}$, $n_{f\,CO}$ and $n_{f\,H_2}$ the final number of moles of each reactant and product in the methane steam reforming reaction.

The equilibrium constant of the MSR reaction is:

$$K_{MSR} = \frac{X_{CO} \times X^3{}_{H_2}}{X_{CH_4} \times X_{H_2O}}$$

where X_{CO}, X_{H_2}, X_{CH_4} and X_{H_2O} are the molar fraction of each reactant and product in the methane steam reforming reaction and can be written as follows:

$$X_{CO} = \frac{n_{f\,CO}}{n_t} \quad ; \quad X_{H_2} = \frac{n_{f\,H_2}}{n_t} \quad ; \quad X_{CH_4} = \frac{n_{f\,CH_4}}{n_t} \quad ; \quad X_{H_2O} = \frac{n_{f\,H_2O}}{n_t}$$

By replacing each component in the equilibrium constant (K_{MSR}) formula, a fourth degree equation is developed as a function of K_{MSR} and x.

Knowing the values of K_{MSR} as they were previously calculated at each temperature, and using a *MATLAB 2008* software, *x* is found.

Therefore, $n_{f\,CH_4}$ could be now calculated, and the theoretical conversion will be established according to the following formula:

$$Conversion(\%) = \frac{n_{i\,CH_4} - n_{f\,CH_4}}{n_{i\,CH_4}} \times 100$$

Same steps are applied to calculate the theoretical conversion of ethanol.

RESUME DE THESE

Présenté publiquement à

L'UNIVERSITE DE BALAMAND

Pour obtenir le grade de

DOCTEUR EN CHIMIE

par

Doris HOMSI

Vaporeformage du méthane et de l'éthanol sur des catalyseurs à base de ruthénium et du cuivre supportés sur des oxydes Co-Mg-Al préparés par voie hydrotalcite

Soutenue le 14 Décembre 2012 devant la commission d'examen

Membres de Jury :

A. ABOUKAÏS	Président
M. LABAKI	Rapporteur
B. TAOUK	Rapporteur
C. GENNEQUIN	Examinateur
T. WEHBE	Examinateur
E. ABI-AAD	Directeur de thèse
S. AOUAD	Directeur de thèse

SOMMAIRE

1 Introduction

La prise de conscience des problèmes climatiques et la nécessité de réduire les émissions de gaz à effet de serre, sont des facteurs déterminants qui en ce début de millénaire, obligent les politiques et les industriels à repenser au futur énergétique et à favoriser la recherche sur la production d'énergie « propre ». D'autres facteurs clés tels que l'épuisement annoncé des ressources fossiles et la croissance de la consommation énergétique par personne encouragent également le développement de nouvelles sources d'énergie renouvelable.

Dans cette optique, l'hydrogène semble être un vecteur énergétique prometteur au vu de son utilisation dans la pile à combustible pour produire de l'énergie propre pour le transport, le secteur résidentiel et l'industrie. L'hydrogène est un vecteur énergétique tout comme l'électricité mais contrairement aux sources primaires d'énergie, il doit être fabriqué juste avant d'être utilisé. Sachant qu'il est difficile de stocker ou de liquéfier l'hydrogène, sa production «in situ» semble une solution parmi les plus prometteuses.

Il existe ainsi différentes méthodes de production d'hydrogène soit à partir de l'électrolyse de l'eau, ou du reformage. Le vaporeformage est le procédé le plus développé et le moins coûteux pour la production d'hydrogène à grande échelle. Le vaporeformage des hydrocarbures, particulièrement du méthane qui est un des principaux constituants du biogaz (47 à 65% de CH_4), est le plus largement utilisé et généralement la méthode la plus économique et compétitive pour la production d'hydrogène [1,2]. De même, la réaction du vaporeformage de l'éthanol est une autre alternative pour la production d'hydrogène. L'éthanol est non toxique et disponible comme il peut être produit par la fermentation de la biomasse [3].

Afin d'être réalisables dans des domaines de température et de pression pas trop élevés, ces réactions sont effectuées en présence d'un catalyseur. L'objectif principal du présent travail consiste à optimiser les paramètres opératoires des 2 réactions et à développer de nouvelles formulations de catalyseurs permettant d'avoir une sélectivité suffisante en produit désiré (H_2) et une grande conversion de méthane et de l'éthanol tout en défavorisant la formation du coke et du monoxyde de carbone. Pour cela, deux familles de catalyseurs sont actuellement développées: les systèmes à base de métaux nobles (Ru) qui sont très actifs et sélectifs pour le vaporeformage du méthane [4-6] et les systèmes à base de métaux de transition (Cu) qui sont moins coûteux que les métaux nobles et montrent aussi une bonne activité catalytique dans la réaction du vaporeforamge de l'éthanol [7, 8]. Ces phases actives sont imprégnées sur des hydrotalcites (Co-Mg-Al). En

raison de leur faible coût, la stabilité thermique et forte basicité, les hydrotalcites peuvent être utilisées dans la réaction de vaporeformage [9, 10].

2 Synthèse des Catalyseurs

2.1 Synthèse des oxydes mixtes $Co_xMg_{6-x}Al_2$ par voie hydrotalcite

Pour combiner plusieurs métaux, au sein d'une même phase homogène, la coprécipitation à pH constant est généralement utilisée. Dans ce mode de synthèse, la structure du composé formé est directement liée à la valeur du pH fixée. Les hydrotalcites à base de Co (II), Mg (II) et Al (III) ont été préparées en précipitant ces ions en solution aqueuse (100 mL) contenant les quantités appropriées de $Co(NO_3)_2,6H_2O$ (SIGMA-ALDRICH, pureté 98%), $Mg(NO_3)_2,4H_2O$ (FLUKA, pureté 99%) et $Al(NO_3)_3,9H_2O$ (FLUKA, pureté 98%) en adéquation avec la formule du produit final désiré, avec une solution de soude NaOH (2 M, HIMEDIA, pureté 99%) et de carbonate de sodium Na_2CO_3 (1 M, HIMEDIA, pureté 99,5 %). La solution contenant les sels métalliques est ajoutée goutte à goutte à 200 mL d'eau déminéralisée chauffée à une température de 60°C, dont le pH est ajusté à 10 par une solution basique de NaOH et Na_2CO_3. Suite à l'addition, le mélange est maintenu pendant 2 heures sous agitation à 300 tr/min à 60°C. Il est ensuite placé dans l'étuve à 60°C pendant 24 heures afin de cristalliser lentement la phase hydrotalcite.

Le précipité ainsi obtenu, est filtré et lavé avec de l'eau déminéralisée chaude (60°C) (700 mL) en vue d'éliminer les ions Na^+. Le solide ainsi obtenu est séché à 60°C pendant 48 heures, et broyé avant d'être caractérisé.

Un rapport atomique $\frac{n_{cations(II)}\,(Mg^{2+}+Co^{2+})}{n_{cations(III)}\,(Al^{3+})}=3$ a été choisi. Les échantillons ainsi obtenus sont nommés Co_6Al_2HT, $Co_4Mg_2Al_2HT$, $Co_2Mg_4Al_2HT$ et Mg_6Al_2HT. La terminologie HT signifie que les échantillons sont préparés par voie hydrotalcite.

Les solides HT sont calcinés sous flux d'air sec de 33 $mL.min^{-1}$ à 500°C (1°C/min, 4 h) afin d'obtenir des oxydes mixtes qui seront testés dans la réaction d'oxydation totale des particules carbonées et du propène. Le choix du palier de calcination à 500°C a été décidé par rapport aux résultats de l'analyse thermique gravimétrique (ATG) révélant qu'à cette température le solide de type hydrotalcite est totalement décomposé en oxyde stable.

2.2 Imprégnation du précurseur nitrate de nitrosyle ruthénium et du nitrate de cuivre sur les supports calcinés

L'objectif de l'imprégnation est d'obtenir la meilleure dispersion possible de l'agent précurseur de façon à ce que la phase active obtenue par décomposition ultérieure soit elle-même bien dispersée, ce qui contribue à une meilleure réactivité des solides.

Les solides $Co_xMg_{6-x}Al_2$ calcinés ont été imprégnés par du ruthénium et aussi par du cuivre. L'imprégnation du ruthénium a été faite par imprégnation à sec et celle du cuivre par imprégnation par excès de volume. La synthèse des solides imprégnés sera détaillée dans ce qui suit.

La synthèse des catalyseurs imprégnés par du ruthénium a été réalisée par imprégnation à sec du ruthénium, sous la forme d'une solution nitrate de nitrosyle ruthénium(III) $Ru(NO)(NO_3)_3$ (ACROS organics), à 1,65% en masse de ruthénium, sur les différents supports préalablement calcinés. Pour réaliser cette imprégnation, un volume défini de la solution $Ru(NO)(NO_3)_3$ est prélevé. Ce volume est déterminé grâce au pourcentage massique de Ru souhaité qui est de 1% dans notre cas, et est introduit sur une masse adéquate de support présente dans un cristallisoir. Ensuite le mélange est agité par un agitateur magnétique pendant 1 h. Le solide obtenu est finalement placé dans l'étuve à 100°C pendant environ 20 heures.

Une autre façon d'imprégnation a été utilisée dans le cas du cuivre. Une masse adéquate du précurseur nitrate de cuivre II $Cu(NO_3)_2.3H_2O$ (PROLABO, 99%) choisie de façon à obtenir le pourcentage massique de Cu souhaité, 5% dans notre cas, a été diluée dans 100 mL d'eau déminéralisée. Les 100 mL de solution sont ensuite ajoutés sur le support. Le tout est mélangé pendant 2 heures. Ensuite, l'eau est lentement évaporée à l'évaporateur rotatif (75°C, sous vide primaire, 60 tours/min). Le résidu sec obtenu est mis dans l'étuve à 100°C pendant 20 heures.

3 Caractérisation des Catalyseurs

Les supports ainsi que les catalyseurs stabilisés ont été par la suite caractérisés par différentes techniques physico-chimiques avant et après tests catalytiques:

- Microscopie électronique à balayage (MEB) couplée à l'analyse par spectrométrie à dispersion d'énergie (EDX)
- Analyse Thermogravimétrique et Différentielle (ATG/ATD)

- Diffraction des rayons X (DRX)
- Brunauer Emmet Teller (BET)
- Réduction et oxydation en Température Programmée (RTP-OTP)
- Spectroscopie Infrarouge à Transformée de Fourier (IRTF)
- Porosimétrie
- Résonance paramagnétique électronique (RPE)

3.1 Microscopie électronique à balayage (MEB) couplée à l'analyse par spectrométrie à dispersion d'énergie (EDX)

Les catalyseurs hétérogènes sont souvent complexes de par la composition, la texture et la structure des phases présentes. Leur étude par microscopie électronique permet de les visualiser avec un pouvoir de résolution modulable entre 10^{-4} et 10^{-8} m. La spectrométrie à dispersion d'énergie EDX (Energy-dispersive X-ray spectroscopy) couplée au MEB permet la détermination de la composition chimique de la surface examinée.

Un microscope de type SERON ASI-210 a été utilisé pour observer la morphologie des catalyseurs et définir les tailles des particules. Cependant cet appareil ne peut pas détecter des particules de taille inférieure à 500 nm. Préalablement à l'étude MEB, les échantillons ont été pulvérisés par un faisceau de carbone graphite afin de les rendre conducteurs et éviter l'accumulation d'électrons sur les solides. Les études MEB ont été effectuées sous un vide de10^{-6} torr avec une tension accélératrice de 20 ou 25 kV. Des images à différents agrandissements ont été prises. Une analyse EDX à l'aide d'un détecteur EDX-EDAX a suivi l'étude MEB de certains échantillons après test catalytique.

L'étude par microscopie électronique à balayage des solides calcinés, a montré pour les catalyseurs contenant du cobalt, une forme irrégulière des particules avec une inhomogénéité dans la répartition des tailles. Alors que pour le catalyseur $1Ru/Mg_6Al_2$, les particules sont sous la forme de plaquettes désordonnées. L'analyse EDX des catalyseurs à base de ruthénium montre que le rapport atomique est respecté.

3.2 Analyses Thermiques Différentielle (DSC) et Gravimétrique (TG)

L'analyse Thermogravimétrique, ATG ou TG sert à mesurer le gain ou la perte de masse de l'échantillon en fonction de la température et du temps pour caractériser le changement de phase résultant d'une décomposition, d'une déshydratation ou d'une oxydation.

Le module TG/DSC combine deux techniques d'analyses thermiques :

- La première sert à la mesure du gain ou de la perte de masse de l'échantillon en fonction de la température et du temps – Analyse Thermogravimétrique, ATG ou TG. L'analyse TG est utilisée pour caractériser le changement de masse résultant d'une décomposition, d'une déshydratation ou d'une oxydation.
- La seconde sert à la mesure de la différence de température due aux changements d'enthalpie de l'échantillon chauffé uniformément en fonction de la température et du temps – Calorimétrie Différentielle à Balayage, DSC (Differential Scanning Calorimetry).

Ces deux mesures s'effectuent simultanément sur un appareil NETZSCH STA 409 de la température ambiante jusqu'à 1000°C (montée en température de 5°C.min^{-1}) sous un flux d'air sec de 75 mL.min^{-1}.

Les courbes ATD (figure 1.a) résultant de la calcination sous flux d'air des échantillons séchés montrent trois pics endothermiques. Chaque pic correspond à une perte de masse (figure 1.b). Le premier pic correspond à la perte d'eau physisorbée à la surface externe des cristallites. Les pics 2 et 3 sont dus à l'effondrement de la structure hydrotalcite et la formation d'oxydes métalliques de type spinelle. L'allure des courbes ATD est modifiée progressivement lorsque Mg^{2+} est substitué par Co^{2+}, notamment pour le pic 3 qui a lieu à une température plus basse lorsque la substitution est plus avancée. Ceci révèle que la stabilité thermique des hydrotalcites change en fonction de la nature des cations qui sont présents dans la couche de type brucite. Ainsi, la stabilité thermique diminue lorsque la quantité de cobalt dans l'échantillon augmente.

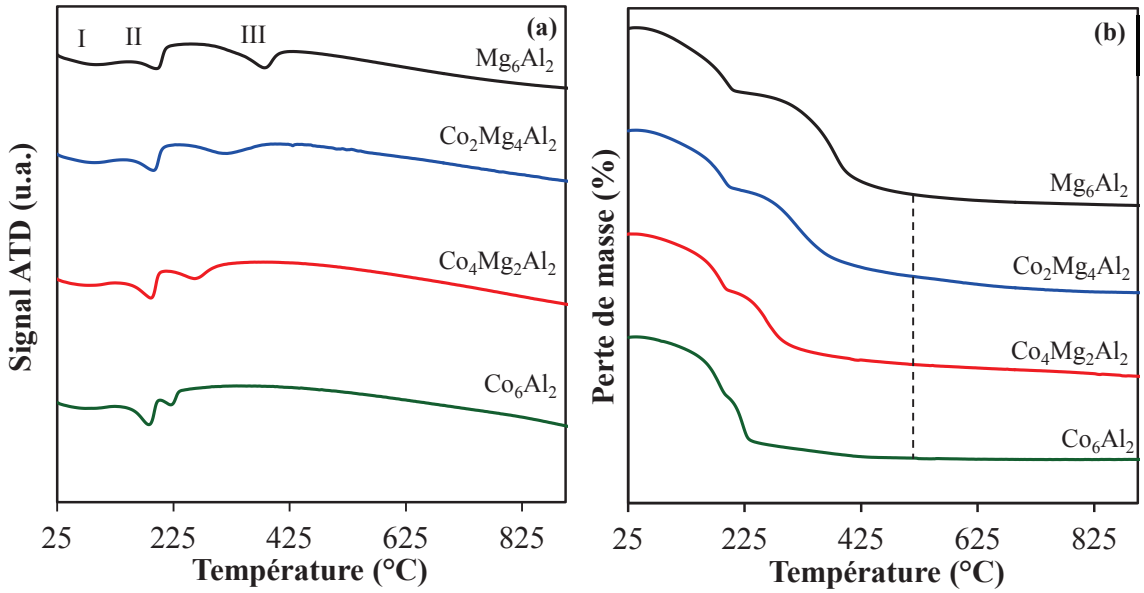

Figure 1 a) Signaux ATD et b) ATG obtenus au cours de la calcination sous air des solides $Co_xMg_{6-x}Al_2HT$

3.3 Diffraction des rayons X (DRX)

Cette technique permet de déterminer la nature des phases cristallisées d'un solide. En effet, un produit présentant la même composition chimique peut exister sous différentes phases cristallographiques. Celles-ci peuvent avoir des caractéristiques et des propriétés catalytiques distinctes. Les analyses DRX ont été réalisées sur un diffractomètre BRÜKER AXS D8 Advance à température ambiante. Ce diffractomètre est équipé d'une anticathode en cuivre émettant la radiation Kα. Les conditions générales d'acquisition correspondent à une plage angulaire en 2θ allant de 20 à 80° avec un pas de mesure de $0{,}02^0$ pour une durée d'intégration de 2 s. Les phases cristallines sont identifiées en comparant les diffractogrammes avec ceux de composés de références dans la base de données du « Joint Committee on Powder Diffraction Standards » (JCPDS).

Les diffractogrammes des rayons X des solides séchés $Co_xMg_{6-x}Al_2$ montrent la présence de la phase hydrotalcite. Après calcination, les clichés DRX de ces solides calcinés montrent l'absence de pics dus à la phase hydrotalcite. Ceci est en accord avec les résultats de l'analyse thermique où des pics endothermiques attribués à la destruction de la structure hydrotalcite ont été détectés. Seules les raies de diffraction de l'oxyde de magnésium MgO, de type périclase sont

observées pour l'échantillon Mg_6Al_2. Pour les solides à plus forte teneur en Co, les différents pics observés peuvent être attribués à ceux d'une structure de type spinelle.

Les résultats de DRX (figure 3) obtenus pour les catalyseurs contenant le cuivre montrent les raies de diffraction X des phases spinelles contenant le cobalt. Ces raies sont analogues à celles des supports correspondants. Les raies du MgO de type périclase sont présentes pour le catalyseur $5Cu/Mg_6Al_2$ mais ces raies sont moins intenses et plus larges que celles des supports avant imprégnation. Une raie de diffraction marquée attribuée à l'oxyde de cuivre CuO sous la forme ténorite est observée pour tous les catalyseurs. Cette raie est plus intense dans le cas des catalyseurs $15Cu/Co_6Al_2$ et $25Cu/Co_6Al_2$. Il semble donc que les espèces oxyde de cuivre sont plus agglomérées sur les échantillons à forte teneur en cuivre.

De même, les clichés DRX (figure 2) des catalyseurs $Ru/Co_xMg_{6-x}Al_2$ montrent que les raies des différents spinelles sont observées pour les catalyseurs contenant le cobalt.

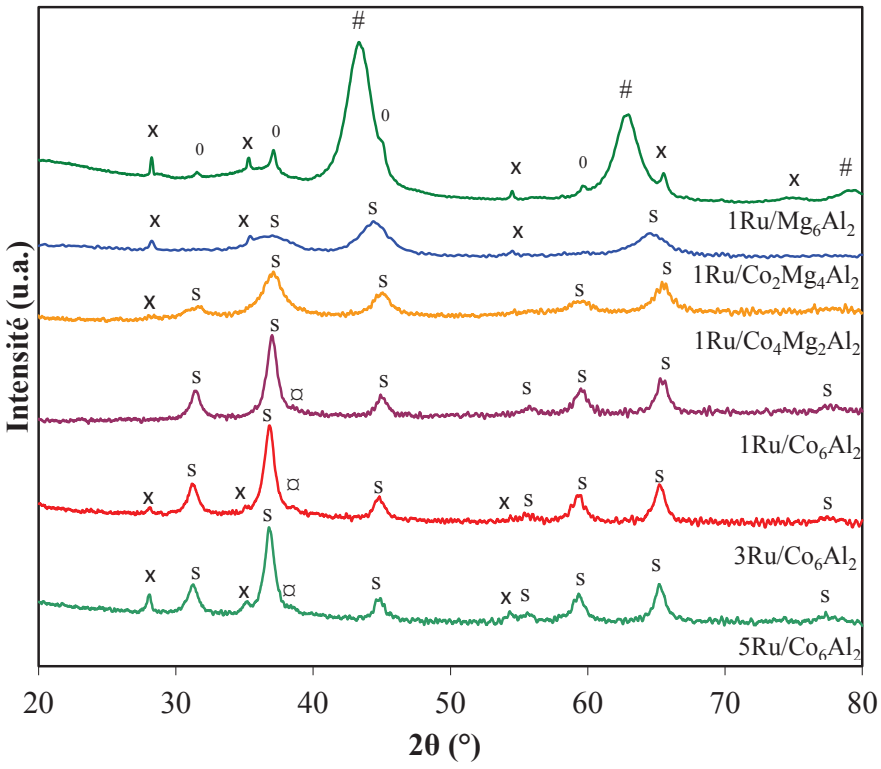

Figure 2 Diffractogrammes de rayons X des solides $Ru/Co_xMg_{6-x}Al_2$

Par contre, le support Mg_6Al_2 qui montrait en DRX les raies de diffraction du MgO périclase, montrent après imprégnation par le ruthénium, en plus de ces raies, des raies marquées x qui sont dues à l'oxyde de ruthénium RuO_2 quadratique. Il en est déduit que l'interaction du

ruthénium avec le support riche en magnésium est différente que celles avec les supports plutôt riches en cobalt. L'interaction du ruthénium avec les supports riches en cobalt induirait une dispersion des espèces RuO_2 qui empêche leur détection par DRX. Il apparaît que les espèces oxydes de ruthénium tendent à s'agglomérer sur les supports riches en magnésium formant ainsi des espèces détectables par DRX.De plus, les catalyseurs à forte teneur en ruthénium ($3Ru/Co_6Al_2$ et $5Ru/Co_6Al_2$) montrent la présence de l'oxyde de ruthénium RuO_2 agglomérées sur les échantillons.

Les solides Co_6Al_2, $1Ru/Co_6Al_2$ et $5Cu/Co_6Al_2$ calcinés à 800°C présentent des raies intenses en raison de l'augmentation de la cristallinité à cause de la température de calcination la plus élevée.

3.4 La mesure de la surface spécifique des solides par la méthode Brunauer, Emmet et Teller (BET)

Les catalyseurs présentent à leur surface des pores de tailles différentes qui augmentent la surface de contact avec le milieu extérieur, c'est la surface active du catalyseur. La valeur de la surface spécifique étant directement liée à la porosité du solide, ce paramètre est très important en catalyse hétérogène où une grande aire spécifique est recherchée. Les aires spécifiques des solides ont été mesurées à l'aide d'un appareil Qsurf M1 (Thermo Electron). La mesure a été effectuée par la méthode BET (Brunauer, Emmet, Teller) par adsorption d'azote à sa température de liquéfaction (- 196°C) sur le solide.

La détermination de la surface spécifique a été faite pour les solides $Co_xMg_{6-x}Al_2$ avant et après calcination à 500ºC. Les résultats obtenus pour les hydrotalcites séchées indiquent que l'échantillon Mg_6Al_2 présente l'aire spécifique la plus élevée. Cette valeur diminue pour les HT où le Mg est partiellement remplacé par le Co. En revanche, les aires spécifiques les plus faibles sont observées lorsque Mg est totalement substitué par Co. Après calcination, les aires spécifiques augmentent pour tous les solides. Conformément aux résultats de la DRX, les solides séchés sont en phase hydrotalcite donc forme cristallisée. Après calcination à 500ºC, les structures hydrotalcite sont détruites, les solides perdent alors leur état cristallisé et par suite leur surface spécifique augmente.

Après imprégnation de la phase active, on remarque que la surface spécifique du catalyseur $1RuCo_6Al_2$ est presque la même par rapport à Co_6Al_2. Pour les autres solides, on remarque une diminution drastique de la surface spécifique entre les catalyseurs et leurs supports

relatifs. Ceci peut être expliqué par le fait que les oxydes de cuivre et de ruthénium agglomérés bloquent les pores de la surface de support conduisant à une diminution de la surface spécifique.

Les surfaces spécifiques des catalyseurs yRu/Co_6Al_2, zCu/Co_6Al_2 calciné à 500°C (où y= 0,5, 1, 3, 5 et z= 0,5, 3, 5, 15, 25) montrent une diminution de la surface avec des teneurs plus élevées de la phase active. Ceci est attribué à la présence d'agglomérats de RuO_2 et CuO (détecté dans DRX) en raison d'une faible interaction entre le support et la phase active. Ces agglomérats peuvent boucher les pores de la surface et de diminuer la surface spécifique. Il est à noter que la surface spécifique diminue significativement avec l'augmentation de la température de calcination où des échantillons calcinés à 500°C présentent des surfaces plus élevés par rapport à ceux calciné à 800°C. Cette diminution de la surface spécifique des catalyseurs calcinés à 800°C est due à l'augmentation de la cristallisation des solides.

3.5 Réduction en Température Programmée (RTP)

Une étude RTP a été effectuée dans le but d'étudier le comportement redox des systèmes catalytiques. L'appareil utilisé est un système AMI-200 de marque ZETON ALTAMIRA qui permet d'effectuer des analyses de Réduction en Température Programmée (RTP). L'analyse est composée de trois parties :

- Une première partie qui consiste en la calibration de la consommation d'hydrogène. Cinq pulses de calibration sont effectués avec des débits de gaz de 30 $mL.min^{-1}$ aussi bien pour l'argon que pour le mélange 5% H_2/Ar qui sera utilisé lors de l'analyse proprement dite.
- Une deuxième partie qui consiste en un prétraitement de l'échantillon sous argon (30 $mL.min^{-1}$) de la température ambiante jusqu'à 150°C avec une montée en température de 5°$C.min^{-1}$ puis une descente en température à raison de 5°$C.min^{-1}$ jusqu'à la température ambiante afin d'activer le catalyseur en éliminant l'eau et les impuretés déposées sur la surface.
- Une troisième partie où s'effectue une réduction en température programmée. Le gaz utilisé est l'hydrogène dilué dans l'argon (5%vol. H_2) à raison de 30 $mL.min^{-1}$. L'analyse est effectuée de la température ambiante jusqu'à 900°C avec une rampe de température de 5°$C.min^{-1}$ et un palier d'une heure à 900°C.

Les profils de réduction en température programmée RTP des supports $Co_xMg_{6-x}Al_2$ montrent que Mg_6Al_2 ne se réduit pas d'une manière significative dans nos conditions dans le domaine de température étudié. Cette absence de réduction s'explique par le fait que les oxydes

de magnésium et/ou d'aluminium ne se réduisent pas facilement dans ce domaine de température. Par contre les supports contenant du cobalt montrent deux pics de réduction, un premier entre 300°C et 360°C attribué à la réduction de Co_3O_4 en Co(0) et un deuxième à des températures supérieures à 600°C correspond à la réduction des espèces Co^{2+}-Al^{3+} ou Co^{3+}-Al^{3+}.

Les résultats de la RTP des catalyseurs imprégnés par le cuivre montrent un pic de réduction à des températures comprises entre 150°C et 230°C est observé pour tous les catalyseurs attribué à la réduction simultanée des espèces d'oxydes de cuivre et de cobalt. La réductibilité des espèces de cobalt est facilitée par la présence du Ru^{4+} puisque la température du maximum de ce pic diminue après impregantion. Les catalyseurs $5Cu/Co_2Mg_4Al_2$ et $5Cu/Co_4Mg_2Al_2$ montrent un pic situé vers 320°C attribué à la réduction de nouvelles espèces oxydes mixtes de cuivre-cobalt, qui se forment en présence du magnésium. Un troisième pic vers les hautes températures est attribuable à la réduction des espèces Co^{3+}-Al^{3+} ou Co^{2+}-Al^{3+}.

Pour les catalyseurs à base du ruthénium (figure 3), on a considéré que c'est l'oxyde de ruthénium RuO_2 qui est présent dans les échantillons préalablement calcinés à 500°C. Tout d'abord, le catalyseur $1Ru/Mg_6Al_2$ montre un pic vers 355°C ayant deux sommets suivi d'un épaulement à 455°C.

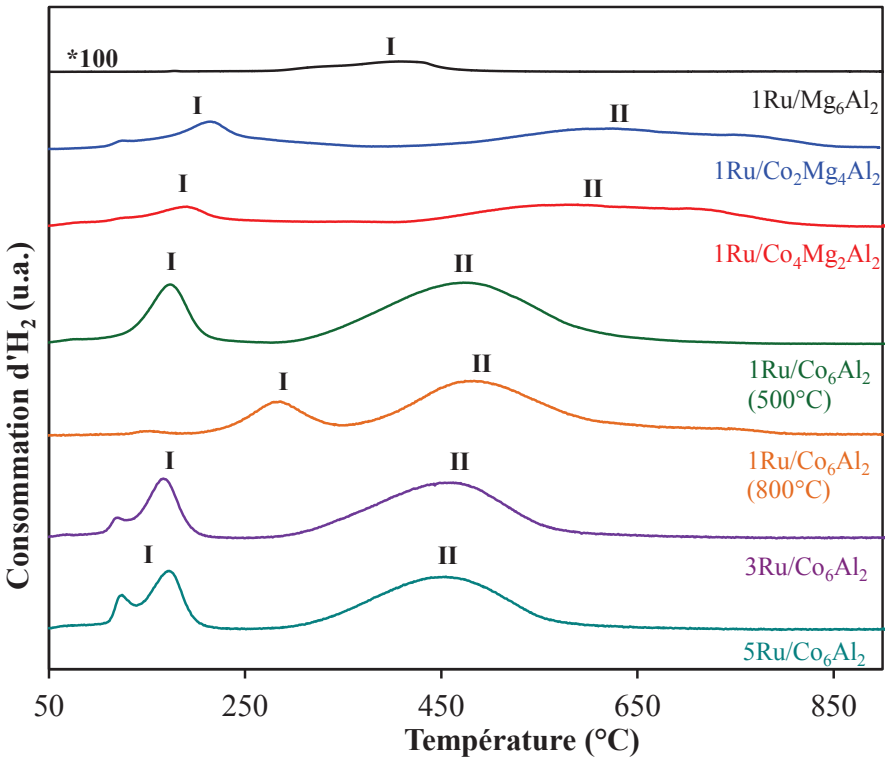

Figure 3 Profils RTP des solides $Ru/Co_xMg_{6-x}Al_2$

Ce pic est attribué à la réduction d'espèces oxyde de ruthénium ayant des tailles différentes. D'ailleurs, l'étude DRX a mis en évidence l'existence d'espèces oxyde de ruthénium dans ce catalyseur. Les échantillons $1Ru/Co_2Mg_4Al_2$ et $1Ru/Co_4Mg_2Al_2$ montrent deux pics de réduction, le premier vers 150°C attribués à la réduction simultanée des espèces oxydes de cobalt et de ruthénium et le deuxième vers 750°C est attribuable à la réduction des espèces Co^{3+}-Al^{3+} ou Co^{2+}-Al^{3+}. La température de ce dernier diminue quand la teneur en cobalt augmente.

3.6 Spectroscopie Infrarouge à Transformée de Fourier (IRTF)

La Spectroscopie Infrarouge à Transformée de Fourier (IRTF) permet l'analyse des fonctions chimiques présentes dans une substance par la détection des vibrations caractéristiques des liaisons chimiques. Les analyses IRTF ont été effectuées à température ambiante sur un spectromètre BRKER EQUINOX 55 FTIR équipé de détecteurs DTGS et MCT.

Les analyses par spectroscopie infrarouge des solides $Co_xMg_{6-x}Al_2$ séchés montrent trois types de bandes de vibrations qui caractérisent les structures de type hydrotalcites. Les spectres IR de ces solides calcinées sont en accord avec la destruction de la phase hydrotalcite et les ions carbonates sont quasiment absents des spectres. Les spectres infrarouges des solides $1Ru/Co_xMg_{6-x}Al_2$ et $5Cu/Co_xMg_{6-x}Al_2$ séchés sont similaires à ceux obtenus pour les hydrotalcite avant calcination. De plus, un léger épaulement peut être attribué à l'élongation de Ru-OH et Cu-OH. Apres calcination des catalyseurs, les bandes caractéristiques des structures spinelles sont observées.

3.7 Porosimétrie

La calcination des hydrotalcites contenant des carbonates ou des nitrates en interfeuillet entraine une caractérisation du solide conduisant à des oxydes poreux. L'étude de la porosité du solide est d'autant plus importante que les pores présents à la surface augmentent la surface de contact et donc la probabilité d'adsorption d'entités réactionnelles sur le catalyseur. L'interprétation des isothermes d'adsorption-désorption est riche en informations sur la texture de l'adsorbant. Parmi les principaux paramètres qui peuvent être évalués, signalons la surface spécifique, la distribution poreuse mais aussi des informations sur la structure (forme des pores). L'analyse de l'échantillon a été réalisée à l'aide d'un appareil Sorptomatic 1990 de Thermo Electron Corporation. C'est un appareil complètement automatisé équipé d'une pompe primaire

et d'une pompe turbomoleculaire permettant d'assurer un vide pendant le traitement et au début de chaque analyse.

Les isothermes d'adsorption et de désorption d'azote réalisées sur les supports calcinés montrent des isothermes de type IV correspondant à un matériau mésoporeux. Le remplacement du magnésium par du cobalt conduit à la modification e la forme des boucles d'hystérésis et de la distribution de la taille des pores. Pour Mg_6Al_2, la boucle est de type H4 associée à des pores en fentes avec des tailles de pores moyennes de 2nm. Pour les échantillons contenant du cobalt la boucle et de type H1 avec des branches d'adsorption et désorption parallèles associées à des pores tubulaires. De plus, après échange avec du cobalt, les résultats mettent en évidence un élargissement des pores vers les mésopores moyens de 2 à 6 nm pour $Co_2Mg_4Al_2$, 14 nm pour $Co_4Mg_2Al_2$ et 8 nm pour Co_6Al_2.

3.8 Résonance paramagnétique électronique (RPE)

La RPE est largement utilisée dans l'étude des environnements d'espèces ayant un ou plusieurs électrons non appariés. La nature des informations obtenues peut varier de la simple confirmation de la présence d'une entité paramagnétique à la description détaillée de la symétrie, de l'état d'oxydation des atomes voisins, du nombre de ligands, de la nature des liaisons, et elle peut également détecter la présence ou non du coke sur la surface du catalyseur avec des grandes précisions. Les spectres RPE (S= 1/2 and I≠ 0) sont obtenus à partir de l'équation de l'hamiltonien de spin:

$$\mathcal{H} = \beta.H_z.g_{//}.S_z+\beta.H_x.g_{\perp}.S_x+\beta.H_y.g_{\perp}.S_y+A_{//}.I_z.S_z+A_{\perp}.I_y.S_y+ A_{\perp}.I_x.S_x$$

où le premier terme correspond à l'effet Zeeman, le second à la structure hyperfine et le troisième à la structure fine. Avec **H** : champ magnétique, **S** : spin électronique, **I** : spin nucléaire, **A** : constante du couplage hyperfin et **D** : constante d'interaction dipolaire.

Le facteur « g » et la constante de couplage hyperfin **A** sont les deux paramètres RPE importants, caractéristiques d'une espèce paramagnétique présente dans un environnement donné. Le facteur « g » est déterminé à une fréquence et à un champ magnétique donnés d'après la relation:

$$h.\nu = g.\beta.\mathbf{H}$$

avec **h** constante de Planck, **β** magnéton de Bohr électronique, **H** le champ magnétique et ν la fréquence.

L'appareil utilisé est un spectromètre EMX de marque BRUKER fonctionnant à une fréquence voisine de 9,5 GHz (bande X). Le champ magnétique est modulé à 100 kHz. Tous les spectres ont été enregistrés avec une puissance de 12,6 mW de façon à éviter la saturation du signal. La fréquence ν et le champ H sont mesurés simultanément. Tous les spectres ont été enregistrés à température ambiante et à la température de l'azote liquide (-196°C). Les spectres obtenus ont été traités grâce au programme WINEPR développé par la société BRUKER.

Les spectres RPE du catalyseur $1Ru/Mg_6Al_2$ traité à 125°C, 250°C et 350°C présentent une anisotropie axiale. Le signal observé peut être attribué aux ions Ru^+. L'intensité de ces spectres diminue avec l'augmentation de la température de traitement en raison de la réduction de Ru^+ en Ru^0. Un autre signal d'environ g = 2,0023 est due à un électron piégé au cours de la réduction d'espèces de ruthénium.

Les spectres RPE du catalyseur $5Cu/Mg_6Al_2$ calciné à 500°C et traité sous vide à des températures différentes (125°C, 250°C et 350°C) a montré une anisotropie axiale avec une structure hyperfine. Deux types d'espèces de cuivre (II) isolés peuvent être distingués. La première composante peut être attribuée aux ions Cu^{2+} situés dans des sites octaédriques dans la masse du support et qui ne sont pas facilement réduits. La deuxième composante Cu^{2+} peut être attribuée aux ions Cu^{2+} situés dans le centre d'un tétraèdre distordu à la surface du support et qui sont facilement réduits. Avec l'augmentation de la température du traitement, une diminution significative de l'intensité du signal est observée et due à la réduction des espèces de cuivre.

4 Vaporeformage du Méthane

4.1 Introduction

Parmi les réactions de reformage du méthane, le vaporeformage est le procédé le plus utilisé sur le plan industriel et plus récemment en combinaison avec l'oxydation partielle [11, 12]. Il conduit à l'obtention d'un mélange gazeux riche en hydrogène, présentant un rapport H_2/CO égale à 3, qui sert à la synthèse de plusieurs produits chimiques et au fonctionnement de piles à combustible.

Dans cette partie, la conversion du méthane en hydrogène par le procédé de vaporeformage est étudiée en présence des catalyseurs préparés afin d'évaluer leur performance catalytique dans cette réaction. La première étude est menée sur des catalyseurs à base de ruthénium et de cuivre à différentes teneurs en métal dans le but de définir les catalyseurs les plus performants. L'influence de différents paramètres tels que la température de réaction, la nature de

support, la température de calcination, la vitesse spatiale horaire du gaz (VSHG) et le rapport H_2O/CH_4 sont étudiés également. L'ajustement de ces paramètres permet en effet d'améliorer le procédé de vaporeformage du méthane. Des tests de vieillissement seront menés sur les catalyseurs présentant les meilleures performances. Les catalyseurs étudiés sont caractérisés après l'ensemble des tests afin d'étudier leur état final et d'expliquer les éventuelles évolutions de leur activité catalytique. Enfin, Les résultats catalytiques obtenus par les catalyseurs du laboratoire sont comparés avec ceux obtenus par les catalyseurs industriels.

4.2 Dispositif Expérimental et Conditions Opératoires

Les tests catalytiques ont été réalisés à pression atmosphérique, dans un réacteur à lit fixe. Le dispositif expérimental a été conçu pour permettre d'étudier les différentes réactions de reformage du méthane en hydrogène et oxydes de carbone, ainsi que l'influence de certains paramètres (température, rapport H_2O/CH_4, etc.).

L'étude de la réaction de vaporeformage du méthane a été réalisée en variant plusieurs paramètres du test :

- Le mélange gazeux contient : 30 mL/min d'Ar, 5-15 mL/min d'H_2O (g) et 5 mL/min du méthane. Le rapport molaire H_2O/CH_4 est égal à 1, 2, 3 et 4.
- Le débit volumique total de gaz introduit est gardé constant et a été fixé à 50 mL/min (soit 3 L/h) pour une masse du catalyseur comprise entre 25 mg et 200 mg.
- Les tests catalytiques sont réalisés à pression atmosphérique dans un réacteur à lit fixe en quartz. Le réacteur est chargé avec le catalyseur (tailles de particules comprises entre 20 et 40 μm) et est porté par un verre fritté de manière à être positionné dans la zone de température uniforme du four.
- La gamme de température des expériences (400°C -800°C) a été choisie pour tous les catalyseurs testés.

Le schéma du montage expérimental comprend trois parties principales:

- Un système d'introduction et de régulation des réactifs.
- Le réacteur catalytique avec un régulateur de la température.
- Un système analytique de détection et de quantification des produits gazeux formés.

4.3 Résultats Expérimentaux

La réactivité catalytique des supports $Co_xMg_{6-x}Al_2$ a montré qu'en augmentant la teneur du cobalt, la quantité d'H_2 produite croit et la conversion du méthane est plus importante. Au contraire, en augmentant la teneur en magnésium, la quantité du CO formée est plus élevée et la conversion du méthane est moins importante. Après imprégnation du ruthénium et du cuivre, une amélioration remarquable de la réactivité catalytique des catalyseurs est observée par rapport à ceux des supports (figure 4). Ensuite, le système ayant comme support Co_6Al_2 demeure le plus actif et celui ayant comme support Mg_6Al_2 est le moins actif. Un comportement intermédiaire est observé pour les 2 autres catalyseurs. L'étude des catalyseurs avant test par DRX a montré la présence des agglomérats de ruthénium et du cuivre pour les catalyseurs contenant du magnésium. Ceci explique la diminution de la réactivité en augmentant la teneur en magnésium dans le support. De ce fait, les catalyseurs à base du ruthénium et cuivre supportés sur Co_6Al_2 seront retenus pour la suite de l'étude.

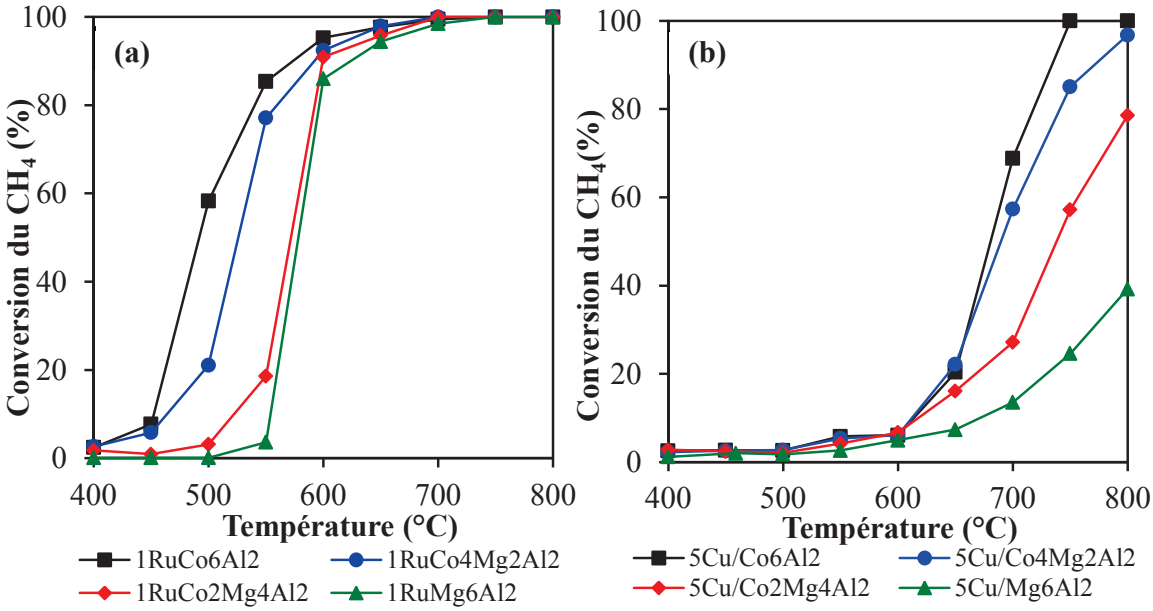

Figure 4 Conversion du CH_4 (%) en présence des catalyseurs a) $1Ru/Co_{6-x}Mg_xAl_2$ et b) $5Cu/Co_{6-x}Mg_xAl_2$

Afin d'optimiser la teneur de la phase active, de différentes teneurs en ruthénium (0.5, 1, 3 et 5% en masse) et cuivre (0.5, 3, 15 et 25%) sont imprégnées sur Co_6Al_2. Les résultats de conversion du méthane et les concentrations en hydrogène montrent clairement que la conversion

du méthane et la quantité d'H_2 produite augmentent avec la teneur du ruthénium mais seulement à basses températures. Ceci indique que le ruthénium est le site d'activation du méthane. Des conversions de méthane très proches sont obtenues à partir de 550°C pour les catalyseurs ayant une teneur plus grande ou égale à 1. Pour les catalyseurs à base de cuivre, on remarque que $15Cu/Co_6Al_2$ et $25Cu/Co_6Al_2$ présentent une grande production d'H_2 à des basses températures, A des températures plus élevées, $3Cu/Co_6Al_2$ et $5Cu/Co_6Al_2$ montrent une conversion de méthane plus importante. Cette diminution de la performance catalytique en fonction de la teneur en ruthénium et cuivre peut être expliquée par la présence des espèces agglomérées de RuO_2 et CuO qui sont détectées par l'étude par DRX. De même, l'étude RTP a également montré de nombreux pics de réduction attribués à la présence de plusieurs types d'espèces de Ru^{4+} et Cu^{2+} en interaction avec le support.

La variation du rapport H_2O/CH_4 a été étudiée en présence des catalyseurs pour obtenir des résultats de conversion convenables dans la réaction de vaporeformage du méthane $1Ru/Co_6Al_2$ et $5Cu/Co_6Al_2$ (figure 5).

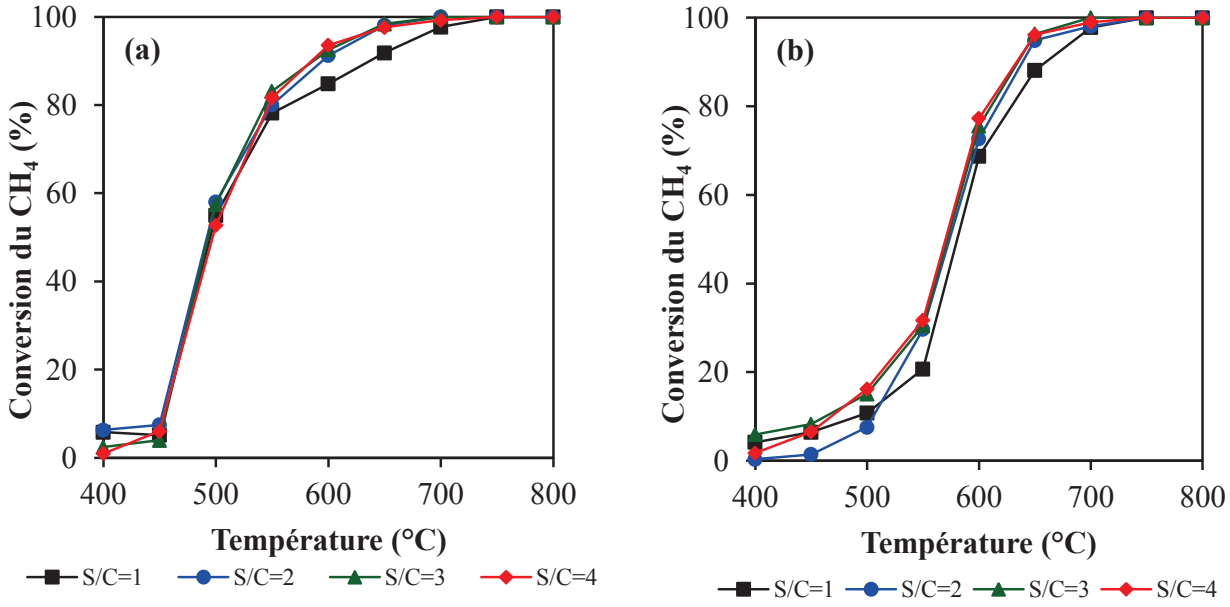

Figure 5 Conversion du CH_4 (%) en présence des catalyseurs a) $1Ru/Co_6Al_2$ et b) $5Cu/Co_6Al_2$ en utilisant les rapports eau/méthane (S/C) = 1, 2, 3 et 4

Une faible réactivité est observée dans le cas du rapport H_2O/CH_4= 1. Ceci est expliqué par le fait que, dans les conditions opératoires moins oxydantes, la réaction de gaz à l'eau est moins favorisée, ce qui limite la quantité d'hydrogène produite dans le mélange gazeux et par

conséquent une formation plus difficile des sites métalliques actifs. Une forte réactivité observée à 600 et 650°C lorsqu'on utilise un rapport H_2O/CH_4 = 2, 3 ou 4. Ceci est dû la formation plus facile des sites métalliques actifs engendrés par l'hydrogène produit par la réaction de vaporeformage du méthane et la réaction de gaz à l'eau. En addition, l'évolution de la sélectivité en CO et le rapport molaire H_2/CO montrent que les rapports H_2O/CH_4 plus grand que 1(et surtout le rapport = 3) favorisent la réaction de conversion du gaz de l'eau conduisant à des rapports H_2/CO plus élevé et une faible sélectivité en CO.

Dans la réaction de vaporeformage du méthane, les espèces métalliques sont considérées comme phase active. Par conséquent, les catalyseurs $1Ru/Co_6Al_2$ et $5Cu/Co_6Al_2$ sont réduits avant test à 230°C pendant 1 heure sous H_2. Le $1Ru/Co_6Al_2$ prétraité indique une conversion plus élevée de méthane seulement à basse température par rapport au catalyseur non réduit, et après, la différence entre les deux courbes est dans la marge d'erreur expérimentale. Il apparaît donc que l'hydrogène produit par la conversion du méthane durant la réaction tend à générer les sites de ruthénium métallique par une réduction (in situ) similaire au processus de réduction sous hydrogène. Au contraire, le $5Cu/Co_6Al_2$ réduit présente une meilleure conversion dans le domaine de température étudiée. Cela peut indiquer que l'hydrogène produit au cours de la réaction n'est pas capable d'activer les sites actifs du cuivre.

En addition, l'étude de la vitesse spatiale horaire du gaz en présence des solides les plus performants montrent qu'une diminution de la VSHG (jusqu'à 15000 $mL.g^{-1}.h^{-1}$) augmente la conversion du méthane. Ceci peut être attribué à la vitesse d'activation des sites métalliques du catalyseur utilisé où une diminution de la VSHG renforce le temps de contact entre le méthane et le solide et par conséquent une activation des sites dans un temps plus court. De même, les rapports H_2/CO et les sélectivités en CO et CO_2, ont montré un profil identique à la conversion de CH_4.

Afin d'étudier l'influence de la température de calcination sur la réactivité catalytique, $1Ru/Co_6Al_2$ et $5Cu/Co_6Al_2$ ont été calcinés à 500°C et 800°C. Les 2 catalyseurs calcinés à différentes températures gardent le même profil au début de la réaction et à haute température. Cependant, entre 500°C et 650°C, le catalyseur calciné à 500°C est plus actif que celui calciné à 800°C. C'est également le cas pour le rapport H_2/CO où un rapport plus élevé dans le cas du catalyseur calciné à 500°C est observé. Pour expliquer la diminution des performances catalytiques des catalyseurs calcinés à 800°C, des analyses DRX et RTP ont été effectuées sur ces catalyseurs avant test. Les catalyseurs calcinés à 800°C montrent une diminution de la

consommation d'hydrogène par rapport aux même catalyseurs calcinés à 500°C, et le pic de consommation d'hydrogène attribué à la réduction de Co_3O_4 est décalé vers des températures plus élevées ce qui montre qu'il n'est pas bien interagi avec le ruthénium par rapport au catalyseur calciné à 500°C. De plus, les analyses DRX avant test montrent la présence des agglomérats de RuO_2 et une augmentation de la cristallinité pour le catalyseur calciné à 800°C. Alors la réduction du cobalt à haute température, la présence des agglomérats et l'augmentation de la cristallinité explique la faible réactivité catalytique du catalyseur calciné à 800°C. Nous pouvons donc conclure qu'il n'est pas nécessaire d'augmenter la température de calcination.

Afin de tester la stabilité du catalyseur $1Ru/Co_6Al_2$, dix cycles successifs ont été réalisés dans la réaction de vaporeformage du méthane. Le catalyseur a présenté une constante stabilité au cours des 10 cycles avec aucune désactivation observable. Le même catalyseur a été testé également dans le temps à une température constante de 550°C pendant une durée de 100 heures et a montré clairement que la conversion de CH_4 reste à peu près constante à environ 70% pendant le temps de réaction.

Enfin, les résultats catalytiques obtenus par le catalyseur $1Ru/Co_6Al_2$ préparé au laboratoire sont comparés avec ceux obtenus par le catalyseur industriel $5Ru/Al_2O_3$. Une nette différence a été observée entre les deux types de solides: la conversion du méthane sur le catalyseur du laboratoire est supérieure à celle des catalyseurs industriels à 600 et 650°C. Il a été démontré précédemment que lorsqu'on augmente la teneur en Ru on favorise la formation des agglomérats de RuO_2 et par conséquent on diminue les sites actifs du catalyseur. C'est la raison pour laquelle nous remarquons une différence entre les 2 catalyseurs. Par contre, à 800°C nous constatons que les profils des valeurs de conversion de CH_4 ont la même allure. En effet, à haute température dans la réaction de vaporeformage du méthane, l'effet thermique est plus dominant sur l'effet catalytique d'où les résultats très proches obtenus entre les solides étudiés.

Les catalyseurs étudiés ont été caractérisés après l'ensemble des tests de vaporeformage du méthane par DRX, TPO, ATD/ATG et RPE. L'étude par oxydation en température programmée (OTP) a montré la présence de 2 pics de consommation d'oxygène attribués à l'oxydation du ruthénium/cuivre et cobalt métallique qui sont réduis durant la réaction. Aucun pic de consommation d'oxygène correspondant à l'oxydation du coke n'a été observé entre 400°C et 500°C. De même la DRX et l'analyse ATD/ATG ont pu détecter la présence du ruthénium, cuivre et cobalt métallique. De plus, la phase hydrotalcite réapparaît après la réaction pour les catalyseurs contenant du magnésium à cause de la forte affinité du magnésium à l'eau conduisant

à la reconstruction de la phase hydrotalcite.

Les analyses précédentes n'ont pas révélé la présence des espèces carbonées lors de la réaction. C'est pour cela une étude RPE a été réalisée en raison de la grande sensibilité de cette technique vers les faibles teneurs en espèces paramagnétiques. Le spectre RPE enregistré à température ambiante pour le catalyseur $1Ru/Co_6Al_2$ après test en isotherme à 800°C a présenté un signal large qui peut être attribué à la présence d'une grande quantité d'espèces paramagnétiques et à l'augmentation de la conductivité de nos solides en raison de la réduction d'espèces paramagnétiques du cobalt. Tandis que le catalyseur $1Ru/Mg_6Al_2$ a présenté un comportement différent. Les spectres RPE enregistrés à température ambiante après test en présence du catalyseur $1Ru/Mg_6Al_2$ à partir de 600°C jusqu'à 850°C a montré un signal isotrope (S1) centrée à g = 2,0029 à partir de 650°C. Il est attribué à la présence d'espèces de carbone formé à la surface du catalyseur. L'intensité de ce signal augmente progressivement avec l'augmentation de la température. A 800°C, un signal (S2) centrée à g = 2,0032 Gauss a été observée. Il est attribué à la présence de coke produit lors de la réaction. Alors ces deux signaux correspondent à deux différentes espèces paramagnétiques: le carbone et le coke. En effet, le carbone est en général le produit de réaction de Boudouard qui est thermodynamiquement favorable au-dessus de 600°C, tandis que le coke est produit par la décomposition du méthane thermodynamiquement favorable à haute température (≥ 800°C). Alors, la RPE a pu détecter et identifier deux types d'espèces carbonées à la surface du catalyseur: le carbone et le coke.

5 Vaporeformage de l'Ethanol

5.1 Introduction

Sachant qu'il est difficile de stocker ou de liquéfier l'hydrogène, sa production «in situ» par vaporeformage de l'éthanol semble une solution parmi les plus prometteuses. Du point de vue environnemental, l'éthanol n'est toxique et il peut être facilement obtenu à partir de la biomasse [13]. Cependant, cette réaction souffre de la formation des sous-produits en particulier l'éthylène qui peut être transformé en carbone conduisant à l'empoisonnement du catalyseur [14]. Par conséquent, l'utilisation d'un catalyseur approprié permet d'éviter la formation de sous-produits ou les réformer. Dans cette partie, la réaction du vaporeformage de l'éthanol est étudiée en absence et en présence de la phase active. En outre, l'influence de certains paramètres tels que la nature du support, la nature et la teneur de la phase active et son contenu, et le rapport eau/carbone seront discutés. Des tests de vieillissement seront menés sur les catalyseurs

présentant les meilleures performances. Les catalyseurs étudiés seront caractérisés par ATD/ATG, DRX et RPE après l'ensemble des tests.

5.2 Dispositif Expérimental et Conditions Opératoires

Le schéma du montage expérimental de la réaction du vaporeformage de l'éthanol est le suivant: un système d'introduction et de régulation des gaz vecteurs et une pompe qui envoie le mélange eau/éthanol. Le méthanol gazeux est entraîné sous pression atmosphérique dans le circuit par le gaz vecteur vers le four où se trouve le réacteur en quartz contenant le catalyseur à étudier. Un condenseur est placé à la sortie du réacteur et à l'extérieur du four dans un bain de glace afin de condenser les sous-produits obtenus ainsi que l'éthanol non converti. Les produits gazeux de la réaction sont injectés automatiquement et analysés par une micro-GC. Les condensats récupérés après test sont placés dans des vials puis analysés par CPG afin d'identifier les sous-produits formés au cours de la réaction.

L'étude de la réaction de vaporeformage de l'éthanol a été réalisée en variant plusieurs paramètres du test:

- La gamme de température des expériences est entre 300°C et 500°C.
- Le rapport molaire H_2O/carbone = 0.75, 1.5 et 3.
- Une masse du catalyseur est égale à 150 mg.

5.3 Résultats Expérimentaux

La réactivité catalytique des supports $Co_xMg_{6-x}Al_2$ a montré que lorsque la température augmente de 300°C à 500°C, les productivités en H_2, CO_2 et CH_4 augmentent. De plus, la productivité en H_2 et CO_2 augmente avec la teneur en cobalt. En outre, l'analyse qualitative des condensats à 450°C révèle la présence de l'éthanol, l'acétone et l'acétaldéhyde pour les supports contenant du cobalt, tandis que l'éthanol et l'acétaldéhyde ne sont pas identifiés dans le cas de Mg_6Al_2. Après imprégnation des phases actives, une amélioration remarquable de la réactivité catalytique des catalyseurs est observée par rapport à ceux des supports.

Les productivités en H_2, CH_4, CO et CO_2 en présence du catalyseur $5Cu/Co_6Al_2$ augmentent avec la température jusqu'à 450°C, puis diminuent à 500°C et des traces de CO sont observés (figure 6). La diminution de la productivité à 500°C est peut être due à la formation du coke qui désactive le catalyseur. En parallèle, l'analyse des condensats montre la présence de

l'acide acétique, l'acétaldéhyde et de l'éthanol non réagi à partir de 300°C. A 450°C et 500°C l'éthanol est 100% converti et les autres produits sont détectés mais en faible quantité. A partir de ces résultats, on peut conclure que 450°C est la température la plus appropriée puisque l'éthanol est totalement converti avec un maximum d'hydrogène produit et seulement des traces de CO et sous-produits sont détectés. Par conséquent, cette température est utilisée pour le reste des tests catalytiques.

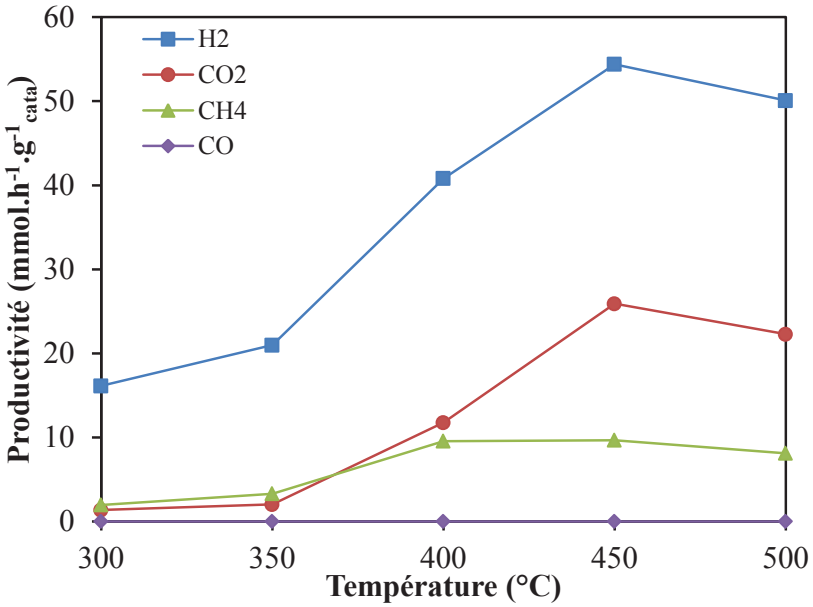

Figure 6 Productivités en H_2, CO_2, CH_4 et CO (mmol.h^{-1}.g^{-1}_{cata}) de 300°C à 500°C en présence du catalyseur 5Cu/Co_6Al_2 (S/C= 1.5)

Les résultats des tests catalytiques à 450°C en présence des 4 catalyseurs à base de cuivre ayant 4 différents supports ont montré que les productivités en dioxyde de carbone et hydrogène augmentent avec la teneur en cobalt (figure 7). Le méthane obtenu peut être produit à partir du vaporeformage de l'acétaldéhyde et de la réaction de décomposition de l'éthanol. De nombreux sous-produits sont identifiés pour les catalyseurs à l'exception du 5Cu/Co_6Al_2 comme l'acide acétique, l'acétone, l'acétaldéhyde, l'acétate d'éthyle, et l'éthanol non- réagi. Parmi ces catalyseurs, seul le 5Cu/Co_6Al_2 présente la productivité la plus élevée en hydrogène et une conversion totale de l'éthanol alors il sera retenu pour le reste des tests catalytiques. Il faut noter qu'en comparant les catalyseurs à base de cuivre à ceux à base de ruthénium, on remarque que les productivités en H_2, CO_2 et CH_4 à 450°C en présence des catalyseurs 1Ru/$Co_4Mg_2Al_2$ et

1Ru/$Co_2Mg_4Al_2$ sont plus élevées que celles en présence de 5Cu/$Co_4Mg_2Al_2$ et 5Cu/$Co_2Mg_4Al_2$. Cependant, 5Cu/Co_6Al_2 reste le meilleur catalyseur parmi le reste des solides préparés.

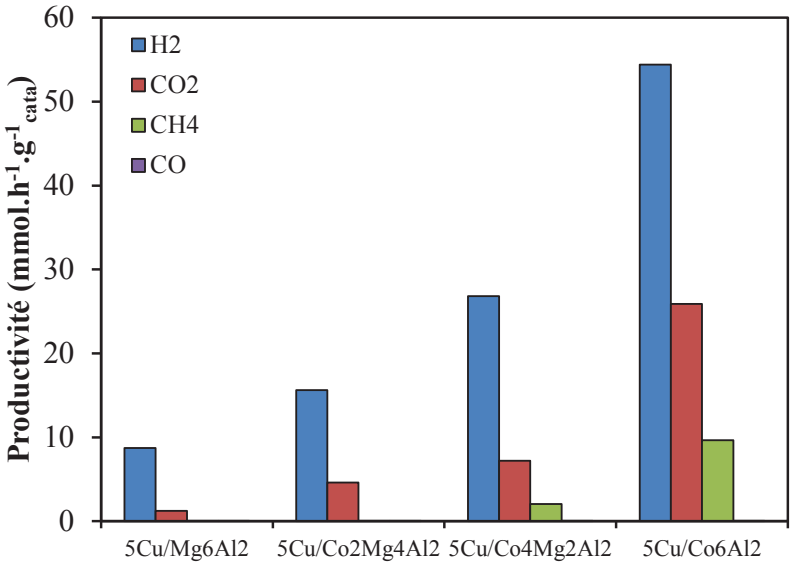

Figure 7 Productivités en H_2, CO_2, CH_4 et CO (mmol.h^{-1}.g^{-1}_{cata}) à 450°C en présence des catalyseurs 5Cu/$Co_xMg_{6-x}Al_2$ (S/C= 1.5)

Afin d'optimiser la teneur en cuivre dans la réaction de vaporeformage de l'éthanol, des catalyseurs contenant 0.5, 3, 5, 15 et 5% en masse de Cu déposés sur le support le plus performant Co_6Al_2 ont été évalués. Les résultats ont montré que la quantité d'hydrogène augmente avec l'augmentation de la teneur en métal de 0.5% jusqu'à 5% en masse, puis elle diminue avec les teneurs les plus élevées. L'analyse des condensats montre que l'éthanol est 100% converti pour tous les catalyseurs et des traces d'acétaldéhyde sont présentes à l'exception d'une importante quantité détectée d'acétaldéhyde et de l'acétone en présence de 0.5Cu/Co_6Al_2. La diminution de la performance catalytique avec l'augmentation de la teneur de la phase active est due à des agglomérats de CuO présents dans le cas des catalyseurs 15Cu/Co_6Al_2 et 25Cu/Co_6Al_2 détectés par DRX avant test. On peut conclure que la teneur optimal est 5% en masse de cuivre déposé sur le support Co_6Al_2.

Les productivités des produits gazeux en présence du catalyseur 5Cu/Co_6Al_2 et en utilisant différents rapports H_2O/C égal à 0.75; 1.5 et 3 ont montré que les productivités en H_2 et CO_2 augmentent avec l'augmentation du rapport. La productivité en méthane est presque similaire pour les trois différents rapports et le CO est présent en quantités négligeables. L'ajout

d'eau au mélange réactionnel favorise donc la réaction de gaz à l'eau, conduisant à la diminution de la concentration en CO et l'augmentation de la concentration en H_2 et CO_2 ce qui justifie la forte activité du catalyseur lorsque le rapport H_2O/C est plus élevé. D'autre part, quelle que soit le rapport introduit, l'éthanol est complètement converti, et des traces de sous-produits sont détectées.

Enfin, la stabilité des catalyseurs $5Cu/Co_6Al_2$ et $5Cu/Co_2Mg_4Al_2$ catalyseurs est étudiée pendant une période de 50 h à 450°C. $5Cu/Co_6Al_2$ a désactivé après 20 heures alors que $5Cu/Co_2Mg_4Al_2$ montre une plus grande stabilité malgré la diminution de la productivité en H_2.
Pour expliquer ces performances catalytiques, des analyses thermogravimétriques ont été effectuées sur ces 2 catalyseurs après test. Tout d'abord, il faut noter qu'une différence importante est envisagée en comparant les pertes de masse des 2 catalyseurs. Cette perte de masse est due à l'oxydation des espèces carbonées déposées sur les catalyseurs. La quantité de ces espèces sur $5Cu/Co_6Al_2$ est beaucoup plus élevée que sur l'autre catalyseur. Ce qui peut expliquer la désactivation plus rapide de $5Cu/Co_6Al_2$ après seulement 20 heures. D'autre part, $5Cu/Co_2Mg_4Al_2$ qui montre une faible quantité d'espèces de carbone et qui ne désactive pas même après 50 heures, contient des oxydes de magnésium détectés par DRX qui sont bien connus pour leurs propriétés basiques qui diminue la formation du dépôt de carbone. De plus, un double pic exothermique entre 300°C et 360°C présenté pour les 2 catalyseurs est dû à une oxydation en deux étapes du carbone graphitique déposé sur des endroits différents du catalyseur au cours de la réaction. En fait, le premier pic exothermique est associé à une oxydation rapide des espèces carbonées de surface tandis que le second pic correspond à l'oxydation des espèces carbonées de masse.

Les spectres RPE enregistrés à température ambiante pour le catalyseur $5Cu/Mg_6Al_2$ après test en isotherme à 450°C a montré la présence des espèces de carbonées formées à la surface du catalyseur au cours de la réaction. De plus, l'intensité des espèces de Cu^{2+} diminue après la réaction en raison de leur réduction en Cu^+ et Cu^0.

6 Conclusion

Enfin, ce travail de thèse a porté sur l'étude des performances de catalyseurs à base de ruthénium ou à base de cuivre supportés sur des hydrotralcites pour les réactions de vaporeformage du méthane et de l'éthanol. Les premiers tests exploratoires de la réaction du vaporeformage du méthane ont permis de fixer la teneur optimale de ruthénium sur le support

Co_6Al_2 à 1% en masse. Lorsque la teneur en métal est plus élevée, une partie des sites métalliques ne participe pas à la réaction. Aucun prétraitement sous hydrogène n'a été choisi ce qui réduit le temps et le coût du procédé. Néanmoins, il semble que des rapports H_2O/CH_4 supérieurs à la stœchiométrie soient nécessaires pour éviter la formation de coke lors du test. Une bonne stabilité des catalyseurs lors d'un test de plusieurs dizaines d'heures a été mise en évidence. Une grande réactivité a été observée pour les systèmes catalytiques développés au laboratoire par rapport aux catalyseurs industriels, testés dans les mêmes conditions opératoires. Enfin, la présence du carbone et du coke issus des réactions de Boudouard et décomposition du méthane respectivement a pu être identifiée.

Concernant le vaporeformage de l'éthanol, $5Cu/Co_6Al_2$ était le plus performant du point de vue conversion de l'éthanol et la productivité en hydrogène mais il se désactive après 20 heures de réaction à cause de la grande quantité d'espèces carbonées formée. $5Cu/Co_2Mg_4Al_2$ est moins performant mais résiste mieux au dépôt de carbone à cause de la basicité du support. Par conséquent, $5Cu/Co_4Mg_2Al_2$ catalyseur pourrait être un bon compromis entre une forte activité et le dépôt carboné faible.

En perspective, il serait intéressant d'élargir ce travail du point de vu étude cinétique et variation de la pression dans le réacteur en présence d'oxygène. Il faudrait faire des études de chimisorption d'hydrogène en vue de déterminer la dispersion des espèces actives. En outre, il serait intéressant d'effectuer des mesures d'acido-basicité sur les échantillons afin de mesurer la présence de sites basiques.

7 Références

[1] A. Fonseca, E.M. Assaf, Production of the hydrogen by methane steam reforming over nickel catalysts prepared from hydrotalcite precursors, Journal of Power Sources, 142 (2005) 154-159

[2] S. Rasi, A. Veijanen, J. Rintala, Trace compounds of biogas from different biogas production plants, Energy, 32 (2007) 1375-1380

[3] A. Denis, W. Grzegorczyk, W. Gac, A. Machocki, Steam reforming of ethanol over Ni/support catalysts for generation of hydrogen for fuel cell applications, Catalysis Today, 137 (2008) 453-459

[4] T. Caillot, P. Gelin, J. Dailly, G. Gauthier, C. Cayron, J. Laurencin, Catalytic steam reforming of methane over La0.8Sr0.2CrO3 based Ru catalysts, Catalysis Today, 128 (2007) 264-268

[5] L. Zhou, Y. Guo, Q. Zhang, M. Yagi, H.B. Li, J. Chen, Self-activation and self-regenerative

activity of trace Ru-doped plate-type anodic alumina supported nickel catalysts in steam reforming of methane, Catalysis Communication, 10 (2008) 325-329
[6] J.G. Jakobsen (2010). Noble metal catalysts for methane steam reforming. Technical University of Denmark
[7] S. Cavallaro, S. Freni, Ethanol steam reforming in a molten carbonate fuel cell. A preliminary kinetic investigation, International Journal of Hydrogen Energy, 21 (1996) 465-469
[8] M. Ni, D.Y.C. Leung, M.K.H. Leung, A review on reforming bio-ethanol for hydrogen production, International Journal of Hydrogen Energy, 32 (2007) 3238-3247
[9] Y. Zhan, D. Li, K. Nishida, T. Shishido, Y. Oumi, T. Sano, K. Takehira, Preparation of "intelligent" Pt/Ni/Mg(Al)O catalysts starting from commercial Mg-Al LDHs for daily start-up and shut-down steam reforming of methane, Applied Clay Science, 45 (2009) 147-154
[10] G. Busca, U. Costantino, T. Montanari, G. Ramis, C. Resini, M. Sisani, Nickel versus cobalt catalysts for hydrogen production by ethanol steam reforming: Ni-Co-Zn-Al catalysts from hydrotalcite-like precursors, International Journal of Hydrogen Energy, 35 (2010) 5356-5366
[11] R.G. Lemus, J.M.M. Duart, Updated hydrogen production costs and parities for conventional and renewable technologies, International Journal of Hydrogen Energy, 35 (2010) 3929-3936
[12] A. Tanksale, J.N. Beltramini, G.M. Lu, A review of catalytic hydrogen production processes from biomass, Renewable and Sustainable Energy Reviews, 14 (2010) 166-182
[13] A. Bshish, Z. Yaakob, B. Narayanan, R. Ramakrishnan, A. Ebshish, Steam-reforming of ethanol for hydrogen production, Chemical Papers, 65 (2011) 251-266
[14] P.D. Vaidya, A.E. Rodrigues, Insight into steam reforming of ethanol to produce hydrogen for fuel cells, Chemical Engineering Journal, 117 (2006) 39-49

Enfin, ces travaux de recherche ont fait l'objet de: 3 publications parues, 6 communications orales et 6 communications par affiches.

3 Publications:

1- **Doris Homsi**, Samer Aouad, Cedric Gennequin, Antoine Aboukaïs and Edmond Abi-Aad, The effect of copper content on the reactivity of Cu/Co_6Al_2 solids in the catalytic steam reforming of methane reaction, Physics Procedia (2012). Acceptée.

2- **Doris Homsi**, Samer Aouad, Cedric Gennequin, Antoine Aboukaïs and Edmond Abi-Aad, Hydrogen production by methane steam reforming over Ru and Cu supported catalysts, Advanced Materials Research, 324 (2011) 453-456

3- **Doris Homsi**, Samer Aouad, John El Nakat, Bilal El Khoury, Pierre Obeid, Edmond Abi-Aad, Antoine Aboukaïs, Carbon black and propylene oxidation over $Ru/Ce_xZr_{1-x}O_2$ catalysts, Catalysis Communications, 12 (2011) 776-780

6 communications orales:

1- **Doris Homsi**, Samer Aouad, Cédric Gennequin, Antoine Aboukaïs and Edmond Abi-Aad., A novel Ruthenium based catalyst for methane steam reforming. Comparison with the widely used catalyst. "The International Conference on Material Science, Beirut – Lebanon, May 28 – 30, 2012".

2- **Doris Homsi**, Samer Aouad, Cédric Gennequin, Antoine Aboukaïs and Edmond Abi-Aad. Catalytic steam reforming of methane over Cu supported on $Co_{6-x}Mg_xAl_2$ oxides. "The "International Conference on Material Science, Beirut – Lebanon, May 28 – 30, 2012".

3- Ruba El-Khawaja, Samer Aouad, **Doris Homsi**, Bilal El Khoury, John El Nakat, Antoine Aboukaïs and Edmond Abi-Aad. Steam reforming of ethanol over Ru/Co_6Al_2 and Cu/Co_6Al_2 catalysts. "LAAS 18th International Science Meeting: New Discoveries in Science, Beirut – Lebanon, March 22 – 23, 2012".

4- Samer Aouad, Ruba El-Khawaja, **Doris Homsi**, Bilal El Khoury, John El Nakat, Antoine Aboukaïs and Edmond Abi-Aad. Hydrogen production by catalytic steam reforming of ethanol over Cu or Ru supported on Co_6Al_2 oxide. "The International Conference on Material Science, Beirut – Lebanon, May 28 – 30, 2012".

5- Samer Aouad, **Doris Homsi**, John El-Nakat, Edmond Abi-Aaad and Antoine Aboukaïs, Carbon Black and Propylene Oxidation Over $Ru/Ce_xZr_{1-x}O_2$ Catalysts. "5th International

Congress of Chemistry and Environment, Malaysia, May 27-29, 2011".

6- **Doris Homsi**, Samer Aouad, Hanna El-Nakat, Bilal El-Khoury, Edmond Abi-aad, Antoine Aboukaïs, Carbon Black and Propylene Oxidation over $Ru/Ce_xZr_{1-x}O_2$ Catalysts, "The 16th International Conference of the Lebanese Association for the Advancement of Science, Beirut – Lebanon, November 13-15, 2009".

6 communications par affiches:

1- **Doris Homsi**, Samer Aouad, Cédric Gennequin, Antoine Aboukaïs and Edmond Abi-Aad, Vaporeformage du méthane sur des catalyseurs à base de ruthénium supportés sur des oxydes Co-Mg-Al préparés par voie hydrotalcite. "Le Groupe d'Etude en Catalyse – GECat, Kerjouanno– France, 21 –24 mai, 2012".

2- **Doris Homsi**, Samer Aouad, Cédric Gennequin, Antoine Aboukaïs and Edmond Abi-Aad, Catalytic methane steam refroming over $Ru/Co_{6-x}Mg_xAl_2$ solids preapred by the hydrotalcite route. "7th International Conference on Environmental Catalysis, Lyon – France, 2 –6 septembre, 2012".

3- **Doris Homsi**, Samer Aouad, John El Nakat, Cedric Gennequin, Antoine Aboukaïs and Edmond Abi-Aad, Oxydation des suies et des COVs sur des catalyseurs à bases de Ruthneium. "Journée Interdisciplinaires de la Qualité de l'Air, Villeneuve d'Ascq- France, 2-3 fevrier, 2012".

4- **Doris Homsi**, Samer Aouad, Cédric Gennequin, Antoine Aboukaïs and Edmond Abi-Aad, Hydrogen Production by Methane Steam Reforming Over Ru and Cu Supported on Hydrotalcite Precursors. "Mediterranean Conference on Innovative Materials and Applications, Beirut – Lebanon, March 15 – 17, 2011".

5- **Doris Homsi**, Samer Aouad, Cedric Gennequin, Antoine Aboukaïs and Edmond Abi-Aad. Methane steam reforming over Cu catalysts prepared from hydrotalcites precursors.. "First Euro-Mediterranean Conference on Materials and Renewable Energies, Marrakech, Morocco, November 21-25, 2011".

6- **Doris Homsi**, Samer Aouad, Hanna El-Nakat, Bilal El-Khoury, Edmond Abi-aad, Antoine Aboukaïs, Carbon black and propylene oxidation over $Ru/Ce_xZr_{1-x}O_2$ catalysts, "Mediterranean Conference on Innovative Materials and Applications, Beirut – Lebanon, March 15-17, 2011".